Journal of Geophysical Research

Supporting Information for

Sounding of the Atmosphere using Broadband Emission Radiometry (SABER): Instrument and Science Measurement Description

The SABER Team

Contents of this file

This file contains the final report entitled SABER Ground Calibration delivered by the Space Dynamics Laboratory to the NASA Langley Research Center in June 2000. The report is included for future researchers to see the level of detail in calibration and performance assessment that was carried out on the SABER instrument prior to launch.

Contents of this file

SDL/99-155

SABER
Ground Calibration Report

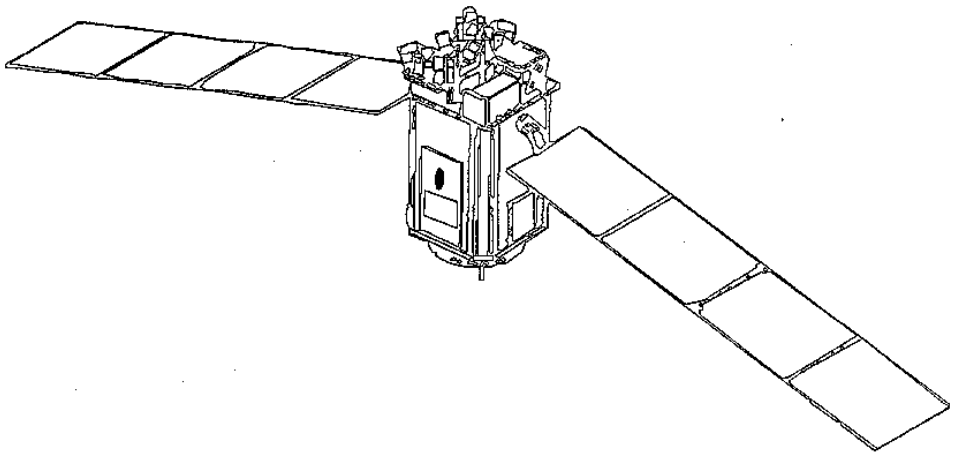

June 2000

Submitted to:
National Aeronautics and Space Administration
Langley Research Center
Hampton, VA 23681-0001

Contract No. NAS1-20467
Partial Fulfillment of DRD Item No. 19

FOREWORD

NASA Langley Research Center (LaRC) awarded contract NAS1-20467 to the Space Dynamics Laboratory at Utah State University (SDL/USU) to develop instrumentation for the Sounding of the Atmosphere using Broadband Emission Radiometry (SABER) investigation.

This report is submitted in compliance with the contract statement of work, DRD item 19, and the requirements of the "SABER Test and Calibration Plan" (SDL/97-069). It describes the test, data analysis, and results of ground calibration.

SDL/USU is responsible for ground calibration testing, data collection, and publication of this report. The data analysis and results shown in this report, however, are a shared effort between SDL/USU, GATS, and LaRC.

APPLICABLE DOCUMENTS

Joint LaRC-SDL/USU SABER proposal, submitted July 1992

Product Breakdown Structure Document, SDL/96-010

SABER Product Assurance Plan, SDL/94-088

SABER Instrument Requirements Document, SDL/95-006

SABER Instrument Specification, SDL/95-009

SABER Systems Engineering Management Plan, SDL/95-024

SABER Instrument Integration and Test Plan, SDL/97-020

TIMED Component Environment Specification, No. 7363-9010

TABLE OF CONTENTS

LIST OF FIGURES

Page

LIST OF TABLES

LIST OF EQUATIONS

1. INTRODUCTION

1.1 Sensor Description

The SABER instrument is a 10-channel earthlimb-viewing sensor that will measure atmospheric emissions in the 1 to 17 μm spectral range. The optical design consists of a high off-axis rejection telescope, a single-axis scan mirror, a chopper, filters, and 10 detector focal plane elements. The focal length of the telescope is 200 mm with an f-number of 2. Each detector, or channel, is spectrally filtered to a unique passband. The fields of view of the 10 detectors are scanned over the earthlimb by means of a one-axis scan mirror to produce vertical spectral radiance profiles of the mesosphere and lower thermosphere.

The focal plane assembly is cooled to 75 K with a miniature pulse-tube refrigerator, and the telescope is cooled to 240 K with a radiator plate. Each detector has an instantaneous field of view (IFOV) of 0.7 by 10 mrad. The 0.7 mrad angular detector width gives a vertical footprint on the earthlimb of approximately 2 km for a 60 km tangent height look angle and 625 km orbit. The scan mirror velocity and detector sample rate give 5 samples per detector IFOV. The angular range of the scan mirror is approximately 16°, allowing SABER to look from cold space to hard earth.

The electrical signals from each of the 10 channels are preamplified and coherently rectified using phase-lock amplifiers synchronized with the chopper. Each channel is multiplexed to a single 12-bit analog-to-digital converter. All 10 channels have a high gain setting; however, additional gain settings are provided for low gain operation.

The instrument contains an in-flight calibrator (IFC) to verify or update sensor calibration during on-orbit operations. During data collection, the scan mirror will periodically rotate to view either cold space (400 km tangent height look angle), a full-aperture blackbody, or tungsten lamps. The cold space view will measure the sensor's dark offset, the full-aperture blackbody view will measure responsivity of long wavelength channels (channels 1 through 7), and the tungsten lamp view will measure responsivity of short wavelength channels (channels 8, 9, and 10).

1.2 Calibration Approach

Radiometric sensors require calibration to verify proper instrument operation, to create algorithms for data reduction, and to estimate measurement uncertainties. The approach used by SDL/USU, GATS, and LaRC involves characterizing the overall responsivity of the sensor in terms of separate radiometric parameters. These parameters are (1) absolute responsivity over the sensor's dynamic range, (2) spectral responsivity, (3) spatial responsivity, and (4) temporal responsivity. The goal of the calibration is to characterize each radiometric parameter independently of the others. Together, these individually characterized radiometric parameters comprise a complete calibration of the radiometric sensor (Wyatt, 1978).

The calibration equation for the SABER instrument relates sensor output to measured flux. The measured flux is then related to the true scene flux using calibration parameters from the radiometric model. This step is accomplished by modeling the interaction of the scene with the sensor and comparing the expected outcome to the measured flux. The calibration parameters that characterize the sensor, but are not part of the calibration equation, collectively form the radiometric model.

SABER calibration parameters are grouped into two categories: parameters for the calibration equation and parameters for the radiometric model.

1.3 Data Collection

Data collection procedures were developed prior to data collection. They were then filled out in real time during the test. This was done to document data collection, ensure data collection repeatability, and optimize data collection efficiency.

During calibration testing, the test conductor followed the procedure, made appropriate changes (if required), filled in log entries, and recorded events that may affect the data. These completed procedures are documented in “SABER Ground Calibration and Preliminary Results” (SDL/98-059).

1.4 Measurement Uncertainties

A complete calibration includes estimates of measurement uncertainties. The approach is to generate a list of uncertainties and descriptions of their applicability to any particular measurement objective. The data analyst must choose appropriate terms to be included. There are several general classes of uncertainties that must be addressed. Among these are random uncertainties, calibration residual uncertainties, nonideal sensor performance uncertainties, and standard source uncertainties (Wyatt, 1991). Random uncertainties include short-term repeatability (noise) and long-term repeatability. Calibration residual uncertainties are uncertainties associated with parameters in the calibration equation, such as the uncertainty of a gain mode normalization parameter. Nonideal sensor performance uncertainties are a result of nonideal sensor characteristics and are addressed in the radiometric model. For example, the radiometric model of the radiometer will characterize the relative spectral responsivity for each channel, which is expected to have some variation across the passband. This variation across the passband gives rise to an uncertainty of absolute flux, unless the spectral distribution of the target is known. Standard source uncertainties include uncertainty in the temperature and emittance of blackbody simulators.

In general, SDL/USU personnel will follow the recommended terminology and practices of the International Organization for Standardization (ISO) in expressing uncertainties (ISO, 1992). Some of these recommendations include (1) reporting all uncertainties as standard uncertainties (i.e., one standard deviation), (2) combining (uncorrelated) uncertainties using the square root of the sum of the squares of the individual standard uncertainties, and (3) using the following equa-

tion to estimate type A uncertainties (type A uncertainties are those that are evaluated using statistical analysis of the results of repeated measurements).

$$S = \sqrt{\frac{\sum (x - \bar{x})^2}{n - 1}} \tag{1}$$

1.5 SABER Measurement Requirements Driving Calibration

The SABER measurement requirements for calibration were determined from the "SABER Instrument Requirements Document" (SDL/95-006), and are summarized in Table 1.

Table 1. SABER instrument measurement requirements driving calibration

Parameter	Instrument Measurement Requirement
System Noise Equivalent Radiance (NER)	Refer to IRD
Radiometric Accuracy[a]	5.0% absolute radiance; 3.0% goal
Long-Term Radiometric Precision[a]	2.0% radiance precision; 1.0% goal
Radiance Bias Drift	≤ 1 NER between space looks (duration of approximately 2.3 min)
Residual Scale Error	≤ 1% linearity over dynamic range
Limb Scan Mirror Jitter (1 σ)	≤ 3 arc seconds
Spectral Response	Refer to IRD
IFOV @ 60 km Earthlimb Tangent Height	2 km FWHM
Limb Vertical Scan Range	Minimum and maximum depression angle to give an on-orbit scan range of -3 km to 400 km
Measurement Altitude Range	10 km to 180 km
Focal Plane Channel Location	Refer to IRD
Boresight Alignment Knowledge	0.1°
Signal Measurement Dynamic Range	Refer to IRD
Limb Vertical Sampling Interval	0.4 km

a. For SNR > 100,% is defined as a percentage of the signal. For SNR ≤ 100, % is defined as a percentage of the signal that produces SNR = 100.

Table 2 shows a matrix of calibration parameters versus instrument measurement requirements. The cells with an X indicate the instrument requirement driving the particular calibration measurement.

1.6 Calibration Test Facility

A calibration test facility was designed and built to measure individual parameters of the calibration equation and radiometric model. For all radiometric testing, the SABER calibration test facility, shown in Figure 1, consisted of a test chamber interfaced with a collimator. SABER was

Table 2. Calibration measurements versus instrument measurement requirement matrix

Calibration Measurement Parameter	Measurement Requirement													
	NER	Radiometric Accuracy	Long-Term Radiometric Precision	Radiance Bias Drift	Residual Scale Error	Limb Scan Mirror Jitter (1 σ)	Spectral Response	IFOV @ 60 km	Limb Vertical Scan Range	Measurement Altitude Range	Focal Plane Channel Location	Boresight Alignment Knowledge	Signal Measurement Dynamic Range	Limb Vertical Sampling Interval
Radiance Responsivity	X	X												
IFC Radiance		X												
Off-Axis Extended Source Throughput Correction		X												
Linearity		X			X									
Gain Mode Normalization		X												
IFC Measurement Long-Term Repeatability			X											
Noise Equivalent Radiance (NER)	X													
Medium-Term Repeatability of Sensor Offset				X										
Saturation Equivalent Radiance (SER)													X	
Relative Spectral Responsivity (RSR)		X					X							
Sensor Boresight												X		
Instantaneous Field of View (IFOV)								X			X			X
Near Angle Scatter		X												
Scan Mirror Transfer Function						X			X	X				
Knife Edge Response		X												
Temporal Frequency Response														X

mounted and operated in the test chamber that also provided blackbody and knife edge calibration sources. The full field collimator provided source configurations for relative spectral response, IFOV, near angle scatter, short wavelength linearity, and temporal frequency response measurements. Detailed specifications for SABER GSE hardware and software are described in an SDL report entitled “SABER Ground Support Equipment Documentation” (SDL97-070). This section provides a top-level GSE hardware summary.

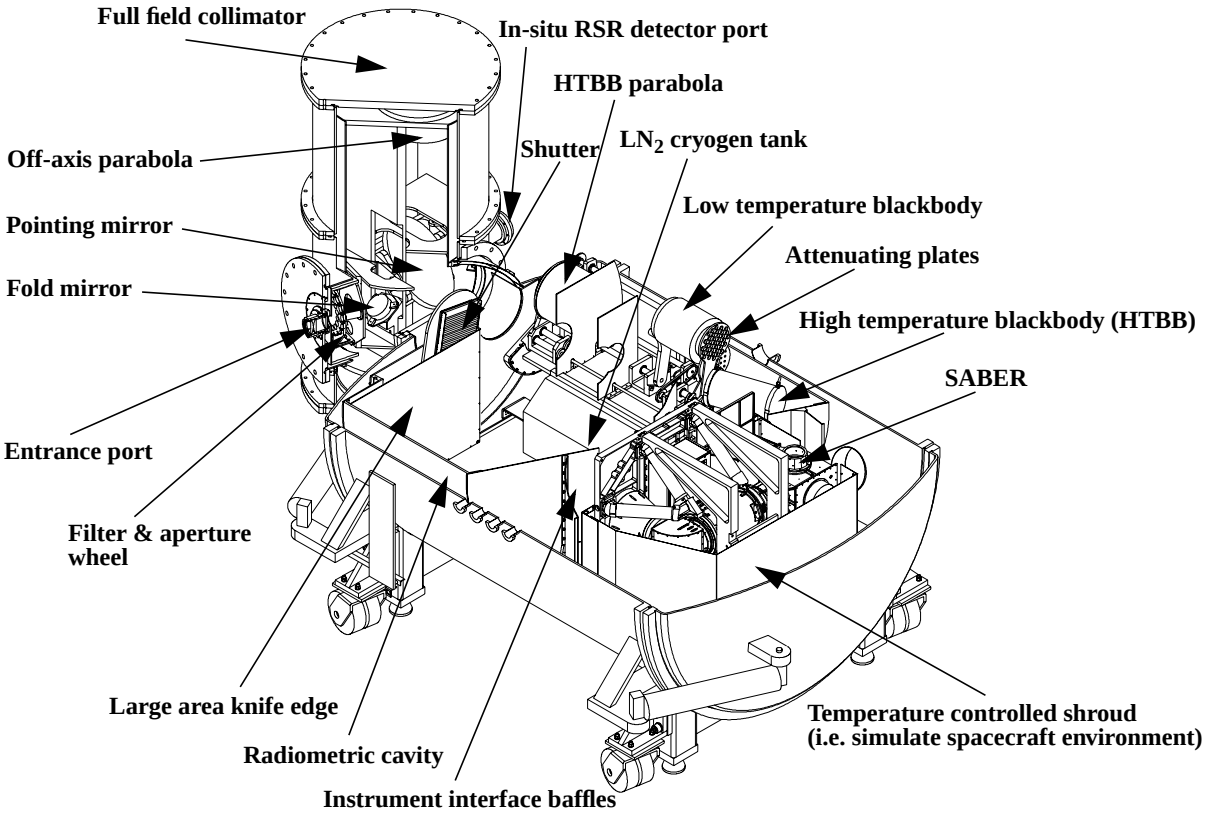

Figure 1. Calibration test facility

1.6.1 GSE Test Chamber

Figure 1 shows how SABER was mounted and operated inside the GSE test chamber. The instrument was thermally controlled in the test chamber to simulate on-orbit operating temperatures. Thermal control was achieved through the use of a liquid nitrogen-cooled cold plate and trim heaters. The cold plate was used to cool the instrument's radiator by radiative heat transfer. Trim heaters were then used to control the temperature of the instrument.

Inside the GSE test chamber, SABER viewed a cryogenically cooled, light-resistant radiometric cavity. Liquid nitrogen was used to cool the radiometric cavity to approximately 90 K. All internal surfaces of the radiometric cavity were painted with Aeroglaze Z306 optical black paint. The design of the cavity interface allowed SABER to rotate about the SABER scan mirror axis for equivalent on-orbit tangent-height look angles.

Calibration sources were housed inside the radiometric cavity of the test chamber and consisted of low- and high-temperature blackbodies and a large area knife edge. When in use, the low temperature blackbody or an off-axis parabola used to image the high temperature blackbody was

rotated in front of SABER. Detailed information on the design and performance of the low and high temperature blackbodies are described in “SABER GSE Low Temperature Blackbody Calibration Source” (SDL/98-112) and “Instruction Manual for Model M360XHTVBB Blackbody Calibration Source” (Mikron Instrument Company). In addition, cryogenically cooled attenuating plates were rotated between SABER and the blackbodies to provide approximately 50%, 90%, and 100% attenuation depending on the combination of plates being used. These data were used to verify linearity of the long wavelength channels (channels 1 to 7).

The angular dimensions of the large area knife edge were 24° in-scan by 34° cross-scan. These angular dimensions were sufficient to overfill SABER’s pointing mirror with off-axis flux. The knife edge distance from SABER produced a geometric blur radius of nearly 1.4° (about equal to the angular dimensions of the focal plane array). The knife edge was heated to 300 K to simulate off-axis flux from the earth during on-orbit operations. The shutter located inside and at the end of the radiometric cavity was closed during the knife edge test. Because the shutter was off-axis to the large area knife edge and was viewed by SABER, it was cooled with liquid nitrogen and cavity enhanced to minimize stray radiation.

1.6.2 Full-Field Collimator

As shown in Figure 1, the full field collimator was interfaced to the exit port of the GSE test chamber.

The collimator was designed to (1) limit the aperture size at the focus of the collimator to less than 0.75 in. when providing a source that overfills a detector element and (2) provide sufficient image quality to characterize each channel’s IFOV. The collimator provided calibration source configurations for relative spectral response, IFOV, near angle scatter, short wavelength linearity, and temporal frequency response measurements.

To limit the cost of the full-field collimator, its optical design used a single-axis pointing mirror, an off-axis parabola, a fold mirror, a filter wheel, and an aperture wheel. Compared to designs with multiple powered elements, an optical design with a single powered element reduces both the cost of manufacturing the mirrors and the difficulties associated with optical alignment. The current optical design contains a single-axis pointing mirror with an angular range of ±1.6° for the instrument’s cross-scan direction. The focal length of the parabola is 1055.25 mm (~41.5 in).

2. RADIOMETRIC CALIBRATION EQUATION

The calibration equation is used to relate sensor output to measured flux. The SABER calibration equation is shown in Equation (2).

$$L_m = \frac{1}{\Re_{ch}} r_{c,ch} = \frac{1}{\Re_{ch}} [\Upsilon_{ch,i}(Scn) L_{ch,i} G_{ch,i} (r_{ch,i} - O_{ch,i})] \quad (2)$$

where
L_m = measured radiance (W cm^{-2} sr^{-1})
$\Re_{ch}$ = peak radiance responsivity (counts/W cm^{-2} sr^{-1})
$\Upsilon_{ch,i}(\ )$ = off-axis extended source throughput correction (unitless)
Scn = scan mirror pointing position (counts)
$r_{c,ch}$ = corrected scene response (counts)
$L_{ch,i}(\ )$ = linearity correction (unitless)
$G_{ch,i}$ = gain mode normalization (unitless)
$r_{ch,i}$ = detector response (counts)
$O_{ch,i}$ = sensor offset (counts)
ch = channel number (1 to 10)
i = gain mode (unitless)

Table 3 lists the calibration equation parameters.

Table 3. Calibration equation parameters

Parameter	Symbol	Measurement Requirement	Report Section	Test Configuration
Sensor Offset (Space Look)	$O_{ch,i}$	Radiometric Accuracy	Section 2.1 "Sensor Offset"	Low Temperature BB
Linearity Correction Function	$L_{ch,i}(\ )$	Radiometric Accuracy Residual Scale Error	Section 2.3 "Peak Radiance Responsivity and Response Linearity"	Low Temperature BB & Full Field Collimator
Gain Mode Normalization	$G_{ch,i}$	Radiometric Accuracy	Section 2.2 "Gain Mode Normalization"	Electronics Subassembly
Peak Radiance Responsivity	$\Re_{ch}$	Radiometric Accuracy	Section 2.3 "Peak Radiance Responsivity and Response Linearity"	GSE Full-Aperture Blackbody
Off-Axis Extended Source Throughput Correction as a Function of Scan Mirror Position	$\Upsilon_{ch,i}(scn)$	Radiometric Accuracy	Section 2.6 "Off-Axis Extended Source Throughput Correction"	GSE Full-Aperture Blackbody

The responsivity coefficient for each channel, $\Re_{ch}$, will be updated periodically during on-orbit operations. This update will be based on a space look to characterize the sensor offset and an in-flight calibrator (IFC) look to measure the sensor response to a known flux. To calibrate the IFC sources, SABER's response was first calibrated with an external ground-based calibration source. This calibration can be transferred to the IFCs by relating the calibrated sensor response to IFC source levels.

The updated responsivity coefficient may be calculated using Equation (3).

$$\Re_{ch} = \frac{r_{c,IFC}}{N_{IFC}} \tag{3}$$

where $\Re_{ch}$ = updated peak radiance responsivity in counts/W cm^{-2} sr^{-1}

$r_{c,IFC}$ = corrected IFC response in counts

N_{IFC} = IFC radiant flux in W cm^{-2} sr^{-1}

ch = channel number (1 to 10)

The on-orbit scene flux is estimated by substituting the updated peak radiance responsivity, shown in Equation (3), into Equation (2). Calibration parameters for each IFC are listed in Table 4.

Table 4. IFC calibration parameters

Parameter	Symbol	Measurement Requirement	Report Section	Test Configuration
IFC Radiance	N_{IFC}	Radiometric Accuracy	Section 2.4 "In-Flight Calibrator (IFC) Radiance"	Low & High Temperature BBs

2.1 Sensor Offset

Sensor offset was evaluated using data obtained from low temperature blackbody (LTBB) measurements documented in “SABER Ground Calibration and Preliminary Results” (SDL/98-059). For these measurements, SABER viewed the LTBB when it was being operated at a stable 110 K temperature. Offset measurements were repeated at multiple telescope, focal plane, and baseplate temperature states, as shown in Table 5.

Table 5. Instrument temperature states for sensor offset measurements

Test #	Telescope (K) TT015V	Focal Plane (K) TF01VG2	Baseplate (K) TM07V
1	224.1 (nominal)	74.5 (nominal)	251.7 (nominal)
2	237.0 (worst case hot)	74.3 (nominal)	252.3 (nominal)
3	216.0 (worst case cold)	74.5 (nominal)	251.2 (nominal)
4	224.2 (nominal)	79.6 (expected worst case hot)	251.7 (nominal)
5	223.8 (nominal)	74.6 (nominal)	237.8 (worst case cold)
6	224.6 (nominal)	74.3 (nominal)	262.3 (worst case hot)

A direct measurement of sensor offset was not obtainable on channels 1 to 7. When viewing the LTBB, SABER’s response is a result of thermal emission of the blackbody, electronic offset, SABER internal thermal emission, and SABER thermal emission reflected off the face of the blackbody. Thermal emission of the LTBB with a temperature of 110 K gives a radiance larger than the noise equivalent radiance (NER) for channels 1 to 4. Although a 110 K blackbody has thermal emission below the NER for channels 5 to 7, a portion of the thermal emission from the instrument optics cavity at around 235 K is reflected off the face of the blackbody into SABER’s FOV. Because a 237 K blackbody (worst case hot telescope temperature) gives radiance below the NER for channels 8 to 10, a direct offset measurement was obtainable for these channels.

2.1.1 Electronic Offset

SABER contains one word for each channel, located in dual port memory, that sets the electronic offset. To measure the relationship between word setting and channel output, the dual port memory was varied between decimal values of 1024 and 3072 with an increment of 28 while viewing a stable 110 K blackbody. Eight packets of SABER data were collected at each word setting.

Figures 2 to 11 show the gain normalized response versus electronic offset word setting for each SABER temperature state and channel while viewing a stable 110 K blackbody. The electronic offset word setting is expressed in decimal units. For each temperature state, a linear curve fit was performed to quantify the relationship between channel response and electronic word setting. The slope of the curve fit is a scale factor with units of [counts/count] or delta change in channel response per delta change in electronic offset word setting by decimal value of 1. Table 6 gives the curve fit slope coefficients for each temperature state. Also shown is the mean and standard deviation of all temperature states. These results show the scale factor to be independent of SABER temperature state.

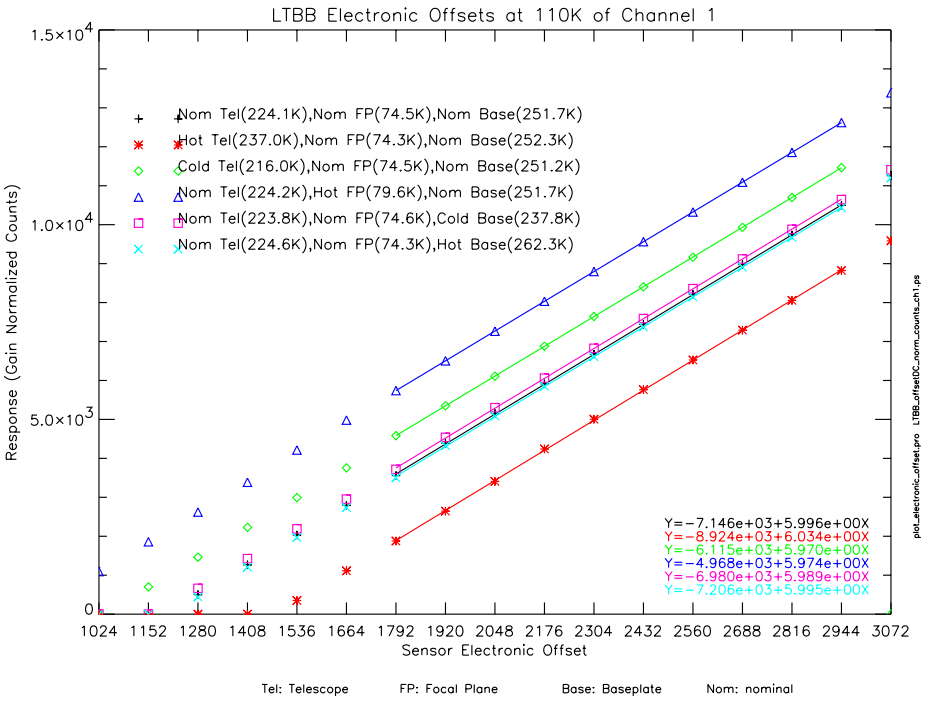

Figure 2. Electronic offset for channel 1

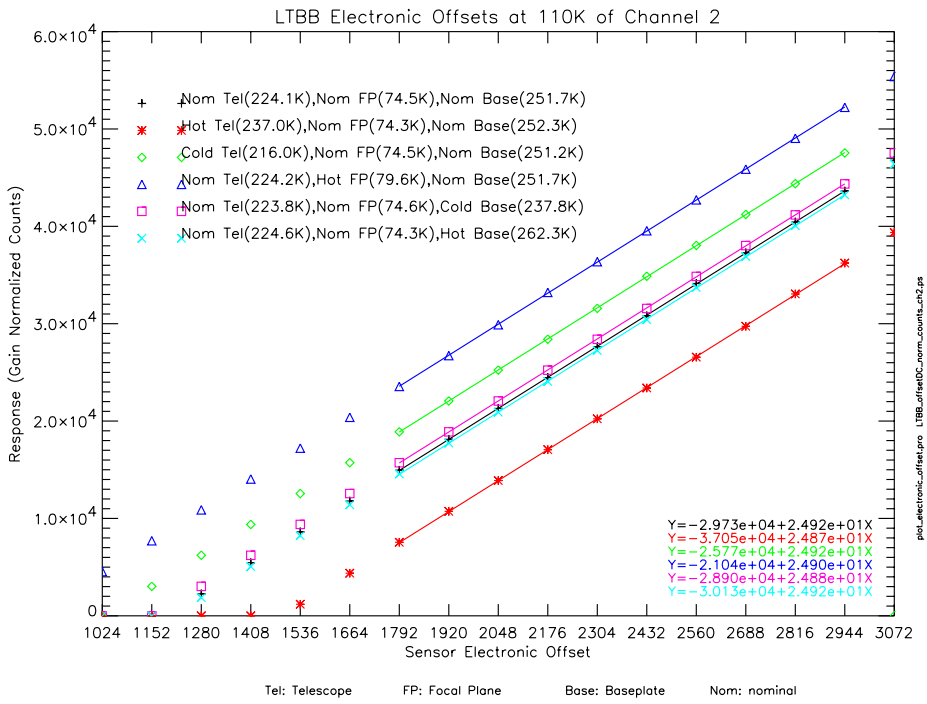

Figure 3. Electronic offset for channel 2

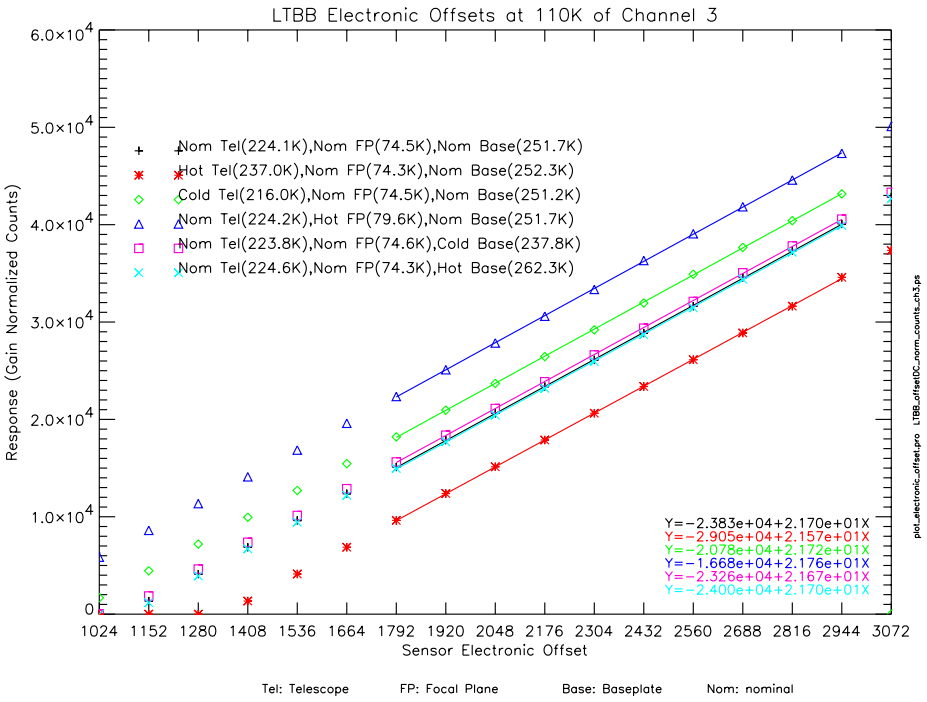

Figure 4. Electronic offset for channel 3

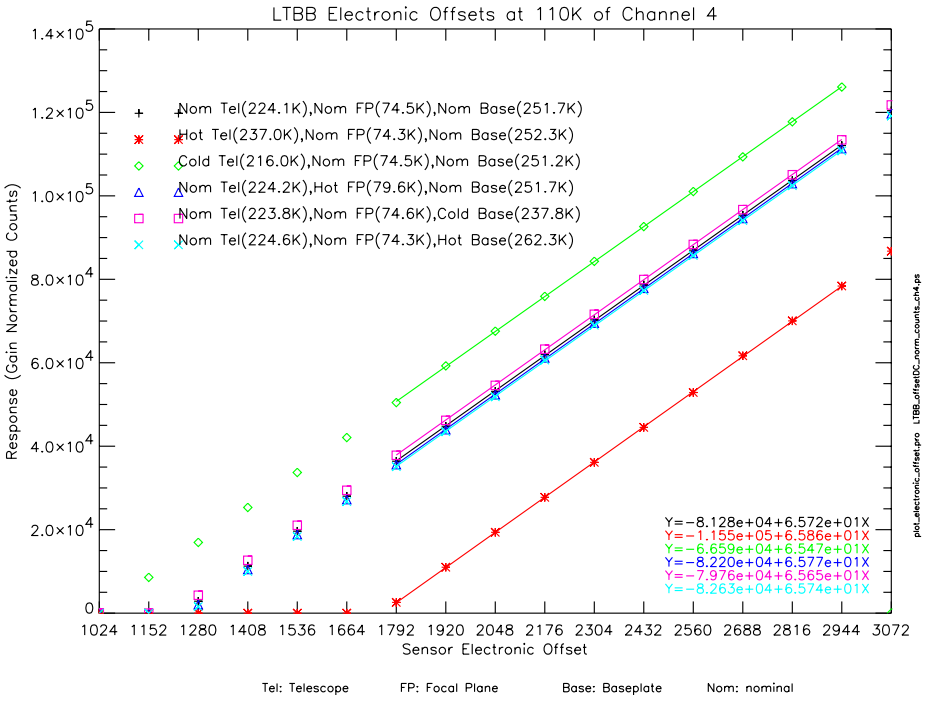

Figure 5. Electronic offset for channel 4

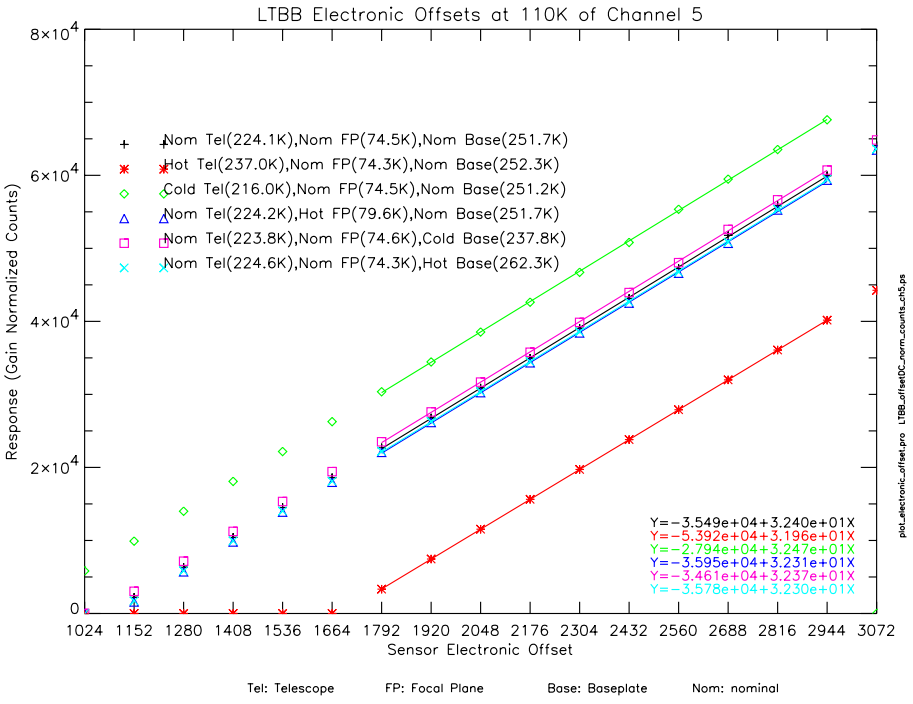

Figure 6. Electronic offset for channel 5

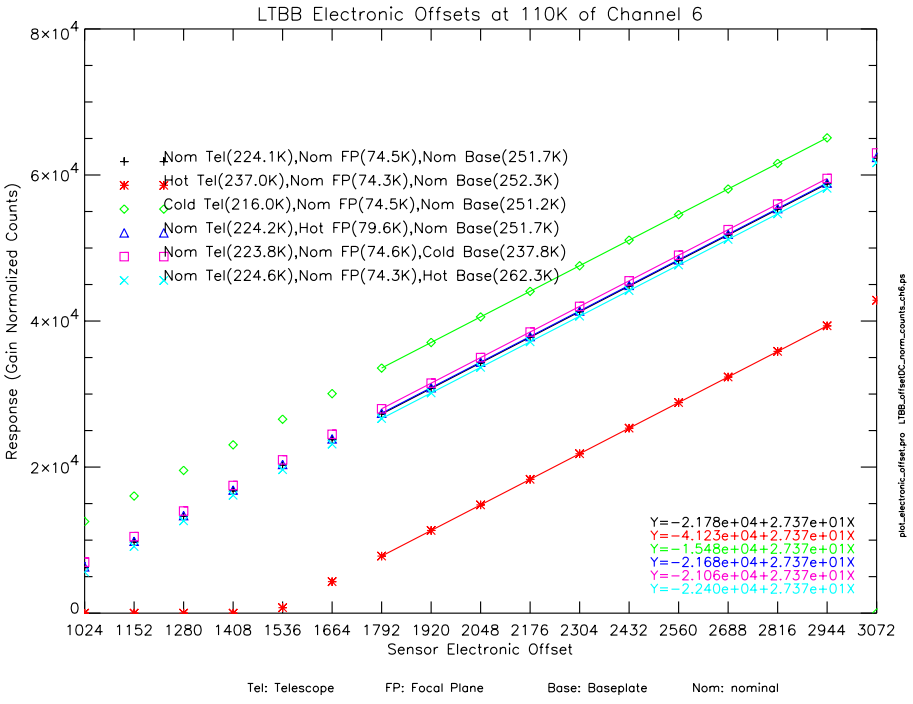

Figure 7. Electronic offset for channel 6

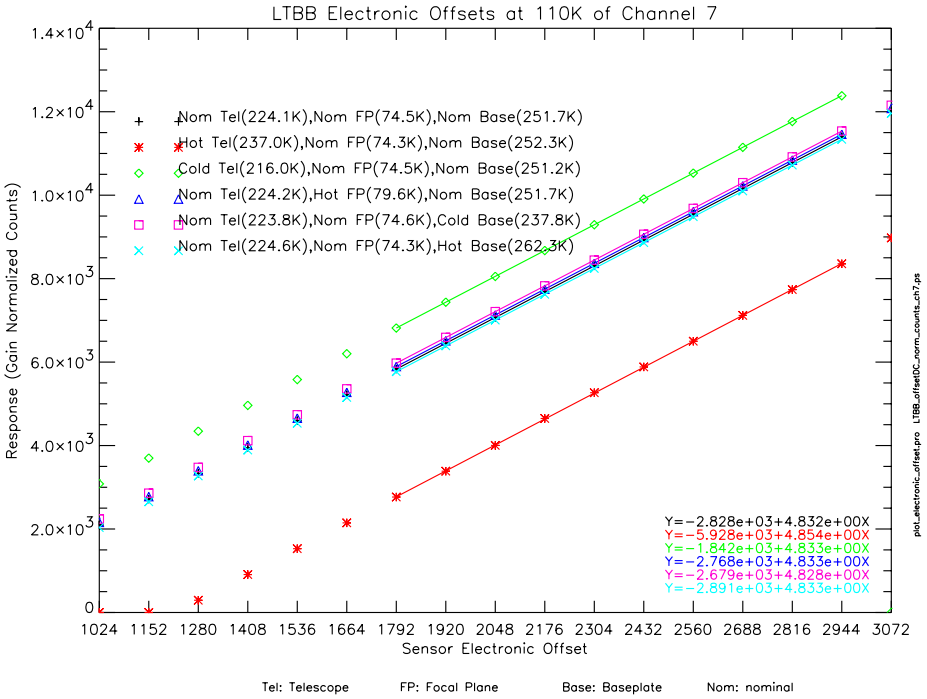

Figure 8. Electronic offset for channel 7

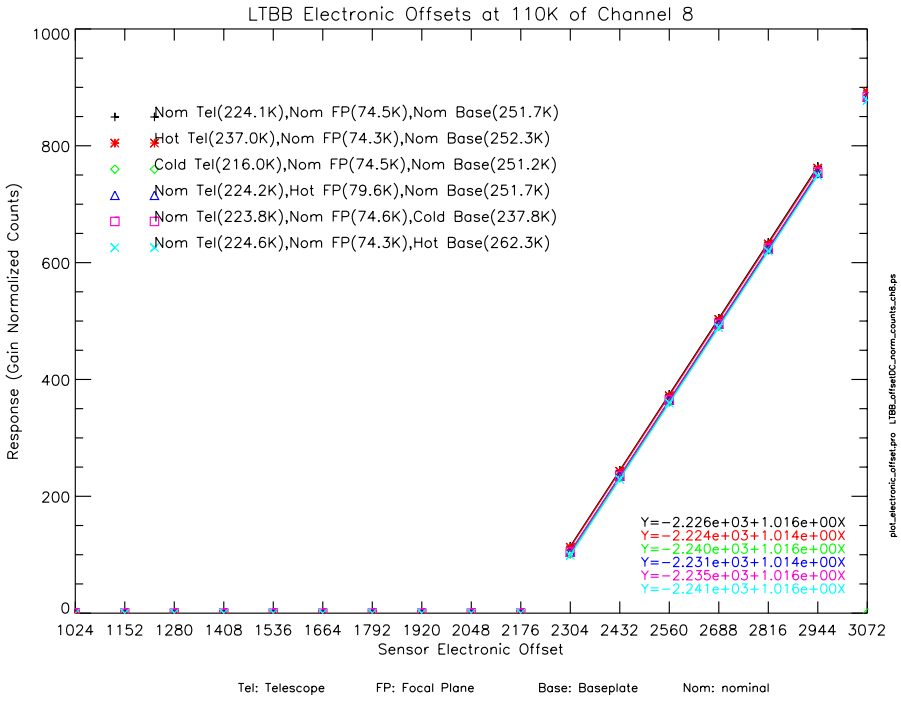

Figure 9. Electronic offset for channel 8

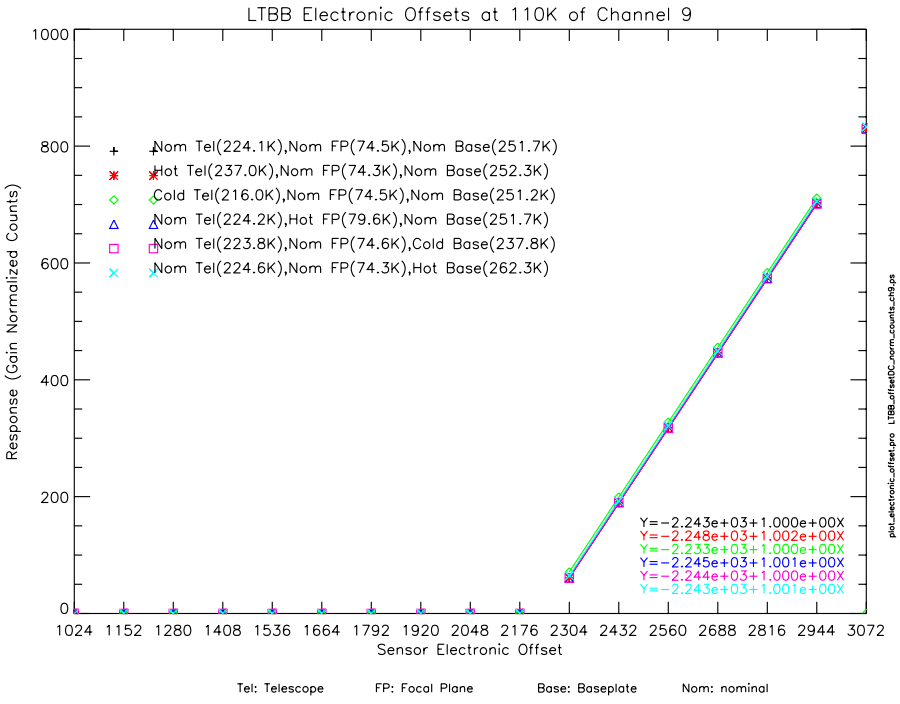

Figure 10. Electronic offset for channel 9

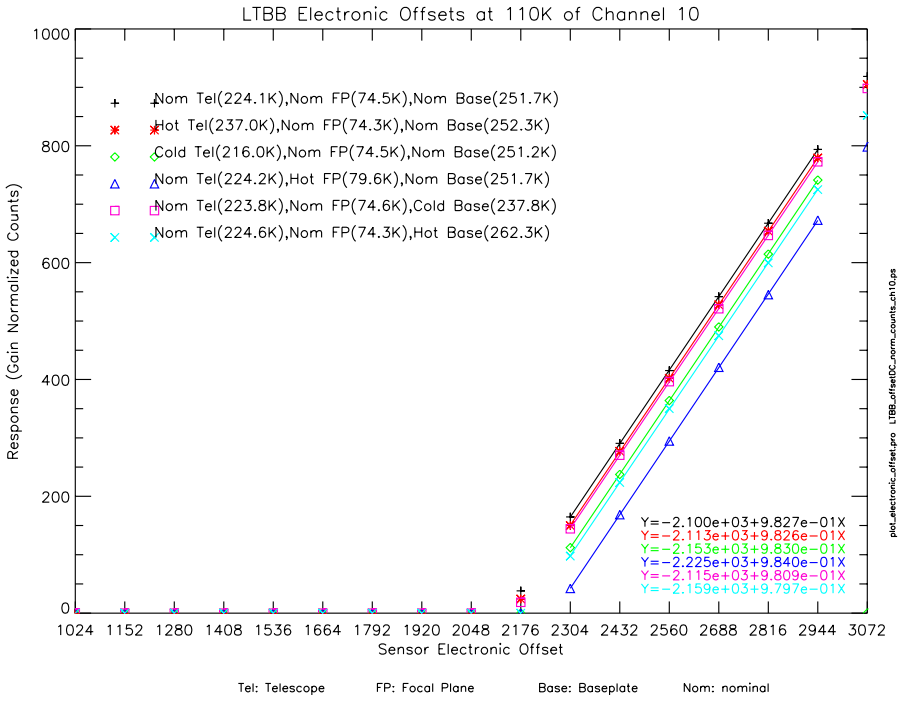

Figure 11. Electronic offset for channel 10

Table 6. Change in channel response per electronic word setting

Ch	Nominal Temp	Hot Focal Plane Temp	Cold Baseplate Temp	Hot Baseplate Temp	Cold Telescope Temp	Hot Telescope Temp	Combined	
	Slope[a]	Slope[a]	Slope[a]	Slope[a]	Slope[a]	Slope[a]	Mean[a]	Stdev[b]
1	6.00	5.97	5.99	6.00	5.97	6.03	5.99	0.0
2	24.92	24.90	24.88	24.92	24.92	24.87	24.90	0.0
3	21.70	21.76	21.67	21.70	21.72	21.57	21.69	0.1
4	65.72	65.77	65.65	65.74	65.47	65.86	65.70	0.1
5	32.40	32.31	32.37	32.30	32.47	31.96	32.30	0.2
6	27.37	27.37	27.37	27.37	27.37	27.37	27.37	0.0
7	4.83	4.83	4.83	4.83	4.83	4.85	4.84	0.0
8	1.02	1.01	1.02	1.02	1.02	1.01	1.02	0.0
9	1.00	1.00	1.00	1.00	1.00	1.00	1.00	0.0
10	0.98	0.98	0.98	0.98	0.98	0.98	0.98	0.0

a. units in [count/count] (i.e. Δ channel response per Δ electronic offset word setting)
b. units in [%] of mean

2.1.2 Offset as Function of SABER Temperature State

To predict the variation in channel output as a function of instrument temperature, a first order offset scale factor was calculated using electronic offset data as a function of telescope, focal plane, and baseplate temperatures. The offset scale factor was calculated using Equation (4).

$$\frac{\Delta Counts}{\Delta Temp}(wd, ch) = \frac{Count_{final}(wd, ch) - Count_{initial}(wd, ch)}{Temp_{final}(wd, ch) - Temp_{initial}(wd, ch)} \quad (4)$$

where

$\frac{\Delta Counts}{\Delta Temp}$ = offset scale factor (counts/K)

$Count$ = channel output (gain normalized counts)

$Temp$ = instrument temperature (K)

wd = electronic offset word setting (counts)

ch = channel (1,2,....10)

Table 7 shows the offset scale factor for each channel and SABER temperature state using multiple word settings to calculate the mean and standard deviation. As expected, these data show channel offset for the long wavelength channels (channels 1 to 7) to be dependent on SABER temperature state. In comparison, channel offset for the short wavelength channels (channels 8 to 10) have a small dependence on SABER temperature state.

Table 7. Offset scale factor as function of instrument temperature change

Ch	$\frac{\Delta Counts}{\Delta Temp}$									
	ΔTel (hot-nom) (counts/K)		ΔTel (cold-nom) (counts/K)		ΔFP (hot-nom) (counts/K)		ΔBase (cold-nom) (counts/K)		ΔBase (hot-nom) (counts/K)	
	mean	stdev	mean	stdev	mean	stdev	mean	stdev	mean	stdev
1[a]	-131	2	-120	2	417	4	-11	0	-6	0
2[a]	-577	5	-487	5	1693	14	-54	1	-37	1
3[a]	-428	7	-385	8	1430	17	-36	1	-15	1
4[a]	-2628	17	-1742	22	-156	5	-98	3	-122	2
5[a]	-1509	17	-953	18	-131	29	-58	1	-50	14
6[a]	-1508	0	-778	0	21	1	-52	0	-58	0
7[a]	-236	1	-122	0	12	0	-10	0	-6	0
8[b]	0	0	2	0	-2	0	1	0	-1	0
9[b]	0	0	-1	0	0	0	0	0	0	0
10[b]	-1	0	6	0	-24	0	1	0	-6	0

a. Word settings 1792 to 2994 used to calculate mean and standard deviation
b. Word settings 2304 to 2944 used to calculate mean and standard deviation

2.1.3 Relative Sensor Offset as Function of Scan Mirror Pointing Angle

The relative difference in sensor offset as a function of SABER scan mirror pointing angle was measured by viewing the 110 K LTBB for equivalent on-orbit tangent height look angles between 0 and 400 km. This was done by rotating SABER inside the test chamber and compensating for this rotation with the SABER scan mirror to ensure a normal blackbody view angle for each measurement. A total of 30 evenly spaced measurements were obtained for SABER scan mirror angles between 14 and 25 degrees. For each measurement, 8 packets of detector data were obtained and averaged. The test duration was approximately 13 minutes. These measurements were repeated for the SABER temperature states shown in Table 5.

For each channel and temperature state, the relative offset was plotted as a function of SABER scan mirror angle. These graphs are shown in Figures 12 to 21 where raw response is plotted versus SABER scan mirror angle. Because the electronic offset was set for each temperature state, the figure captions are titled “relative offset versus scan angle.” Therefore, these data can not be used to quantify offset as function of these SABER temperature states. What can be quantified, however, is the relative difference in sensor offset as function of scan angle.

For the hot telescope temperature state (i.e., worst case), Figures 12 to 21 show the peak offset variation to range from no systematic variation on channels 8 to 10 to about 70 counts for channel 4. The large variation on channel 4 is expected because channel 4 is the most sensitive to

telescope temperature. For the same responsivity value, longer wavelength channels will generally be more sensitive to telescope temperature. However, channel 4 is more responsive than channels 1 to 3 (longer wavelength channels), making it more sensitive to telescope temperature. No offset variation as a function of scan angle is expected for channels 8 to 10 because these channels are not sensitive to telescope temperature.

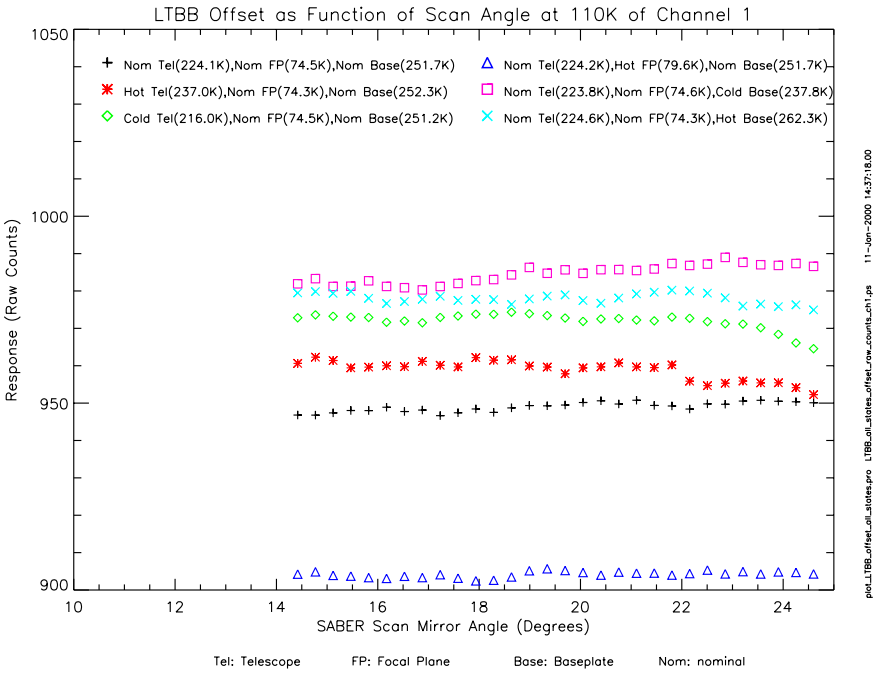

Figure 12. Relative offset versus scan angle for channel 1

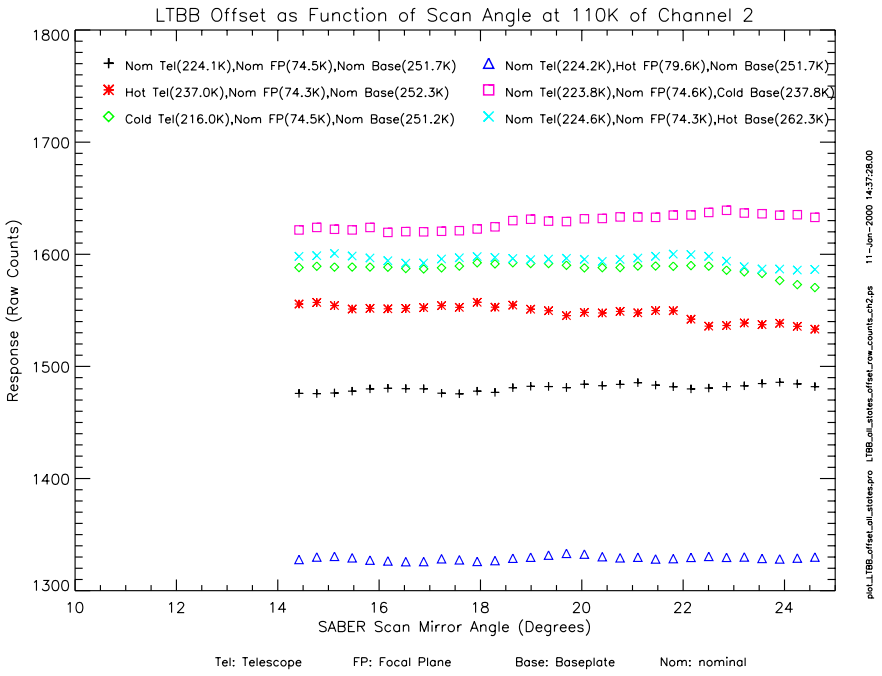

Figure 13. Relative offset versus scan angle for channel 2

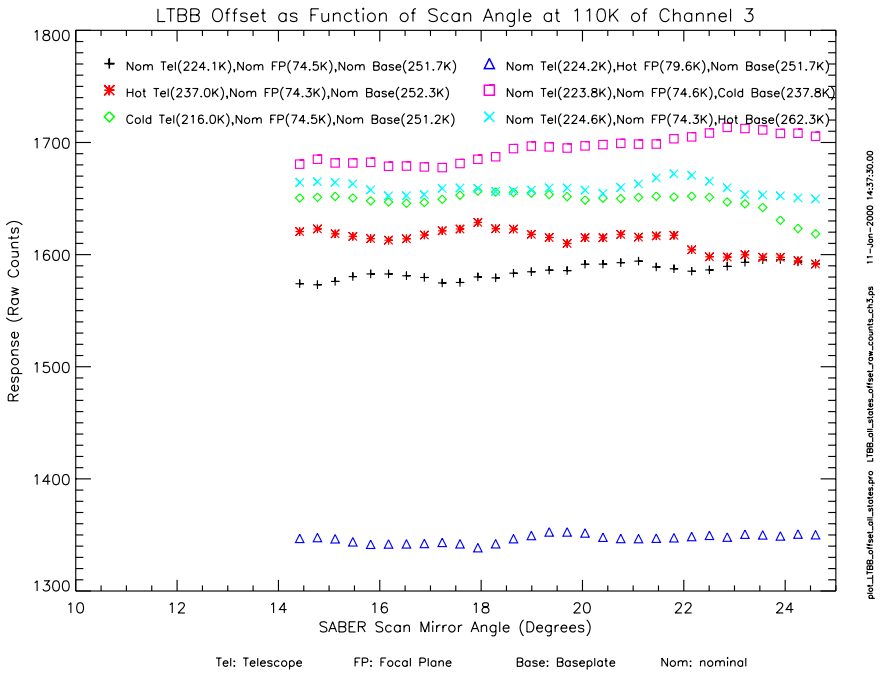

Figure 14. Relative offset versus scan angle for channel 3

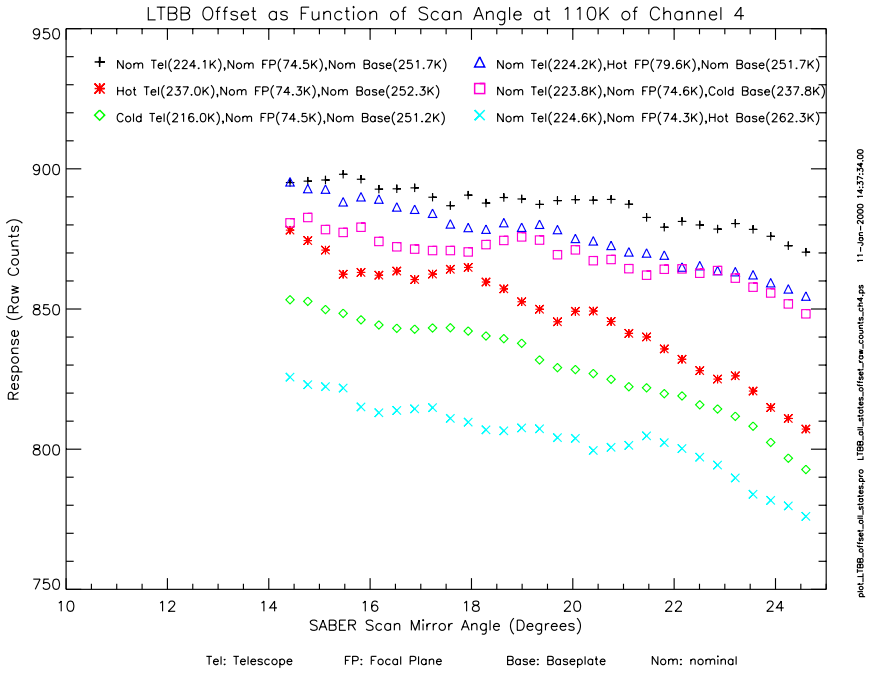

Figure 15. Relative offset versus scan angle for channel 4

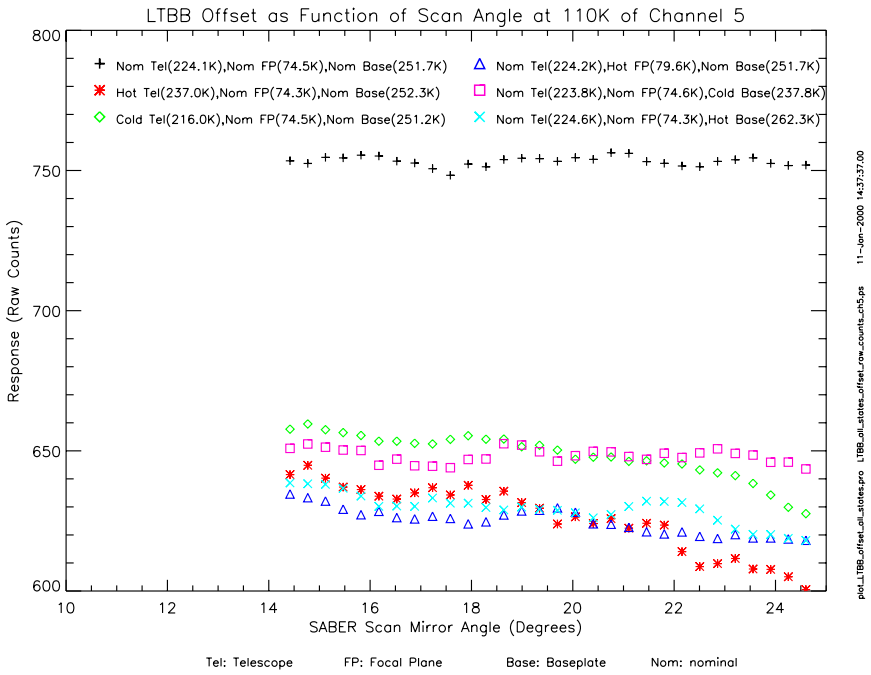

Figure 16. Relative offset versus scan angle for channel 5

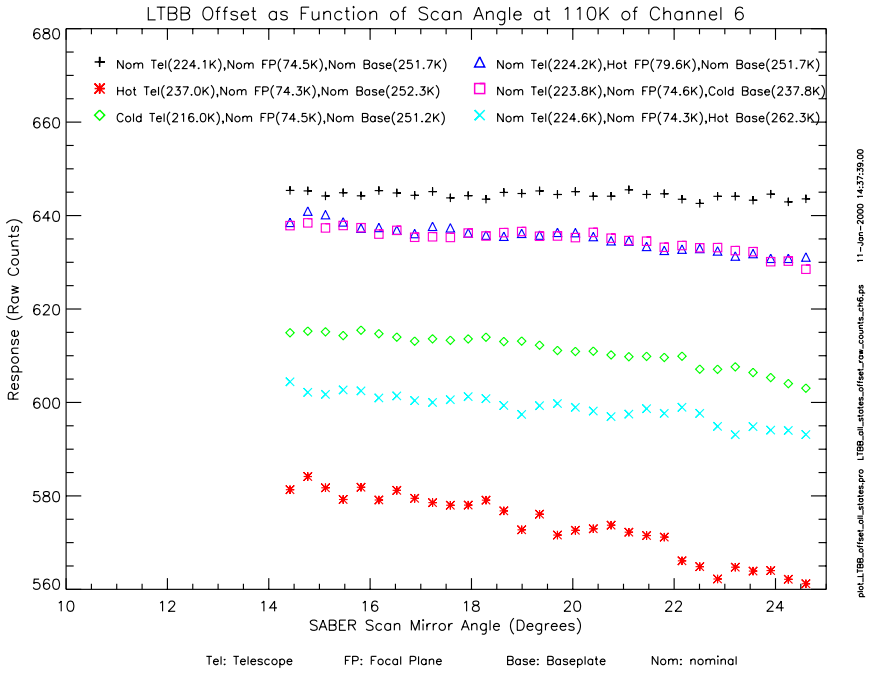

Figure 17. Relative offset versus scan angle for channel 6

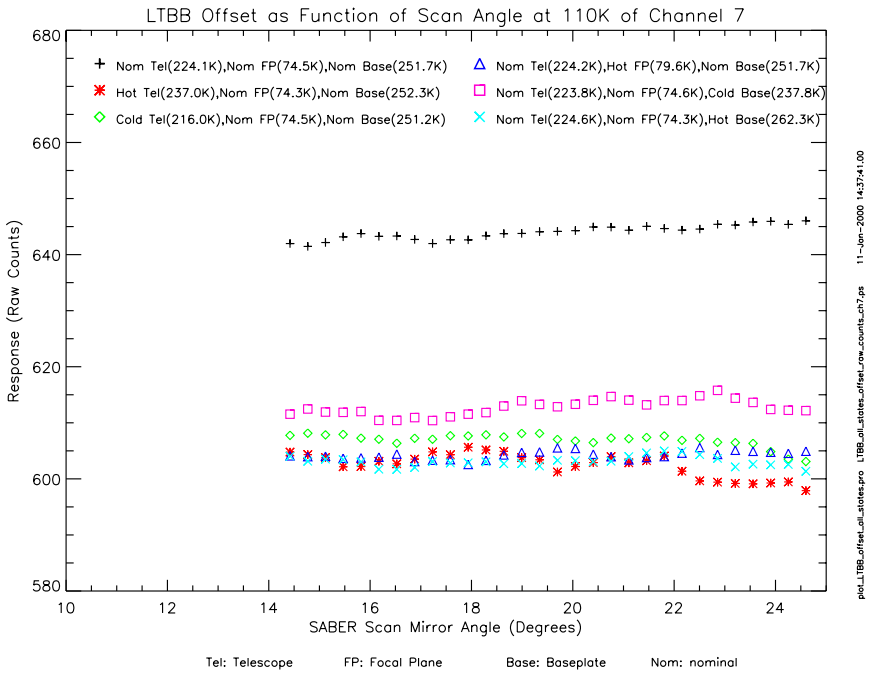

Figure 18. Relative offset versus scan angle for channel 7

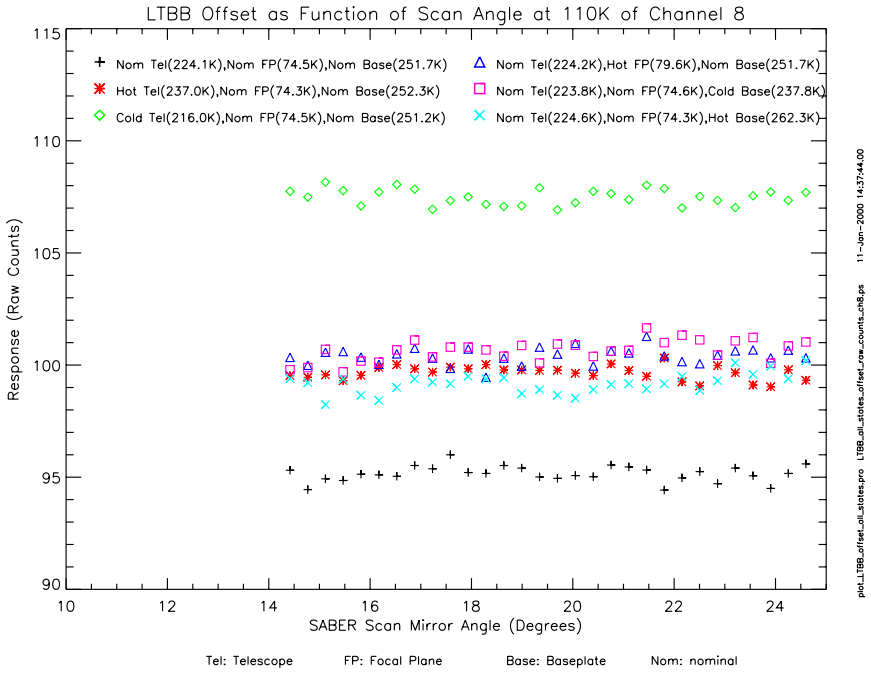

Figure 19. Relative offset versus scan angle for channel 8

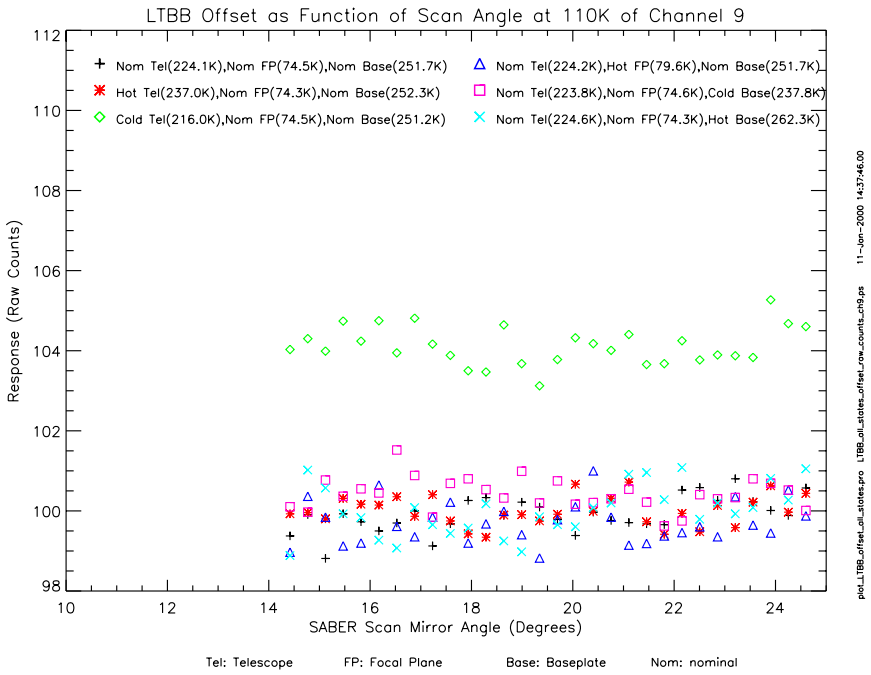

Figure 20. Relative offset versus scan angle for channel 9

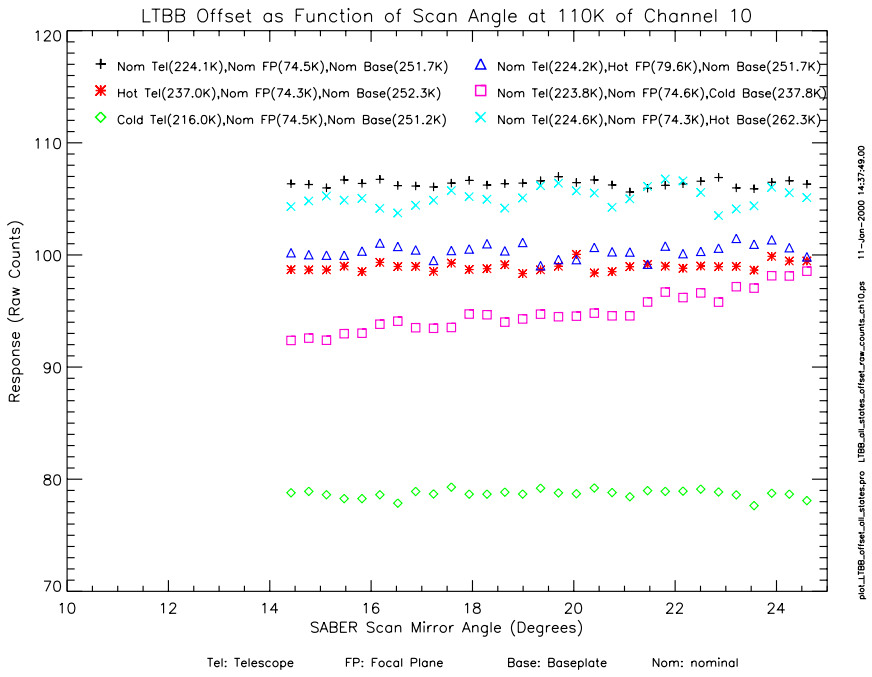

Figure 21. Relative offset versus scan angle for channel 10

To better understand the source of this offset variation, SABER channel offset drift and GSE radiometric performance were then evaluated.

To investigate the effect of SABER channel offset drift on offset variability as a function of scan angle, channel response was plotted versus time using sensor offset medium term repeatability data and sensor offset as a function of scan angle measurements. Except for the SABER cold temperature state, the medium term repeatability data (Section 2.1.4) were obtained immediately before the offset as function of scan mirror angle measurements. During both measurements, SABER viewed a 110 K blackbody, but in the medium term repeatability measurement SABER stared at the blackbody for 15 minutes without SABER being rotated. Figures 22 to 31 show the results of this comparison. For these graphs, medium term repeatability data are more closely spaced than offset as a function of scan angle data. These figures show that only channels 4, 5, and 6 show a larger relative offset variability as a function of scan angle than can be explained by channel drift. The observed sensor offset variability for the other channels can be explained by offset drift.

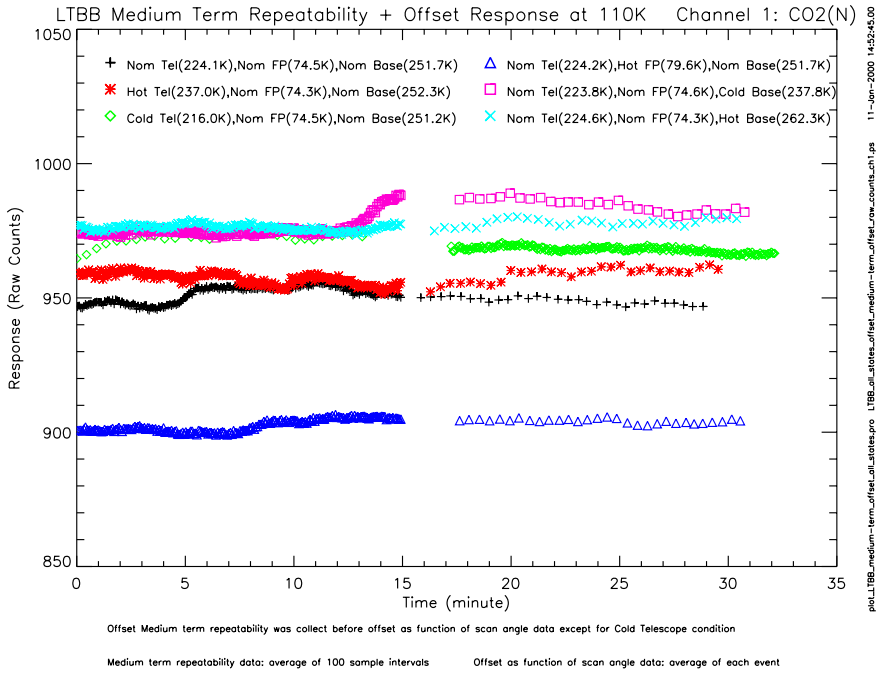

Figure 22. Relative offset time series for channel 1

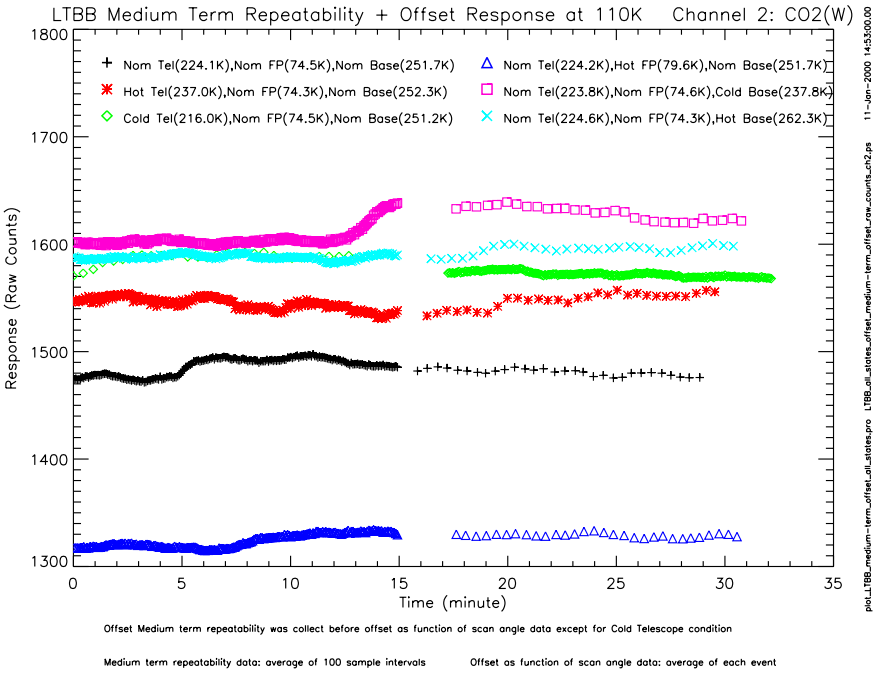

Figure 23. Relative offset time series for channel 2

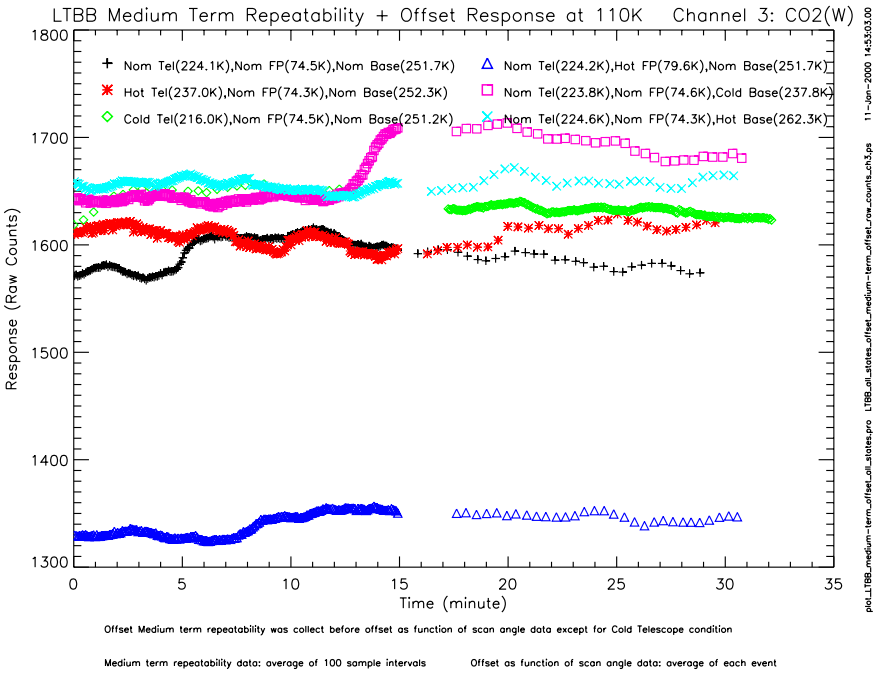

Figure 24. Relative offset time series for channel 3

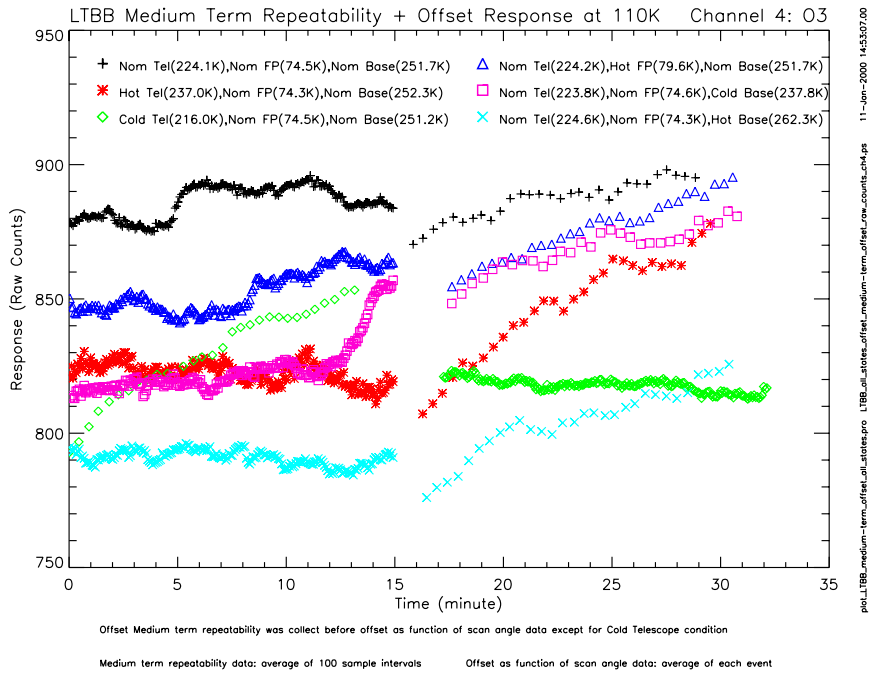

Figure 25. Relative offset time series for channel 4

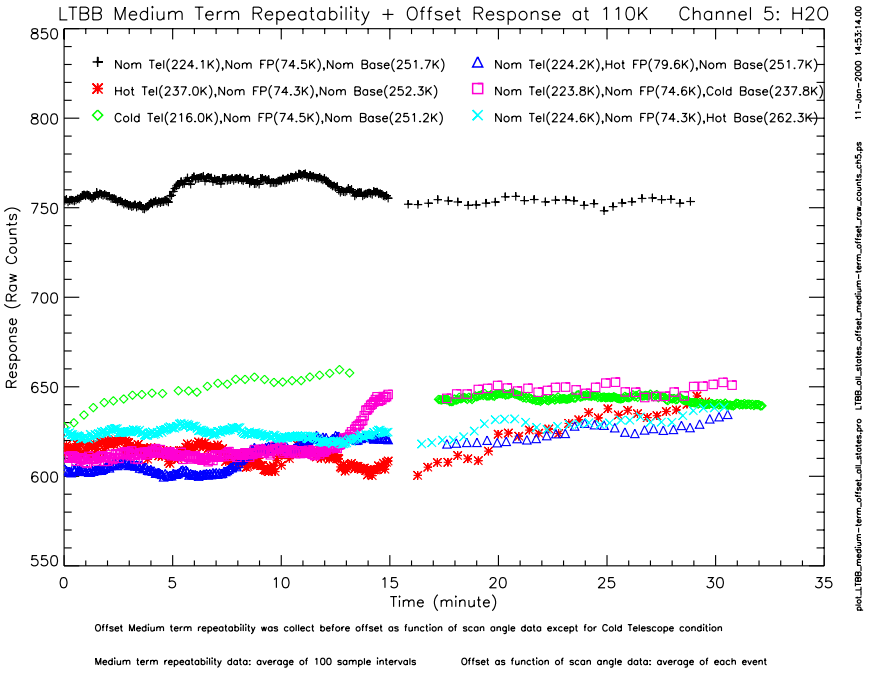

Figure 26. Relative offset time series for channel 5

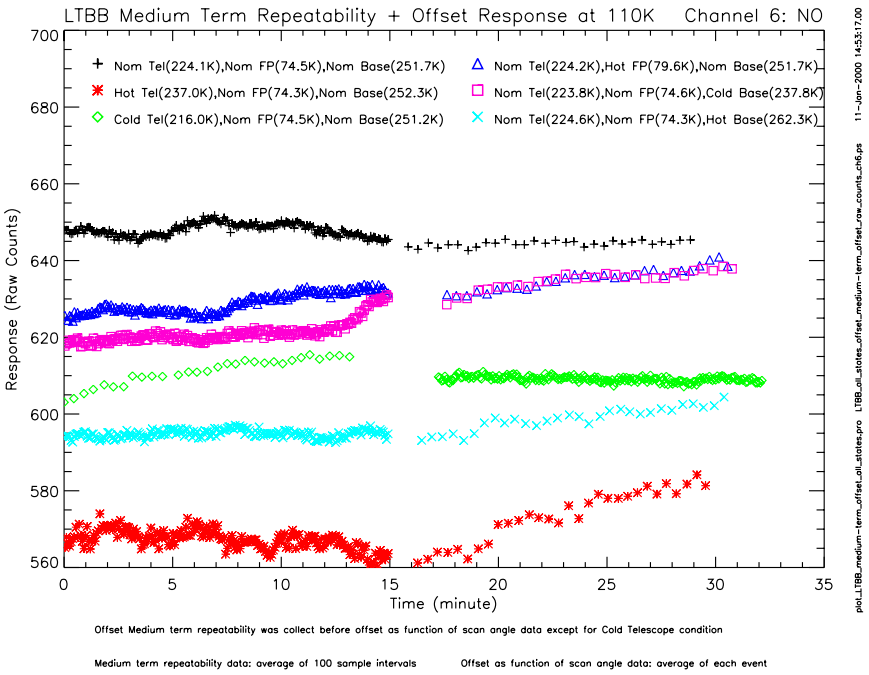

Figure 27. Relative offset time series for channel 6

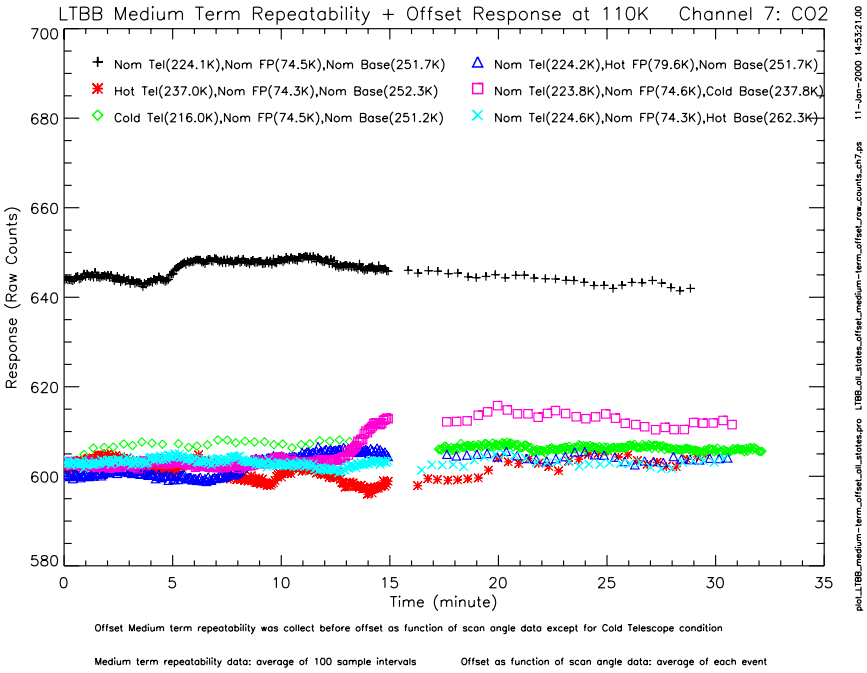

Figure 28. Relative offset time series for channel 7

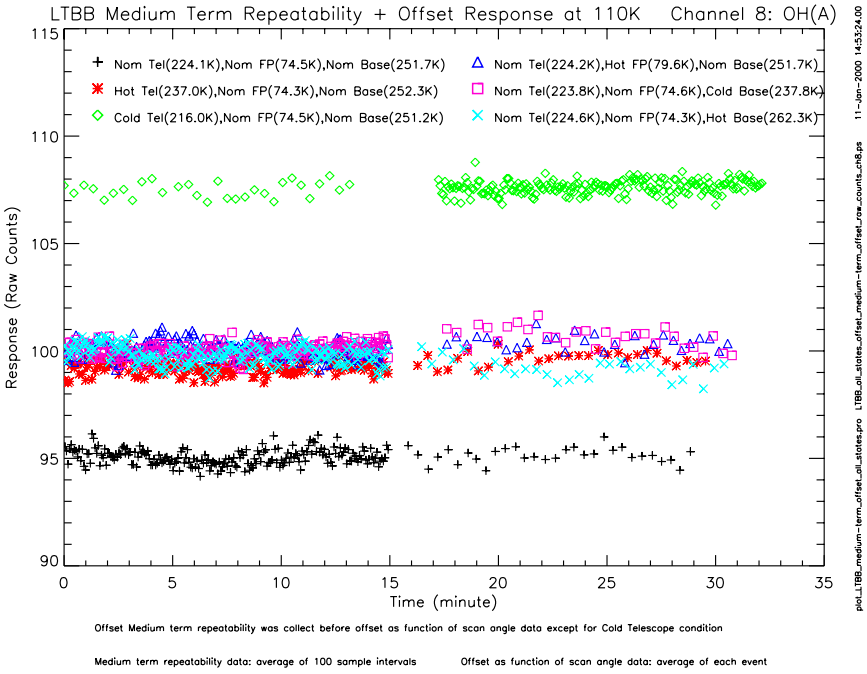

Figure 29. Relative offset time series for channel 8

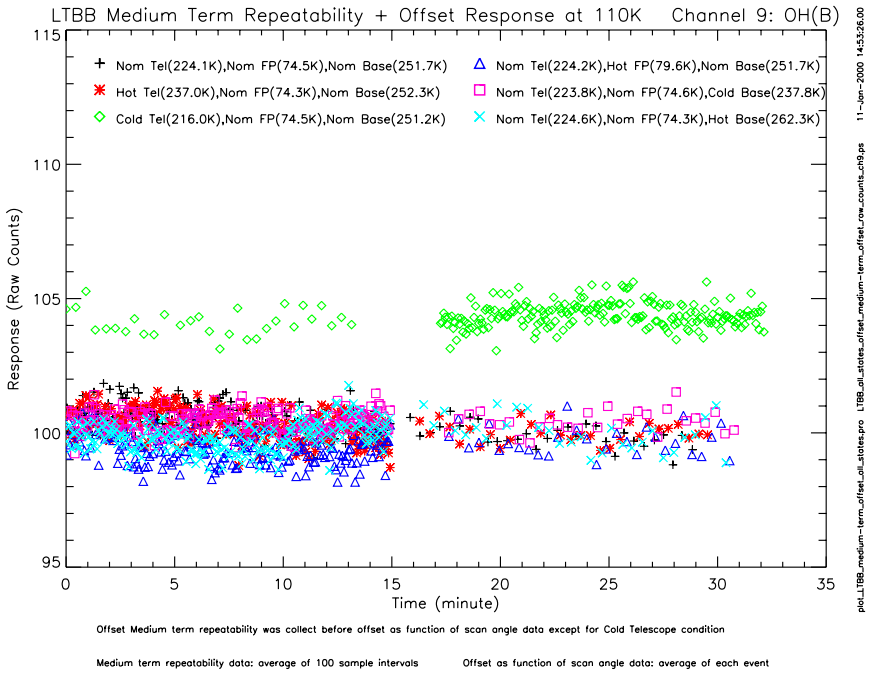

Figure 30. Relative offset time series for channel 9

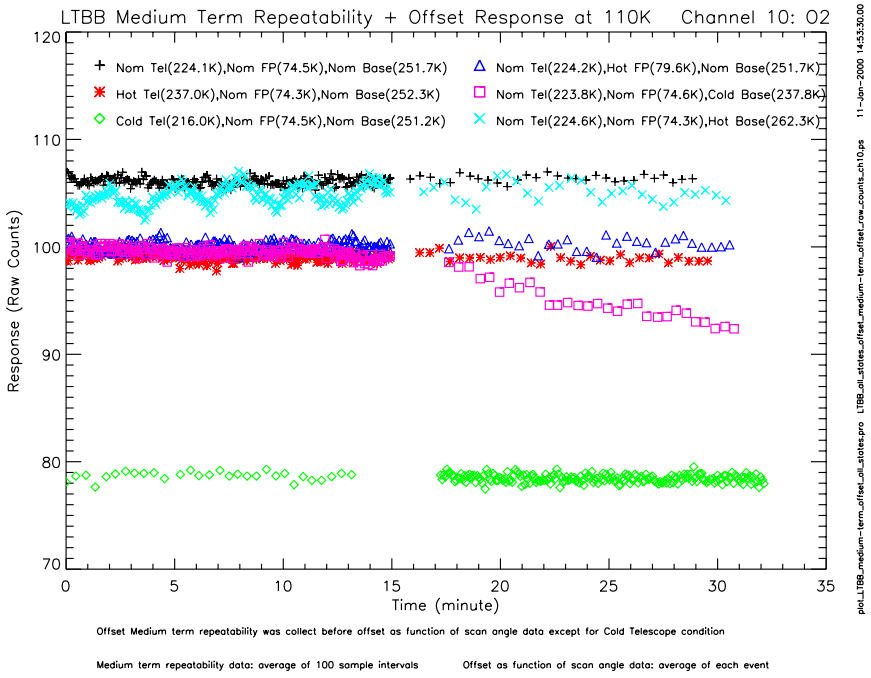

Figure 31. Relative offset time series for channel 10

A simple radiometric model of relative sensor offset as a function of scan angle was then developed to determine if the observed scan angle-dependent offset variation is a result of SABER or due to GSE radiometric performance. The radiometric model was developed in MathCad and is shown in Appendix E. The model assumes that flux from thermal emission of the telescope optics (T_{SAB}=237 K) and background flux from a small test chamber leak of 300 K are reflected off the face of the blackbody into SABER's FOV. Model results are shown in Table 8 along with compared-to-measured values for the SABER hot telescope temperature state. The results show that (1) the model gives results that are of the same order of magnitude as measurements and (2) the relative offset angular dependence shown in the model is consistent with measurements. The latter conclusion can be made by comparing a graph of model results shown in Appendix E with the relative sensor offset measurements shown in Figures 12 to 21. A linear curve fit of the measured data given in these figures shows a cosine scan angle dependence, which is also predicted by the model. Therefore, the measured variation in relative sensor offset as function of SABER scan angle is likely due to GSE radiometric performance and not the SABER instrument.

Table 8. Radiometric model relative offset variability

Ch	Relative Sensor Offset[a]			
	Measurement		Model Prediction	Scan Variability Comparison
	Drift Variability over 15 Minutes (Counts)	Scan Variability 14° to 25° (Counts)	Scan Variability 14° to 25° (Counts)	Model/Measurement
1	8	8	4	0.5
2	15	16	14	0.9
3	25	20	16	0.8
4	10	68	45	0.7
5	12	35	34	1.0
6	7	19	31	1.6
7	7	5	12	2.4

a. SABER hot telescope temperature state

However, in the unlikely event the measured scan angle dependance is from SABER, this variation is not large enough to significantly affect science measurements. For example, assume the measured relative offset variability as function of scan angle is from SABER (worst case scenario). Channel 4 contains the largest measured offset variability as a function of scan angle. For this channel, the linear dependence is approximately -10 counts per scan angle of 1 degree or approximately 50 km equivalent on-orbit tangent height altitude. This is not considered to be significant for science measurements (Wang, 2000).

2.1.4 Sensor Offset Medium Term Repeatability (Channel Drift)

The channel offset drift while viewing a stable 110 K LTBB was measured and calculated for six SABER temperature states. During each test event, SABER viewed a stable 110 K LTBB for 15 minutes. The standard deviation of the response, which represents the NER in counts, was calculated using the first 10 seconds of data. The planned duration between on-orbit space looks is approximately 1 minute. The average and largest 1-minute drift in units of counts per minute over 15 minutes was determined for each SABER temperature state. Figure 32 shows an example of this drift calculation for channel 2 with nominal instrument temperatures.

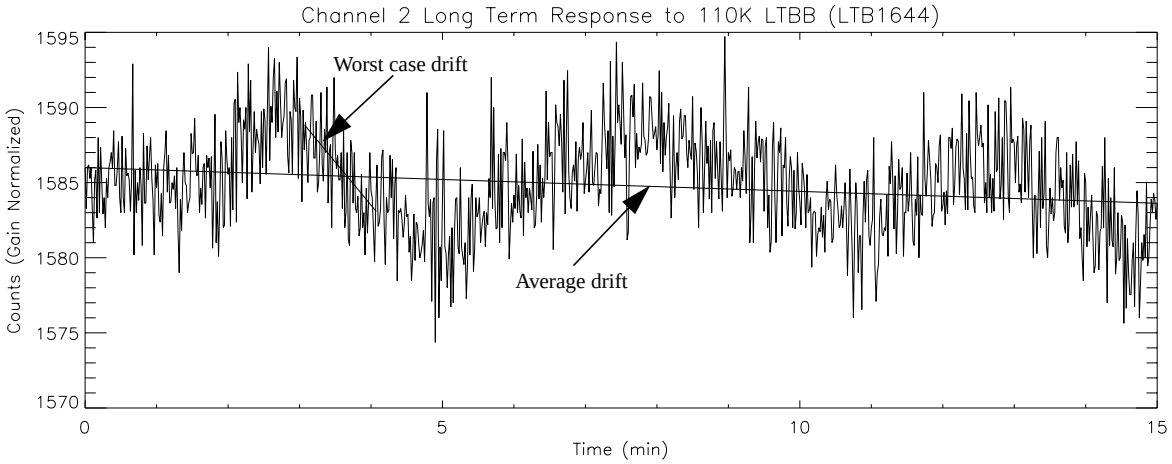

Figure 32. Example offset drift for channel 2

The drift in terms of NER/min was calculated by taking the ratio of the drift in counts/min to the standard deviation (counts/NER). These data were tabulated for each channel and temperature state. Time series graphs of individual channel response are shown in Figures 22 to 31. For these graphs, medium term repeatability data are more closely spaced than offset as function of scan angle data, which are also shown on the time series. Table 9 gives the overall average and standard deviation for all temperature states for the largest 1 minute drift (worst case) and the average drift over 15 minutes. Also given is the on-orbit radiance bias drift requirement of ≤ 1 NER per space look. The duration between on-orbit space looks is planned to be nearly once every minute. The measured worst case drift over a 15 minute interval exceeds the radiance bias drift requirement for channels 1 to 7 and is better than required for channels 8 to 10. The measured average drift over a 15 minute interval is better than the radiance bias drift requirement for all SABER channels.

Table 9. SABER drift during ground calibration

Channel	Drift [NER/min]				Radiance Bias Drift Requirement
	Largest 1 Minute Drift over 15 Minutes		Average Drift over 15 Minutes		
	Avg	Stdev	Avg	Stdev	
1	1.26	0.53	0.08	0.07	≤ 1 NER between space looks (~1 minute)
2	2.30	0.44	0.17	0.18	
3	3.91	1.32	0.34	0.30	
4	2.86	1.20	0.28	0.20	
5	2.25	0.86	0.22	0.18	
6	1.09	0.27	0.09	0.07	
7	1.21	0.45	0.09	0.08	
8	0.55	0.11	0.01	0.00	
9	0.60	0.06	0.01	0.01	
10	0.62	0.31	0.01	0.01	

2.2 Gain Mode Normalization

Gain mode normalization was determined during electronic subsystem measurements and subsequently verified during radiometric calibration. Measuring gain mode normalization at the subsystem level is possible because the electronic gain circuitry in SABER appears after the signal processing electronics and before the analog-to-digital converter (ADC), making it independent of detector/preamp nonlinearity. Each channel has three gain settings, designated as high, medium, and low. The high gain mode is the most sensitive setting. The gain-mode normalization normalizes the SABER output to high gain mode. For example, 100 counts in medium gain with a gain mode normalization value of 12 is equivalent to 1,200 counts (100 x 12) of response in high gain mode.

2.2.1 Electronic Subsystem Calibration

Electronic subsystem measurements were obtained on flight electronics to determine gain mode normalization values for each detector and gain setting combination. This test procedure is documented in Appendix A. During this test, the flight ADC output was recorded as a function of PGA (Programable Gain Amplifier) input voltage. For each detector and gain setting, approximately 20 data points were collected for input voltage values that gave ADC output values between 0 and 4095 counts. The output of the ADC was then plotted versus PGA input voltage. A linear least squares curve fit was performed to determine the slope of the best fit line. A constant term was included in the fit to account for any offset inherent in the electronics. The curve fit residuals were plotted to identify outliers. If the magnitude of a curve fit residual for a particular data point was larger than 5 sigma from zero mean, that data point was identified as an outlier and removed from the data. The curve fit was then repeated and the new residuals were examined to ensure they were near randomly distributed. The results of this analysis is documented in Appendix A.

The high gain-mode normalization values are set equal to 1. The gain-mode normalization values for the low and medium gain settings were calculated by dividing the high gain slope coefficient by the low and medium gain slope coefficients, respectively. Table 10 gives the gain mode normalization values as determined from electronic subsystem measurements.

Table 10. Gain-mode normalization values from subsystem electronic measurements

Channel	Gain Setting		
	G_{low}	G_{med}	G_{high}
1	21.114	1.000	1.000
2	60.103	7.816	1.000
3	68.858	8.318	1.000
4	183.558	13.454	1.000
5	152.916	12.547	1.000
6	209.571	19.157	1.000
7	76.758	8.647	1.000
8	1108.443	33.552	1.000
9	1080.965	32.730	1.000
10	375.434	19.198	1.000

Uncertainties due to measurement noise, electronics operating temperature, and on-orbit radiation exposure were combined using Equation (5) to estimate the uncertainty of gain-mode normalization values.

$$\sigma_{Gain} = \sqrt{(\sigma_{meas})^2 + (\sigma_T)^2 + (\sigma_{rad})^2} \quad (5)$$

where σ_{Gain} = uncertainty of gain normalization values (%)

σ_{meas} = measurement noise uncertainty (%)

σ_T = uncertainty due to electronics operating temperature (%)

σ_{rad} = uncertainty due to on-orbit radiation exposure (%)

To estimate measurement noise uncertainty, the standard error of the two slope coefficients used to calculate each gain value were combined in quadrature. Table 11 shows the estimated measurement noise uncertainty for each channel and gain mode. These calculations are documented in Appendix A. The measurement noise uncertainty for the high gain setting, which is the largest uncertainty among all gain settings, was used as the measurement noise uncertainty in Equation (5).

Table 11. Gain-mode normalization measurement noise uncertainty from electronic subsystem measurements

Channel	High Gain (%)	Medium Gain (%)	Low Gain (%)
1	0.083	0.059	0.059
2	0.081	0.057	0.057
3	0.093	0.065	0.066
4	0.289	0.204	0.204
5	0.235	0.167	0.166
6	0.386	0.273	0.273
7	0.110	0.078	0.078
8	0.086	0.061	0.061
9	0.072	0.051	0.051
10	0.023	0.016	0.016

The uncertainty due to electronics operating temperature was estimated by evaluating the temperature dependence on the gain stage electronic circuit design. The uncertainty of gain values due to electronic operating temperature are documented in Appendix B and the results are shown in Table 12.

The uncertainty due to on-orbit radiation exposure was estimated by evaluating the radiation exposure of the electronic components in the gain stage of the signal processing electronics. This analysis is documented in Appendix B and the results are shown in Table 12.

Table 12 also gives individual uncertainty terms and the combined gain-mode normalization uncertainty, σ_{Gain}, calculated using Equation (5). The combined uncertainty values range from 0.03% to 0.39%, depending on channel.

Table 12. Uncertainty of gain-mode normalization values derived from electronic subsystem measurements

Channel	σ_{meas} (%)	σ_T (%)	σ_{rad} (%)	σ_{Gain} (%)
1	0.083	0.016	0.01	0.085
2	0.081			0.083
3	0.093			0.095
4	0.289			0.289
5	0.235			0.236
6	0.386			0.386
7	0.110			0.112
8	0.086			0.088
9	0.072			0.074
10	0.023			0.030

2.2.2 Radiometric Verification

Data from low and high temperature blackbody measurements, documented in “SABER Ground Calibration and Preliminary Results” (SDL/98-059), were used to provide a radiometric verification of gain-mode normalization values determined from electronic subsystem testing. For each blackbody temperature, measurements were obtained with the blackbody un-attenuated, attenuated with 2X plate, and attenuated with 10X plate. For each measurement combination, the

channel response was obtained in auto-, low-, medium-, and high-gain settings. Equation (6) was used to calculate gain-mode normalization values from radiometric blackbody measurements.

$$Gain_{mode}(T_{BB1}, T_{BB2}) = \frac{R_{high}(T_{BB1}) - R_{high}(T_{BB2})}{R_{mode}(T_{BB1}) - R_{mode}(T_{BB2})} \quad (6)$$

where

$Gain$ = gain mode normalization value (unitless)
$mode$ = gain mode designation (low, medium, or high)
T_{BB1} = first blackbody temperature (K)
T_{BB2} = second blackbody temperature, $T_{BB2} < T_{BB1}$, (K)
R = channel response (raw counts)

Blackbody temperatures for each channel and attenuating plate combinations were chosen to give good signal to noise in all gain settings. Tables 13 to 18 show the blackbody temperature, raw response for each gain setting, and the calculated gain-mode normalization values using Equation (6) for unattenuated, 2X attenuated, and 10X attenuated blackbody measurements. Each table shows the data for a specific instrument temperature setting. Table 19 shows a summary of gain values for each gain-mode and instrument temperature setting. Also shown is the mean and standard deviation for all temperature settings.

Figures 33 and 34 show low and medium gain values determined from radiometric measurements for each instrument temperature setting. Each data point is shown with an X and ± 1 standard deviation is shown with a vertical line. Consistent with measurement variability and as expected from analyses of the electronic gain circuit (Appendix B) these data show gain values to be independent of instrument temperature setting.

Figures 35 and 36 give a comparison of low- and medium-gain values determined from electronic subsystem measurements with those determined from radiometric measurements. These data verify that gain values determined from electronic subsystem measurements are consistent with gain values determined from radiometric measurements within measurement variability.

Table 13. Channel gains for nominal telescope, nominal focal plane, and nominal baseplate temperatures

Channel		1	2	3	4	5	6	7	8	9	10
Unattenuated blackbody											
T_{BB2} (K)		110	110	110	127	150	161	180	300	400	509
Response (Counts)	Low gain	49.0	29.9	27.0	10.0	11.4	7.1	13.4	3.7	4.3	4.0
	Medium gain	973.2	208.1	199.8	94.6	103.8	47.2	94.0	14.7	42.2	21.6
	High gain	973.8	1604.7	1638.2	1236.5	1267.8	848.3	788.6	379.9	1279.2	357.3
T_{BB1} (K)		150	127	127	140	161	180	206	351	430	570
Response (Counts)	Low gain	148.1	60.0	55.0	18.3	19.0	15.1	38.8	6.9	6.0	9.1
	Medium gain	3064.1	441.1	432.6	211.7	193.9	135.3	319.0	120.0	102.7	121.4
	High gain	3064.4	3424.1	3577.7	2811.1	2400.5	2540.1	2731.7	3919.0	3257.0	2264.8
Gain (unitless)	Low gain	21.102	60.502	69.193	189.415	148.955	211.469	76.478	1106.702	1130.166	376.796
	Medium gain	1.000	7.811	8.331	13.448	12.566	19.188	8.637	33.593	32.730	19.125
	High gain	1.000	1.000	1.000	1.000	1.000	1.000	1.000	1.000	1.000	1.000
Blackbody attenuated with 2X plate											
T_{BB2} (K)		110	110	110	127	150	170	180	300	400	525
Response (Counts)	Low gain	52.4	33.0	30.4	13.0	10.4	8.0	12.1	3.5	4.0	4.0
	Medium gain	1043.9	232.9	228.8	140.1	92.1	56.1	84.5	10.5	26.0	21.2
	High gain	1044.6	1797.4	1878.9	1845.3	1122.2	1020.0	705.9	234.6	753.1	345.5
T_{BB1} (K)		150	127	127	140	161	180	206	351	460	570
Response (Counts)	Low gain	99.9	47.8	43.4	17.4	14.0	11.0	24.6	5.0	7.5	6.2
	Medium gain	2042.6	346.6	336.5	198.1	135.5	88.4	193.2	61.1	145.8	64.5
	High gain	2042.8	2687.0	2776.2	2626.8	1666.3	1640.2	1646.1	1935.9	4095.0	1172.0
Gain (unitless)	Low gain	21.001	60.020	69.081	180.768	150.539	209.625	75.340	1118.663	943.599	377.861
	Medium gain	1.000	7.826	8.335	13.483	12.542	19.192	8.644	33.647	27.900	19.093
	High gain	1.000	1.000	1.000	1.000	1.000	1.000	1.000	1.000	1.000	1.000
Blackbody attenuated with 10X plate											
T_{BB2} (K)		192	140	140	157	180	215	206	350	430	570
Response (Counts)	Low gain	104.9	44.8	42.0	19.7	13.7	16.8	14.0	3.8	3.6	4.1
	Medium gain	2147.0	322.1	324.6	228.1	130.2	151.3	99.9	17.0	15.2	22.1
	High gain	2147.2	2492.4	2674.2	3041.8	1601.2	2849.7	838.1	461.5	402.2	365.9
T_{BB1} (K)		221	150	161	170	192	221	240	400	509	620
Response (Counts)	Low gain	151.5	49.9	54.8	24.0	18.7	20.9	39.3	6.9	7.0	6.2
	Medium gain	3135.5	361.5	429.4	286.2	190.7	196.7	325.5	122.7	125.1	64.0
	High gain	3137.1	2799.3	3550.5	3815.3	2361.8	3724.6	2788.8	4001.8	3993.2	1168.3
Gain (unitless)	Low gain	21.209	59.889	68.566	180.667	154.048	210.495	77.096	1117.995	1054.242	372.110
	Medium gain	1.002	7.787	8.362	13.310	12.564	19.250	8.647	33.498	32.686	19.156
	High gain	1.000	1.000	1.000	1.000	1.000	1.000	1.000	1.000	1.000	1.000

Table 14. Channel gains for cold telescope, nominal focal plane, and nominal baseplate temperatures

Channel		1	2	3	4	5	6	7	8	9	10
Unattenuated blackbody											
T_{BB2} (K)		110	115	115	115	140	157	180	300	300	300
Response (Counts)	Low gain	54.4	45.9	40.8	10.3	12.0	9.1	14.3	3.9	3.6	3.8
	Medium gain	1084.3	330.1	311.8	100.5	111.0	69.2	101.8	15.1	10.9	8.5
	High gain	1084.6	2557.5	2572.9	1317.3	1358.5	1272.2	855.1	395.2	255.7	102.8
T_{BB1} (K)		150	127	127	140	161	170	206	350	350	350
Response (Counts)	Low gain	153.9	70.1	63.0	24.0	23.0	12.1	39.1	6.9	3.9	3.8
	Medium gain	3184.3	518.0	497.2	287.2	243.6	101.1	322.1	116.4	16.6	8.7
	High gain	3187.6	4022.5	4095.0	3833.8	3025.2	1883.0	2760.2	3798.2	442.2	103.7
Gain (unitless)	Low gain	21.122	60.595	68.344	183.298	151.670	205.007	76.811	-	-	-
	Medium gain	1.001	7.796	8.212	13.483	12.572	19.161	8.650	-	-	-
	High gain	1.000	1.000	1.000	1.000	1.000	1.000	1.000	-	-	-
Blackbody attenuated with 2X plate											
T_{BB2} (K)		110	120	127	127	157	180	188	300	300	300
Response (Counts)	Low gain	56.2	49.0	50.0	16.5	16.0	13.4	14.9	3.8	3.4	3.7
	Medium gain	1123.6	354.0	390.0	183.8	159.8	115.1	105.2	11.0	8.8	7.1
	High gain	1124.0	2743.0	3223.3	2440.1	1974.0	2155.8	883.9	251.3	183.7	76.0
T_{BB1} (K)		150	133	136	140	170	192	215	350	350	350
Response (Counts)	Low gain	105.0	64.8	62.0	21.6	24.0	21.1	38.8	5.1	3.8	3.8
	Medium gain	2150.9	475.1	488.8	253.9	256.8	200.3	316.8	61.7	13.2	9.0
	High gain	2151.2	3690.6	4045.0	3386.5	3192.3	3792.3	2714.2	1956.6	329.4	110.9
Gain (unitless)	Low gain	21.052	59.766	68.362	183.185	152.092	212.879	76.698	-	-	-
	Medium gain	1.000	7.822	8.312	13.499	12.557	19.206	8.650	-	-	-
	High gain	1.000	1.000	1.000	1.000	1.000	1.000	1.000	-	-	-
Blackbody attenuated with 10X plate											
T_{BB2} (K)		150	133	136	140	170	180	221	300	300	300
Response (Counts)	Low gain	72.1	49.0	45.7	20.0	15.0	10.0	20.6	3.7	3.3	3.5
	Medium gain	1458.2	355.8	353.3	231.4	146.0	75.8	156.4	7.6	6.9	6.0
	High gain	1458.9	2756.6	2915.7	3082.2	1798.5	1395.3	1328.3	141.4	121.5	51.9
T_{BB1} (K)		215	150	161	161	192	206	245	350	350	350
Response (Counts)	Low gain	144.9	57.0	60.0	24.3	22.6	15.0	50.0	3.9	3.3	3.6
	Medium gain	2992.4	416.7	471.1	291.7	237.2	130.0	418.1	17.4	7.6	6.8
	High gain	2993.4	3233.1	3895.3	3889.8	2944.0	2440.2	3592.6	472.5	149.8	68.5
Gain (unitless)	Low gain	21.057	59.633	68.496	188.161	151.466	208.538	76.974	-	-	-
	Medium gain	1.000	7.821	8.315	13.401	12.567	19.264	8.652	-	-	-
	High gain	1.000	1.000	1.000	1.000	1.000	1.000	1.000	-	-	-

Table 15. Channel gains for hot telescope, nominal focal plane, and nominal baseplate temperatures

Channel		1	2	3	4	5	6	7	8	9	10
Unattenuated blackbody											
T_{BB2} (K)		110	110	110	110	150	161	180	300	300	300
Response (Counts)	Low gain	48.2	28.9	26.6	7.7	12.0	7.1	14.9	3.8	3.3	3.8
	Medium gain	957.5	200.1	196.1	64.0	110.4	48.0	106.4	14.7	10.8	10.8
	High gain	957.1	1539.6	1608.8	820.4	1352.7	867.1	896.6	387.5	249.2	150.1
T_{BB1} (K)		150	127	127	140	161	180	206	350	350	350
Response (Counts)	Low gain	148.1	59.0	54.9	19.6	19.4	15.1	38.9	6.8	3.7	3.8
	Medium gain	3064.4	431.3	429.9	226.4	200.3	135.2	318.3	116.0	16.9	10.8
	High gain	3066.0	3345.6	3553.4	3014.0	2484.1	2545.7	2727.4	3788.6	455.5	147.0
Gain (unitless)	Low gain	21.107	60.012	68.683	183.915	152.968	210.099	76.453	-	-	-
	Medium gain	1.001	7.813	8.317	13.508	12.577	19.244	8.642	-	-	-
	High gain	1.000	1.000	1.000	1.000	1.000	1.000	1.000	-	-	-
Blackbody attenuated with 2X plate											
T_{BB2} (K)		110	120	127	127	157	180	188	300	300	300
Response (Counts)	Low gain	53.8	41.5	45.7	16.5	14.0	11.1	15.2	3.7	3.2	3.6
	Medium gain	1071.3	297.9	353.8	184.1	133.3	91.8	111.7	10.5	8.5	9.4
	High gain	1071.6	2305.8	2928.7	2449.4	1636.8	1703.8	938.5	239.9	179.2	121.3
T_{BB1} (K)		150	140	136	140	170	192	215	350	350	350
Response (Counts)	Low gain	102.0	69.0	56.9	20.7	21.6	19.0	38.0	5.0	3.5	3.8
	Medium gain	2084.5	509.9	446.3	241.4	226.4	176.4	313.4	60.8	13.2	11.0
	High gain	2083.8	3959.6	3691.0	3216.8	2807.0	3333.4	2686.3	1931.0	331.2	150.5
Gain (unitless)	Low gain	21.024	60.184	67.642	181.905	153.676	206.660	76.651	-	-	-
	Medium gain	0.999	7.803	8.243	13.371	12.569	19.249	8.665	-	-	-
	High gain	1.000	1.000	1.000	1.000	1.000	1.000	1.000	-	-	-
Blackbody attenuated with 10X plate											
T_{BB2} (K)		150	150	140	136	170	180	221	300	300	300
Response (Counts)	Low gain	72.1	52.3	45.5	21.9	13.4	8.1	21.0	3.3	3.1	3.5
	Medium gain	1455.8	381.8	352.1	257.3	127.6	58.9	161.0	7.0	6.5	8.1
	High gain	1453.7	2955.5	2903.9	3431.6	1565.6	1073.6	1367.6	130.7	114.9	97.3
T_{BB1} (K)		215	157	161	157	192	221	245	350	350	350
Response (Counts)	Low gain	146.3	57.0	58.9	24.7	20.6	21.3	48.1	3.9	3.2	3.6
	Medium gain	3025.4	416.4	463.6	295.3	213.5	201.4	403.0	17.2	7.3	8.6
	High gain	3026.8	3234.6	3841.5	3946.2	2654.5	3818.7	3459.5	466.6	143.3	105.1
Gain (unitless)	Low gain	21.196	59.407	69.559	186.426	150.200	207.504	77.031	-	-	-
	Medium gain	1.002	8.070	8.409	13.542	12.678	19.260	8.645	-	-	-
	High gain	1.000	1.000	1.000	1.000	1.000	1.000	1.000	-	-	-

Table 16. Channel gains for nominal telescope, nominal focal plane, and cold baseplate temperatures

Channel		1	2	3	4	5	6	7	8	9	10
Unattenuated blackbody											
T_{BB2} (K)		110	110	110	110	140	161	180	300	351	510
Response (Counts)	Low gain	49.0	29.8	27.0	7.2	9.6	8.0	13.9	3.3	3.3	4.0
	Medium gain	977.4	208.6	201.7	62.8	83.0	56.9	98.2	14.9	16.6	19.1
	High gain	978.0	1609.5	1658.1	813.4	1004.3	1037.0	826.7	387.1	444.6	309.7
T_{BB1} (K)		150	127	127	140	157	180	206	350	400	570
Response (Counts)	Low gain	144.1	56.9	53.0	20.3	16.9	16.0	38.5	6.3	4.0	9.0
	Medium gain	2987.3	417.7	416.7	242.1	170.1	144.4	319.1	115.3	41.9	117.9
	High gain	2987.8	3240.1	3445.4	3222.9	2100.2	2721.7	2735.3	3769.9	1278.2	2200.3
Gain (unitless)	Low gain	21.141	60.185	68.772	183.724	151.587	210.593	77.473	1131.550	1096.202	378.118
	Medium gain	1.000	7.796	8.312	13.433	12.591	19.245	8.639	33.667	32.959	19.123
	High gain	1.000	1.000	1.000	1.000	1.000	1.000	1.000	1.000	1.000	1.000
Blackbody attenuated with 2X plate											
T_{BB2} (K)		110	110	110	110	157	161	180	287	400	510
Response (Counts)	Low gain	52.1	32.8	30.1	12.0	13.6	7.4	12.6	3.1	3.8	3.8
	Medium gain	1044.0	232.2	228.8	129.0	131.9	52.4	88.2	8.8	26.5	14.0
	High gain	1044.7	1790.9	1881.6	1704.5	1624.8	950.7	739.8	185.9	770.7	211.4
T_{BB1} (K)		150	127	127	140	170	180	206	351	460	595
Response (Counts)	Low gain	96.0	44.9	41.4	19.1	21.4	11.6	24.7	4.9	7.2	9.8
	Medium gain	1967.0	324.0	320.8	225.9	228.2	97.7	196.3	62.2	145.3	130.9
	High gain	1967.9	2510.6	2651.6	3009.5	2831.5	1818.9	1673.1	1984.6	4095.0	2450.0
Gain (unitless)	Low gain	21.011	59.820	68.068	185.043	155.701	206.831	77.166	981.129	981.950	374.404
	Medium gain	1.000	7.837	8.363	13.463	12.542	19.170	8.640	33.667	27.974	19.163
	High gain	1.000	1.000	1.000	1.000	1.000	1.000	1.000	1.000	1.000	1.000
Blackbody attenuated with 10X plate											
T_{BB2} (K)		188	136	133	157	188	192	215	300	430	570
Response (Counts)	Low gain	97.5	38.3	36.1	21.2	18.0	9.3	16.9	3.0	3.2	4.0
	Medium gain	2000.8	276.8	277.6	256.0	185.2	73.9	126.9	7.1	15.2	19.5
	High gain	2001.7	2141.0	2288.6	3411.6	2296.9	1362.3	1073.8	133.6	401.1	318.2
T_{BB1} (K)		221	150	150	161	192	206	240	400	510	660
Response (Counts)	Low gain	150.1	45.0	44.1	22.2	20.0	13.0	38.8	6.3	6.8	11.2
	Medium gain	3117.4	327.5	343.7	269.2	210.6	112.9	320.9	114.8	124.3	165.2
	High gain	3119.9	2537.3	2841.0	3585.8	2610.8	2116.2	2750.0	3746.8	3970.3	3111.2
Gain (unitless)	Low gain	21.249	59.541	68.781	177.888	156.930	204.461	76.737	1122.533	981.794	389.734
	Medium gain	1.001	7.811	8.358	13.166	12.364	19.332	8.638	33.529	32.705	19.169
	High gain	1.000	1.000	1.000	1.000	1.000	1.000	1.000	1.000	1.000	1.000

Table 17. Channel gains for nominal telescope, nominal focal plane, and hot baseplate temperatures

Channel		1	2	3	4	5	6	7	8	9	10
Unattenuated blackbody											
T_{BB2} (K)		120	115	115	120	136	170	180	287	400	510
Response (Counts)	Low gain	55.7	33.1	31.1	9.6	9.0	10.0	14.2	3.3	4.1	4.0
	Medium gain	1116.0	235.4	235.3	92.4	77.1	78.6	103.9	11.3	42.1	21.1
	High gain	1117.6	1814.8	1931.1	1213.7	933.2	1453.5	875.3	271.6	1282.3	345.9
T_{BB1} (K)		150	127	127	136	161	180	206	350	430	570
Response (Counts)	Low gain	144.1	51.0	49.0	17.0	20.3	15.7	39.1	6.4	6.0	9.0
	Medium gain	2987.7	372.1	383.2	192.9	214.4	141.1	325.4	115.2	103.1	119.6
	High gain	2986.1	2890.9	3172.5	2563.8	2657.9	2658.5	2790.3	3766.9	3283.5	2235.8
Gain (unitless)	Low gain	21.148	60.133	69.409	181.787	153.453	210.706	76.887	1126.010	1079.248	376.423
	Medium gain	0.998	7.870	8.395	13.433	12.564	19.257	8.648	33.619	32.805	19.191
	High gain	1.000	1.000	1.000	1.000	1.000	1.000	1.000	1.000	1.000	1.000
Blackbody attenuated with 2X plate											
T_{BB2} (K)		120	127	120	111	150	161	180	260	400	540
Response (Counts)	Low gain	53.5	39.4	32.0	12.4	12.0	7.1	13.1	3.1	3.7	4.3
	Medium gain	1070.6	283.9	243.1	131.5	110.7	49.5	94.8	7.1	26.2	28.2
	High gain	1071.7	2198.7	2002.6	1739.0	1358.5	898.3	797.6	138.9	770.5	486.4
T_{BB1} (K)		150	136	136	136	161	180	206	351	430	570
Response (Counts)	Low gain	95.0	52.0	49.8	18.0	15.8	11.3	25.2	4.9	4.7	6.1
	Medium gain	1946.3	380.9	390.1	205.9	157.2	94.9	201.8	62.4	57.2	63.2
	High gain	1949.0	2955.3	3223.1	2736.3	1940.5	1768.5	1721.3	1990.5	1784.0	1156.1
Gain (unitless)	Low gain	21.140	60.026	68.677	179.973	153.501	208.843	76.769	982.092	1046.140	367.382
	Medium gain	1.002	7.801	8.299	13.402	12.497	19.182	8.637	33.470	32.692	19.117
	High gain	1.000	1.000	1.000	1.000	1.000	1.000	1.000	1.000	1.000	1.000
Blackbody attenuated with 10X plate											
T_{BB2} (K)		192	140	150	157	180	192	206	351	460	540
Response (Counts)	Low gain	52.0	36.0	41.8	22.0	15.6	7.0	15.0	3.4	3.8	3.7
	Medium gain	1038.2	257.1	324.4	262.8	155.3	46.7	110.1	17.1	30.1	14.8
	High gain	1037.6	1991.6	2674.5	3500.9	1918.7	844.1	929.0	473.0	891.3	226.3
T_{BB1} (K)		221	157	161	161	192	206	240	400	510	595
Response (Counts)	Low gain	152.0	45.1	49.4	23.0	11.0	13.0	40.0	6.4	6.7	4.8
	Medium gain	3146.7	328.4	386.9	275.3	98.3	110.8	330.1	114.1	125.9	35.4
	High gain	3147.5	2545.2	3195.1	3677.0	1198.7	2076.1	2831.6	3725.8	4025.9	624.2
Gain (unitless)	Low gain	21.105	60.666	68.550	183.765	155.316	206.037	76.230	1103.439	1074.739	381.918
	Medium gain	1.001	7.767	8.318	14.102	12.619	19.233	8.648	33.542	32.699	19.289
	High gain	1.000	1.000	1.000	1.000	1.000	1.000	1.000	1.000	1.000	1.000

Table 18. Channel gains for nominal telescope, hot focal plane, and nominal baseplate temperatures

Channel		1	2	3	4	5	6	7	8	9	10
Unattenuated blackbody											
T_{BB2} (K)		120	120	120	120	140	161	180	300	351	540
Response (Counts)	Low gain	54.0	35.7	32.0	9.9	9.8	8.0	13.9	3.8	3.6	5.6
	Medium gain	1076.4	252.5	242.1	91.9	81.9	57.0	97.6	13.9	16.6	46.4
	High gain	1077.2	1953.0	1992.3	1199.2	989.5	1037.5	818.8	352.3	443.3	829.4
T_{BB1} (K)		150	133	133	140	161	180	206	350	433	570
Response (Counts)	Low gain	116.0	59.0	53.4	21.0	20.9	16.0	39.0	6.8	6.6	9.4
	Medium gain	2388.5	433.1	418.4	243.9	215.3	145.0	320.0	114.1	111.5	121.2
	High gain	2389.8	3363.0	3463.2	3249.4	2671.6	2727.2	2741.4	3723.3	3557.6	2262.5
Gain (unitless)	Low gain	21.167	60.454	68.677	184.629	151.482	211.487	76.744	1104.496	1052.722	375.894
	Medium gain	1.000	7.805	8.343	13.489	12.607	19.203	8.644	33.647	32.796	19.148
	High gain	1.000	1.000	1.000	1.000	1.000	1.000	1.000	1.000	1.000	1.000
Blackbody attenuated with 2X plate											
T_{BB2} (K)		120	127	127	110	136	170	180	287	400	460
Response (Counts)	Low gain	52.8	38.9	35.0	13.0	10.0	9.0	13.0	3.4	4.0	3.8
	Medium gain	1050.6	277.8	266.5	135.5	84.3	66.0	88.1	8.3	26.8	11.2
	High gain	1050.7	2149.4	2195.2	1788.7	1021.7	1210.3	738.8	169.8	776.0	157.1
T_{BB1} (K)		150	133	133	140	161	180	206	351	433	540
Response (Counts)	Low gain	82.4	45.0	40.3	19.9	15.9	12.0	25.0	5.0	5.0	4.7
	Medium gain	1678.3	324.5	310.2	229.1	154.8	98.0	195.9	62.7	61.8	28.1
	High gain	1677.7	2513.2	2559.4	3049.2	1910.2	1828.5	1667.8	1997.3	1924.5	480.1
Gain (unitless)	Low gain	21.173	60.309	68.167	182.234	150.973	206.804	77.349	1117.448	1113.716	356.448
	Medium gain	0.999	7.784	8.350	13.460	12.600	19.283	8.613	33.590	32.795	19.226
	High gain	1.000	1.000	1.000	1.000	1.000	1.000	1.000	1.000	1.000	1.000
Blackbody attenuated with 10X plate											
T_{BB2} (K)		192	136	136	140	170	188	188	351	460	540
Response (Counts)	Low gain	87.9	36.1	33.6	19.1	13.0	9.0	12.1	3.8	4.0	3.9
	Medium gain	1789.8	258.0	253.5	223.4	121.4	68.0	83.9	17.5	30.2	14.2
	High gain	1789.1	1994.3	2085.7	2969.4	1491.2	1247.6	701.5	476.6	889.7	216.5
T_{BB1} (K)		221	157	150	161	192	215	240	400	510	595
Response (Counts)	Low gain	122.0	44.0	38.7	23.0	20.6	17.7	39.1	6.9	7.0	5.0
	Medium gain	2512.5	318.1	296.5	274.8	214.7	160.8	322.8	117.1	125.8	35.3
	High gain	2511.9	2462.4	2441.5	3677.9	2662.2	3032.7	2766.9	3817.9	4012.6	619.0
Gain (unitless)	Low gain	21.163	59.288	69.438	180.899	154.417	204.742	76.468	1080.017	1048.238	375.148
	Medium gain	1.000	7.786	8.288	13.783	12.559	19.238	8.644	33.539	32.686	19.006
	High gain	1.000	1.000	1.000	1.000	1.000	1.000	1.000	1.000	1.000	1.000

Table 19. Summary of gain values determined from radiometric measurements

Channel	Low gain													
	Nominal		Hot focal plane		Cold baseplate		Hot baseplate		Cold telescope		Hot telescope		All	
	Mean	Stdev (%)	Mean	Stdev (%)	Mean	Stdev (%)	Mean	Stdev (%)	Mean	Stdev (%)	Mean	Stdev (%)	Mean	Stdev (%)
1	21.104	0.493	21.168	0.024	21.134	0.564	21.131	0.108	21.077	0.185	21.109	0.407	21.120	0.332
2	60.137	0.537	60.017	1.059	59.849	0.540	60.275	0.569	59.998	0.869	59.868	0.682	60.024	0.668
3	68.947	0.485	68.761	0.930	68.540	0.597	68.879	0.673	68.401	0.121	68.628	1.398	68.692	0.733
4	183.617	2.735	182.587	1.035	182.218	2.090	181.842	1.043	184.881	1.537	184.082	1.230	183.205	1.572
5	151.181	1.724	152.291	1.221	154.739	1.808	154.090	0.689	151.743	0.210	152.281	1.206	152.721	1.369
6	210.530	0.438	207.678	1.664	207.295	1.492	208.529	1.127	208.808	1.888	208.088	0.861	208.488	1.236
7	76.305	1.167	76.854	0.586	77.125	0.479	76.629	0.457	76.828	0.181	76.712	0.383	76.742	0.619
8	1114.453	0.603	1100.654	1.727	1078.404	7.823	1070.514	7.230	-	-	-	-	1091.006	4.842
9	1042.669	8.998	1071.559	3.414	1019.982	6.472	1066.709	1.683	-	-	-	-	1050.230	5.351
	375.434	0.815	369.163	2.985	380.752	2.100	375.241	1.956	-	-	-	-	375.186	2.125
Channel	Medium gain													
	Nominal		Hot focal plane		Cold baseplate		Hot baseplate		Cold telescope		Hot telescope		All	
	Mean	Stdev (%)	Mean	Stdev (%)	Mean	Stdev (%)	Mean	Stdev (%)	Mean	Stdev (%)	Mean	Stdev (%)	Mean	Stdev (%)
1	1.001	0.115	1.000	0.058	1.000	0.058	1.000	0.208	1.000	0.058	1.001	0.153	1.000	0.108
2	7.808	0.252	7.792	0.149	7.815	0.265	7.813	0.672	7.813	0.189	7.895	1.917	7.823	0.842
3	8.343	0.202	8.327	0.408	8.344	0.337	8.337	0.610	8.280	0.708	8.323	0.999	8.326	0.575
4	13.414	0.682	13.577	1.316	13.354	1.224	13.646	2.898	13.461	0.391	13.474	0.672	13.488	1.439
5	12.557	0.106	12.589	0.206	12.499	0.956	12.560	0.486	12.565	0.061	12.608	0.482	12.563	0.495
6	19.210	0.181	19.241	0.208	19.249	0.421	19.224	0.199	19.210	0.269	19.251	0.043	19.231	0.227
7	8.643	0.059	8.634	0.207	8.639	0.012	8.644	0.073	8.651	0.013	8.651	0.145	8.644	0.118
8	33.579	0.225	33.592	0.161	33.621	0.237	33.544	0.222	-	-	-	-	33.584	0.201
9	31.105	8.924	32.759	0.193	31.213	8.995	32.732	0.193	-	-	-	-	31.952	5.875
	19.198	0.165	19.127	0.583	19.152	0.131	19.199	0.449	-	-	-	-	19.150	0.365
Channel	High gain													
	Nominal		Hot focal plane		Cold baseplate		Hot baseplate		Cold telescope		Hot telescope		All	
	Mean	Stdev (%)	Mean	Stdev (%)	Mean	Stdev (%)	Mean	Stdev (%)	Mean	Stdev (%)	Mean	Stdev (%)	Mean	Stdev (%)
all	1.000	0.000	1.000	0.000	1.000	0.000	1.000	0.000	1.000	0.000	1.000	0.000	1.000	0.000

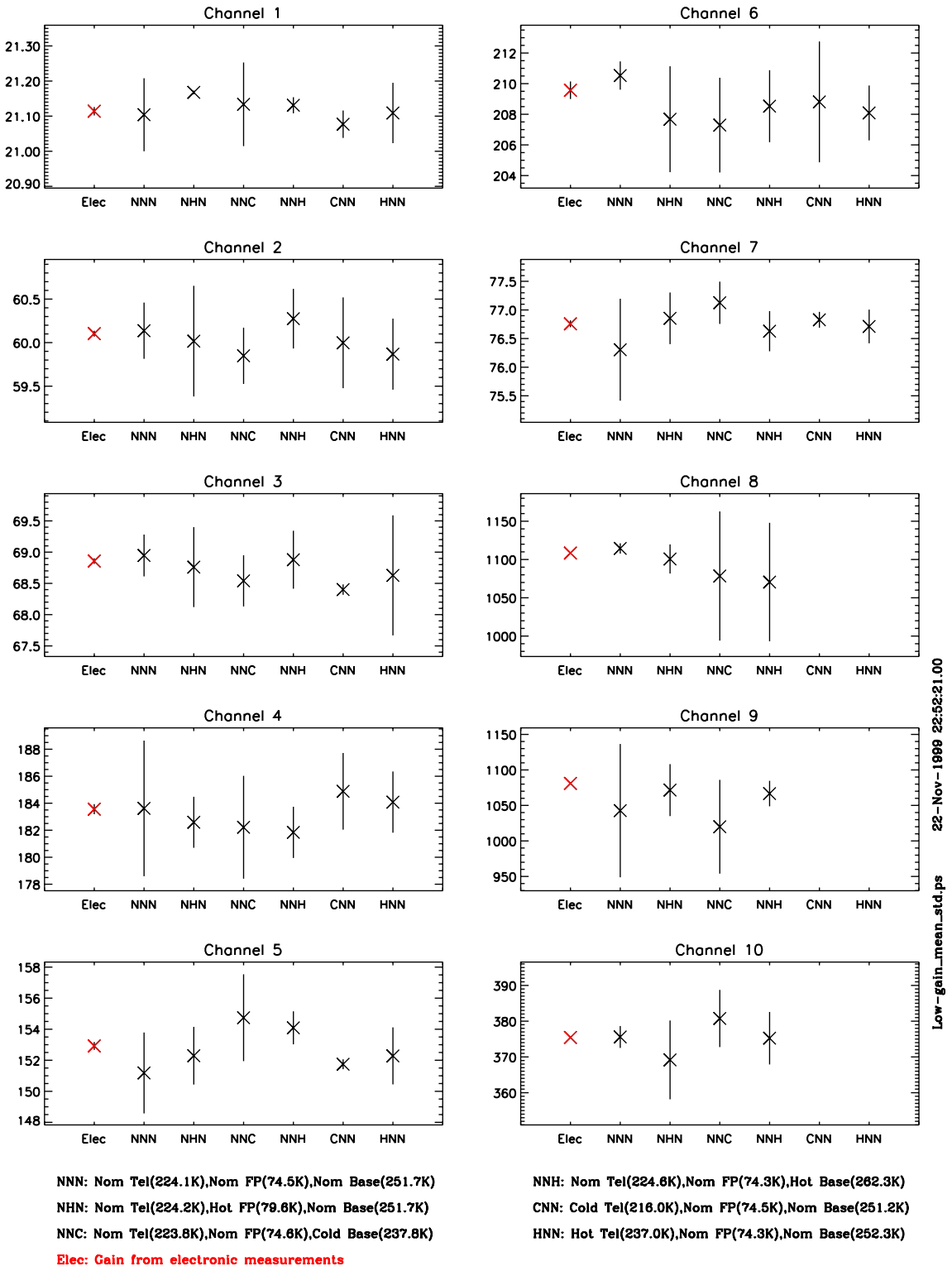

Figure 33. Radiometric low gain as function of SABER temperature

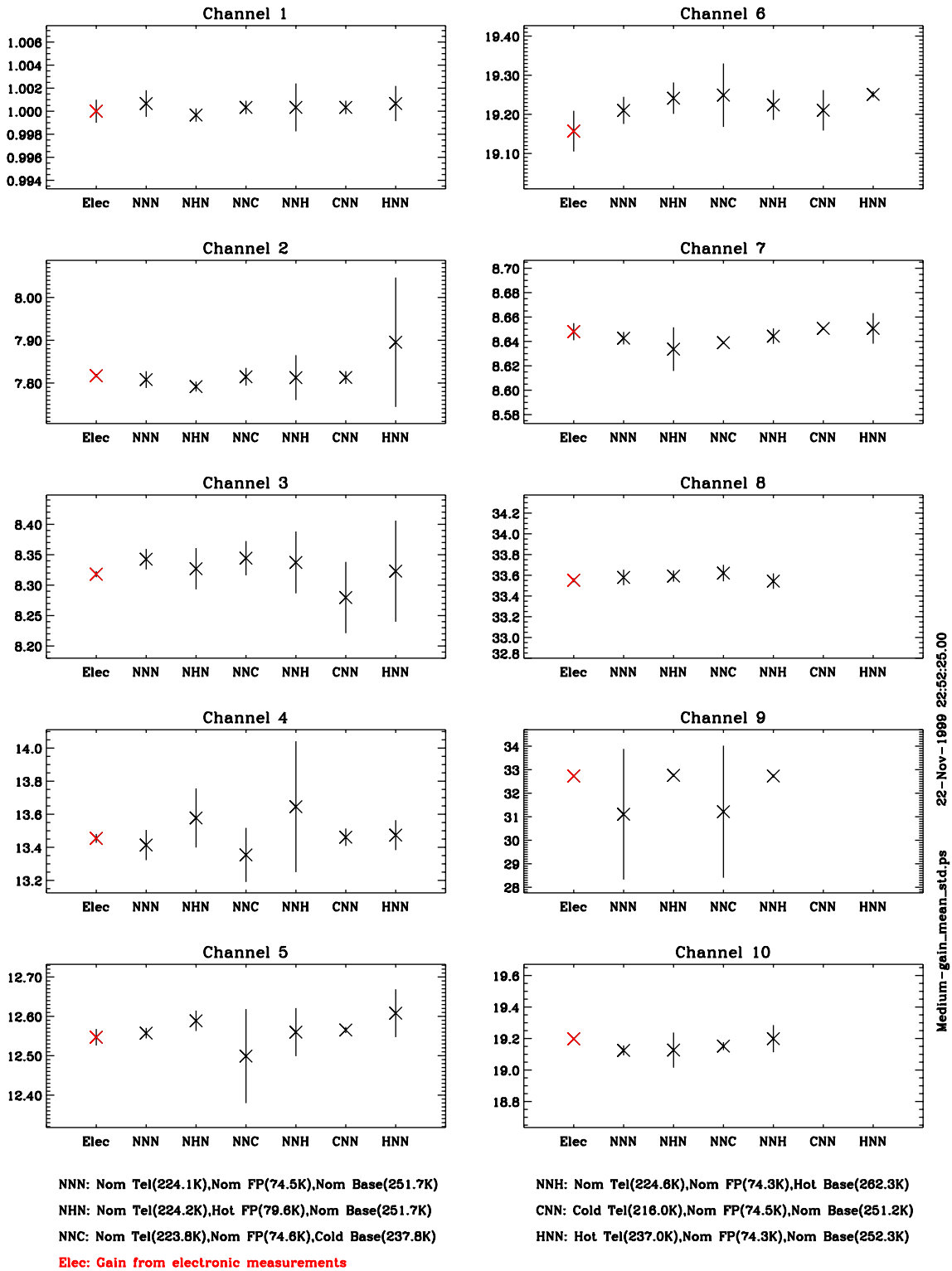

Figure 34. Radiometric medium gain as function of SABER temperature

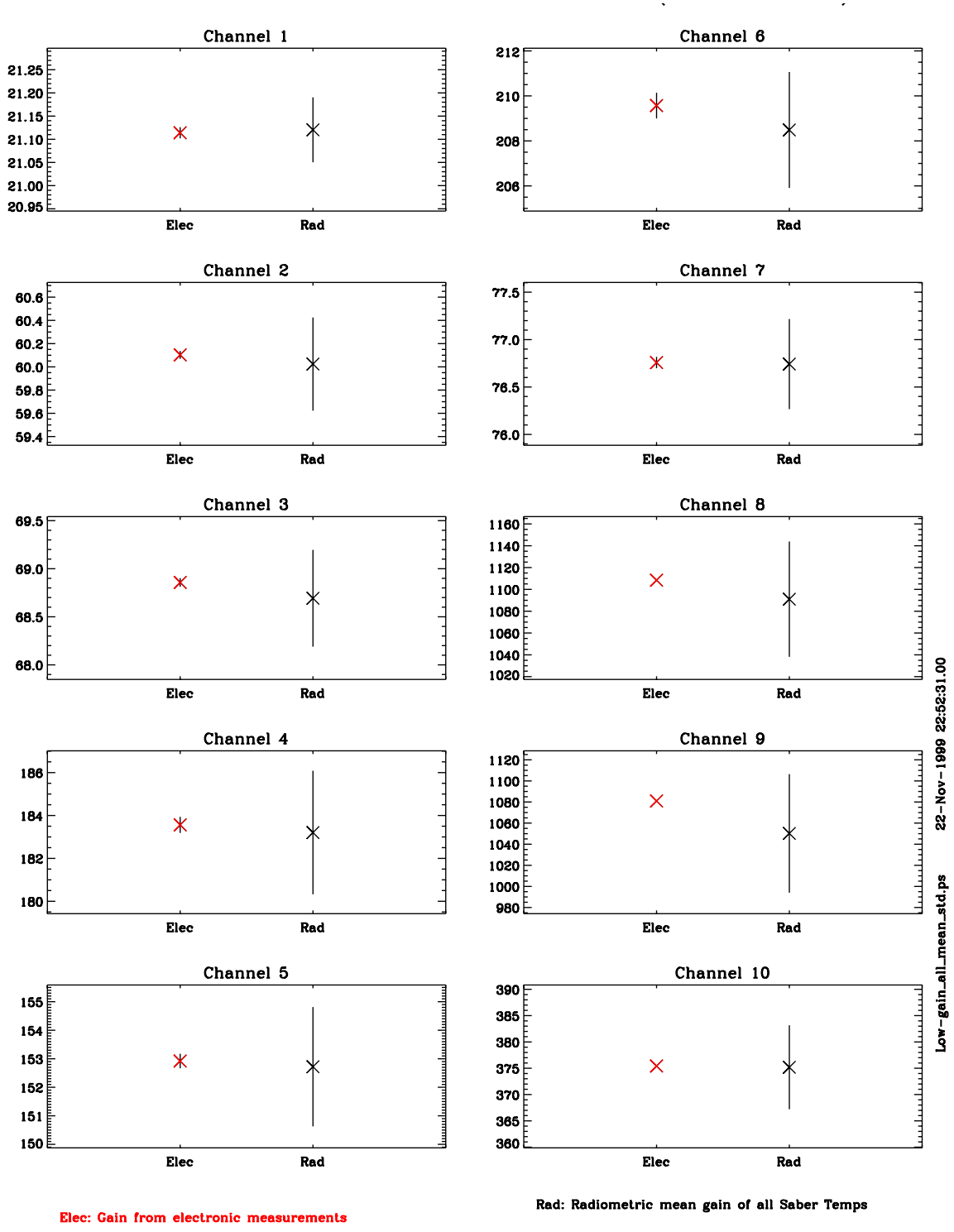

Figure 35. Comparison of low gain values determined from electronic bench measurements with values determined from radiometric measurements

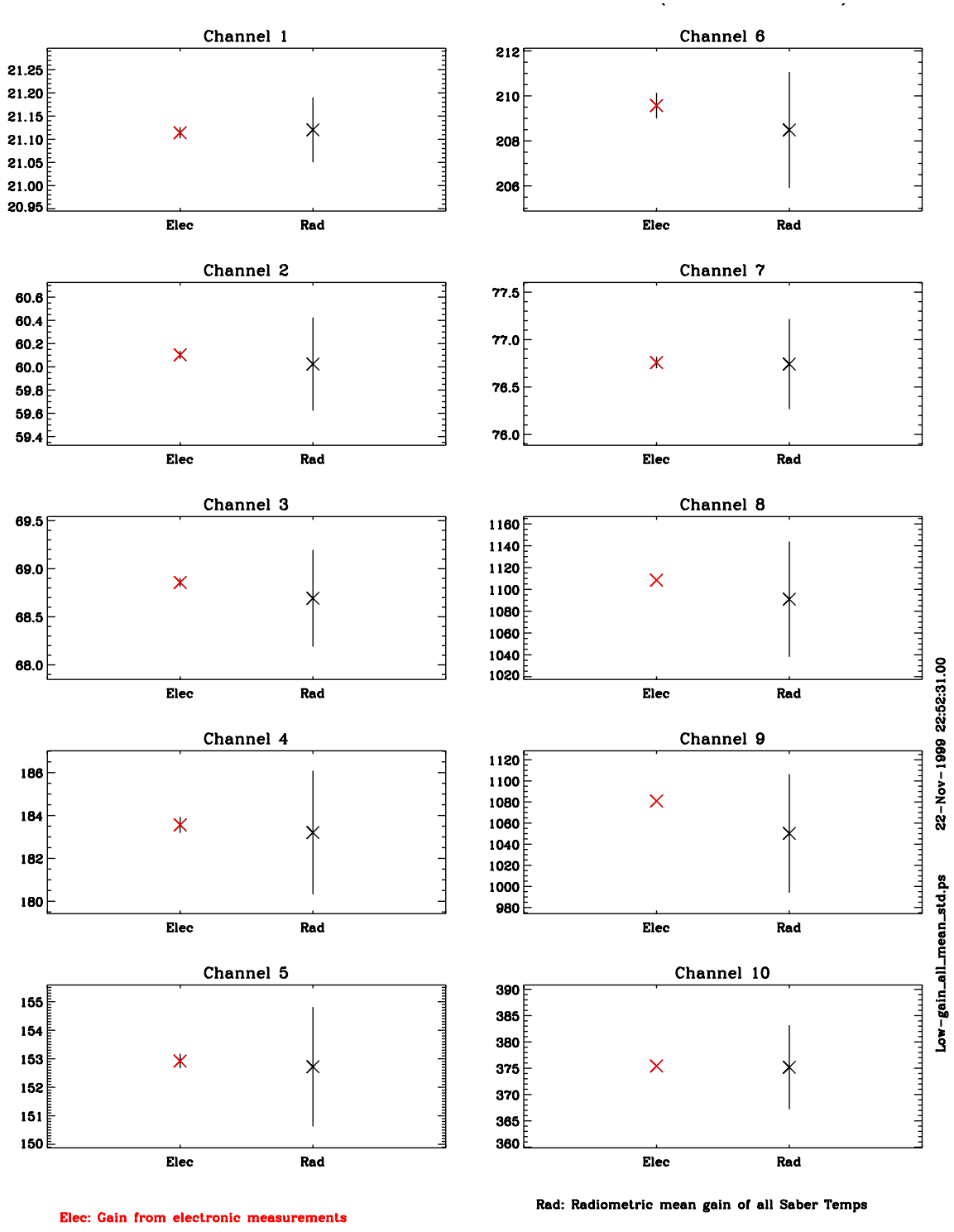

Figure 36. Comparison of medium gain values determined from electronic bench measurements with values determined from radiometric measurements

2.3 Peak Radiance Responsivity and Response Linearity

Low temperature blackbody (LTBB) and high temperature blackbody (HTBB) measurements were used to quantify peak radiance responsivity and response linearity. The blackbodies were mounted and operated inside the radiometric cavity of the test chamber. When a blackbody measurement was being made, either the LTBB or a parabola that images the HTBB was rotated into SABER's FOV. For each blackbody measurement, one or two attenuating plates were rotated in front of SABER to attenuate the blackbody flux while maintaining the blackbody temperature. LTBB measurements were made at blackbody temperatures between 110 and 350 K to give at least three measurements per decade of SABER long wavelength response (channels 1 to 7). HTBB measurements were made at blackbody temperatures between 350 and 710 K to give approximately one measurement per decade of short wavelength response (channels 8 to 10). Data collection is documented in "SABER Ground Calibration Test and Preliminary Results" (SDL/98-059).

Low temperature blackbody measurements were made at each of the instrument temperature states shown in Table 20, and high temperature blackbody measurements were made at each of the instrument temperature states shown in Table 21.

Table 20. LTBB instrument temperature states

Test Event	Telescope (K) TT015V	Focal Plane (K) TF01VG2	Baseplate (K) TM07V
1	224.1 (nominal)	74.5 (nominal)	251.7 (nominal)
2	237.0 (worst case hot)	74.3 (nominal)	252.3 (nominal)
3	216.0 (worst case cold)	74.5 (nominal)	251.2 (nominal)
4	224.2 (nominal)	79.6 (expected worst case hot)	251.7 (nominal)
5	223.8 (nominal)	74.6 (nominal)	237.8 (worst case cold)
6	224.6 (nominal)	74.3 (nominal)	262.3 (worst case hot)

Table 21. HTBB instrument temperature states

Test Event	Telescope (K) TT015V	Focal Plane (K) TF01VG2	Baseplate (K) TM07V
1	224.3 (nominal)	74.4 (nominal)	251.7 (nominal)
2	224.4 (nominal)	79.7 (expected worst case hot)	251.7 (nominal)
3	224.8 (nominal)	74.1 (nominal)	237.8 (worst case cold)
4	224.6 (nominal)	74.3 (nominal)	262.3 (worst case hot)

Effective blackbody radiance was calculated using Equation (7).

$$L_{BBeff(ch)} = \int_{\lambda_1}^{\lambda_2} L(\lambda, T_{BB})\varepsilon_{BB}(\lambda)\rho_M(\lambda)RSR_{(ch)}(\lambda)d\lambda \quad (7)$$

where

$L_{BBeff(ch)}$ = effective radiance (W cm^{-2} sr^{-1}) for channel ch

$L(\lambda, T_{BB})$ = Planck function (W cm^{-2} sr^{-1} μm^{-1})

λ = wavelength (μm)

T_{BB} = temperature of ground support equipment (GSE) blackbody (K)

$\varepsilon_{BB}(\lambda)$ = spectral emittance of GSE blackbody

$\rho_M(\lambda)$ = spectral reflectivity of HTBB parabola

= 1.0 for LTBB (i.e., SABER does not view LTBB through mirror)

$RSR_{(ch)}(\lambda)$ = peak normalized relative spectral responsivity (RSR) for channel ch

The spectral emittance of the LTBB is described in "GSE Low Temperature Blackbody Performance Report" (SDL/98-112). The spectral emittance of the HTBB is described in Appendix D, and the spectral reflectance of the HTBB parabola is described in Appendix C. The peak normalized relative spectral responsivity (RSR) for the nominal focal plane temperature is described in Section 3.3. The integral limits were determined by out-of-band RSR measurements and are shown in Table 22. Only out-of-band RSR measurements above the measurement noise floor were used in the integration.

Table 22. Integral limits for effective blackbody radiance calculation

Channel	λ_1 (μm)	λ_2 (μm)
1	1.950	28.000
2	1.490	17.630
3	1.480	17.660
4	1.680	10.640
5	1.720	7.510
6	1.200	6.240
7	1.200	5.180
8	1.520	5.350
9	1.539	6.830
10	1.220	1.569

2.3.1 Peak Radiance Responsivity

For each channel and temperature state, offset corrected and gain mode normalized response was plotted versus the full range of blackbody temperatures and effective blackbody radiance. Data

for the gain-dependent offset correction was obtained by viewing a stable 110 K blackbody in each gain mode. To calculate peak radiance responsivity and to evaluate response linearity, a linear curve fit of the offset and gain normalized response versus blackbody radiance was performed for a range of blackbody temperatures. The lowest blackbody temperature was chosen to give good signal to noise and to avoid offset errors due to GSE radiometric performance, and ranged from 170 K to 221 K for channels 1 to 7 and 430 K to 570 K for channels 8 to 10. The highest blackbody temperatures were chosen to give effective blackbody radiances that exceed levels given by the science dynamic range and in-flight calibration sources. The highest blackbody temperature was approximately 260 K for channels 1 to 7 and ranged from 509 K to 690 K for channels 8 to 10.

Graphs of offset corrected and gain normalized response versus blackbody temperature and effective blackbody radiance for the nominal SABER temperature state are shown in Figures 37 to 46. Each figure shows the data for a single channel. Also shown is a linear curve fit of offset and gain corrected response versus effective blackbody radiance and curve fit residuals expressed in percent of response. Graphs of other SABER temperature states are not shown because they are similar to the graphs shown in Figures 37 to 46.

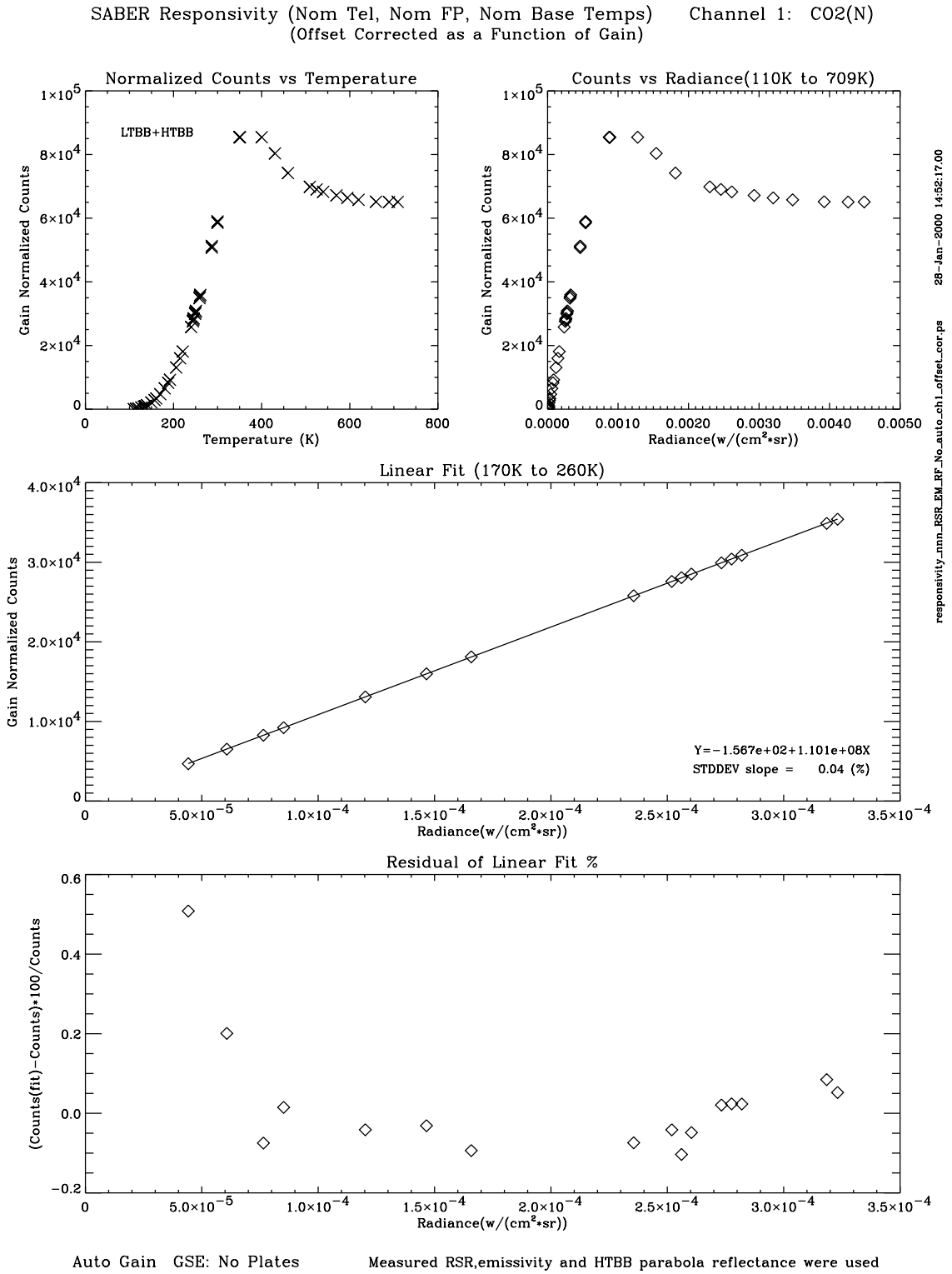

Figure 37. Channel 1 responsivity and linearity for nominal SABER temperatures

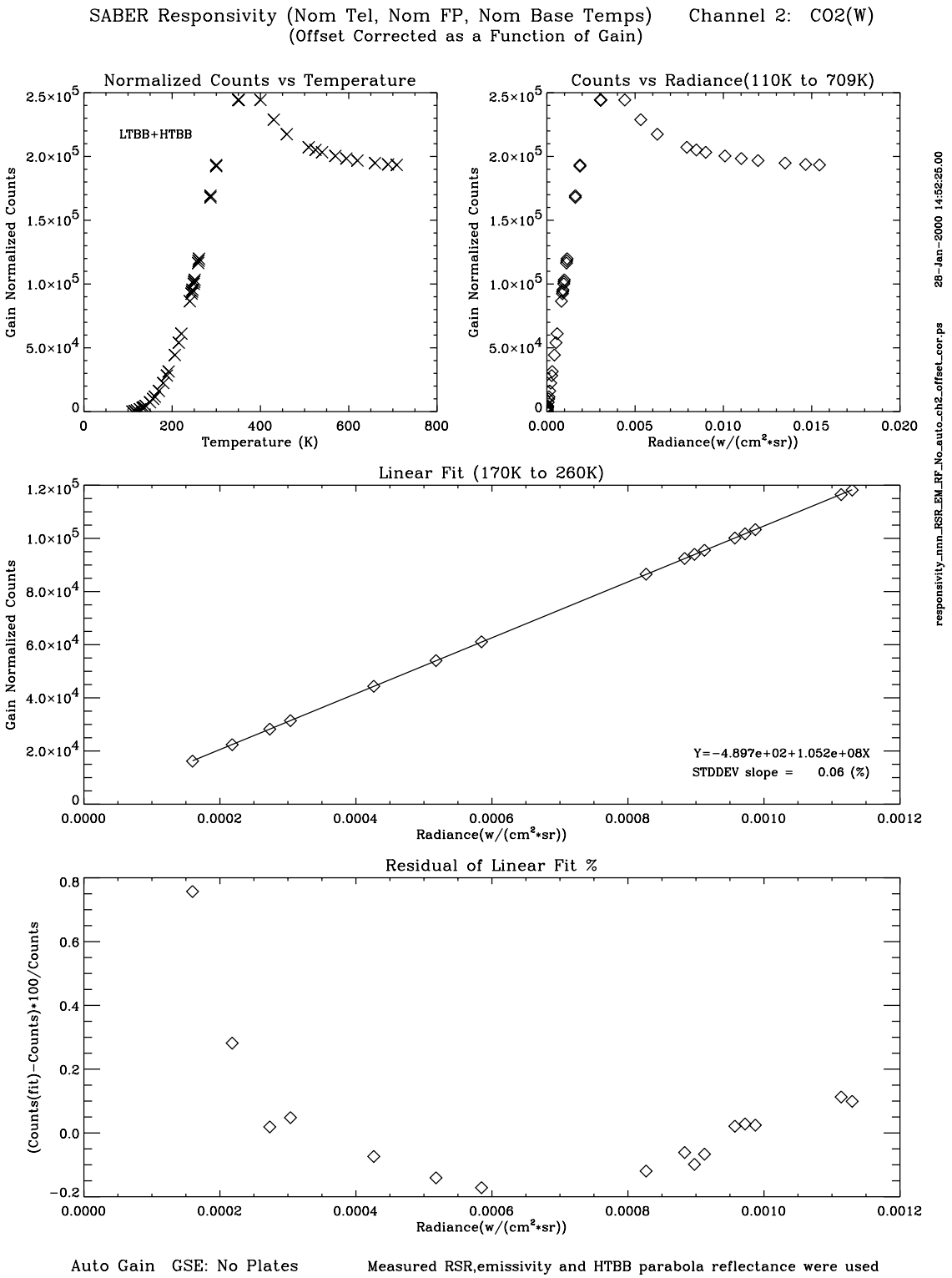

Figure 38. Channel 2 responsivity and linearity for nominal SABER temperatures

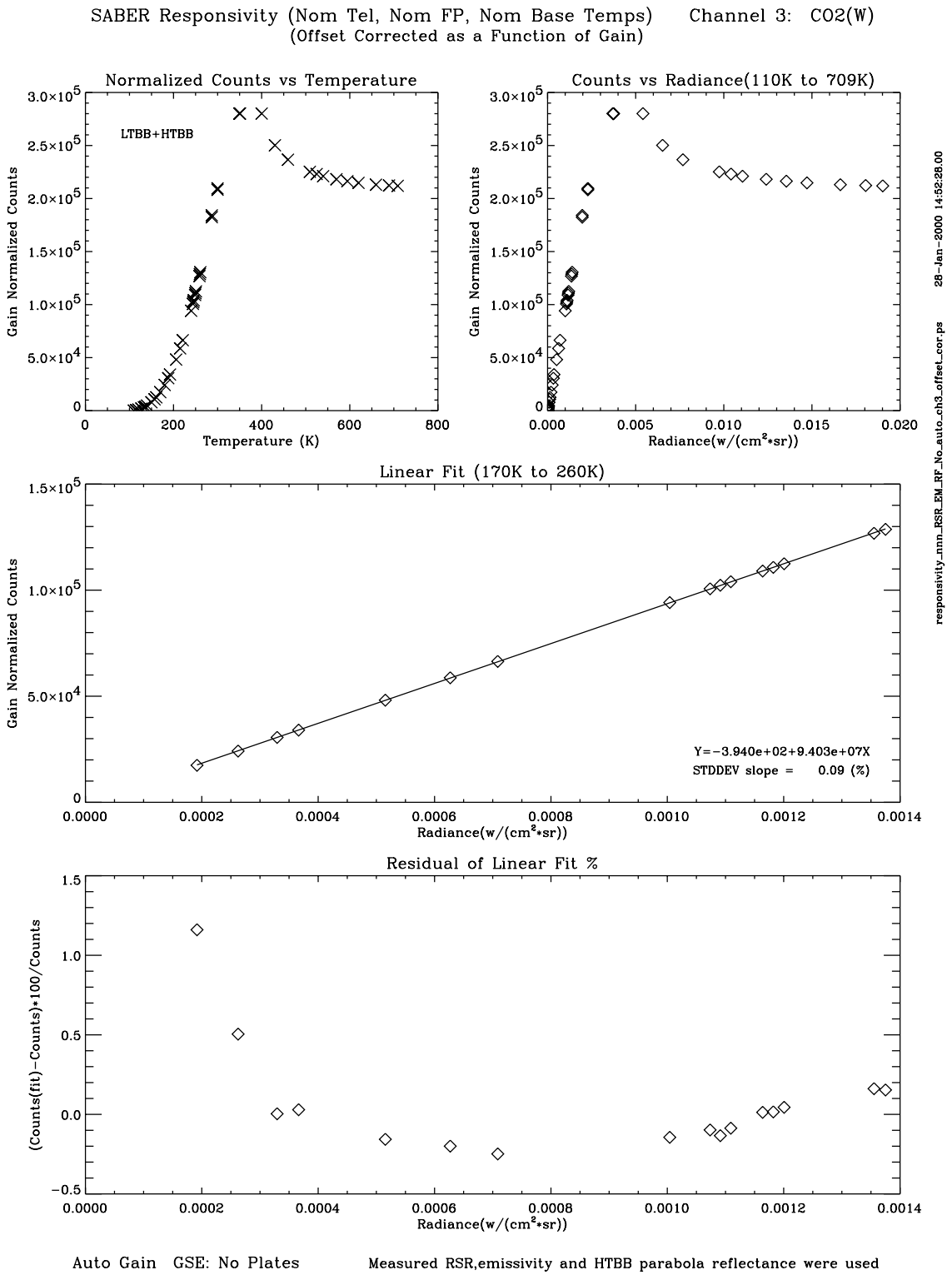

Figure 39. Channel 3 responsivity and linearity for nominal SABER temperatures

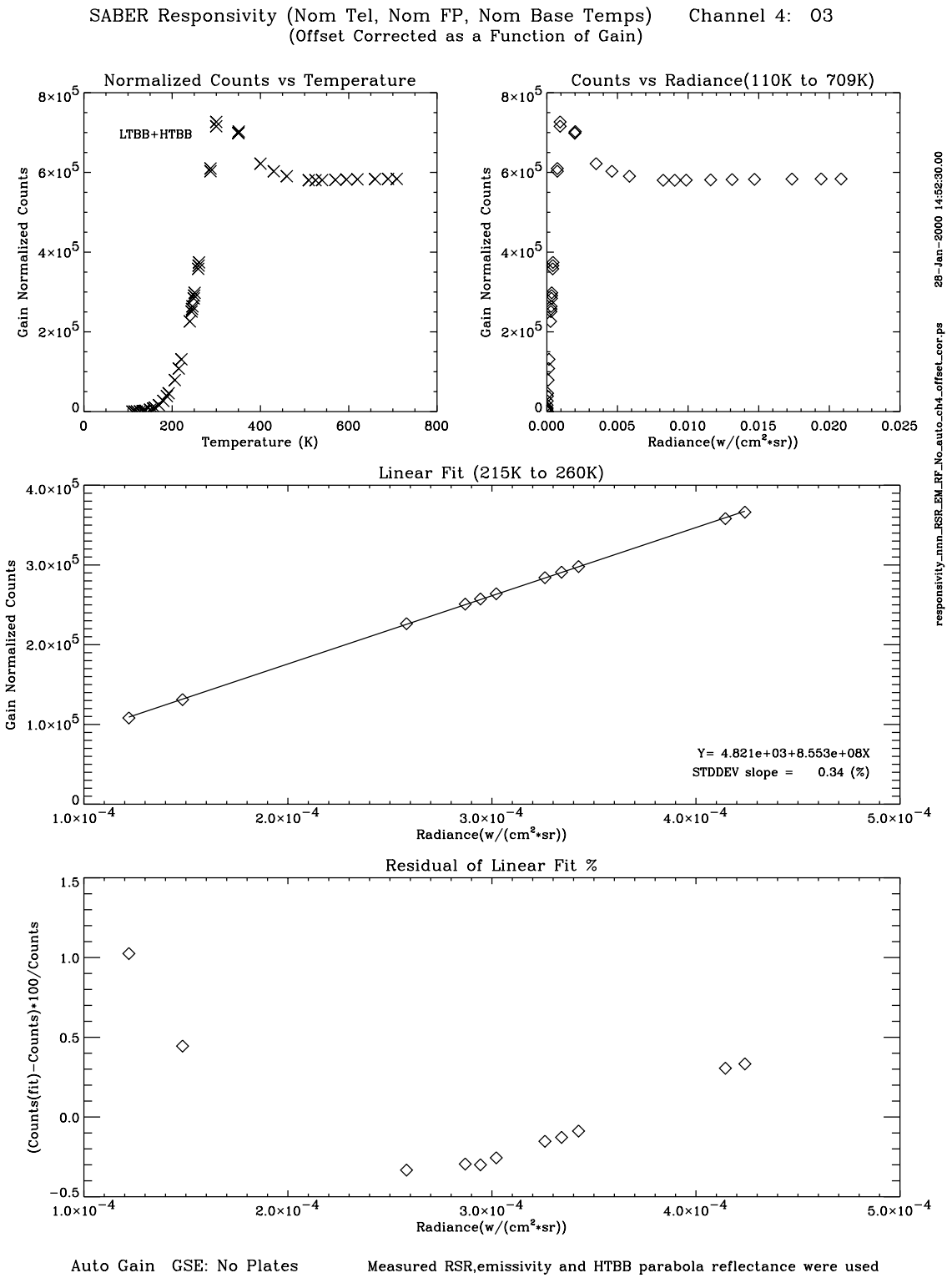

Figure 40. Channel 4 responsivity and linearity for nominal SABER temperatures

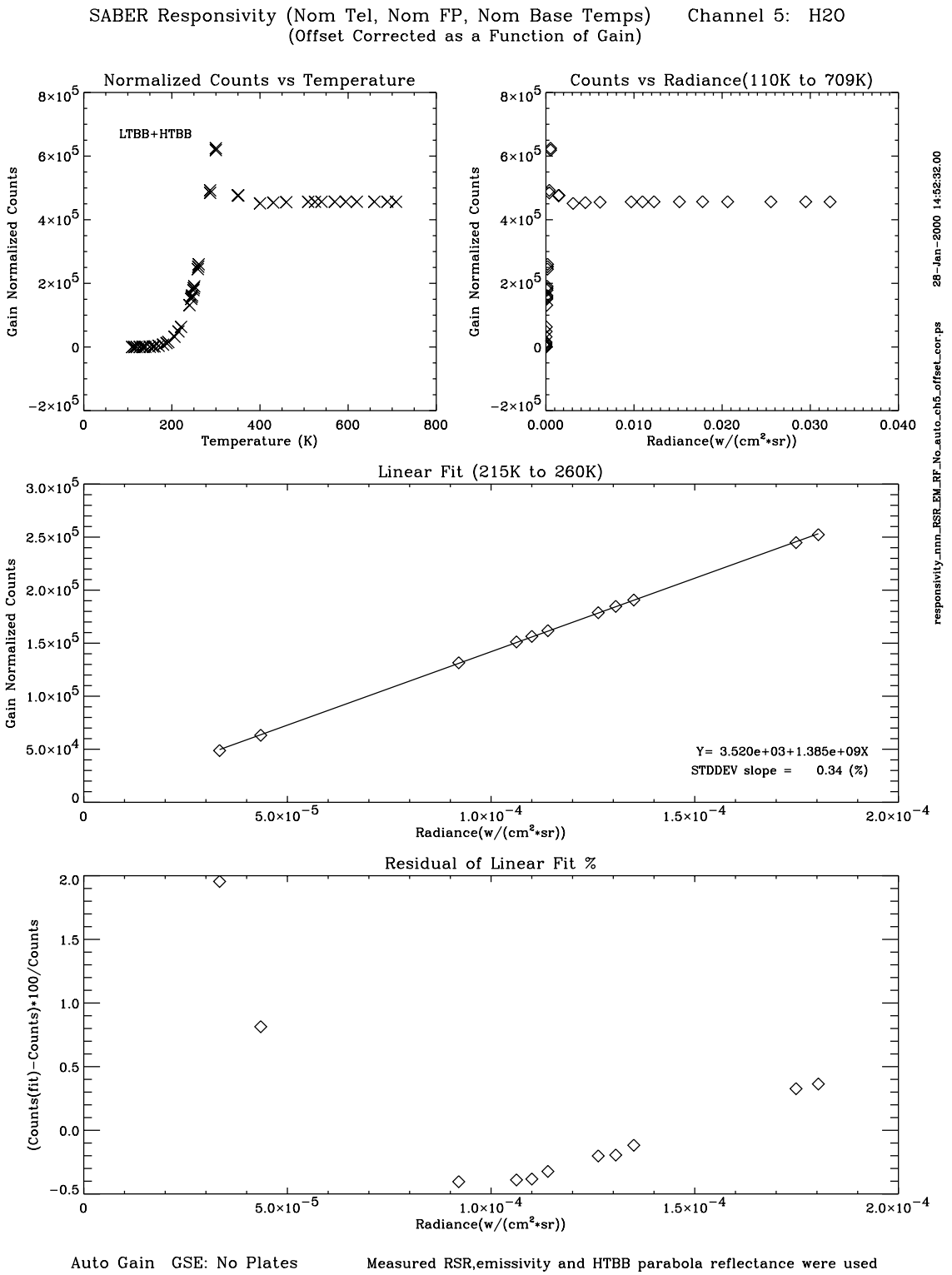

Figure 41. Channel 5 responsivity and linearity for nominal SABER temperatures

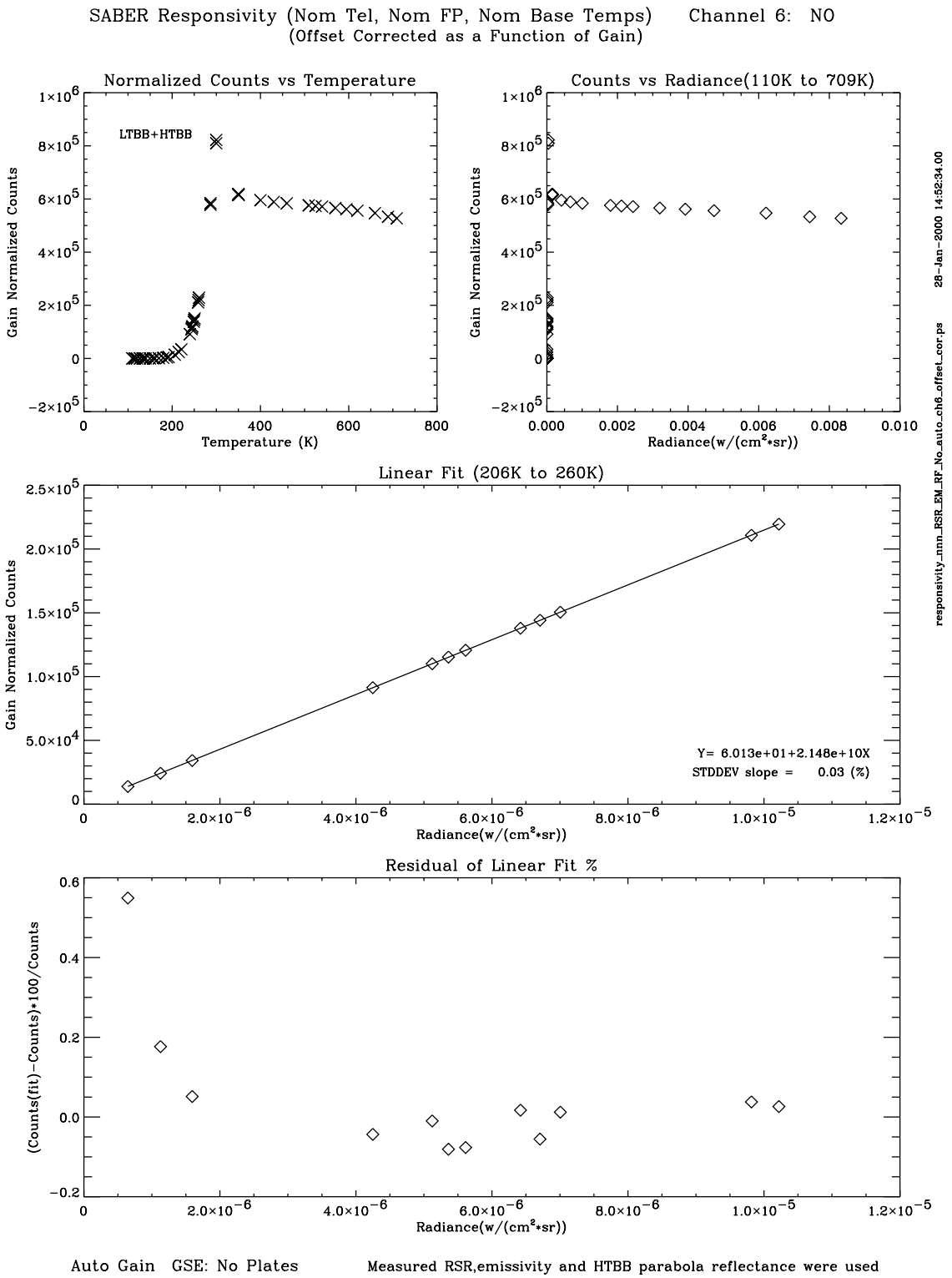

Figure 42. Channel 6 responsivity and linearity for nominal SABER temperatures

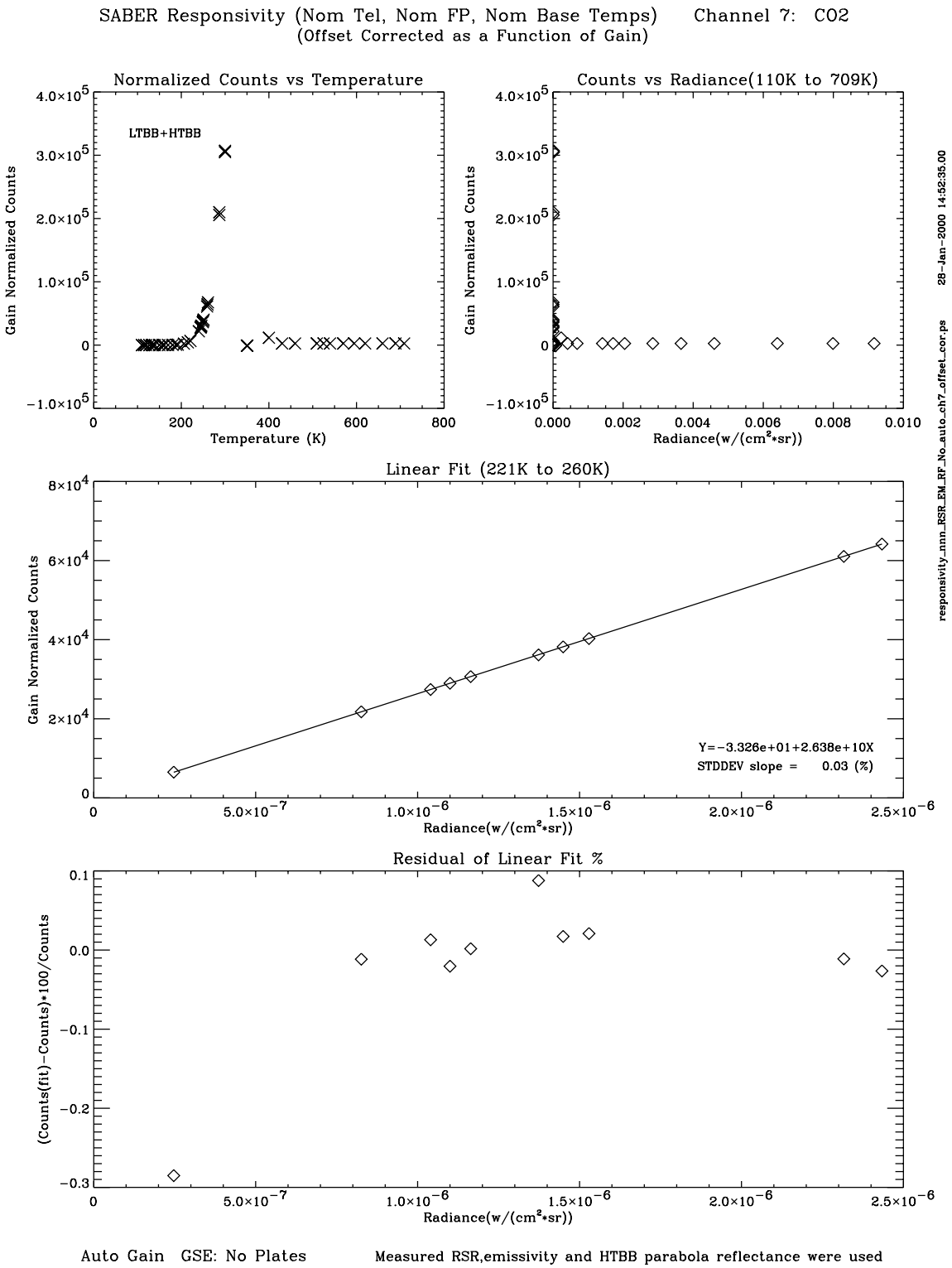

Figure 43. Channel 7 responsivity and linearity for nominal SABER temperatures

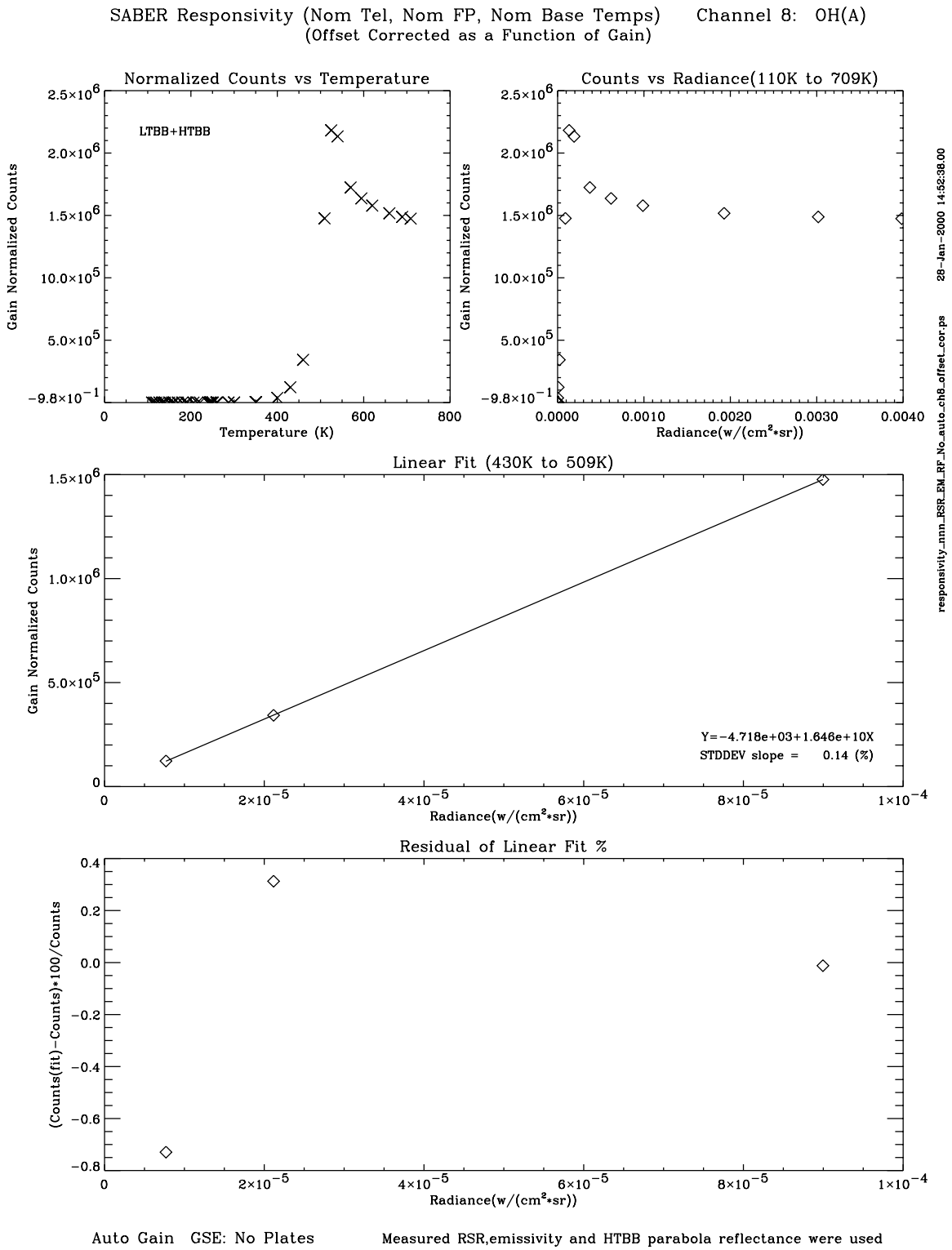

Figure 44. Channel 8 responsivity and linearity for nominal SABER temperatures

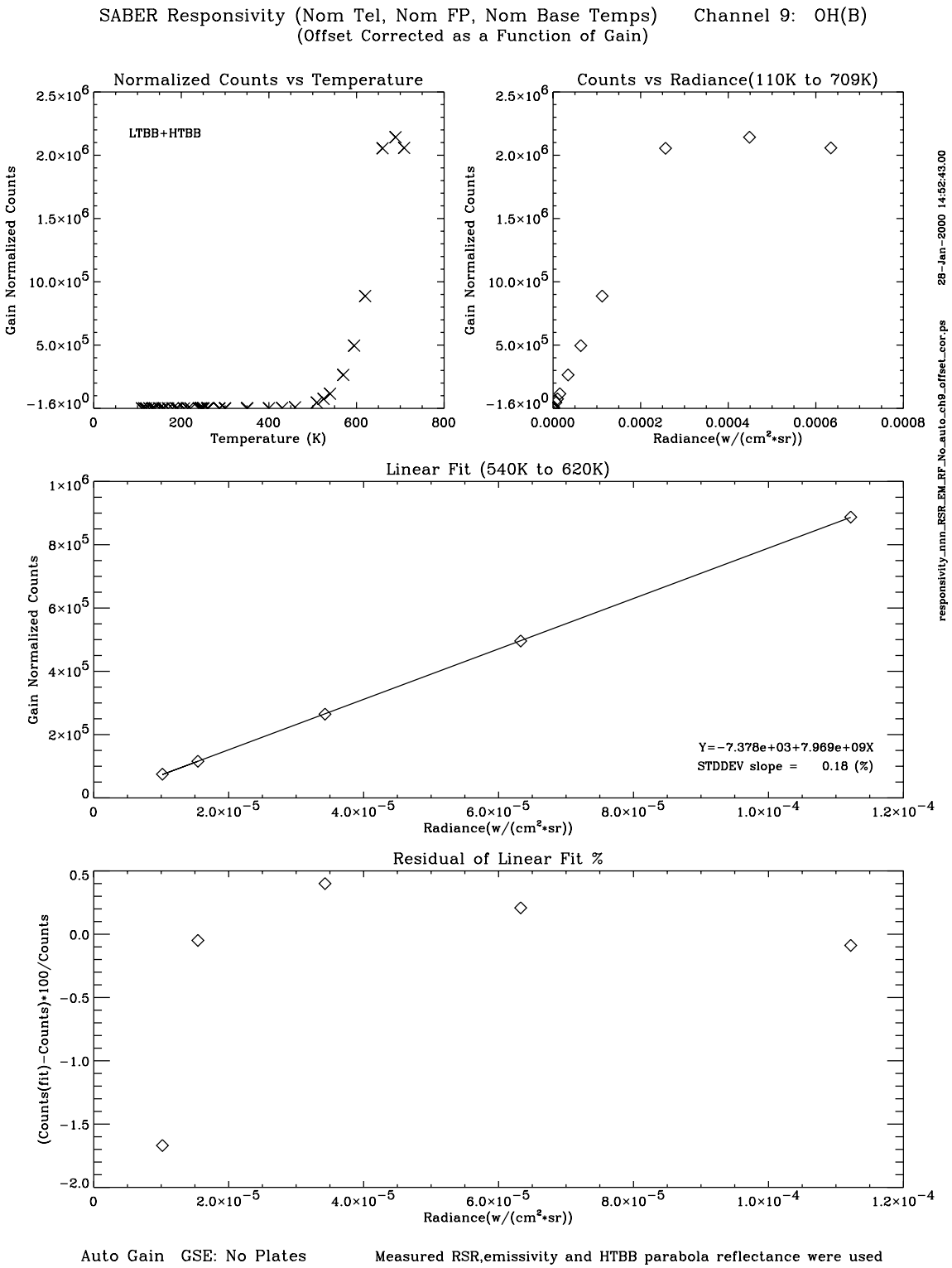

Figure 45. Channel 9 responsivity and linearity for nominal SABER temperatures

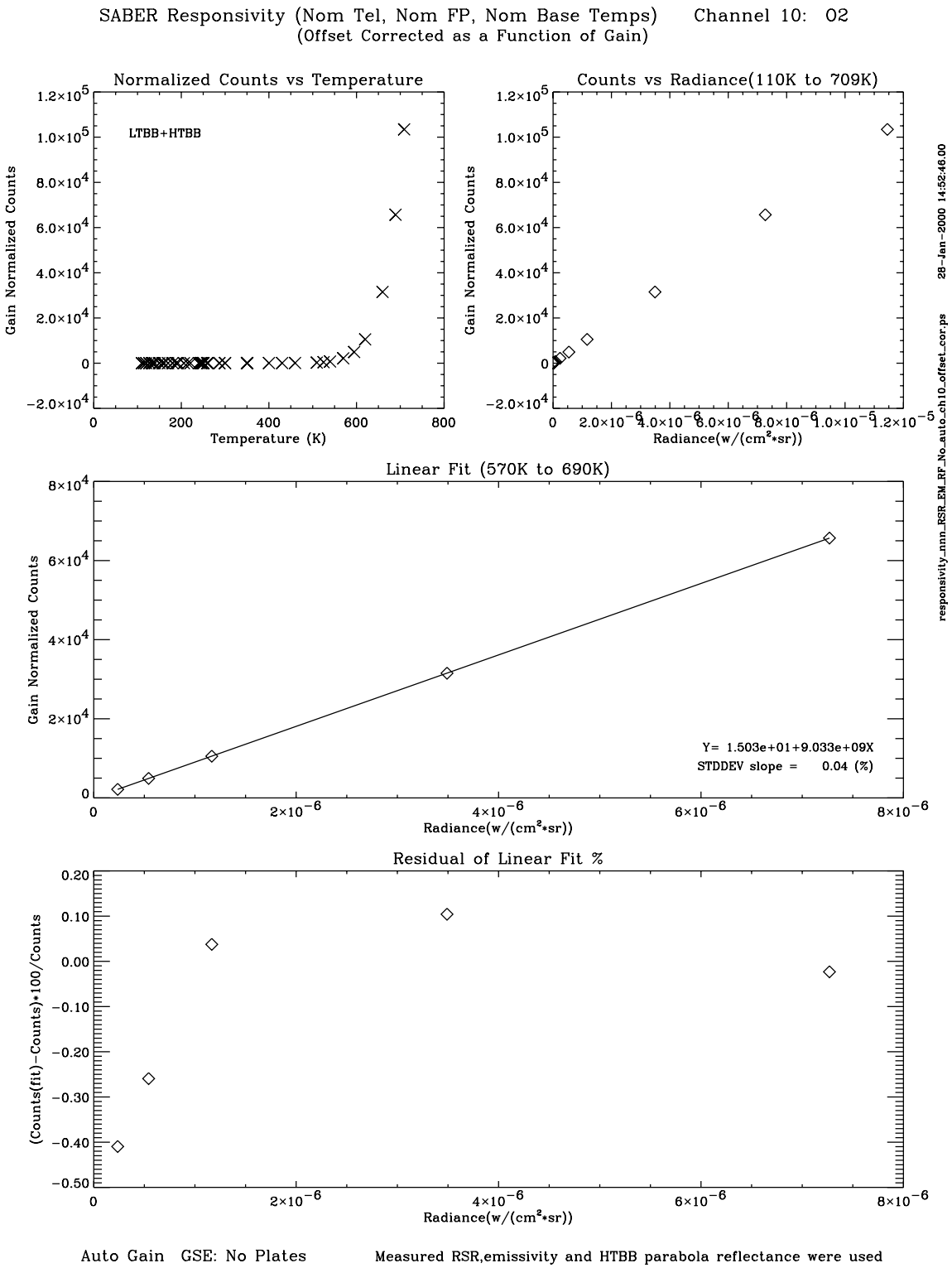

Figure 46. Channel 10 responsivity and linearity for nominal SABER temperatures

The radiance responsivity and the curve fit standard error for each channel and instrument temperature state is given in Table 23, which also shows the average and standard deviation for all temperature states. Because the hot focal plane temperature state clearly reduces responsivity on some channels, it was not included in the average or standard deviation calculation.

Table 23. Peak radiance responsivity for each SABER temperature state

Channel	Responsivity													
	Temperature State[a]												Average [Counts per W/(cm^2*sr)	Standard deviation [Counts per W/(cm^2*sr)
	N, N, N		N, H, N[b]		N, N, C		N, N, H		C, N, N		H, N, Nl			
	Value [Counts per W/(cm^2*sr)	Standard error [%]	Value [Counts per W/(cm^2*sr)	Standard error [%]	Value [Counts per W/(cm^2*sr)	Standard error [%]	Value [Counts per W/(cm^2*sr)	Standard error [%]	Value [Counts per W/(cm^2*sr)	Standard error [%]	Value [Counts per W/(cm^2*sr)	Standard error [%]		
1	1.10e+08	0.04	7.79e+07	0.05	1.12e+08	0.16	1.14e+08	0.04	1.10e+08	0.01	1.10e+08	0.02	1.11e+08	1.53e+06
2	1.05e+08	0.06	7.50e+07	0.07	1.07e+08	0.13	1.08e+08	0.07	1.06e+08	0.04	1.06e+08	0.03	1.06e+08	1.31e+06
3	9.40e+07	0.09	6.55e+07	0.08	9.59e+07	0.15	9.72e+07	0.10	9.42e+07	0.06	9.50e+07	0.05	9.53e+07	1.31e+06
4	8.55e+08	0.34	8.62e+08	0.48	8.49e+08	0.32	8.56e+08	0.44	8.53e+08	0.36	8.48e+08	0.34	8.52e+08	3.60e+06
5	1.38e+09	0.34	1.43e+09	0.47	1.37e+09	0.32	1.38e+09	0.46	1.38e+09	0.37	1.37e+09	0.31	1.38e+09	5.85e+06
6	2.15e+10	0.03	2.15e+10	0.05	2.13e+10	0.02	2.15e+10	0.04	2.15e+10	0.05	2.14e+10	0.03	2.14e+10	8.70e+07
7	2.64e+10	0.03	2.64e+10	0.04	2.60e+10	0.04	2.63e+10	0.06	2.64e+10	0.03	2.54e+10	0.03	2.61e+10	4.22e+08
8	1.65e+10	0.14	1.64e+10	0.11	1.63e+10	0.07	1.63e+10	0.02	0.00e+00	NA[c]	0.00e+00	NA[c]	1.63e+10	1.02e+08
9	7.97e+09	0.18	7.94e+09	0.23	7.89e+09	0.21	7.95e+09	0.23	0.00e+00	NA	0.00e+00	NA	7.94e+09	3.87e+07
10	9.03e+09	0.04	8.92e+09	0.02	8.93e+09	0.06	8.93e+09	0.03	0.00e+00	NA	0.00e+00	NA	8.97e+09	5.90e+07

a. Telescope, focal plane, baseplate temperature state. C=cold, N=nominal, and H=hot
b. Not used for average and standard deviation calculation over all temperature states
c. HTBB measurements were not obtained in this temperature state

Uncertainties due to blackbody radiance, SABER relative spectral response, and the responsivity measurement were combined using Equation (8) to estimate the uncertainty of peak radiance responsivity.

$$\sigma_{\Re} = \sqrt{(\sigma_{BB})^2 + (\sigma_{RSR})^2 + (\sigma_{meas})^2} \quad (8)$$

where $\sigma_{\Re}$ = uncertainty of peak radiance responsivity (%)

σ_{BB} = total blackbody radiance uncertainty (%)

σ_{RSR} = spectral response uncertainty (%)

σ_{meas} = peak radiance responsivity measurement uncertainty (%)

Blackbody radiance uncertainty for various flux levels and blackbody temperatures are documented in “SABER Ground Support Equipment Specifications” (SDL/97-070). The average blackbody radiance uncertainty was calculated by taking an average of blackbody radiance uncertainties for the largest and smallest blackbody operating temperatures that were used during peak radiance responsivity analyses. For the LTBB, the total blackbody radiance uncertainty was set equal to the average blackbody radiance uncertainty. A parabola was used during HTBB operations to image the blackbody cavity onto the sensor focal plane. For HTBB measurements, the parabola reflectance uncertainty, radiance uncertainty due to parabola BRDF (bidirectional reflectance distribution function), and average blackbody radiance uncertainty were combined using the RSS operation to give the total blackbody radiance uncertainty. These uncertainties are given in Table 24.

Table 24. Total blackbody radiance uncertainty for peak radiance responsivity measurement

Ch	Blackbody radiance uncertainty (%)							
	LTBB		HTBB		Average blackbody radiance uncertainty	HTBB parabola reflectance uncertainty	HTBB radiance uncertainty due to parabola BRDF	σ_{BB}
	SNR=100	T=250K	T=450K (ch 8) T=550K (ch 9) T=575K (ch 10)	T=525K (ch 8) T=625K (ch 9) T=700K (ch 10)				
1	0.9	0.3	-	-	0.6	-	-	0.6
2	1.1	0.3	-	-	0.7	-	-	0.7
3	1.1	0.3	-	-	0.7	-	-	0.7
4	1.1	0.4	-	-	0.8	-	-	0.8
5	1.0	0.5	-	-	0.8	-	-	0.8
6	1.2	0.6	-	-	0.9	-	-	0.9
7	1.0	0.7	-	-	0.9	-	-	0.9
8	-	-	2.5	1.1	1.8	0.8	0.25	2.0
9	-	-	1.1	0.7	0.9	0.9	0.25	1.3
10	-	-	1.2	0.8	1.0	1.2	0.25	1.6

SABER relative spectral response is required to calculate effective blackbody radiance and is required to determine the peak radiance responsivity. The uncertainty of the relative spectral response is documented in Section 3.6.

Peak radiance responsivity measurement uncertainty was quantified using the standard error of the linear coefficient in the curve fit. These values are shown for each channel and temperature state in Table 23. The peak radiance responsivity measurement uncertainties were set equal to the standard error for the nominal temperature state because they are sufficiently small and similar in value to other temperature states.

Table 25 gives individual uncertainty terms and the combined peak radiance responsivity uncertainty, $\sigma_{\Re}$, calculated using Equation (8). The combined uncertainty values range from 1.3% to 2.9% depending on channel.

*

Table 25. Peak radiance responsivity uncertainty

Channel	σ_{BB} (%)	σ_{RSR} (%)	σ_{meas} (%)	$\sigma_{\Re}$ (%)
1	0.6	1.57	0.04	1.7
2	0.7	1.95	0.06	2.1
3	0.7	1.73	0.09	1.9
4	0.8	2.43	0.34	2.6
5	0.8	1.00	0.34	1.3
6	0.9	2.72	0.03	2.9
7	0.9	1.48	0.03	1.7
8	2.0	1.90	0.14	2.8
9	1.3	1.80	0.18	2.2
10	1.6	1.18	0.04	2.0

Figure 47 shows a graph of responsivity versus SABER temperature state for each channel. The value is shown with an X, and ± peak radiance responsivity uncertainty is overplotted with a vertical bar. These graphs show (1) a decrease in responsivity (channels 1 to 3) by about 41% when warming the focal plane from 75 K to 80 K, (2) a slight increase in responsivity (channel 5) when warming the focal plane from 75 K to 80 K, and (3) the dependence of responsivity for all other channels and temperature states are independent of SABER temperature state within the limits given by measurement uncertainty.

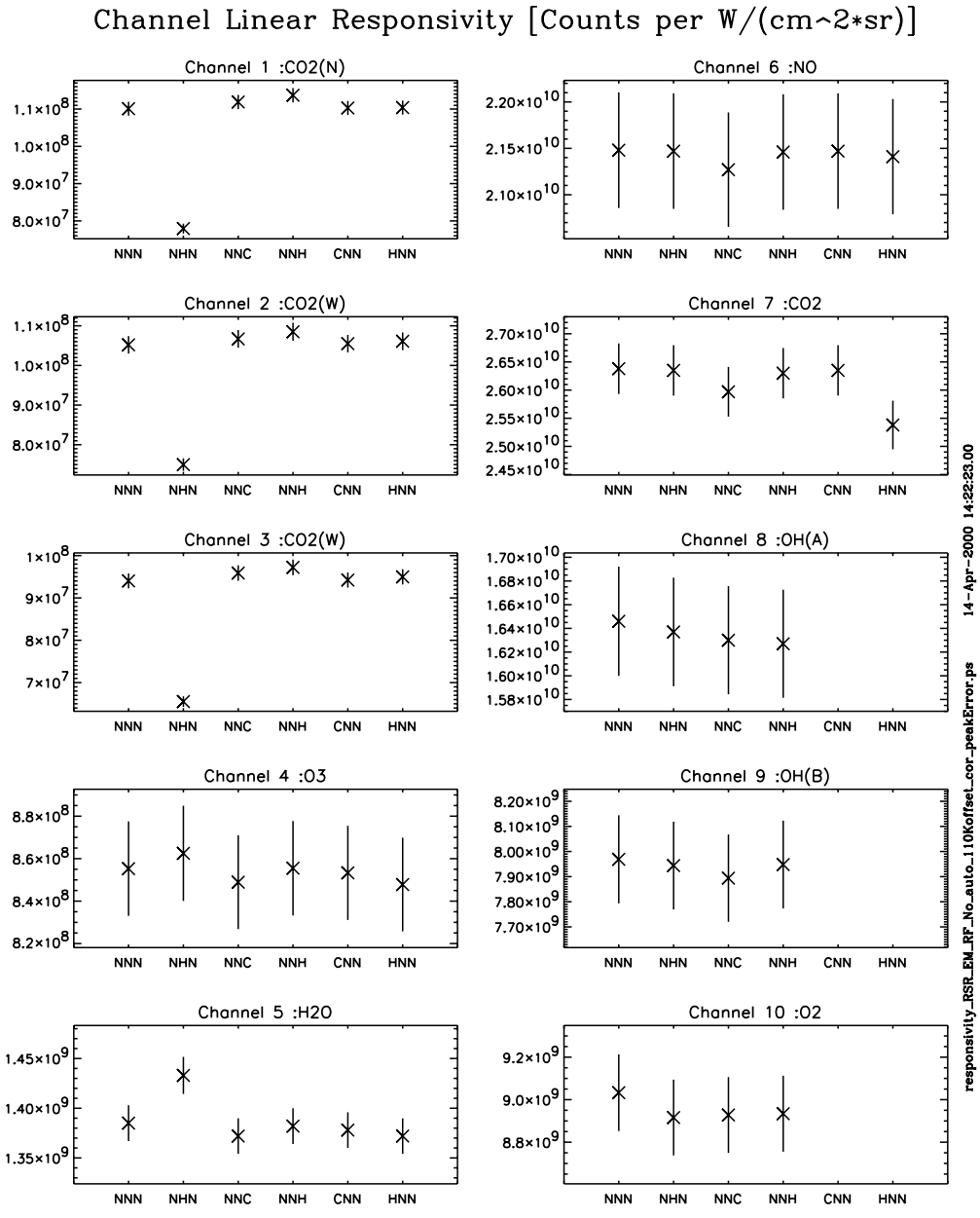

Figure 47. Channel responsivity for each SABER temperature state

2.3.2 Long Wavelength Linearity

As described in Section 2.3, one or two attenuating plates were rotated in front of SABER to attenuate the blackbody flux while maintaining the blackbody at temperature. This was done to quantify linearity independent of absolute blackbody measurements. These data were analyzed as part of the quick look analysis and the results are reported in “SABER Ground Calibration and Preliminary Results” (SDL/98-059).

Because of the high quality and small degree of response nonlinearity displayed with absolute blackbody measurements, nonlinearity uncertainty was quantified using these measurements. The degree of nonlinearity was quantified by calculating the standard deviation of the linear curve fit residuals shown in Figures 37 to 46. Details of the linear curve fits are described in Section 2.3.1. The standard deviation of the curve fit residual expressed in percent of response for each channel and instrument temperature state is shown in Table 26, which also shows the average and standard deviation for all temperature states. These data show channel response nonlinearity to be less than 1% for all temperature states and over the response range given by blackbody temperatures used for the linear curve fit. The selection of these blackbody temperatures is discussed in Section 2.3.1.

Table 26. Degree of response nonlinearity from absolute blackbody measurements

Channel	Response Nonlinearity (%)							
	Temperature State[a]						Average	Standard deviation
	N, N, N	N, H, N	N, N, C	N, N, H	C, N, N	H, N, Nl		
1	0.15	0.13	0.66	0.16	0.04	0.03	0.20	0.23
2	0.22	0.23	0.51	0.27	0.14	0.13	0.25	0.14
3	0.34	0.26	0.52	0.39	0.24	0.20	0.33	0.12
4	0.43	0.46	0.40	0.43	0.45	0.42	0.43	0.21
5	0.72	0.74	0.69	0.73	0.79	0.67	0.72	0.04
6	0.17	0.22	0.08	0.15	0.29	0.21	0.19	0.07
7	0.10	0.11	0.21	0.19	0.05	0.15	0.14	0.06
8	0.53	0.40	0.26	0.07	-	-	0.32	0.20
9	0.82	0.54	0.53	0.56	-	-	0.61	0.14
10	0.22	0.27	0.56	0.23	-	-	0.32	0.16

a. Telescope, focal plane, baseplate temperature state. C=cold, N=nominal, and H=hot

The largest radiance used in the linearity analysis is given by the effective blackbody radiance of the maximum blackbody temperature used in the linear curve fit. The largest blackbody temperature and corresponding effective blackbody radiance, calculated using Equation (7), is shown in Table 27. The maximum gain normalized response can be determined for each temperature state using maximum radiance values shown in Table 27 and peak radiance responsivities values

shown in Table 23. The minimum radiance for linear responsivity is essentially zero because the response is assumed to be linear for radiance values less than values given by the minimum blackbody temperature used in the linear curve fit.

Table 27. Maximum radiance for blackbody linearity analyses

Channel	Blackbody Temperature [K]	Radiance [W/(cm^2*sr)]
1	260	3.2e-4
2	260	1.1e-3
3	260	1.4e-3
4	260	4.2e-4
5	260	1.8e-4
6	260	1.0e-5
7	260	2.4e-6
8	510	9.3e-5
9	620	1.1e-4
10	689	7.6e-6

2.3.3 Short Wavelength Linearity (Channels 8 to 10)

The short wavelength linearity measurements obtained small-signal response levels at flux levels throughout the response dynamic range of channels 8 through 10. The data collection is documented in “SABER Ground Calibration Test and Preliminary Results” (SDL/98-059). This test was performed by placing an integrating sphere and two blackbodies at the entrance port of the full field collimator, as shown in Figure 48. The large signal blackbody was used to give background flux levels. The blackbody aperture wheel was used to change the throughput between the blackbody and integrating sphere, providing background flux levels that give three measurements per decade for approximately two orders of magnitude. Neutral density filters were used to attenuate the output of the integrating sphere and give measurements low in the instrument’s dynamic range. The lens was used to image the exit port of the integrating sphere at the focus of the full field collimator. The small-signal response was measured by collecting data with the small-signal blackbody shutter opened and closed. The mean and difference between the two measurements are the instrument large- and small-signal responses, respectively.

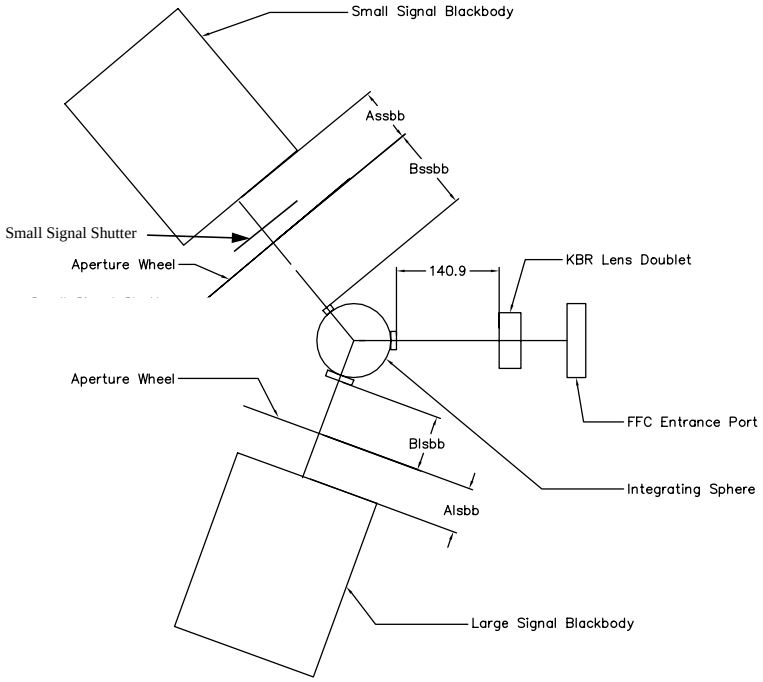

Figure 48. Small-signal linearity test configuration for channels 8, 9, and 10

Short wavelength linearity tests were performed at instrument temperature combinations shown in Table 28.

Table 28. Short wavelength linearity instrument temperature states

Test Event	Telescope (K) TT015V	Focal Plane (K) TF01VG2	Baseplate (K) TM07V
1	223.9 (nominal)	74.4 (nominal)	237.3 (worst case cold)
2	224.6 (nominal)	74.3 (nominal)	262.3 (worst case hot)
3	224.3 (nominal)	79.9 (expected worst case hot)	251.7 (nominal)

Gain dependent offset correction was performed on all short wavelength linearity data using low temperature blackbody measurements obtained at identical SABER temperature states. The blackbody temperature was approximately 110 K.

Offset corrected channel response to the integrating sphere with the small-signal shutter open and closed for each large signal blackbody aperture setting was calculated by taking the average detector response of 8 packets (96 samples). The mean of the two responses was calculated to give the large signal response, and the difference of the two responses was calculated to give the small

signal response. To reduce measurement noise, five measurements were averaged for each large signal blackbody aperture setting.

Because neutral density filters were used to attenuate the output of the integrating sphere, the large and small signal flux levels were both attenuated. For this reason, it was necessary to normalize the small signal response between adjacent neutral density filter settings. This was done by calculating the ratio of the small signal responses between adjacent neutral density filtering settings.

Figures 49 to 51 show the normalized small signal response versus large signal response for each channel and temperature state. Neutral density filter settings can be uniquely identified with data symbols that have different shapes and colors. An indication of nonlinearity is observed when the small signal response decreases for increasing large signal response levels. These graphs show that channels 8 to 10 are linear over a large part of their dynamic range. Figure 52 shows the normalized small signal response versus large signal response for each channel with all temperature states over-plotted. This graph shows that short wavelength linearity is independent of SABER temperature state.

The small signal responsivity is proportional to the inverse of the small signal response. A linearity correction function can be determined by integrating the small signal responsivity over the desired large signal response range. Because data show linear responsivity for responses that exceed the science dynamic range, it was determined that linearity correction is not required.

Short wavelength linearity uncertainty was quantified by calculating the standard deviation of the small signal responses shown in Figures 49 to 52. This calculation was performed on data with response levels smaller than the maximum response that gives linear responsivity. These levels were identified as the largest large-signal response before nonlinearity causes the small signal response to be less than unity. Table 29 shows the maximum gain normalized response, low gain response, and equivalent blackbody radiance for the maximum signal that gives linear responsivity as measured during ground calibration. Table 30 shows the short wavelength linearity uncertainty (channels 8 to 10) for each and all temperature states obtained during ground calibration. This uncertainty is 0.5% or less for all temperature states.

Table 29. Maximum signal for short wavelength linear responsivity

Channel	N,N,C[a]			N,N,H[a]			N,H,N[a]		
	Gain Normalized Response (counts)	Low Gain Response (counts)	Equivalent Radiance (W/(cm^2sr))	Gain Normalized Response (counts)	Low Gain Response (counts)	Equivalent Radiance (W/(cm^2sr))	Gain Normalized Response (counts)	Low Gain Response (counts)	Equivalent Radiance (W/(cm^2sr))
8	1441274	1300	8.84e-05	1431729	1292	8.78e-05	1524116	1375	9.29e-05
9	1391361	1287	1.76e-04	1381660	1278	1.74e-04	1463259	1354	1.84e-04
10	405841	1081	4.54e-05	410178	1093	4.59e-05	472134	1258	5.29e-05

a. Telescope, focal plane, baseplate temperature state. C=cold, N=nominal, and H=hot

Table 30. Short wavelength linearity uncertainty

Channel	Uncertainty (%)			
	N,N,C[a]	N,N,H[a]	N,H,N[a]	All
8	0.3	0.3	0.3	0.3
9	0.5	0.1	0.2	0.3
10	0.3	0.4	0.5	0.5

a. Telescope, focal plane, baseplate temperature state. C=cold, N=nominal, and H=hot

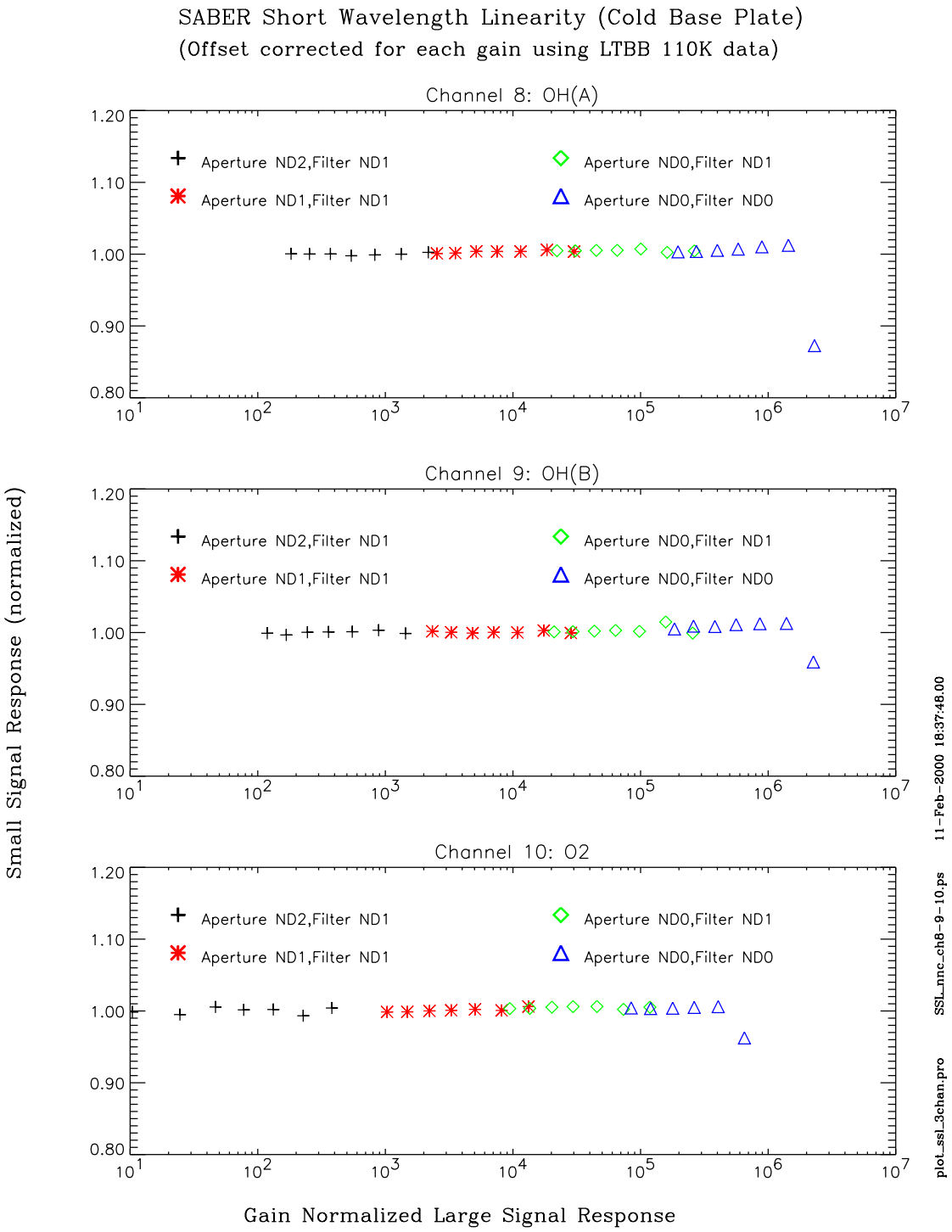

Small signal response was normalized between ND filter settings by calculating the ratio of overlapping two points between adjacent ND settings.

Figure 49. Short wavelength linearity for cold baseplate temperature state

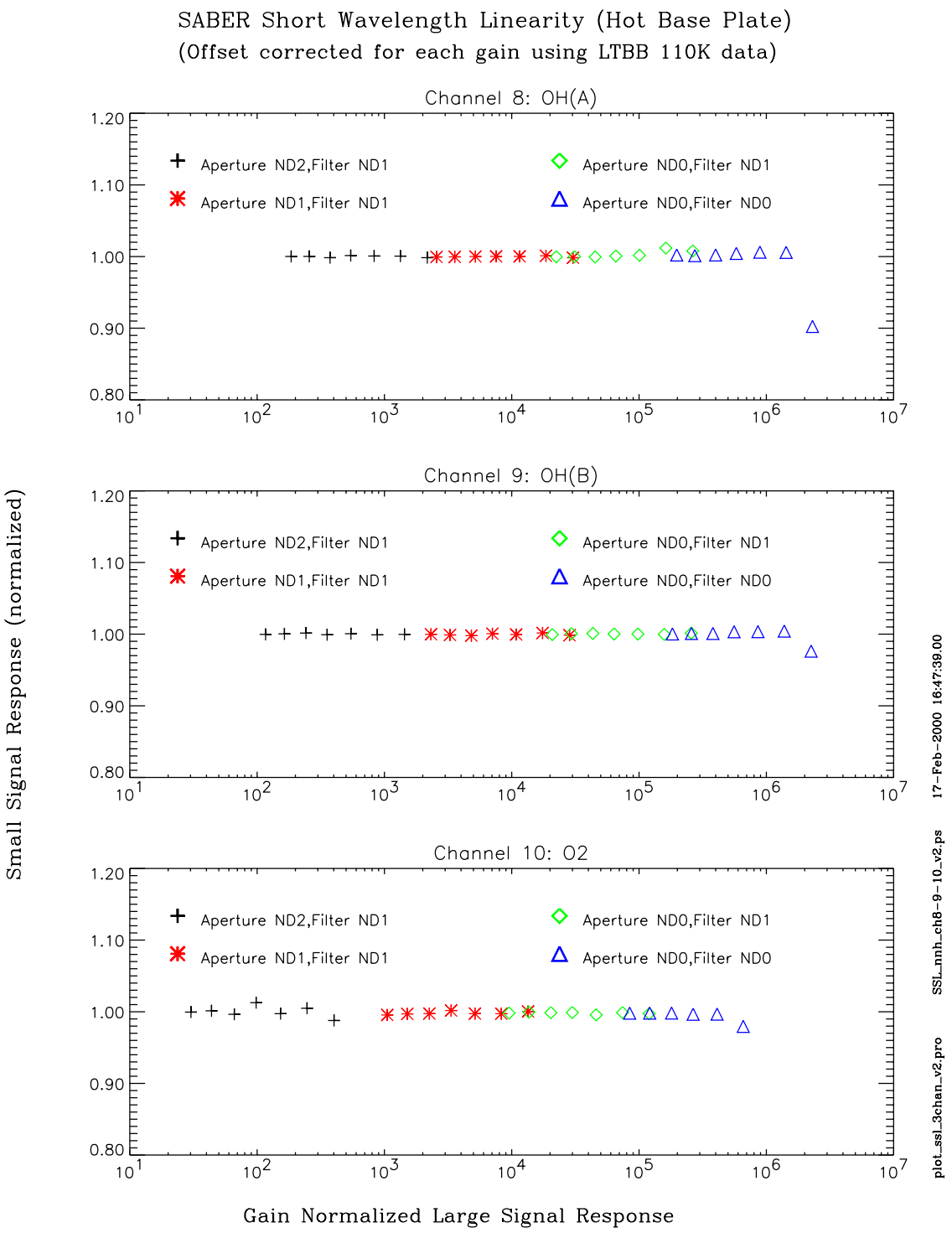

Small signal response was normalized between ND filter settings by calculating the ratio of overlapping two points between adjacent ND settings except ch8(ND0−ND1).

Figure 50. Short wavelength linearity for hot baseplate temperature state

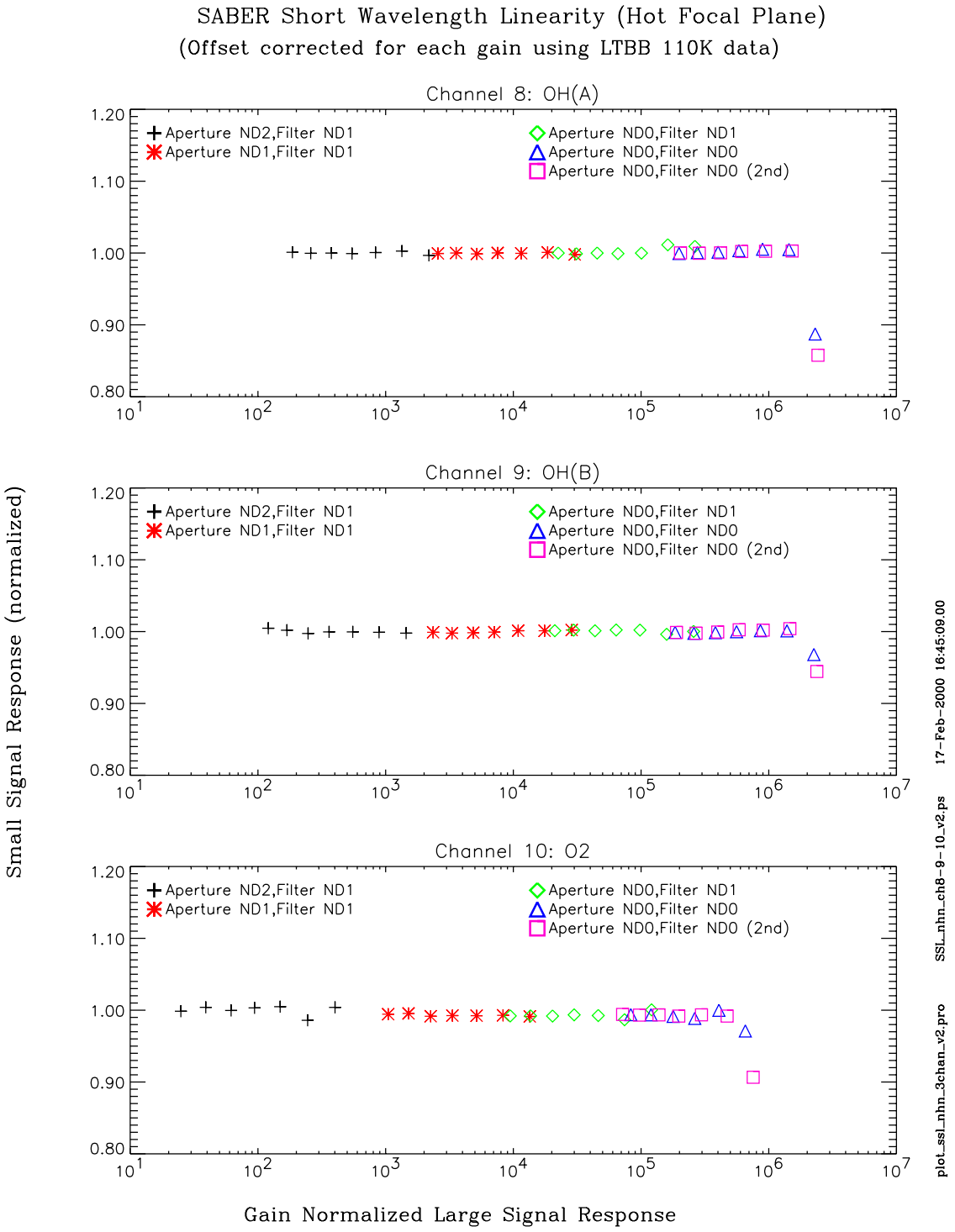

Small signal response was normalized between ND filter settings by calculating the ratio of overlapping two points between adjacent ND settings except ch8(ND0−ND1).

Figure 51. Short wavelength linearity for hot focal plane temperature state

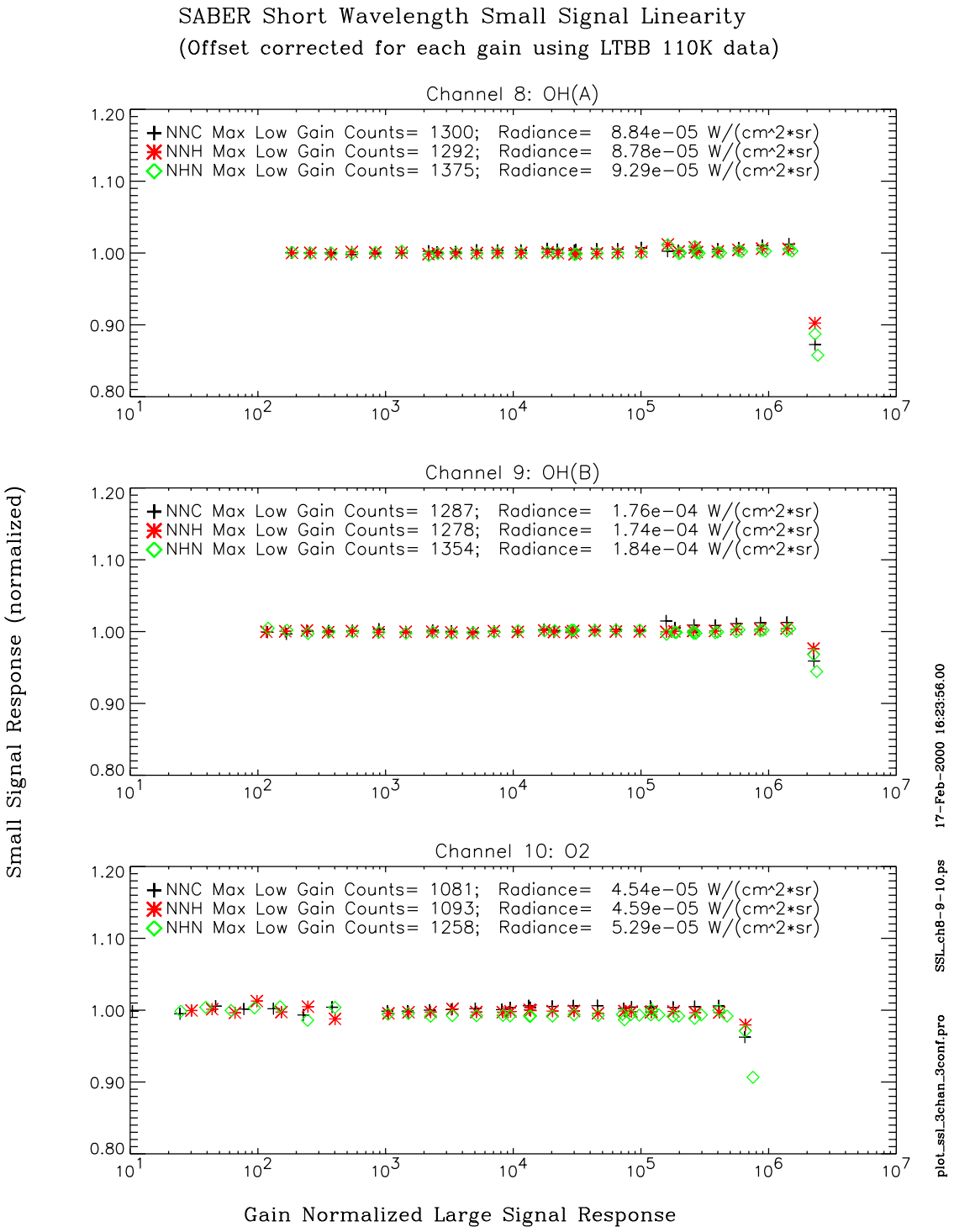

Figure 52. Short wavelength linearity for all temperature states

2.4 In-Flight Calibrator (IFC) Radiance

The in-flight calibrator (IFC) radiance can be determined from ground calibration measurements by relating SABER's IFC response to GSE low and high temperature blackbody responses with known flux levels. These analyses are planned to be performed by GATS Incorporated. A comparison of calculated and measured IFC blackbody radiance is given in the summary section of "SABER Ground Calibration and Preliminary Results" (SDL/98-059). The offset corrected and gain normalized IFC channel response for different source settings and focal plane temperatures are reported in this section for reference.

2.4.1 IFC Response for Channels 1 to 7

The long wavelength IFC (full-aperture blackbody) was viewed periodically during calibration data collection documented in "SABER Ground Calibration and Preliminary Results" (SDL/98-059). Most of the time, the IFC blackbody was set to its nominal temperature of 247.6 K. During the low temperature blackbody data collection procedure, the IFC blackbody was also set to 253 K and 260 K. Figure 53 shows data for the IFC blackbody temperature between July 31 to September 3, 1999.

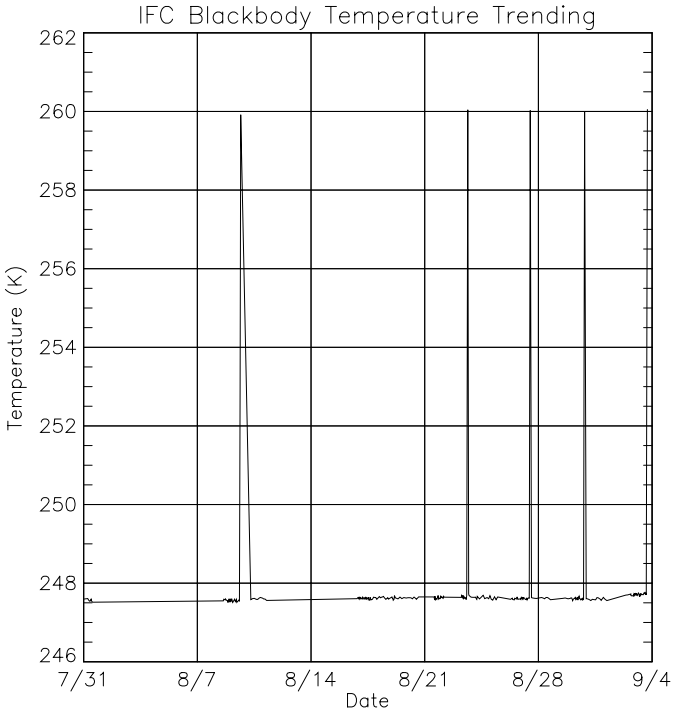

Figure 53. IFC temperature trending

Table 31 shows the IFC blackbody temperature range, mean, and standard deviation for each of the three temperature settings during ground calibration. The standard deviation of the measured IFC blackbody temperature for each setpoint is 0.05K.

Table 31.IFC blackbody temperature statistics during ground calibration

IFC Blackbody Dual Port Memory Setting (hex)	Equivalent IFC Blackbody Temp Setting (K)	Temperature (K)			
		Minimum	Maximum	Mean	Standard Deviation
0xC000	247. 6	247.51	247.76	247.62	0.05
0xD430	253.0	252.92	253.07	252.97	0.05
0xE690	260.0	259.92	260.05	260.01	0.05

Eight packets of data (~96 samples) were obtained in each test event while viewing either the LTBB or IFC full-aperture blackbody. The gain-mode normalized response was calculated using the mean response of each test event and the gain normalization coefficients given in Section 2.2. The offset corrected IFC response was calculated using Equation (9). This method of offset correction uses the measured gain dependent response and effective blackbody radiance when viewing a 110 K blackbody. The response to a 110 K blackbody was obtained for each SABER temperature state during the low temperature blackbody procedure.

$$\begin{aligned} R_{IFC,\,off}(ch) &= R_{IFC}(ch) - R_{offset}(ch) \\ &= R_{IFC}(ch) - [R_{LTBB}(110K) - L_{BBeff(ch)}(110K)\Re(ch)] \end{aligned} \tag{9}$$

where

$R_{IFC,\,off}$ = gain normalized and offset corrected IFC response (counts)

ch = SABER channel (1,2,3.....7)

R_{IFC} = gain normalized response while viewing IFC blackbody (counts)

R_{offset} = estimated response for zero input radiance (counts)

$\Re$ = radiance responsivity coefficient (refer to Section 2.3.1) (counts / ($Wcm^{-2}sr^{-1}$))

$R_{LTBB}(110K)$ = gain normalized response to 110 K blackbody (counts)

$L_{BBeff(ch)}(110K)$ = calculated channel radiance for 110 K blackbody using Equation (7) ($Wcm^{-2}sr^{-1}$)

The IFC blackbody and FPA temperatures significantly affect the channel IFC response (Section 2.5.1). Table 32 shows the gain-mode and offset corrected IFC blackbody response for each channel, IFC blackbody temperature, and FPA temperature combination. As expected, all seven channels show larger responses with increasing IFC blackbody temperature. Channels 1 to 3 show a decrease in response and channels 4 to 7 show a slight increase in response from 75 K to 80 K FPA operating temperature. This can be attributed to detector responsivity as function of FPA operating temperature.

Table 32.Gain-mode and offset corrected IFC blackbody response

Channel	Mean gain-mode and offset corrected response (counts)					
	$T_{IFCBB} = 247.6K$		$T_{IFCBB} = 253K$		$T_{IFCBB} = 260K$	
	FPA temp 75 K	FPA temp 80 K	FPA temp 75 K	FPA temp 80 K	FPA temp 75 K	FPA temp 80 K
1	29605	20801	32339	22765	35859	25279
2	99257	70159	108351	76651	119960	85004
3	108119	74495	118127	81482	130781	90394
4	273703	276937	310844	314700	363970	368399
5	169879	176230	201893	209645	250355	259968
6	129196	129458	163365	163674	218340	218745
7	33158	33397	43996	44624	62946	63875

The process of transferring radiance of the GSE low temperature blackbody to the IFC blackbody requires knowledge of low temperature blackbody radiance, channel response to the low temperature blackbody, and channel response of the IFC blackbody. The process of relating the GSE low temperature blackbody response to the IFC response will require numerical methods. This process will have an uncertainty and is defined as the relative uncertainty of IFC radiance, $\sigma_{N_{IFC}(ch)}$. Although radiance transfer from the GSE low temperature blackbody to the IFC blackbody has not yet been completed, this uncertainty was quantified using the linear curve fit residuals reported in Section 2.3.2. Table 33 shows the average curve fit residual for all SABER temperature states expressed in percent of response. This uncertainty ranges from 0.20% to 0.72% depending on channel.

Table 33.Relative uncertainty of IFC radiance due to calibration transfer (channels 1 to 7)

Channel	$\sigma_{N_{IFC}(ch)}$ (%)
1	0.20
2	0.25
3	0.33
4	0.43
5	0.72
6	0.19
7	0.14

2.4.2 IFC Response for Channels 8 to 10

The IFC tungsten bulbs are positioned behind the IFC full-aperture blackbody and are used to verify or update radiance calibration for channels 8 to 10 during on-orbit operations. The physical location of the bulbs make them a near small area source located inside SABER's Jones Cone (Wyatt, 1978). As a result, the detector assembly is fully illuminated by stimulating a single bulb although the entrance pupil is only partially filled. The equivalent extended source radiance of the bulb output flux for a given drive current is determined from measurements with the HTBB (high temperature blackbody). This data collection is documented in "SABER Ground Calibration and Preliminary Results" (SDL/98-059). In this procedure, SABER's response to the high temperature blackbody at various temperatures and SABER's response to each of 3 IFC bulbs were measured. Each bulb was set to 2 different drive settings during each calibration sequence (cal_sequence.cmd) that was performed periodically throughout data collection. Each bulb was also set to 6 different drive settings during the Jones source sequence (HTBB_JS.cmd), which was performed at the end of each HTBB data collection. These settings are shown in Table 34.

Table 34.IFC Jones source bulb drive current settings

Drive Settings for cal_sequence.cmd	Drive Settings for HTBB_JS.cmd	Dual Port Ram Value (hex)	Current (mA)	Note
	x	0x7000	53.9	
x	x	0x8000	61.5	Nominal setting for channels 8, 9
	x	0x9000	69.2	
	x	0xB000	84.6	
x	x	0xC000	92.2	Nominal setting for channel 10
	x	0xD000	99.9	

The Jones source current is reported in SABER housekeeping. This current is reported approximately every 17 seconds. Since these bulbs were illuminated for less than 17 seconds, the drive current reported in the following test event was used to obtain the measured drive current for the previous test event. Table 35 gives the mean and standard deviation of the measured drive current for each of the two settings obtained during radiometric calibration sequences. These sequences were performed periodically during calibration data collection to quantify IFC repeatability.

Table 35.Measured Jones source drive current during calibration

Dual port RAM setting	Bulb	Mean (ma)	Stdev (ma)
0x8000	JS1	61.61	0.11
	JS2	61.54	0.10
	JS3	61.73	0.29
0xC000	JS1	92.30	0.06
	JS2	92.24	0.09
	JS3	NA[a]	NA[a]

a. Not available in test event. Manual analysis of calibration data following each test event is required.

Eight packets of radiometric data (96 samples) were obtained in each test event while viewing either the high temperature blackbody or IFC Jones sources. The gain-mode normalized response was calculated using the mean response of each test event and the gain normalization coefficients given in Section 2.2. The offset corrected IFC response was calculated using Equation (10). This method of offset correction uses the measured gain dependent response when viewing a 110 K blackbody. The response to a 110 K blackbody was obtained for each SABER temperature state during the low temperature blackbody procedure.

$$\begin{aligned} R_{IFC,\,off}(ch) &= R_{IFC}(ch) - R_{offset}(ch) \\ &= R_{IFC}(ch) - R_{LTBB}(110K) \end{aligned} \tag{10}$$

where

$R_{IFC,\,off}$ = Gain normalized and offset corrected IFC response (counts)

ch = SABER channel (8,9, 10)

R_{IFC} = gain normalized response while viewing IFC blackbody (counts)

R_{offset} = estimated response for zero input radiance (counts)

$\Re$ = radiance responsivity coefficient (refer to Section 2.3.1) (counts / ($Wcm^{-2}sr^{-1}$))

$R_{LTBB}(110K)$ = gain normalized response to 110 K blackbody (counts)

No direct and consistent correlation between Jones source response variability and SABER temperature state has been identified (Section 2.5.2). Table 36 shows the mean and standard deviation of the short wavelength IFC Jones source response for each current setting shown in Table 34.

Table 36.IFC Gain-mode and offset corrected Jones source response

Bulb	Drive Current (ma)	Channel 8		Channel 9		Channel 10	
		Mean	Stdev	Mean	Stdev	Mean	Stdev
JS1	53.9	113483	38	35845	36	4877	23
	61.5[a]	181848	1207	62270	39	9728	22
	69.2	263047	737	96029	37	16694	24
	84.6	463680	1043	185926	804	37921	23
	92.2[b]	581717	915	242118	749	52568	21
	99.9	711232	1148	305828	692	70093	24
JS2	53.9	107472	38	19765	35	380	6
	61.5[a]	165054	1255	32764	37	703	6
	69.2	232749	1164	49094	33	1157	6
	84.6	398259	923	92048	37	2509	6
	92.2[b]	495288	838	118727	36	3428	6
	99.9	601445	1284	149100	587	4525	25
JS3	53.9	147960	1172	1842	9	7629	20
	61.5[a]	227987	1152	3017	8	14311	24
	69.2	322498	1166	4491	35	23698	24
	84.6	553834	1208	8372	37	51659	24
	92.2[b]	689300	1324	10768	37	70662	24
	99.9	837254	1236	13461	38	93196	424

a. Nominal current setting for channels 8 and 9
b. Nominal current setting for channel 10

The process of transferring radiance of the GSE high temperature blackbody to the IFC Jones source requires knowledge of high temperature blackbody radiance, channel response to the high temperature blackbody, and channel response of the IFC Jones source. The process of relating the GSE high temperature blackbody response to the IFC response will require numerical methods. This process will have an uncertainty and is defined as the relative uncertainty of IFC radiance, $\sigma_{N_{IFC}(ch)}$. This radiance transfer from the GSE high temperature blackbody to the IFC is planned to be performed by GATS. At present, this uncertainty was quantified using the linear curve fit residuals reported in Section 2.3.2. Table 37 shows the average curve fit residual for channels 8 to 10 expressed in percent of response. This uncertainty ranges from 0.16% to 0.20% depending on channel.

Table 37.Relative uncertainty of IFC radiance due to calibration transfer (channels 8 to 10)

Channel	$\sigma_{N_{IFC}(ch)}$ (%)
8	0.20
9	0.14
10	0.16

2.5 IFC Radiance Long-Term Repeatability

2.5.1 Long Wavelength IFC Repeatability (Channels 1 to 7)

The IFC full aperture blackbody has been designed to be repeatable over a 2-year mission life (SDL/95-006). The long-term radiance repeatability was determined from design analyses and subsystem testing to be less than 1.2% for SABER channels 1 to 7. This section summarizes this analysis. A complete description of this analysis is given in “SABER IFC Blackbody Performance Report” (SDL/98-112).

The full aperture IFC blackbody radiance repeatability was determined using temperature and emissivity uncertainties. Temperature uncertainty is comprised of 3 terms: blackbody temperature gradient variation, temperature measurement repeatability, and temperature control repeatability. The blackbody temperature gradient variation is caused by changing heat loads from a range of optics cavity temperatures of 216 K to 242 K, which are expected to be worst case temperatures for on-orbit operations. Temperature measurement repeatability is due to thermistor and readout electronics repeatability, and temperature control repeatability is due to control stability and set point drift.

Radiance repeatability due to emissivity uncertainty is caused by a drift in blackbody emissivity over the lifetime of the mission. Because the blackbody is essentially hidden behind the scan mirror during on-orbit operations, no significant contamination or atomic oxygen degradation is expected. However, for the purpose of estimating uncertainty and to be conservative, a blackbody surface emittance variation over the lifetime of the mission was set to 2%. This causes a change in blackbody cavity enhanced emissivity of 0.2% to 0.6% depending on SABER channel.

The uncertainties associated with IFC blackbody temperature and emittance were converted to radiance uncertainties for each SABER channel. The root sum square of these individual terms was calculated to give the total radiance repeatability of the IFC blackbody, and are given in Table 38. Because the on-orbit radiance responsivity coefficient is updated based on periodic IFC measurements during on-orbit operation, the long-term radiometric precision was quantified using the IFC blackbody radiance repeatability. This requirement is also shown in Table 38. The IFC blackbody long-term radiance repeatability is approximately 1% for channels 1 to 7, which is less than the long-term radiometric precision requirement of 2%.

Table 38: Long-wavelength IFC radiance repeatability over mission life[a]

SABER Channel	Temperature Uncertainty (%)	Emittance Drift (%)	$\sigma_{IFC,\,repeat}$ Total IFC Radiance Repeatability (%)	Long-Term Radiometric Precision Requirement
1	0.9	0.3	0.9	2% radiance precision 1% goal
2	1.0	0.3	1.1	
3	1.0	0.3	1.1	
4	1.1	0.4	1.1	
5	1.0	0.4	1.0	
6	1.2	0.5	1.2	
7	1.0	0.5	1.0	
8	1.3	0.3	1.4	

a. Documented in SDL/98-112

Trend analyses were performed on ground calibration data to evaluate and verify repeatability of the IFC radiance and instrument response. Trending analyses were performed to quantify response repeatability for each long-wavelength channel (channels 1 to 7). SABER temperatures that may affect IFC response repeatability include IFC blackbody, focal plane, telescope, and baseplate temperatures. Figure 54 shows a time series of each of these temperatures for dates between July 31 and September 3, 1999. Each of the SABER temperature states during calibration measurements are identified by a specific combination of these temperatures at any given time.

Linear regression analyses were performed to identify which of these SABER temperatures significantly affect response repeatability. As expected, the IFC response is affected by IFC blackbody and focal plane temperatures. The IFC blackbody temperature determines the thermal emission of the blackbody and the responsivity of the detectors become less for larger focal plane temperatures. The mean offset corrected IFC response as a function of these temperatures are discussed in Section 2.4.1.

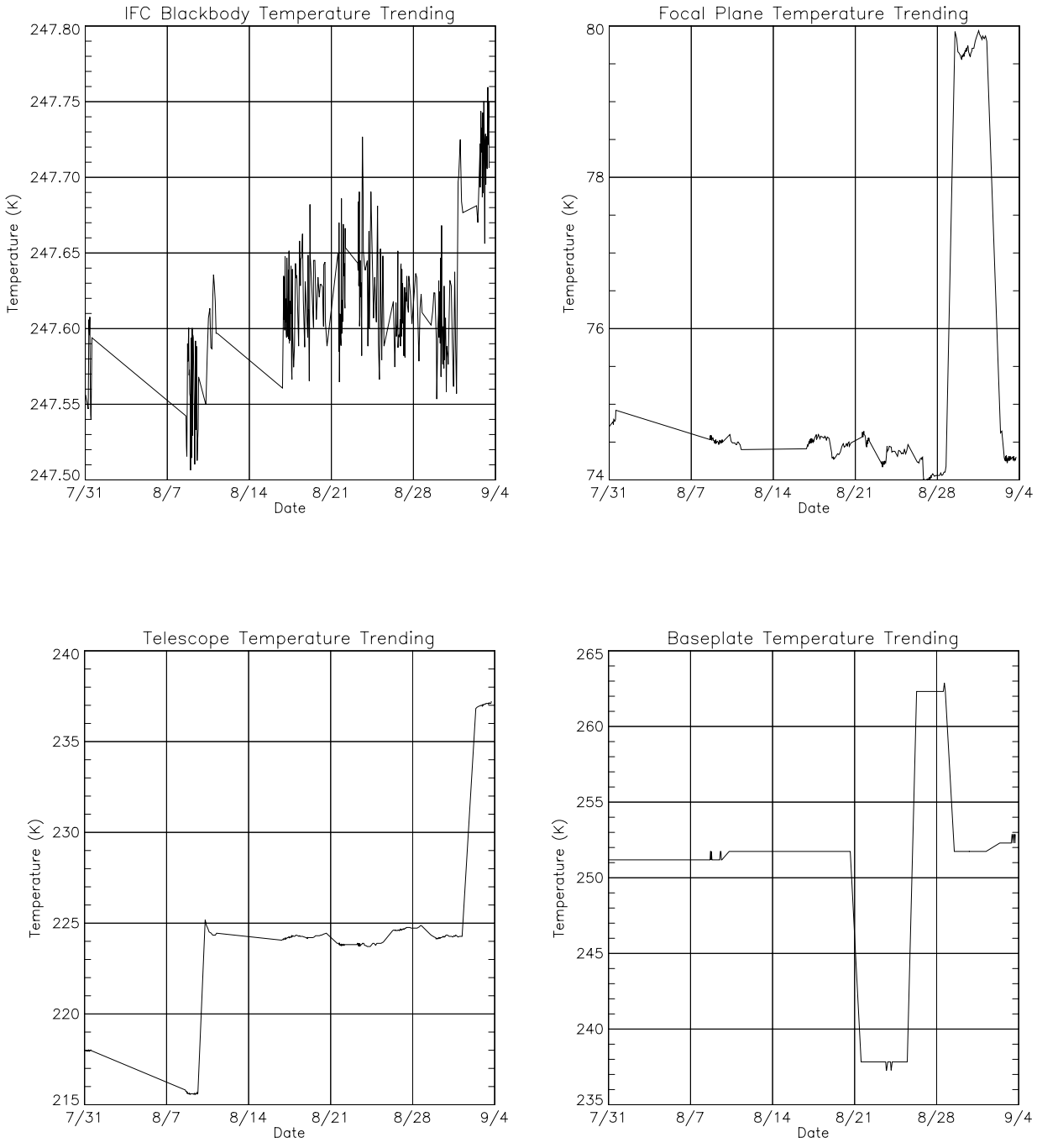

Figure 54. Independent variable temperature trending

To quantify temperature dependence on IFC response repeatability, a linear curve fit of offset corrected gain normalized response versus each SABER temperature was performed. The standard deviation of the curve fit residuals divided by the mean response were then used to quantify repeatability with the temperature dependence removed. The results are shown in Table 39 where

the first column is the variation without any temperature dependence removed. To minimize IFC response variation due to dependence of IFC blackbody and focal plane temperatures, repeatability analysis used data with the IFC blackbody and focal plane temperatures set to 247.6 K and 75 K, respectively. These are nominal temperatures. With the focal plane set to 75 K, the actual focal plane temperature varied between 74.0 and 74.9 K. This explains the focal plane temperature dependence shown in Table 39. The response repeatability for channels 1 to 5 are less than 0.4% when corrected for focal plane temperature variations. Variations in IFC blackbody (nominal setting), telescope, and baseplate temperature do not have a significant effect on response repeatability for these channels. Channels 6 and 7 are relatively insensitive to small fluctuations in focal plane temperature; however, only small improvements to the repeatability can be made by correcting for the other temperature terms as shown in Table 39. The response repeatabilities for channels 1 to 7 are below the IFC radiance repeatabilities shown in Table 38. This verifies the IFC response repeatability for these channels during ground calibration.

Table 39. SABER response repeatability to IFC blackbody[a]

	Channel	Independent Term in Linear Prediction Model				
		None	FPA Temp	IFC Temp	Telescope Temp	Baseplate Temp
Response Repeatability (%)	1	1.09	0.34	1.08	1.06	0.89
	2	0.99	0.31	0.97	0.94	0.79
	3	1.10	0.25	1.06	1.03	0.93
	4	0.27	0.27	0.26	0.26	0.17
	5	0.31	0.31	0.29	0.29	0.24
	6	0.46	0.46	0.46	0.43	0.29
	7	0.97	0.96	0.73	0.73	0.88

a. Analysis performed on data taken from 7/29/99 to 9/3/99. IFC blackbody was set to 247.6 K (0xC000) and the FPA temperature was set to approximately 75 K.

2.5.2 Short Wavelength IFC Repeatability (Channels 8, 9, and 10)

The short wavelength IFC uses tungsten bulbs configured in a Jones source arrangement. There was no need to remove the glass envelope for use with these short wavelength channels. This design uses the same make tungsten bulb and similar electronic circuit driver design as the CERES instrument (Folkman and Flannery, 1993).

The long-term radiance repeatabilities of the short wavelength IFCs were determined from design and subsystem testing. The total radiance uncertainty was quantified from tungsten bulb radiance repeatability measurements and performance of drive circuit electronics.

Subsystem tests were performed to qualify each bulb and to evaluate the long-term radiometric repeatability of the tungsten lamps. These tests are described in “SABER Jones Source Incandescent Lamp Test Plan” (SDL/97-065), and results are described in more detail in “Test and Qualification Results of SABER Jones Source Incandescent Lamps” (SDL/99-040).

Qualification tests were performed to qualify each bulb for flight operation. These tests included visual examination, powered resistance measurement before and after burn-in, vibration test, and 10% of life radiometric repeatability. All three of the flight bulbs passed these tests.

Radiant bulb repeatability and radiant bulb repeatability due to vibration, electronic drive current repeatability, electronics operating temperature, and on-orbit radiation exposure were combined using Equation (11) to estimate short wavelength IFC radiance repeatability.

$$\sigma_{IFC,\,repeat} = \sqrt{(\sigma_{bulb})^2 + (\sigma_{vib})^2 + (\sigma_{current})^2 + (\sigma_T)^2 + (\sigma_{rad})^2} \tag{11}$$

where

$\sigma_{IFC,\,repeat}$ = IFC radiance repeatability (%)

σ_{bulb} = radiant bulb repeatability (%)

σ_{vib} = radiant bulb repeatability due to vibration (%)

$\sigma_{current}$ = radiant bulb repeatability due to electronic drive current repeatability (%)

σ_T = radiant bulb repeatability due to electronics operating temperature (%)

σ_{rad} = radiant bulb repeatability due to on-orbit radiation exposure (%)

Radiant bulb repeatability, σ_{bulb}, was determined from radiometric intensity stability measurements obtained during initial screening of tungsten bulbs. The test and results are documented in “Test and Qualification Results of SABER Jones Source Incandescent Lamps” (SDL/99-040). The 10% of life results were extrapolated to estimate repeatability for a two year mission life. This assumes a single flash every two minutes.

Radiant bulb repeatability due to vibration, σ_{vib}, was determined from burn-in measurements obtained before and after mechanical vibration tests obtained during initial screening of the tungsten bulbs. The test and results are documented in “Test and Qualification Results of SABER Jones Source Incandescent Lamps” (SDL/99-040).

The standard deviation of the Jones source bulb drive current as reported in SABER housekeeping during calibration measurements (Section 2.4.2) was used to quantify radiant bulb repeatability due to electronic drive current repeatability, $\sigma_{current}$. To determine a drive current radiance sensitivity, radiant output and current were measured at multiple levels around the nominal 100 ma current during bulb radiometric bench measurements. The sensitivity was determined to be 6% change in radiance per 1 ma change in electronic drive current. This is documented in “Test and Qualification Results of SABER Jones Source Incandescent Lamps” (SDL/99-040). Hence,

the Jones source radiance repeatability due to electronic drive current repeatability is 6% multiplied by the drive current repeatability expressed in units of milliamps.

Radiant bulb repeatability due to electronics operating temperature, σ_T, and on-orbit radiation exposure, σ_{rad}, are documented in Appendix G.

Table 40 gives individual repeatability terms and the combined short wavelength IFC repeatability, $\sigma_{IFC,\,repeat}$, calculated using Equation (11). The combined uncertainty ranges from 1.2% to 2% depending on the bulb.

Table 40: Short wavelength IFC radiance repeatability over mission life

Bulb Designation	σ_{bulb} (%)	σ_{vib} (%)	$\sigma_{current}$ (%)	σ_T (%)	σ_{rad} (%)	$\sigma_{IFC,\,repeat}$ (%)
JS1 (61.5 ma)	0.04	0.3	0.66	0.31	0.86	1.2
JS2 (61.5 ma)	0.4		0.6			1.2
JS3 (61.5 ma)	0.5		1.7			2.0

The short wavelength IFC (tungsten bulb in Jones source arrangement) was viewed periodically during calibration data collection. Trend analyses were performed on these data to verify short wavelength IFC repeatability. The gain normalized response for channels 8, 9, and 10 to each tungsten bulb is plotted over a range of dates between 31 July 31 and 3 September 1999. Figure 55 shows the channel responses to bulb 1 at two different current settings. The drop in all the responses from 8/22 to 8/24 appears to be a result of the planned drop in baseplate temperature over the same time period. Similarly, the response to bulbs 2 and 3 are shown in Figure 56 and Figure 57, respectively.

Linear regression analyses were performed to quantify the influence of SABER temperatures and Jones source bulb currents on short-wavelength response repeatability. Jones source current analyses were limited to test events where Jones source current information were available. Jones source currents are included in SABER housekeeping but were only updated every 16.9 seconds, so that current values for one test event were not written in housekeeping until the following test event. During data processing, these Jones source current values were copied into the proper test event. However, for some test events the Jones source current was not sampled while the lamp was turned on, so no Jones source current information was available. These test events were excluded from this analysis. Graphs of available Jones source current data for the duration of ground calibration are shown in Figure 58.

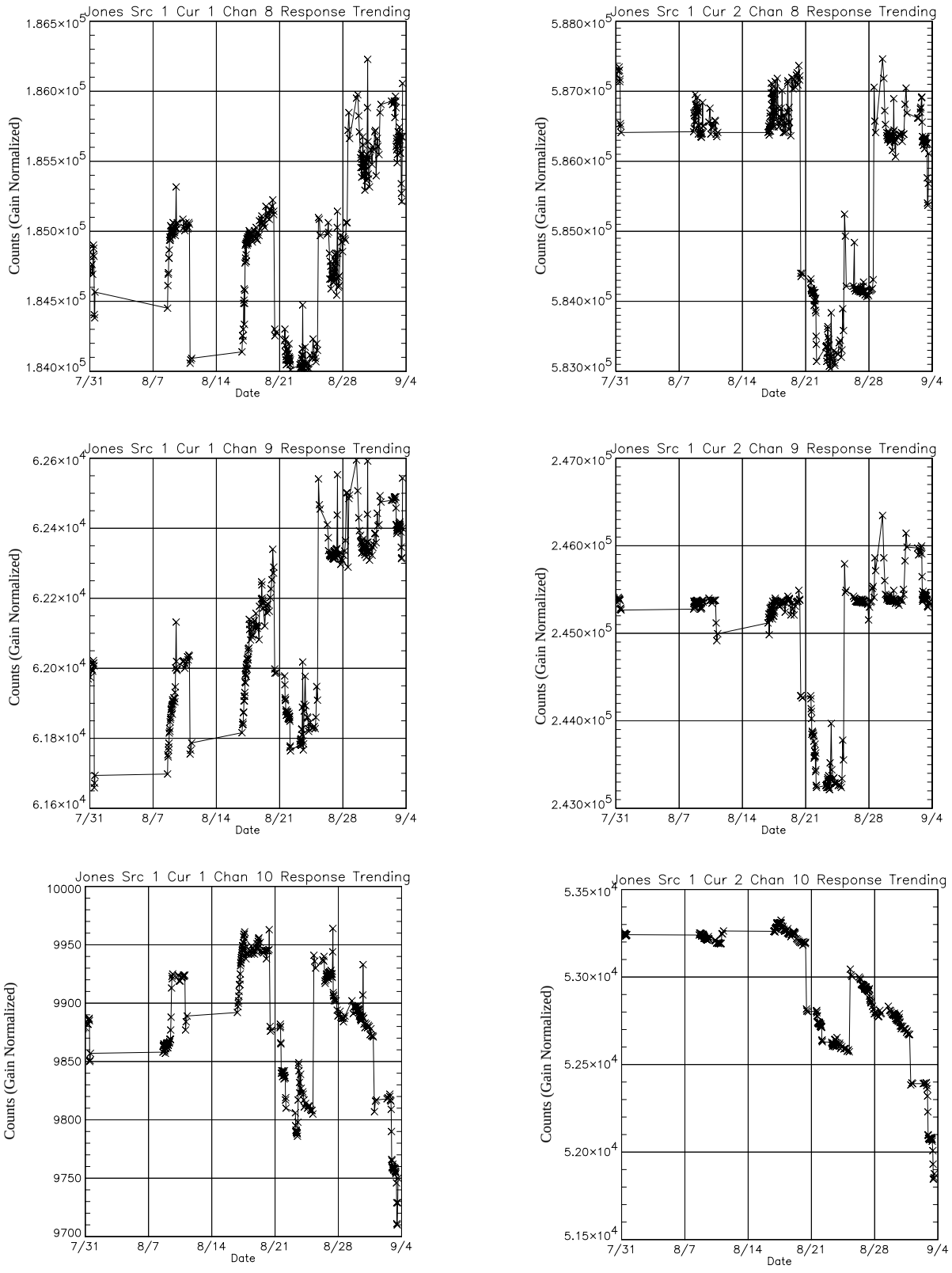

Figure 55. Short wavelength channel response to Jones source 1

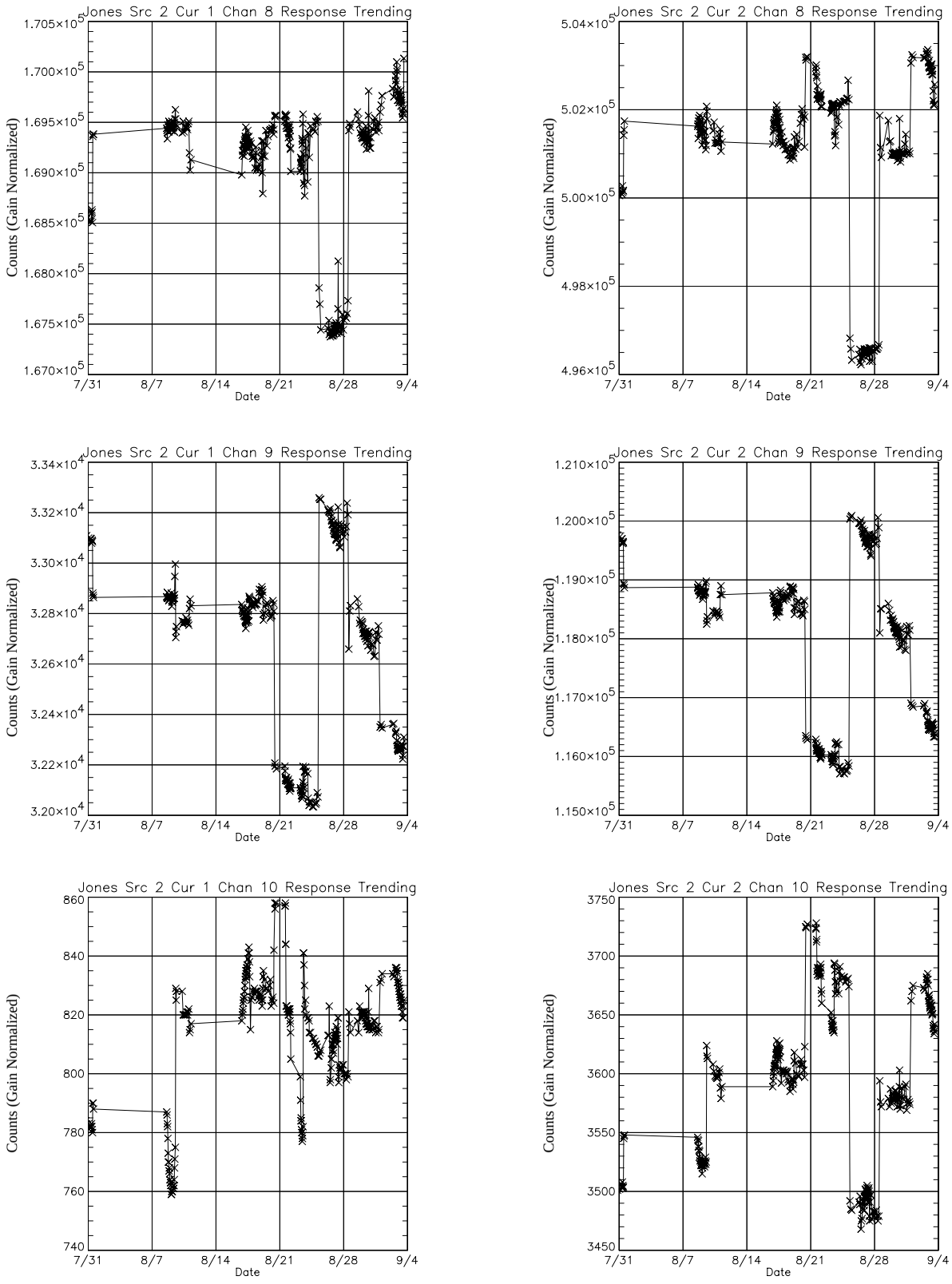

Figure 56. Short wavelength channel response to Jones source 2

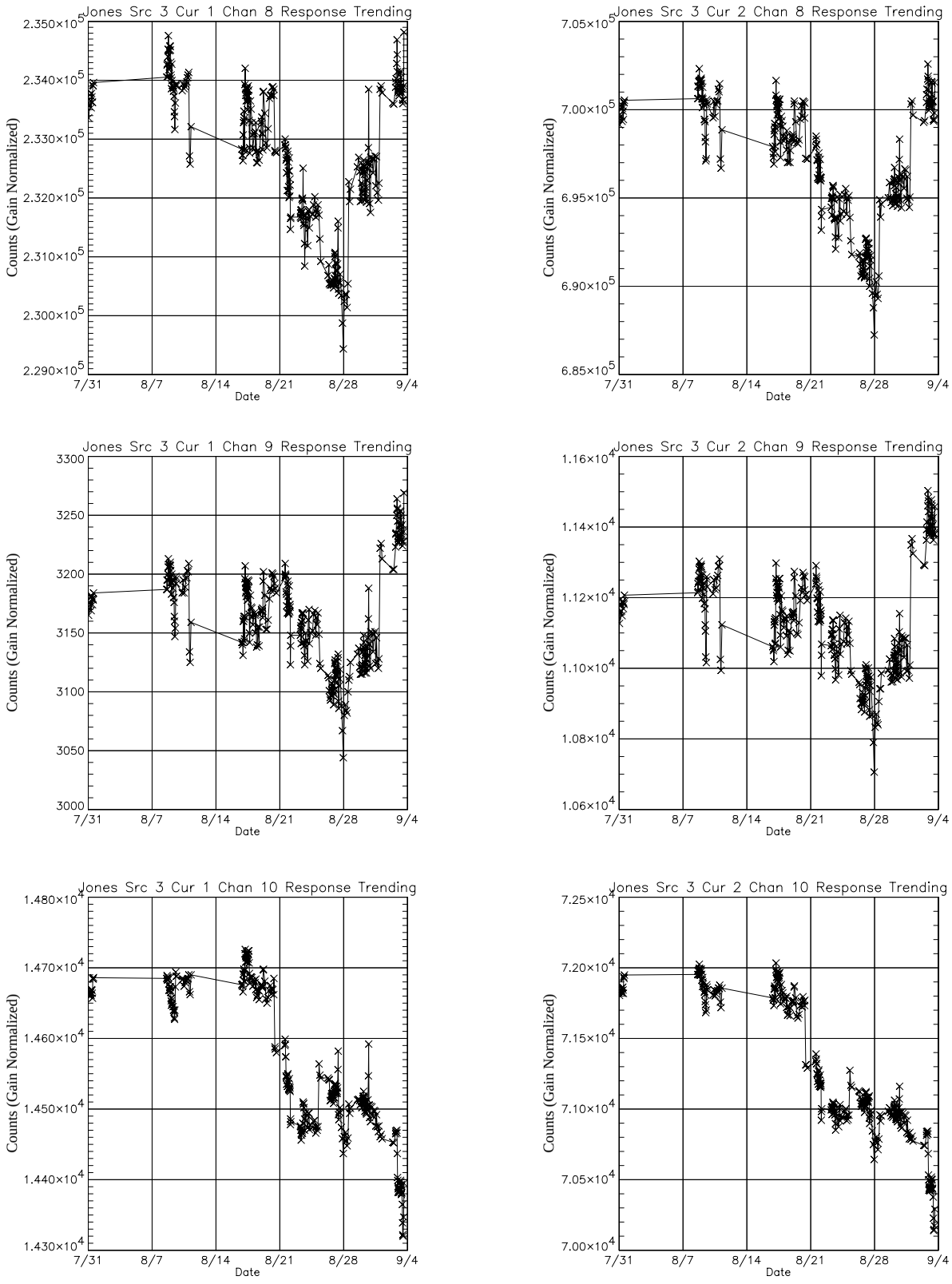

Figure 57. Short wavelength channel response to Jones source 3

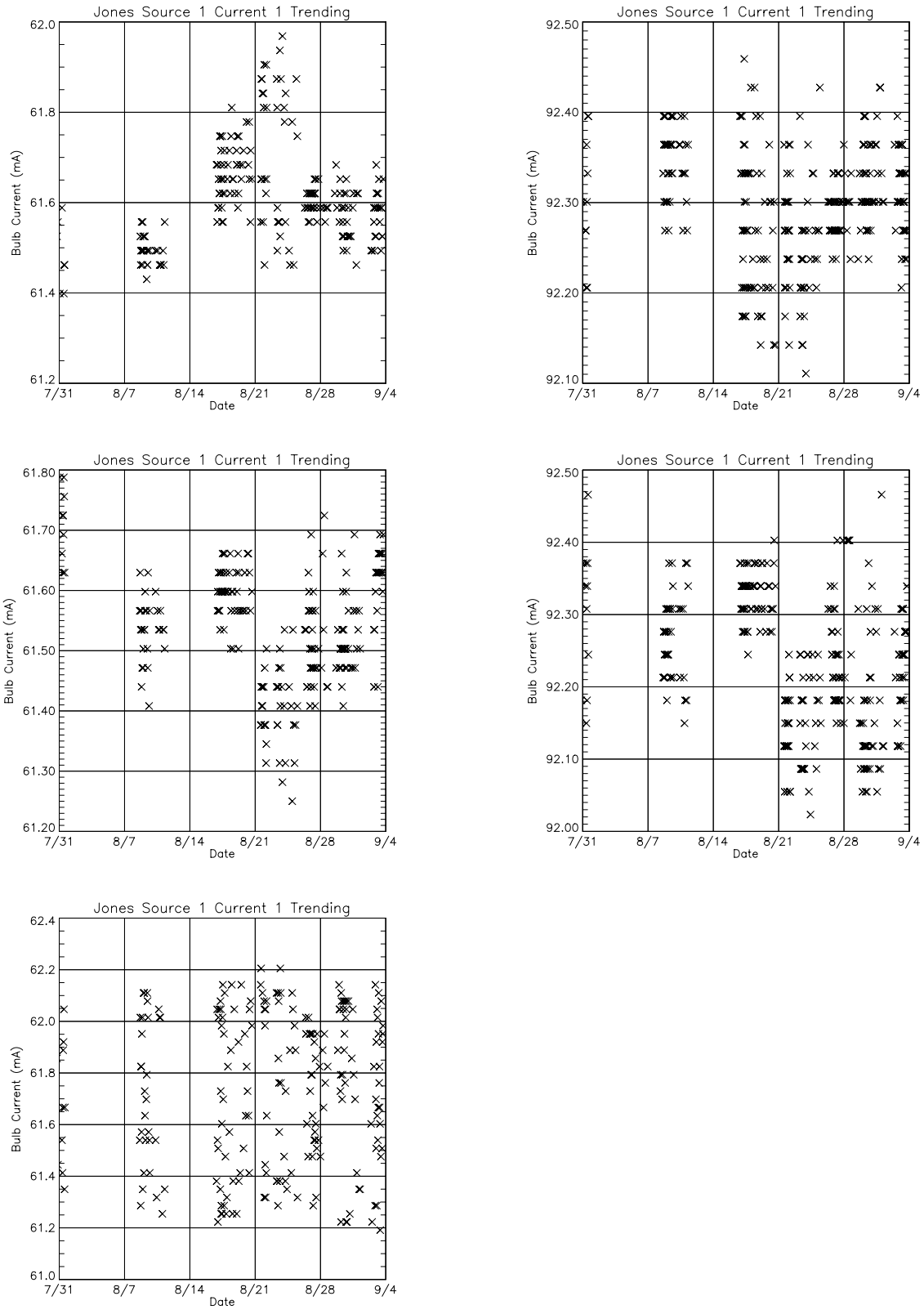

Figure 58. Jones source current

A linear curve fit of offset corrected and gain normalized IFC responses were made versus each SABER temperature and Jones source current. Gain dependent offset correction values were determined from LTBB data while viewing a 110 K blackbody. The standard deviation of the curve fit residuals divided by the mean response was then used to quantify repeatability with the temperature or bulb current dependence removed. The results given in Table 41 indicate that channel 8, 9, and 10 responses are not consistently dependent on temperature or current variations. The response repeatability for these channels ranged from 0.22% to 2.24% depending on the channel, bulb, and current setting.

Many of the Jones source response repeatability values reported in Table 41 are less than or comparable to the uncertainties determined from subsystem measurements and analyses shown in Table 40. Jones source bulb 1 produced the best repeatability at less than 0.7% regardless of channel or current setting. The response repeatability for bulb 2 is acceptable for channel 8 (< 0.5%), marginal for channel 9 (~1%), and larger than expected for channel 10 (~2%). The response repeatability for bulb 3 is acceptable for channels 8 and 10 (< 0.8%) but larger than expected for channel 9 (~1.3%). It is suggested that the current 1 setting be used to calibrate channels 8 and 9 and current 2 setting be used to calibrate channel 10 because they produce radiance values that are most closely matched to science radiance values.

Table 41. SABER response repeatability to IFC Jones sources[a]

	Jones Source		Channel	Independent Term in Linear Prediction Model					
	Bulb	Current[b]		None	IFC Temp	FPA Temp	Tele-scope Temp	Base-plate Temp	Bulb Current (mA)
Response Repeatability (%)	1	1	8	0.29	0.29	0.24	0.25	0.26	0.29
	1	2		0.22	0.21	0.20	0.22	0.20	0.21
	2	1		0.42	0.42	0.39	0.41	0.30	0.42
	2	2		0.39	0.39	0.38	0.38	0.26	0.38
	3	1		0.47	0.47	0.47	0.47	0.46	0.47
	3	2		0.47	0.47	0.47	0.47	0.46	NA
	1	1	9	0.38	0.38	0.36	0.31	0.30	0.38
	1	2		0.30	0.30	0.29	0.29	0.17	0.28
	2	1		1.10	1.09	1.10	1.01	0.59	1.01
	2	2		1.13	1.13	1.13	1.02	0.64	1.02
	3	1		1.34	1.34	1.29	1.23	1.29	1.34
	3	2		1.35	1.35	1.30	1.24	1.30	NA
	1	1	10	0.56	0.56	0.56	0.48	0.50	0.56
	1	2		0.71	0.70	0.70	0.44	0.70	0.71
	2	1		2.24	2.23	2.23	2.01	2.14	2.24
	2	2		1.90	1.90	1.90	1.75	1.08	1.84
	3	1		0.76	0.76	0.74	0.55	0.76	0.76
	3	2		0.70	0.70	0.68	0.50	0.70	NA

a. Analysis performed on data taken from 7/29/99 to 9/3/99. IFC blackbody was set to 247.6 K (0xC000).
b. The settings for currents 1 and 2 are 61.5 mA (0x8000) and 92.2 mA (0xC000), respectively.

2.6 Off-Axis Extended Source Throughput Correction

The off-axis extended source throughput correction is a normalized correction to SABER's extended source response as a function of scan mirror pointing angle. This correction was measured by viewing the low temperature GSE blackbody (channels 1 to 7) or the high temperature blackbody (channels 8 to 10) at numerous scan mirror pointing angles. The Low Temperature Blackbody and High Temperature Blackbody procedures were used to make these measurements (SDL/98-059). During these procedures, the blackbody response was measured at 29 scan mirror pointing angles between -10 km and 210 km (equivalent on-orbit tangent height look angles). At each scan mirror pointing angle, the FOV (field-of-view) of the instrument was maintained near the center of the blackbody. This was done by compensating rotation of the SABER scan mirror with rotation of the instrument rotary table.

The blackbody temperatures were 287 K for channels 1 to 7, 510 K or 525 K for channels 8 and 9, and 689 K for channel 10. At each scan mirror pointing angle, a test event consisting of 8 SABER data packets (96 detector samples) was generated. The mean detector response was calculated for each test event. The response was then plotted as a function of SABER scan angle and peak normalized to unity. Figures 59 to 64 show the peak normalized response versus scan angle for each channel and SABER temperature state, and Table 42 summarizes the maximum response variation, and gives the average maximum response variation over all temperature states for each channel. The maximum variation as a function of scan angle is less than 0.1% for channels 1 to 7 and less than 0.42% for channels 8 to 10. Because this variation is small and can be identified as an uncertainty without significantly affecting overall radiance uncertainty, the extended source throughput correction can be set to unity for equivalent on-orbit scan angles between -10 km and 210 km. Because the shape and magnitude of the peak normalized response versus scan angle doesn't appear to be systematically consistent among different SABER temperature states (especially true for channels 8 to 10), the average variation over all temperature states is used to quantify uncertainty.

Table 42. Maximum variation of response as function of SABER scan angle

Channel	Maximum Variation (%)						
	Temperature State[a]						Average
	N, N, N	N, H, N	N, N, C	N, N, H	C, N, N	H, N, N	
1	0.04	0.05	0.05	0.015	0.02	0.03	0.034
2	0.035	0.05	0.07	0.01	0.03	0.03	0.038
3	0.055	0.06	0.08	0.01	0.04	0.03	0.046
4	0.06	0.06	0.095	0.05	0.09	0.05	0.068
5	0.06	0.06	0.10	0.06	0.095	0.055	0.072
6	0.04	0.03	0.04	0.06	0.04	0.03	0.04
7	0.05	0.035	0.06	0.055	0.04	0.045	0.048
8	0.085	0.30	0.22	0.21	-	-	0.204
9	0.055	0.23	0.14	0.32	-	-	0.186
10	0.12	0.11	0.42	0.18	-	-	0.208

a. Telescope, focal plane, baseplate temperature state. C=cold, N=nominal, and H=hot

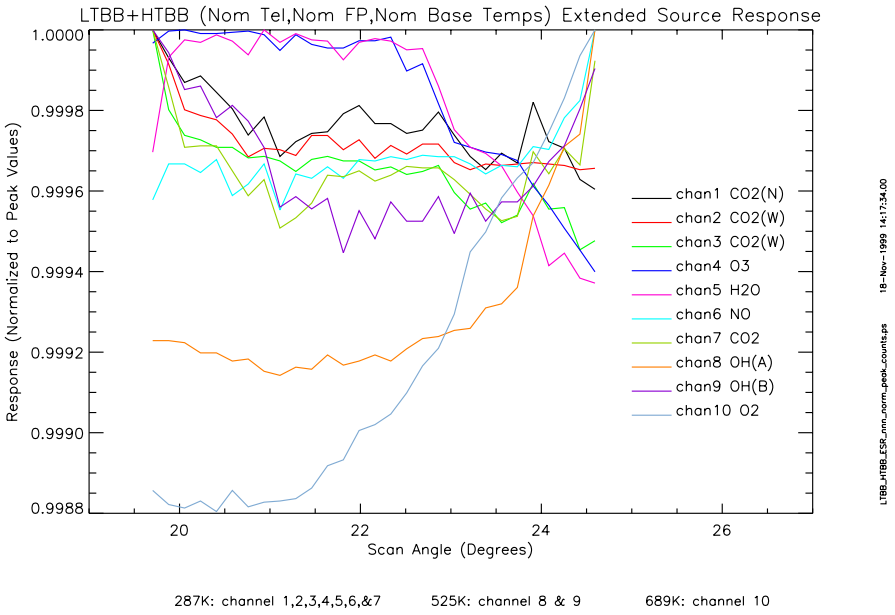

Figure 59. Peak normalized response as a function of scan mirror pointing angle nominal temperatures

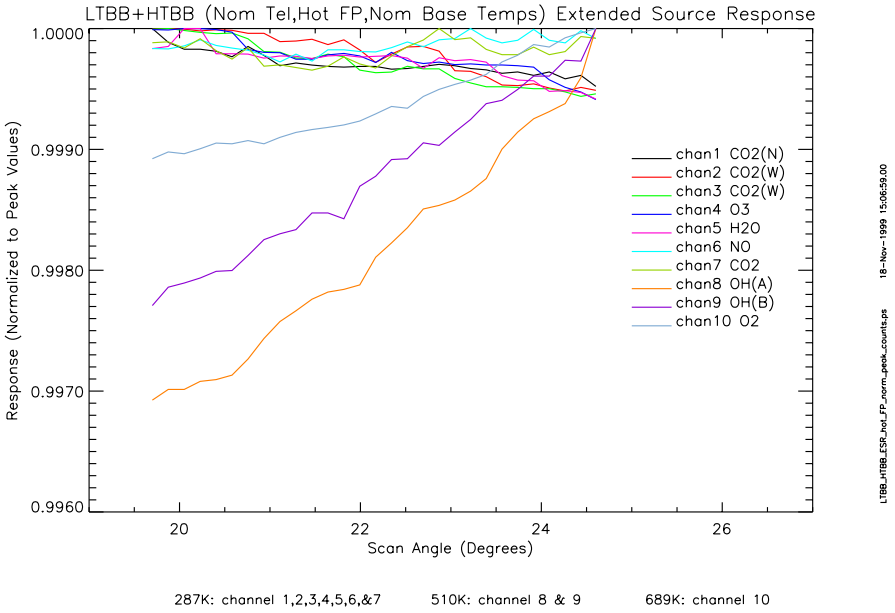

Figure 60. Peak normalized response as a function of scan mirror pointing angle hot focal plane

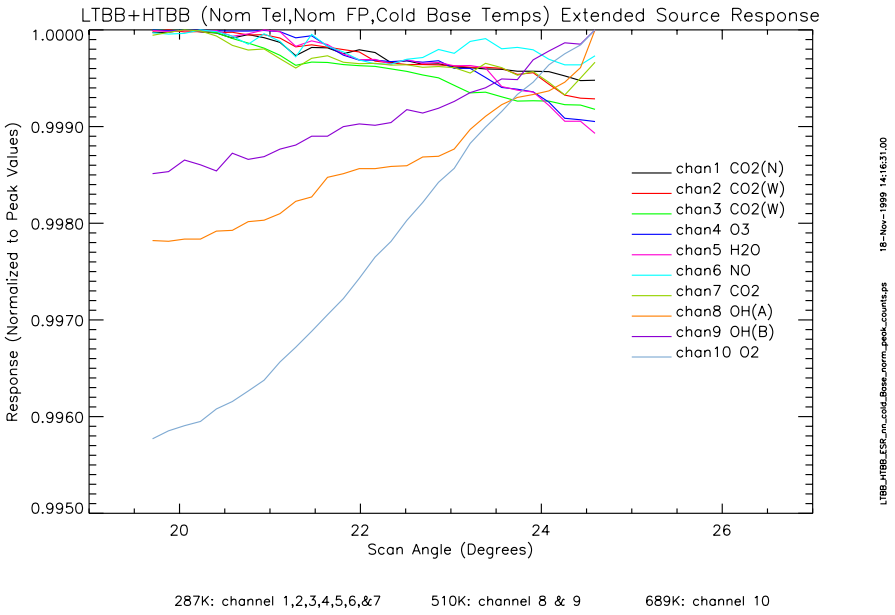

Figure 61. Peak normalized response as a function of scan mirror pointing angle cold baseplate

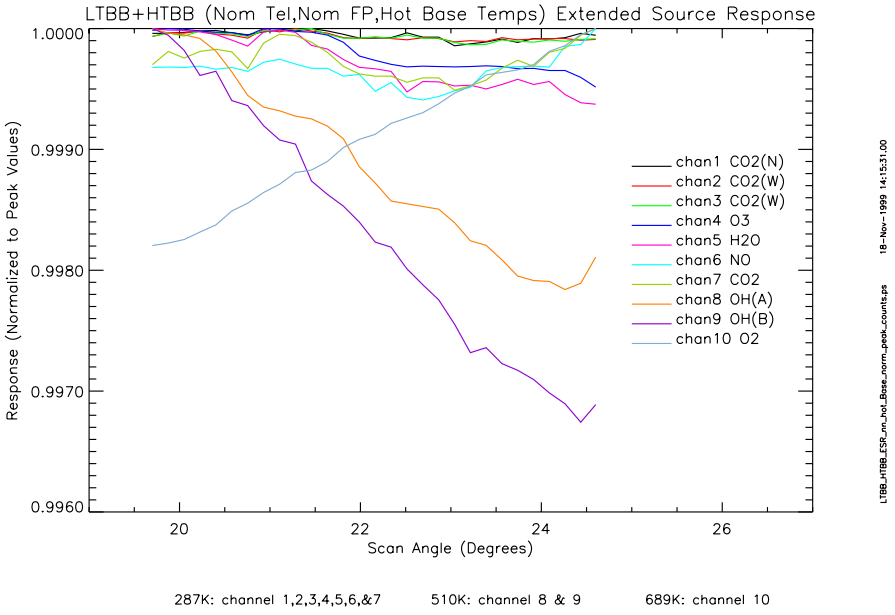

Figure 62. Peak normalized response as a function of scan mirror pointing angle hot baseplate

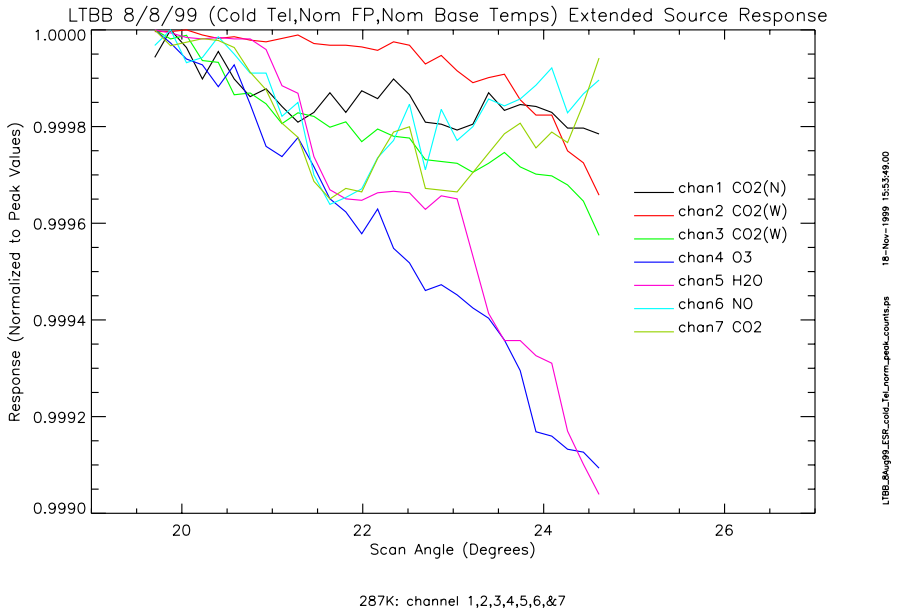

Figure 63. Peak normalized response as a function of scan mirror pointing angle cold telescope

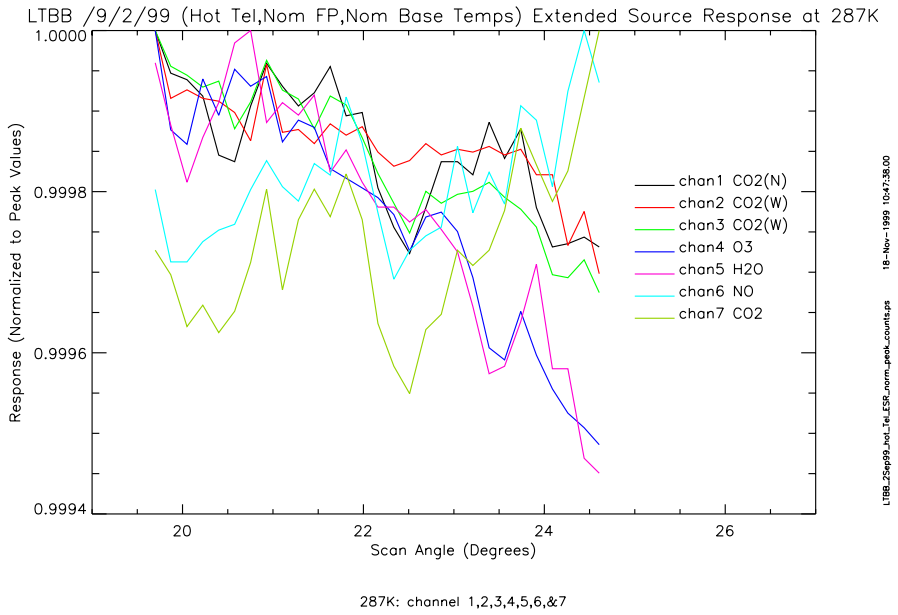

Figure 64. Peak normalized response as a function of scan mirror pointing angle hot telescope

2.7 Radiance Uncertainty

An on-orbit calibration equation was estimated by substituting the on-orbit updated radiance responsivity, Equation (3), into the calibration equation, Equation (2). The fractional radiometric uncertainty was estimated by differentiating the on-orbit calibration equation, dividing by the measured radiance, and taking the root-sum-square with respect to each of the variables. This calculation yields the radiometric uncertainty equation shown in Equation (12) where the errors are assumed to be uncorrelated.

$$\sigma_{L_M} = \frac{\Delta L_M}{L_M}100 = \sqrt{\left(\frac{\Delta r_{c,sig}}{r_{c,sig}}100\right)^2 + \left(\frac{\Delta r_{c,IFC}}{r_{c,IFC}}100\right)^2 + \left(\frac{\Delta N_{IFC}}{N_{IFC}}100\right)^2} \quad (12)$$

$$= \sqrt{\sigma^2_{r_{c,sig}} + \sigma^2_{r_{c,IFC}} + \sigma^2_{IFC}}$$

where

σ_{L_M}	=	relative standard uncertainty of measured scene radiance (%)
$r_{c,sig}$	=	measured corrected response (counts)
$\Delta r_{c,sig}$	=	uncertainty of corrected response (counts)
$r_{c,IFC}$	=	measured IFC corrected response (counts)
$\Delta r_{c,IFC}$	=	uncertainty of IFC corrected response (counts)
N_{IFC}	=	IFC radiant flux (W cm^{-2} sr^{-1})
ΔN_{IFC}	=	uncertainty of IFC radiant flux (W cm^{-2} sr^{-1})
$\sigma_{r_{c,sig}}$	=	uncertainty of signal corrected response (%)
$\sigma_{r_{c,IFC}}$	=	uncertainty of IFC corrected response (%)
σ_{IFC}	=	uncertainty of IFC radiance (%)

Equation (12) identifies three main categories of uncertainty for an on-orbit scene measurement, assuming an on-orbit radiance calibration based on an IFC-look measurement. These categories include uncertainty of SABER response to external source, uncertainty of SABER response to IFC, and uncertainty of IFC radiance. Each category is comprised of individual sources of uncertainty. For each of these individual uncertainty terms, a description along with assumptions or report section references are shown in Table 43.

Table 43. Individual terms for radiance calibration uncertainty

$\sigma_{r_{c,sig}}$ - Uncertainty of Signal Corrected Response		
Term	Description	Assumptions/Reference
σ_O	Sensor offset measurement uncertainty	Assumes (1) sensor offset is calculated from average of 10 samples and (2) the illuminated signal-to-noise is 100. Therefore, this uncertainty is 1% divided by the square root of 10.
$\sigma_{o,med}$	Medium-term uncertainty of sensor offset. (i.e., variability of sensor offset between space looks)	Section 2.1.4 "Sensor Offset Medium Term Repeatability (Channel Drift)" and assumes signal-to-noise of 100
σ_N	Signal noise uncertainty	Assumes signal-to-noise of 100.
σ_L	Linearity correction uncertainty	Section 2.3 "Peak Radiance Responsivity and Response Linearity"
σ_G	Gain mode normalization uncertainty	Section 2.2 "Gain Mode Normalization"
$\sigma_{\Upsilon_{ext}}$	Uncertainty of off-axis extended source throughput correction (i.e., throughput correction as function of scan angle)	Section 2.6 "Off-Axis Extended Source Throughput Correction"
$\sigma_{r_{c,IFC}}$ - Uncertainty of IFC Corrected Response		
σ_O	Sensor offset measurement uncertainty	Calculated from ground calibration measurements. This uncertainty was estimated by dividing the standard deviation of the sensor offset by the mean IFC response (expressed as percent of response). The following conditions apply: (1) nominal SABER temperatures, (2) gain dependent offset measurement obtained from viewing a 110 K BB, (3) IFC BB = 247.6K, and (4) JS1 with nominal current setting.
σ_N	IFC look response uncertainty	Calculated from ground calibration measurements. This uncertainty was estimated by dividing the IFC response standard deviation by the mean IFC response (expressed as percent of response). The following conditions apply: (1) nominal SABER temperatures, (2) gain dependent offset correction, (3) IFC BB = 247.6K, and (4) JS1 with nominal current setting.
σ_L	Linearity correction uncertainty	Section 2.3 "Peak Radiance Responsivity and Response Linearity"
σ_G	Gain mode normalization uncertainty	Section 2.2 "Gain Mode Normalization"
σ_{IFC} - Uncertainty of IFC Radiance		
$\sigma_{\Re,BB}$	Radiance uncertainty of full-aperture blackbody	Section 2.4 "In-Flight Calibrator (IFC) Radiance"
σ_{RSR}	Uncertainty of IFC channel radiance due to uncertainty of instrument relative spectral response	Section 3.6 "Total RSR Uncertainty for Ground Calibration"
$\sigma_{N_{IFC}}$	Uncertainty of IFC radiance (calibration transfer to IFC)	Section 2.4 "In-Flight Calibrator (IFC) Radiance"
$\sigma_{IFC,repeat}$	Uncertainty due to IFC radiance long-term repeatability	Section 2.5 "IFC Radiance Long-Term Repeatability"

The radiance uncertainty for SABER is channel dependent. Tables 44 to 53 give the radiance uncertainty for each SABER channel. The uncertainty and total uncertainty of the three main categories were estimated by taking the root-sum-of-squares of the individual terms. The uncertainties range form 2.0% for channel 5 to 3.3% for channels 6 and 8. Six of the ten channels have a total radiance uncertainty less than the 3% goal and all of the channels meet the 5% requirement with margin.

Table 44. Radiance calibration uncertainty for channel 1

$\sigma_{r_{c,sig}}$ - Uncertainty of Signal Corrected Response				Total RSS Uncertainty (%) 3% Goal 5% Requirement
Term	Description	Relative Uncertainty Error Budget (%)	Combined RSS Uncertainty (%)	
σ_O	Sensor offset measurement uncertainty	0.32	1.08	2.4
$\sigma_{o,med}$	Medium-term uncertainty of sensor offset. (i.e., time between space looks)	0.08		
σ_N	Signal noise uncertainty (SNR = 100)	1.00		
σ_L	Linearity correction uncertainty	0.23		
σ_G	Gain mode normalization uncertainty	0.085		
$\sigma_{\Upsilon_{ext}}$	Uncertainty of off-axis extended source throughput correction (i.e., throughput correction as function of scan angle)	0.034		
$\sigma_{r_{c,IFC}}$ - Uncertainty of IFC Corrected Response				
σ_O	Sensor offset measurement uncertainty (average 10 samples)	0.035	1.12	
σ_N	IFC signal noise uncertainty	1.09		
σ_L	Linearity correction uncertainty	0.23		
σ_G	Gain mode normalization uncertainty	0.09		
σ_{IFC} - Uncertainty of IFC Radiance				
$\sigma_{\Re,BB}$	Radiance uncertainty of full-aperture blackbody	0.3	1.85	
σ_{RSR}	Uncertainty of IFC channel radiance due to uncertainty of instrument relative spectral response	1.57		
$\sigma_{N_{IFC}}$	Uncertainty of IFC radiance (calibration transfer to IFC)	0.20		
$\sigma_{IFC,repeat}$	Uncertainty due to IFC radiance long-term repeatability	0.9		

Table 45. Radiance calibration uncertainty for channel 2

$\sigma_{r_{c,sig}}$ - Uncertainty of Signal Corrected Response				Total RSS Uncertainty (%) 3% Goal 5% Requirement
Term	Description	Relative Uncertainty Error Budget (%)	Combined RSS Uncertainty (%)	
σ_O	Sensor offset measurement uncertainty	0.32	1.08	2.7
$\sigma_{o,med}$	Medium-term uncertainty of sensor offset. (i.e., time between space looks)	0.17		
σ_N	Signal noise uncertainty (SNR = 100)	1.00		
σ_L	Linearity correction uncertainty	0.14		
σ_G	Gain mode normalization uncertainty	0.083		
$\sigma_{\Upsilon_{ext}}$	Uncertainty of off-axis extended source throughput correction (i.e., throughput correction as function of scan angle)	0.038		
$\sigma_{r_{c,IFC}}$ - Uncertainty of IFC Corrected Response				
σ_O	Sensor offset measurement uncertainty (average 10 samples)	0.01	1.01	
σ_N	IFC signal noise uncertainty	1.0		
σ_L	Linearity correction uncertainty	0.14		
σ_G	Gain mode normalization uncertainty	0.08		
σ_{IFC} - Uncertainty of IFC Radiance				
$\sigma_{\Re,BB}$	Radiance uncertainty of full-aperture blackbody	0.3	2.27	
σ_{RSR}	Uncertainty of IFC channel radiance due to uncertainty of instrument relative spectral response	1.95		
$\sigma_{N_{IFC}}$	Uncertainty of IFC radiance (calibration transfer to IFC)	0.25		
$\sigma_{IFC,repeat}$	Uncertainty due to IFC radiance long-term repeatability	1.1		

Table 46. Radiance calibration uncertainty for channel 3

$\sigma_{r_{c,sig}}$ - Uncertainty of Signal Corrected Response				Total RSS Uncertainty (%) 3% Goal 5% Requirement
Term	Description	Relative Uncertainty Error Budget (%)	Combined RSS Uncertainty (%)	
σ_O	Sensor offset measurement uncertainty	0.32	1.11	2.6
$\sigma_{o,med}$	Medium-term uncertainty of sensor offset. (i.e., time between space looks)	0.34		
σ_N	Signal noise uncertainty (SNR = 100)	1.0		
σ_L	Linearity correction uncertainty	0.12		
σ_G	Gain mode normalization uncertainty	0.095		
$\sigma_{\Upsilon_{ext}}$	Uncertainty of off-axis extended source throughput correction (i.e., throughput correction as function of scan angle)	0.046		
$\sigma_{r_{c,IFC}}$ - Uncertainty of IFC Corrected Response				
σ_O	Sensor offset measurement uncertainty (average 10 samples)	0.02	1.11	
σ_N	IFC signal noise uncertainty	1.1		
σ_L	Linearity correction uncertainty	0.12		
σ_G	Gain mode normalization uncertainty	0.10		
σ_{IFC} - Uncertainty of IFC Radiance				
$\sigma_{\Re,BB}$	Radiance uncertainty of full-aperture blackbody	0.3	2.10	
σ_{RSR}	Uncertainty of IFC channel radiance due to uncertainty of instrument relative spectral response	1.73		
$\sigma_{N_{IFC}}$	Uncertainty of IFC radiance (calibration transfer to IFC)	0.33		
$\sigma_{IFC,repeat}$	Uncertainty due to IFC radiance long-term repeatability	1.1		

Table 47. Radiance calibration uncertainty for channel 4

$\sigma_{r_{c,sig}}$ - Uncertainty of Signal Corrected Response				Total RSS Uncertainty (%) 3% Goal 5% Requirement
Term	Description	Relative Uncertainty Error Budget (%)	Combined RSS Uncertainty (%)	
σ_O	Sensor offset measurement uncertainty	0.32	1.1	3.0
$\sigma_{o,med}$	Medium-term uncertainty of sensor offset. (i.e., time between space looks)	0.28		
σ_N	Signal noise uncertainty (SNR = 100)	1.00		
σ_L	Linearity correction uncertainty	0.21		
σ_G	Gain mode normalization uncertainty	0.29		
$\sigma_{\Upsilon_{ext}}$	Uncertainty of off-axis extended source throughput correction (i.e., throughput correction as function of scan angle)	0.07		
$\sigma_{r_{c,IFC}}$ - Uncertainty of IFC Corrected Response				
σ_O	Sensor offset measurement uncertainty (average 10 samples)	0.01	0.45	
σ_N	IFC signal noise uncertainty	0.27		
σ_L	Linearity correction uncertainty	0.21		
σ_G	Gain mode normalization uncertainty	0.29		
σ_{IFC} - Uncertainty of IFC Radiance				
$\sigma_{\Re,BB}$	Radiance uncertainty of full-aperture blackbody	0.4	2.7	
σ_{RSR}	Uncertainty of IFC channel radiance due to uncertainty of instrument relative spectral response	2.43		
$\sigma_{N_{IFC}}$	Uncertainty of IFC radiance (calibration transfer to IFC)	0.43		
$\sigma_{IFC,repeat}$	Uncertainty due to IFC radiance long-term repeatability	1.1		

Table 48. Radiance calibration uncertainty for channel 5

$\sigma_{r_{c,sig}}$ - Uncertainty of Signal Corrected Response				Total RSS Uncertainty (%) 3% Goal 5% Requirement
Term	Description	Relative Uncertainty Error Budget (%)	Combined RSS Uncertainty (%)	
σ_O	Sensor offset measurement uncertainty	0.32	1.1	2.0
$\sigma_{o,med}$	Medium-term uncertainty of sensor offset. (i.e., time between space looks)	0.22		
σ_N	Signal noise uncertainty (SNR = 100)	1.0		
σ_L	Linearity correction uncertainty	0.04		
σ_G	Gain mode normalization uncertainty	0.236		
$\sigma_{\Upsilon_{ext}}$	Uncertainty of off-axis extended source throughput correction (i.e., throughput correction as function of scan angle)	0.07		
$\sigma_{r_{c,IFC}}$ - Uncertainty of IFC Corrected Response				
σ_O	Sensor offset measurement uncertainty (average 10 samples)	0.01	0.39	
σ_N	IFC signal noise uncertainty	0.31		
σ_L	Linearity correction uncertainty	0.04		
σ_G	Gain mode normalization uncertainty	0.24		
σ_{IFC} - Uncertainty of IFC Radiance				
$\sigma_{\Re,BB}$	Radiance uncertainty of full-aperture blackbody	0.5	1.7	
σ_{RSR}	Uncertainty of IFC channel radiance due to uncertainty of instrument relative spectral response	1.0		
$\sigma_{N_{IFC}}$	Uncertainty of IFC radiance (calibration transfer to IFC)	0.72		
$\sigma_{IFC,repeat}$	Uncertainty due to IFC radiance long-term repeatability	1.0		

Table 49. Radiance calibration uncertainty for channel 6

$\sigma_{r_{c,sig}}$ - Uncertainty of Signal Corrected Response				Total RSS Uncertainty (%) 3% Goal 5% Requirement
Term	Description	Relative Uncertainty Error Budget (%)	Combined RSS Uncertainty (%)	
σ_O	Sensor offset measurement uncertainty	0.32	1.1	3.3
$\sigma_{o,med}$	Medium-term uncertainty of sensor offset. (i.e., time between space looks)	0.09		
σ_N	Signal noise uncertainty (SNR = 100)	1.0		
σ_L	Linearity correction uncertainty	0.07		
σ_G	Gain mode normalization uncertainty	0.39		
$\sigma_{\Upsilon_{ext}}$	Uncertainty of off-axis extended source throughput correction (i.e., throughput correction as function of scan angle)	0.04		
$\sigma_{r_{c,IFC}}$ - Uncertainty of IFC Corrected Response				
σ_O	Sensor offset measurement uncertainty (average 10 samples)	0.03	0.61	
σ_N	IFC signal noise uncertainty	0.46		
σ_L	Linearity correction uncertainty	0.07		
σ_G	Gain mode normalization uncertainty	0.39		
σ_{IFC} - Uncertainty of IFC Radiance				
$\sigma_{\Re,BB}$	Radiance uncertainty of full-aperture blackbody	0.6	3.0	
σ_{RSR}	Uncertainty of IFC channel radiance due to uncertainty of instrument relative spectral response	2.72		
$\sigma_{N_{IFC}}$	Uncertainty of IFC radiance (calibration transfer to IFC)	0.19		
$\sigma_{IFC,repeat}$	Uncertainty due to IFC radiance long-term repeatability	1.2		

Table 50. Radiance calibration uncertainty for channel 7

$\sigma_{r_{c,sig}}$ - Uncertainty of Signal Corrected Response				Total RSS Uncertainty (%) 3% Goal 5% Requirement
Term	Description	Relative Uncertainty Error Budget (%)	Combined RSS Uncertainty (%)	
σ_O	Sensor offset measurement uncertainty	0.32	1.06	2.4
$\sigma_{o,med}$	Medium-term uncertainty of sensor offset. (i.e., time between space looks)	0.09		
σ_N	Signal noise uncertainty (SNR = 100)	1.0		
σ_L	Linearity correction uncertainty	0.06		
σ_G	Gain mode normalization uncertainty	0.112		
$\sigma_{\Upsilon_{ext}}$	Uncertainty of off-axis extended source throughput correction (i.e., throughput correction as function of scan angle)	0.048		
$\sigma_{r_{c,IFC}}$ - Uncertainty of IFC Corrected Response				
σ_O	Sensor offset measurement uncertainty (average 10 samples)	0.11	0.96	
σ_N	IFC signal noise uncertainty	0.95		
σ_L	Linearity correction uncertainty	0.06		
σ_G	Gain mode normalization uncertainty	0.11		
σ_{IFC} - Uncertainty of IFC Radiance				
$\sigma_{\Re,BB}$	Radiance uncertainty of full-aperture blackbody	0.7	1.92	
σ_{RSR}	Uncertainty of IFC channel radiance due to uncertainty of instrument relative spectral response	1.48		
$\sigma_{N_{IFC}}$	Uncertainty of IFC radiance (calibration transfer to IFC)	0.14		
$\sigma_{IFC,repeat}$	Uncertainty due to IFC radiance long-term repeatability	1.0		

Table 51. Radiance calibration uncertainty for channel 8

$\sigma_{r_{c,sig}}$ - Uncertainty of Signal Corrected Response				Total RSS Uncertainty (%) 3% Goal 5% Requirement
Term	Description	Relative Uncertainty Error Budget (%)	Combined RSS Uncertainty (%)	
σ_O	Sensor offset measurement uncertainty	0.32	1.11	3.3
$\sigma_{o,med}$	Medium-term uncertainty of sensor offset. (i.e., time between space looks)	0.01		
σ_N	Signal noise uncertainty (SNR = 100)	1.0		
σ_L	Linearity correction uncertainty	0.3		
σ_G	Gain mode normalization uncertainty	0.09		
$\sigma_{\Upsilon_{ext}}$	Uncertainty of off-axis extended source throughput correction (i.e., throughput correction as function of scan angle)	0.20		
$\sigma_{r_{c,IFC}}$ - Uncertainty of IFC Corrected Response				
σ_O	Sensor offset measurement uncertainty (average 10 samples)	0.29	0.79	
σ_N	IFC signal noise uncertainty	0.66		
σ_L	Linearity correction uncertainty	0.3		
σ_G	Gain mode normalization uncertainty	0.09		
σ_{IFC} - Uncertainty of IFC Radiance				
$\sigma_{\Re,BB}$	Radiance uncertainty of full-aperture blackbody	2.0	3.01	
σ_{RSR}	Uncertainty of IFC channel radiance due to uncertainty of instrument relative spectral response	1.90		
$\sigma_{N_{IFC}}$	Uncertainty of IFC radiance (calibration transfer to IFC)	0.20		
$\sigma_{IFC,repeat}$	Uncertainty due to IFC radiance long-term repeatability	1.2		

Table 52. Radiance calibration uncertainty for channel 9

$\sigma_{r_{c,sig}}$ - Uncertainty of Signal Corrected Response				Total RSS Uncertainty (%) 3% Goal 5% Requirement
Term	Description	Relative Uncertainty Error Budget (%)	Combined RSS Uncertainty (%)	
σ_O	Sensor offset measurement uncertainty	0.32	1.11	2.8
$\sigma_{o,med}$	Medium-term uncertainty of sensor offset. (i.e., time between space looks)	0.01		
σ_N	Signal noise uncertainty (SNR = 100)	1.0		
σ_L	Linearity correction uncertainty	0.30		
σ_G	Gain mode normalization uncertainty	0.074		
$\sigma_{\Upsilon_{ext}}$	Uncertainty of off-axis extended source throughput correction (i.e., throughput correction as function of scan angle)	0.19		
$\sigma_{r_{c,IFC}}$ - Uncertainty of IFC Corrected Response				
σ_O	Sensor offset measurement uncertainty (average 10 samples)	0.60	0.67	
σ_N	IFC signal noise uncertainty	0.063		
σ_L	Linearity correction uncertainty	0.30		
σ_G	Gain mode normalization uncertainty	0.07		
σ_{IFC} - Uncertainty of IFC Radiance				
$\sigma_{\Re,BB}$	Radiance uncertainty of full-aperture blackbody	1.30	2.53	
σ_{RSR}	Uncertainty of IFC channel radiance due to uncertainty of instrument relative spectral response	1.80		
$\sigma_{N_{IFC}}$	Uncertainty of IFC radiance (calibration transfer to IFC)	0.14		
$\sigma_{IFC,repeat}$	Uncertainty due to IFC radiance long-term repeatability	1.20		

Table 53. Radiance calibration uncertainty for channel 10

$\sigma_{r_{c,sig}}$ - Uncertainty of Signal Corrected Response				Total RSS Uncertainty (%) 3% Goal 5% Requirement
Term	Description	Relative Uncertainty Error Budget (%)	Combined RSS Uncertainty (%)	
σ_O	Sensor offset measurement uncertainty	0.32	1.12	3.1
$\sigma_{o,med}$	Medium-term uncertainty of sensor offset. (i.e., time between space looks)	0.01		
σ_N	Signal noise uncertainty (SNR = 100)	1.0		
σ_L	Linearity correction uncertainty	0.5		
σ_G	Gain mode normalization uncertainty	0.03		
$\sigma_{\Upsilon_{ext}}$	Uncertainty of off-axis extended source throughput correction (i.e., throughput correction as function of scan angle)	0.21		
$\sigma_{r_{c,IFC}}$ - Uncertainty of IFC Corrected Response				
σ_O	Sensor offset measurement uncertainty (average 10 samples)	0.37	0.63	
σ_N	IFC signal noise uncertainty	0.04		
σ_L	Linearity correction uncertainty	0.5		
σ_G	Gain mode normalization uncertainty	0.03		
σ_{IFC} - Uncertainty of IFC Radiance				
$\sigma_{\Re,BB}$	Radiance uncertainty of full-aperture blackbody	1.6	2.83	
σ_{RSR}	Uncertainty of IFC channel radiance due to uncertainty of instrument relative spectral response	1.18		
$\sigma_{N_{IFC}}$	Uncertainty of IFC radiance (calibration transfer to IFC)	0.16		
$\sigma_{IFC,repeat}$	Uncertainty due to IFC radiance long-term repeatability	2.0		

3. RADIOMETRIC MODEL

3.1 Radiometric Model Description

The radiometric model characterizes the spatial, spectral, and temporal responsivity domains and random uncertainties. The SABER spatial domain is characterized by the instantaneous field of view (IFOV), object space detector position, modulation transfer function (MTF), scan mirror pointing angle, off-axis scatter, and sensor boresight. The spectral domain is characterized by the in-band and out-of-band relative spectral response. The temporal domain is characterized by the temporal frequency and phase response.

The calibration parameters of the radiometric model are listed in Table 54.

Table 54. Radiometric model calibration parameters

Parameter	Symbol	Measurement Requirement	Report Section	Test Configuration
Noise Equivalent Radiance	NER	System Noise Equivalent Radiance (NER)	Section 3.2 "Noise Equivalent Radiance (NER)"	Low and High Temperature BBs
Medium-Term Repeatability of Sensor Offset. (i.e., time between space looks)	$\sigma_{O,\,med}$	Radiance Bias Drift	Section 2.1.4 "Sensor Offset Medium Term Repeatability (Channel Drift)"	Low Temperature BB
Relative Spectral Responsivity	$RSR(\lambda)$	Spectral Response	Section 3.3 "Relative Spectral Responsivity"	Full Field Collimator & External Interferometer
Sensor Boresight	$P_{bor}(in, cr)$	Boresight Alignment Knowledge	Section 3.8 "Sensor Boresight"	GSE Test Chamber & Collimating Optics
IFOV	$IFOV(in, cr)$	IFOV @ 60 km Earth-limb Tangent Height	Section 3.7 "Instantaneous Field of View (IFOV)"	Full Field Collimator
Near Angle Scatter	$Scat$	Radiometric Accuracy	Section 3.7 "Instantaneous Field of View (IFOV)"	Full Field Collimator
Object Space Detector Positions	$P(in, cr)$	Focal Plane Channel Location	Section 3.7 "Instantaneous Field of View (IFOV)"	Full Field Collimator
Scan Mirror Transfer Function (encoder to angle)	$F_{scan}(\ )$	Limb Vertical Scan Range Measurement Altitude Range	Section 3.9 "Scan Mirror Transfer Function"	Encoder Manufacture Acceptance Test
Knife Edge Response (off-axis response far from IFOV)	S_{Knife}	Radiometric Accuracy	Section 3.10 "Knife Edge Response"	GSE Test Chamber
Temporal Frequency Response (amplitude versus frequency)	$A_{mp}(f)$	Limb Vertical Sampling Interval	Section 3.11 "Temporal Frequency Response"	Theoretical LPF Response
Temporal Frequency Response (phase versus frequency)	$P_{hase}(f)$	Limb Vertical Sampling Interval	Section 3.11 "Temporal Frequency Response"	Theoretical LPF Response

3.2 Noise Equivalent Radiance (NER)

The noise equivalent radiance (NER) of a sensor is its dark noise expressed in units of radiance. The low temperature blackbody procedure was used to make these measurements and is documented in Appendix A. Equation (13) was used to calculate the SABER NER.

$$NER_{ch} = \frac{\sigma_{ch}}{\Re_{ch}} \tag{13}$$

where NER_{ch} = measured noise equivalent radiance (W cm^{-2} sr^{-1})

$\Re_{ch}$ = peak radiance responsivity (counts/W cm^{-2} sr^{-1})

σ_{ch} = standard deviation of channel response (counts)

ch = channel number (1 to 10)

Peak radiance responsivity was obtained as described in Section 2.3.1. The channel response noise, σ_{ch}, was calculated using sensor offset medium term repeatability measurements (Section 2.1.4). For this measurement, SABER viewed a stable 110 K low temperature blackbody (LTBB) for 15 minutes. This was done for each SABER temperature state. The 15 minute measurement was broken into approximately 200 contiguous blocks of data, with each containing 8 packets or 96 samples of channel response. The response standard deviation for each data block was calculated. The mean and standard deviation of all data blocks was used to quantify the channel response noise and uncertainty due to SABER noise variation, respectively.

The noise equivalent radiance for each channel and instrument temperature state is given in Table 55, which also shows the average and standard deviation for all temperature states. Because the hot focal plane temperature state reduces responsivity on some channels (Section 2.3.1), it was not included in the average or standard deviation calculation.

Table 55. Channel NER for each SABER temperature state

Channel	Noise Equivalent Radiance (NER) [Counts per W/(cm^2*sr)]							
	Temperature State[a]						Average	Standard deviation
	N, N, N	N, H, N[b]	N, N, C	N, N, H	C, N, N	H, N, N		
1	2.44e-08	3.18e-08	2.40e-08	2.40e-08	2.38e-08	2.63e-08	2.45e-08	1.0e-09
2	2.59e-08	3.48e-08	2.73e-08	2.78e-08	2.53e-08	3.54e-08	2.84e-08	4.1e-09
3	2.89e-08	3.85e-08	3.09e-08	3.26e-08	2.94e-08	4.39e-08	3.32e-08	6.2e-09
4	3.16e-09	3.35e-09	3.38e-09	4.14e-09	3.11e-09	6.02e-09	3.96e-09	1.2e-09
5	2.04e-09	2.03e-09	2.20e-09	2.27e-09	2.02e-09	3.26e-09	2.36e-09	5.1e-10
6	1.39e-10	1.41e-10	1.35e-10	1.46e-10	1.21e-10	1.99e-10	1.48e-10	3.0e-11
7	7.67e-11	8.68e-11	7.47e-11	8.12e-11	7.21e-11	9.64e-11	8.02e-11	9.6e-12
8	1.27e-10	1.28e-10	1.25e-10	1.32e-10	NA[c]	NA[c]	1.28e-10	3.6e-12
9	3.31e-10	4.18e-10	3.29e-10	3.40e-10	NA	NA	3.33e-10	6.1e-12
10	2.48e-10	2.57e-10	2.39e-10	2.60e-10	NA	NA	2.49e-10	1.1e-11

a. Telescope, focal plane, baseplate temperature state. C=cold, N=nominal, and H=hot
b. Not used for average and standard deviation calculation over all temperature states
c. HTBB measurements were not obtained in this temperature state

Uncertainties due to peak radiance responsivity and measurement noise were combined using Equation (14) to estimate noise equivalent radiance uncertainty.

$$\sigma_{NER} = \sqrt{(\sigma_{\Re_{ch}})^2 + (\sigma_{\sigma_{ch}})^2} \tag{14}$$

where
σ_{NER} = uncertainty of noise equivalent radiance (%)
$\sigma_{\Re_{ch}}$ = uncertainty due to peak radiance responsivity (%)
$\sigma_{\sigma_{ch}}$ = uncertainty due to SABER noise variation (%)
ch = channel (1 to 10)

Peak radiance responsivity uncertainty was obtained from Section 2.3.1. The uncertainty due to SABER noise variation is described above with the channel response noise discussion.

Table 56 gives individual uncertainty terms and the combined noise equivalent radiance uncertainty, σ_{NER}, calculated using Equation (14). The uncertainty due to SABER noise variation is the dominate uncertainty at around 10%. Channels 1 to 7 have larger values by as much as 5%, depending on channel for the hot telescope temperature state. For the purpose of estimating noise equivalent radiance uncertainty, the average uncertainty due to SABER noise variation was used in Equation (14). The combined uncertainty values range from 8.9% to 11.4%, depending on channel.

Table 56. Noise equivalent radiance uncertainty

Channel	$\sigma_{\Re_{ch}}$ (%)	$\sigma_{\sigma_{sh}}$ (%)							σ_{NER} (%)
		Temperature State[a]						Average	
		N, N, N	N, H, N	N, N, C	N, N, H	C, N, N	H, N, N		
1	1.7	9.81	9.42	9.73	9.26	9.65	11.49	9.9	10.0
2	2.1	10.29	10.20	11.26	9.33	8.42	12.87	10.4	10.6
3	1.9	10.04	9.80	12.44	8.28	9.39	14.75	10.8	11.0
4	2.6	10.31	10.98	11.09	8.33	11.18	10.65	10.4	10.7
5	1.3	10.64	10.48	11.31	11.13	10.30	14.23	11.3	11.4
6	2.9	9.07	9.38	10.05	10.08	9.48	10.74	9.8	10.2
7	1.7	9.64	10.39	8.90	9.38	9.40	10.59	9.7	9.8
8	2.8	8.21	8.87	8.10	8.84	NA[b]	NA[b]	8.5	8.9
9	2.2	9.76	8.95	9.56	9.41	NA	NA	9.4	9.7
10	2.0	9.22	9.72	8.97	9.48	NA	NA	9.3	9.5

a. Telescope, focal plane, baseplate temperature state. C=cold, N=nominal, and H=hot
b. HTBB measurements were not obtained in this temperature state

For comparison to instrument requirements, the ratio of the measured NER values in Table 55 to the required noise equivalent radiance given in “SABER Instrument Requirements Document” (SDL/95-006) were computed, and are shown in Table 57. The NER for channels 4 to 10 are better than required while channels 1 to 3 are outside the requirement by 1% to 40%, depending on channel.

Table 57. Ratio of measured NER to required NER for each SABER temperature state

Channel	(NER) / (Required NER)							
	SABER Temperature State[a]						Avg	Stdev
	N, N, N	N, H, N[b]	N, N, C	N, N, H	C, N, N	H, N, N		
1	1.39	1.82	1.37	1.37	1.36	1.50	1.40	0.06
2	0.93	1.24	0.98	0.99	0.90	1.27	1.01	0.15
3	1.03	1.38	1.11	1.17	1.05	1.57	1.18	0.22
4	0.28	0.30	0.30	0.37	0.28	0.54	0.35	0.11
5	0.55	0.55	0.59	0.61	0.54	0.87	0.63	0.14
6	0.06	0.06	0.05	0.06	0.05	0.08	0.06	0.01
7	0.06	0.07	0.06	0.06	0.05	0.07	0.06	0.01
8	0.27	0.27	0.27	0.28	NA[c]	NA	0.27	0.01
9	0.47	0.60	0.47	0.49	NA	NA	0.48	0.01
10	0.35	0.37	0.34	0.37	NA	NA	0.36	0.02

a. Telescope, focal plane, baseplate temperature state. C=cold, N=nominal, and H=hot
b. Not used for average and standard deviation calculation over all temperature states
c. HTBB measurements were not obtained in this temperature state

3.3 Relative Spectral Responsivity

The relative spectral responsivity (RSR) of a sensor is the peak-normalized responsivity at different wavelengths both inside and outside the passband of each channel. The RSR is used to calculate channel dependant blackbody radiance and to verify the spectral response instrument requirement. These data are used to calculate the effective flux for radiance responsivity calibrations and to interpret on-orbit science measurements. The in-band RSR and out-of-band RSR are measured separately for each channel. RSR data collection details are documented in "SABER Ground Calibration and Preliminary Results" (SDL/98-059).

A Bio-Rad model FTS60A step-scan Fourier transform interferometer (FTI) located at the entrance port of the full field collimator (FFC) provided an interference modulated source to measure the RSR of each SABER channel. A KBr lens was used to focus the output of the FTI through a KRS-5 vacuum window onto the FFC input aperture. A glowbar source and KBr beamsplitter were used in the FTI for channels 1 through 7, while a tungsten-halogen lamp and quartz beamsplitter were used for channels 8 through 10. RSR measurements were performed in April 1999, and repeated in July 1999.

The output spectrum of the interferometer and full field collimator optics were measured following the first set of RSR measurements using a focusing mirror and pyroelectric spectral reference detector mounted in a vacuum chamber attached to the exit port of the full field collimator. This measurement was performed in June 1999. A separate smaller in-situ pyroelectric spectral measurement detector (SMD) mounted on the full field collimator was used to monitor changes in the spectral output of the full field collimator during these reference detector measurements, as well as during SABER RSR measurements. Details of these measurements are described in this section.

3.3.1 FFC Exit Beam Relative Spectral Intensity

The relative spectral intensity of the FFC exit beam was measured using a spectral reference detector (Hansen and Tansock, 1997). This detector uses a large (0.5 in^2) pyroelectric element coated with Z306 diffuse black paint as a spectral standard. The RSR of the spectral reference detector is given by the detector element absorptance, which was determined from total hemispherical reflectance measurements of two detector element witness samples performed in August 1998 by Surface Optics Corp. (SOC).

During both spectral reference detector and SABER calibration measurements, benchmark spectra were measured in addition to instrument RSR spectra using the SMD transfer detector mounted on the FFC. These spectra were used to look for and avoid contamination of the FFC optics. Similar spectra were obtained using the FTI internal detector to monitor changes in FTI internal beamsplitter alignment and source temperature drifts.

Following RSR data collection, the output spectrum of the FTI and FFC system measured using the spectral reference detector was combined with the reference detector relative spectral responsivity and appropriate benchmark spectra, and divided by the reference detector focusing mirror

reflectance, to calculate the relative spectral intensity of the FTI and FFC output beam. Benchmark spectra measured using the FTI internal detector were used in calculations for SABER channels 1 through 7, because FFC SMD transfer detector benchmarks for these channels contained excessive noise. FFC SMD transfer detector benchmarks were used for channels 8 through 10.

The complete equation used to calculate the relative spectral intensity of the FTI and FFC output beam is given in Equation (15):

$$S_i(\bar{\upsilon}) = \frac{(S_{\mathrm{BR}}(\bar{\upsilon}))(ST_{\mathrm{IC}}(\bar{\upsilon}))}{(\tau_{\mathrm{FM}}(\bar{\upsilon}))(RSR_{\mathrm{RD}}(\bar{\upsilon}))(ST_{\mathrm{RD}}(\bar{\upsilon}))}\left(\frac{1}{K_{Norm}}\right) \tag{15}$$

where

$S_i(\bar{\upsilon})$ = relative spectral intensity of the FFC exit beam

$S_{\mathrm{BR}}(\bar{\upsilon})$ = mean reference detector measured interferometer output spectrum

$\tau_{\mathrm{FM}}(\bar{\upsilon})$ = reference detector focusing mirror reflectance

$RSR_{\mathrm{RD}}(\bar{\upsilon})$ = reference detector relative spectral responsivity

$ST_{\mathrm{IC}}(\bar{\upsilon})$ = mean benchmark spectrum during instrument calibration

$ST_{\mathrm{RD}}(\bar{\upsilon})$ = mean benchmark spectrum during reference detector measurement

K_{Norm} = spectral intensity peak normalization factor

$\bar{\upsilon}$ = wavenumber (cm^{-1})

The reference detector relative spectral responsivity, $RSR_{\mathrm{RD}}(\bar{\upsilon})$, was determined from the SOC measurement of the single witness sample that was the best match to the actual reference detector element. This match was determined from separate single-angle reflectance measurements made at SDL in June 1997, on both witness samples and the reference detector itself. In these measurements, one witness sample showed better agreement with the actual detector element than the other sample. The differences observed in the witness samples in these measurements were of the same qualitative nature as differences observed in the SOC measurements, therefore only data for this witness sample were used in calculations of the reference detector RSR. Data from both witness samples were used in estimating the uncertainty of the reference detector RSR.

The remaining mean spectral quantities on the right side of Equation (15) were calculated independently for each SABER channel from individual raw spectra that were normalized to the mean within each band before averaging. This operation was performed to reduce relative uncertainties within each passband.

The standard uncertainty of the FFC output beam relative spectral intensity within each SABER band is based on NIST guidelines (NIST, 1994) as given in Equation (16):

$$\sigma_{S_i}(\bar{\upsilon}) = \sqrt{\sigma^2_{S_{\mathrm{BR}}}(\bar{\upsilon}) + \sigma^2_{\tau_{\mathrm{FM}}}(\bar{\upsilon}) + \sigma^2_{RSR_{\mathrm{RD}}}(\bar{\upsilon}) + \sigma^2_{ST_{\mathrm{IC}}}(\bar{\upsilon}) + \sigma^2_{ST_{\mathrm{RD}}}(\bar{\upsilon})} \qquad (16)$$

where

$\sigma_{S_i}(\bar{\upsilon})$ = standard uncertainty of the output beam relative spectral intensity (%)

$\sigma_{S_{\mathrm{BR}}}(\bar{\upsilon})$ = interferometer output spectrum measurement uncertainty (%)

$\sigma_{\tau_{\mathrm{FM}}}(\bar{\upsilon})$ = reference detector focusing mirror reflectance uncertainty (%)

$\sigma_{RSR_{\mathrm{RD}}}(\bar{\upsilon})$ = spectral reference detector relative spectral response uncertainty (%)

$\sigma_{ST_{\mathrm{IC}}}(\bar{\upsilon})$ = instrument calibration benchmark spectrum uncertainty (%)

$\sigma_{ST_{\mathrm{RD}}}(\bar{\upsilon})$ = reference detector measurement benchmark spectrum uncertainty (%)

$\bar{\upsilon}$ = wavenumber (cm^{-1})

The spectral reference detector relative spectral response uncertainty, $\sigma_{RSR_{\mathrm{RD}}}(\bar{\upsilon})$, was determined by taking the standard deviation of the two reference detector RSR estimates determined separately from the two reference detector element witness sample measurements. These individual RSR estimates were normalized to the combined mean within each SABER band as previously explained, before calculation of the standard deviation. The other uncertainties in Equation (16) are given for each SABER channel by the standard error in the mean of the individual mean-normalized spectra.

The peak-normalized FFC exit beam relative spectral intensity, given by Equation (15), for the quartz beamsplitter and tungsten-halogen source, is shown as a function of wavelength from 1 to 3 μm in Figure 65. The corresponding uncertainty given by Equation (16) is also shown as the lower curve in the figure, plotted against the axis on the right side of the page. This plot shows the relative spectral intensity calculated using data that were band normalized in channel 10. The results obtained using band normalization in channels 8 and 9 were similar.

The FFC exit beam relative spectral intensity for the KBr beamsplitter and glowbar source is shown as a function of wavelength from 3 to 17 μm in Figure 66, again with the corresponding uncertainty given by Equation (16). This plot shows the relative spectral intensity calculated using data that were band normalized in channel 7. The results obtained using band normalization in the remaining channels were again similar.

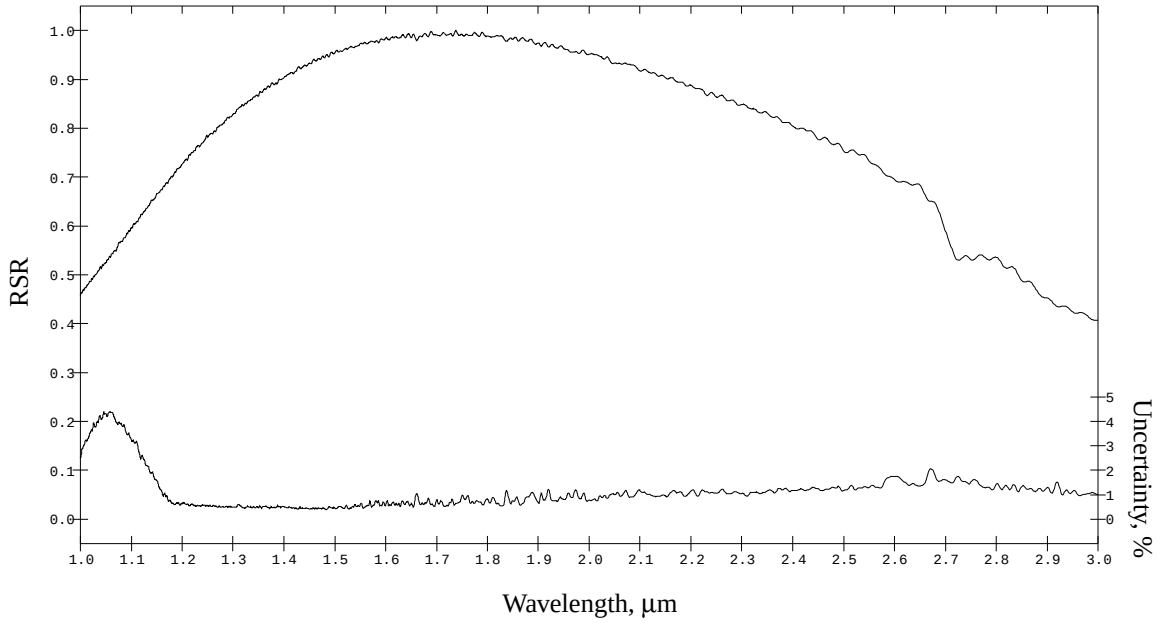

Figure 65. Example FFC output beam relative spectral intensity for channel 10

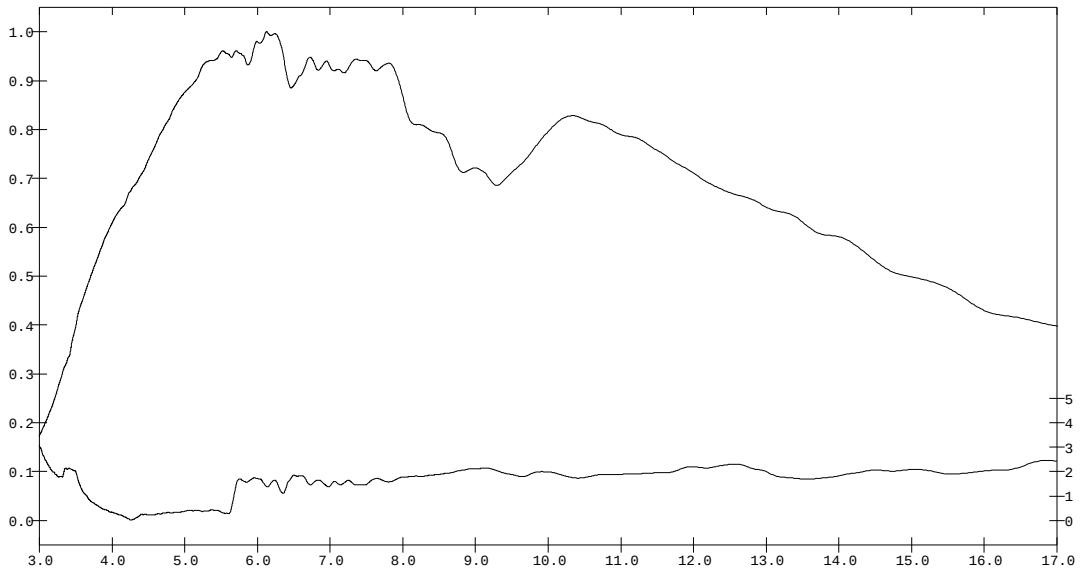

Figure 66. Example FFC output beam relative spectral intensity for channel 7

3.3.2 In-Band RSR

The Fourier transform interferometer was placed on an adjustable mechanical table and positioned at the entrance port of the full-field collimator. The mechanical table supporting the FTI was adjusted as needed, as were the FFC rotary table and SABER scan mirror, to maximize the signal on the detector under test. Adjustment of the FTI position in this way minimized spectral wavelength scale errors, caused by changes in the angle traversed through the interferometer by the observed radiation, when testing different detectors. No FFC aperture was used, although different neutral density filters in the FFC aperture and filter wheels were selected as needed to avoid saturating SABER. The spectral transmittance of these filters was measured after being installed in the FFC using the FTI to illuminate the pyroelectric transfer detector mounted on the FFC. Spectra collected while a neutral density filter was positioned in the optical path of the FFC were ratioed by an unattenuated spectrum to determine the neutral density filter transmittance. These measurements were performed while the FFC was at cold operating temperature.

The FTI was operated in 1-second step scan mode for the in-band RSR measurements. The spectral resolution of the in-band RSR measurements was determined from cut-on and cut-off specifications of the SABER filters (Peterson, 1998). The spectral resolution used for in-band RSR measurements was 2 cm^{-1} for channels 1 through 3, 4 cm^{-1} for channels 4 through 7, and 8 cm^{-1} for channels 8, 9, and 10.

During data collection, approximately 22 SABER data samples were collected at each interferogram step. When the data were processed, only the last 16 points from each step were coadded to generate interferograms. The first part of each 1-second step was ignored to allow the instrument response to stabilize following the change in flux. The interferograms calculated from the raw SABER data were plotted and visually inspected before beginning tests on another detector to avoid anomalies such as data spikes or baseline trends.

The response interferograms were converted into raw response spectra using SDL FTS software. This processing included offset correction of the interferogram, multiplication by a Kaiser-Bessel apodization function that gives a spectral sidelobe attenuation of 1e-5, zero padding by a factor of 2, Fourier transformation into amplitude spectra, normalization by the sample interval in cm, and position rotation. These steps created raw response amplitude spectra as a function of wavenumber in cm^{-1}.

The raw response amplitude spectra were converted to in-band RSRs by correcting for the relative spectral intensity of the incident beam and peak normalizing. The effects of the neutral density filters used in the data collection were removed by dividing by the filter transmittances measured earlier.

The complete conversion equation used to calculate SABER RSR is given in Equation (17):

$$RSR_i(\bar{\upsilon}) = \frac{S_{Raw}(\bar{\upsilon})}{(S_i(\bar{\upsilon}))(S_{nd}(\bar{\upsilon}))}\left(\frac{1}{K_{Norm}}\right) \tag{17}$$

where

$RSR_i(\bar{\upsilon})$ = in-band relative spectral responsivity

$S_{Raw}(\bar{\upsilon})$ = raw response spectrum

$S_i(\bar{\upsilon})$ = relative spectral intensity of FFC exit beam (from Equation (15))

$S_{nd}(\bar{\upsilon})$ = relative spectral transmissivity of neutral density filtering

K_{Norm} = RSR peak normalization factor

$\bar{\upsilon}$ = wavenumber (cm^{-1})

The standard uncertainty of the in-band RSR is based on NIST guidelines (NIST, 1994) as given in Equation (18):

$$\sigma_{RSR,\, inband_i}(\bar{\upsilon}) = \sqrt{\sigma^2_{S_{\mathrm{RAW}}}(\bar{\upsilon}) + \sigma^2_{S_i}(\bar{\upsilon}) + \sigma^2_{S_{\mathrm{ND}}}(\bar{\upsilon})} \tag{18}$$

where

$\sigma_{RSR,\, inband_i}(\bar{\upsilon})$ = standard uncertainty of the in-band RSR(%)

$\sigma_{S_{\mathrm{RAW}}}(\bar{\upsilon})$ = measurement repeatability uncertainty (%)

$\sigma_{S_i}(\bar{\upsilon})$ = uncertainty of FFC exit beam (from Equation (16))

$\sigma_{S_{\mathrm{ND}}}(\bar{\upsilon})$ = ND filter transmittance uncertainty (%)

$\bar{\upsilon}$ = wavenumber (cm^{-1})

The measurement repeatability uncertainty, $\sigma_{S_{\mathrm{RAW}}}(\bar{\upsilon})$, is given by half the difference between two separate RSR measurements. These measurements were made in April and July of 1999. The KBr beamsplitter used in the first set of measurements failed in June 1999 during measurements of the FTI - FFC output spectra, and a different beamsplitter was used in the July 1999 RSR measurements. This change was successfully accommodated by use of the benchmark spectra discussed previously.

The uncertainty of the incident beam relative spectral intensity, $\sigma_{S_i}(\bar{\upsilon})$, is given by Equation (16). The uncertainty of the ND filter attenuation, $\sigma^2_{ND}(\bar{\upsilon})$, is given by the standard error in the mean of the SDL ND filter transmittance measurements. The spectral standard uncertainties ex-

pressed in percent of in-band RSR, $\sigma_{RSR,\,inband_i}(\bar{\upsilon})$, are shown in Figures 67 through 76 for each SABER channel. To obtain an understanding of the dominant sources of uncertainty, all of the component uncertainties that appear in Equations 16 and 18 are summarized in Table 58. The numbers shown are the mean uncertainty within each SABER band, calculated between points of 50% of peak transmittance. The dominant uncertainty for channels 1 to 7 is contributed by measurement uncertainty, while for channels 8 to 10 the neutral density filter transmittance uncertainty dominates.

Table 58. RSR in-band uncertainty summary

SABER Channel	Uncertainty, %							$\sigma_{RSR,\,inband}(\upsilon)$ RSS Total
	$\sigma_{S_{BR}}$	$\sigma_{\tau_{FM}}$	$\sigma_{RSR_{RD}}$	$\sigma_{ST_{IC}}$	$\sigma_{ST_{RD}}$	σ_{MR}	σ^2_{ND}	
1	0.76	< 0.01	0.092	0.034	0.014	0.54	0.35	1.07
2	1.2	< 0.01	0.10	0.16	0.019	1.14	0.65	1.86
3	1.2	< 0.01	0.10	0.16	0.019	0.60	0.65	1.57
4	0.36	< 0.01	0.019	0.51	0.041	1.77	0.18	1.97
5	0.20	< 0.01	0.11	0.086	0.25	0.70	0.28	0.87
6	0.091	< 0.01	0.015	< 0.01	0.019	1.61	0.28	1.65
7	0.021	< 0.01	0.036	0.029	0.045	1.10	0.37	1.21
8	0.25	0.024	0.11	0.046	0.052	0.11	1.1	1.16
9	0.18	0.026	0.43	0.058	0.069	0.28	1.0	1.18
10	0.18	< 0.01	0.46	0.066	0.060	0.29	0.70	0.96

The in-band RSR measurement was made under nominal as well as warm and cold focal plane temperature conditions. The temperatures recorded for the SABER focal plane during each set of tests are shown in Table 59.

Table 59. RSR focal plane temperatures

Temperature Condition	Nominal Temperature, K	Recorded Temperature, K
Cold	72	71.6
Nominal	75	74.7
Warm	80	79.7

RSR plots for each SABER channel at all 3 temperature conditions are shown in Figures 67 through 76. Nominal temperature plots are shown as a solid line, while warm and cold focal plane temperature data are shown as dashed and dash-dotted lines, respectively. These plots also show spectral graphs of the RSS total uncertainty as a dotted line plotted against the axis on the right.

Visual examination of the RSR plots does not reveal any obvious temperature dependence in the shape of the RSR curves. Although not shown in the peak normalized data, there was generally a decrease in response in the un-normalized response with increasing focal plane temperature for the long wavelength channels. This is reasonable given the expected detector responsivity temperature dependence.

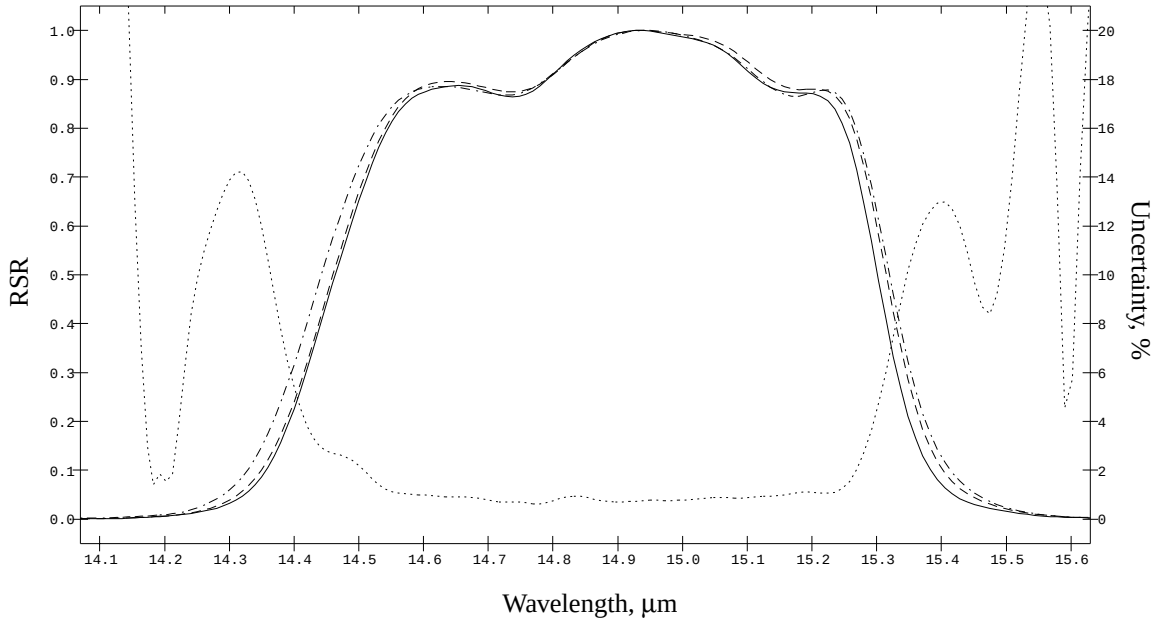

Figure 67. SABER channel 1 RSR

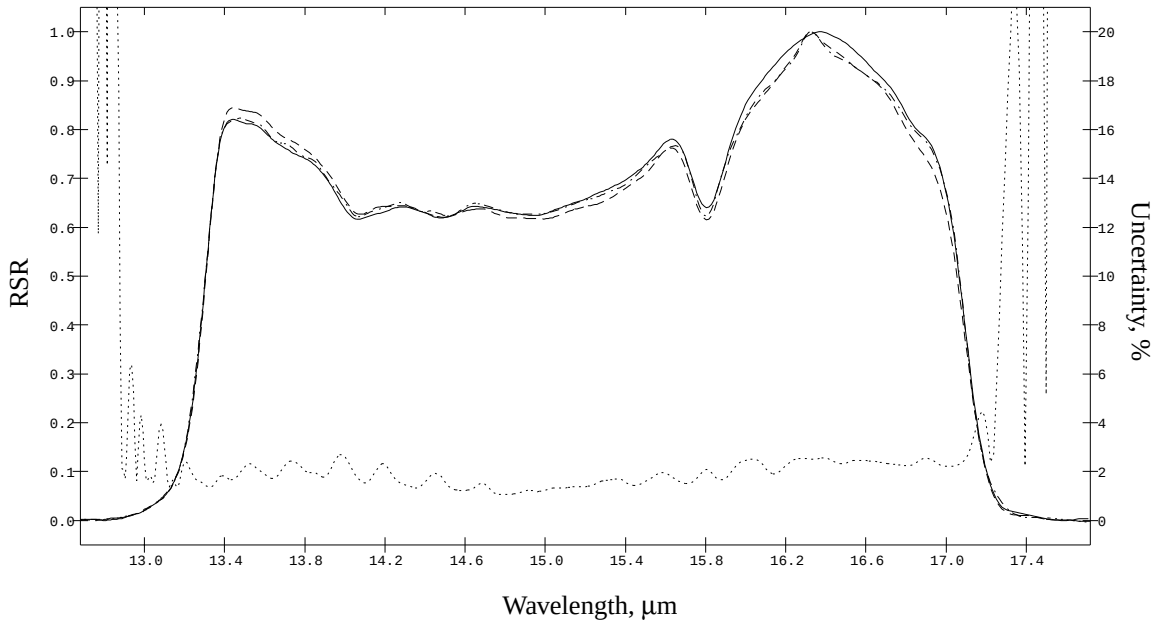

Figure 68. SABER channel 2 RSR

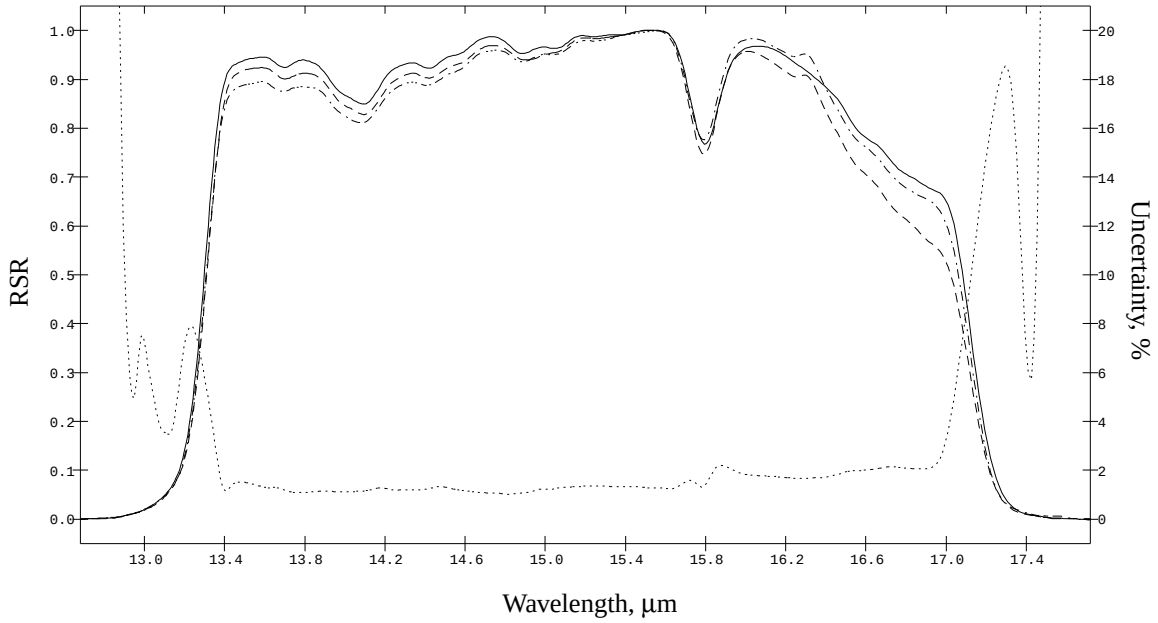

Figure 69. SABER channel 3 RSR

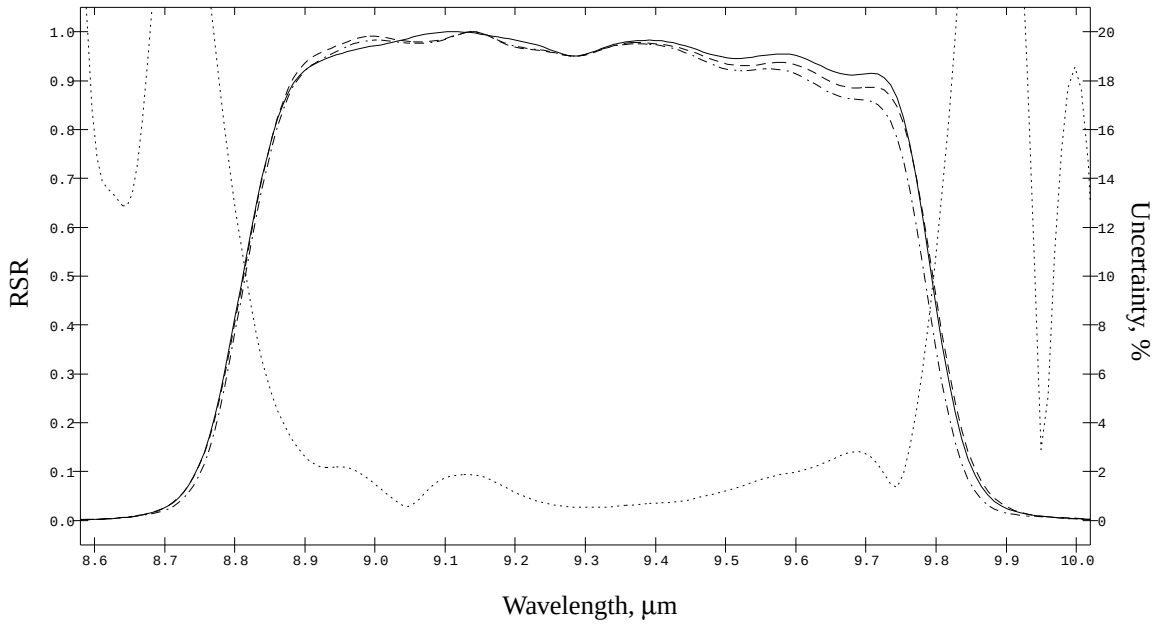

Figure 70. SABER channel 4 RSR

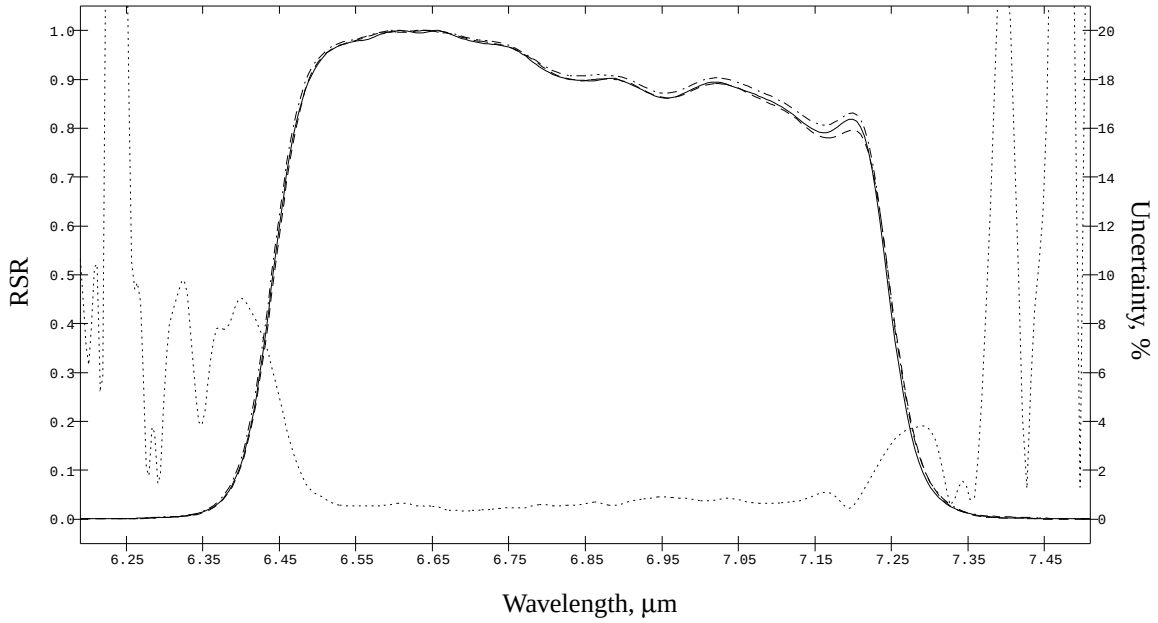

Figure 71. SABER channel 5 RSR

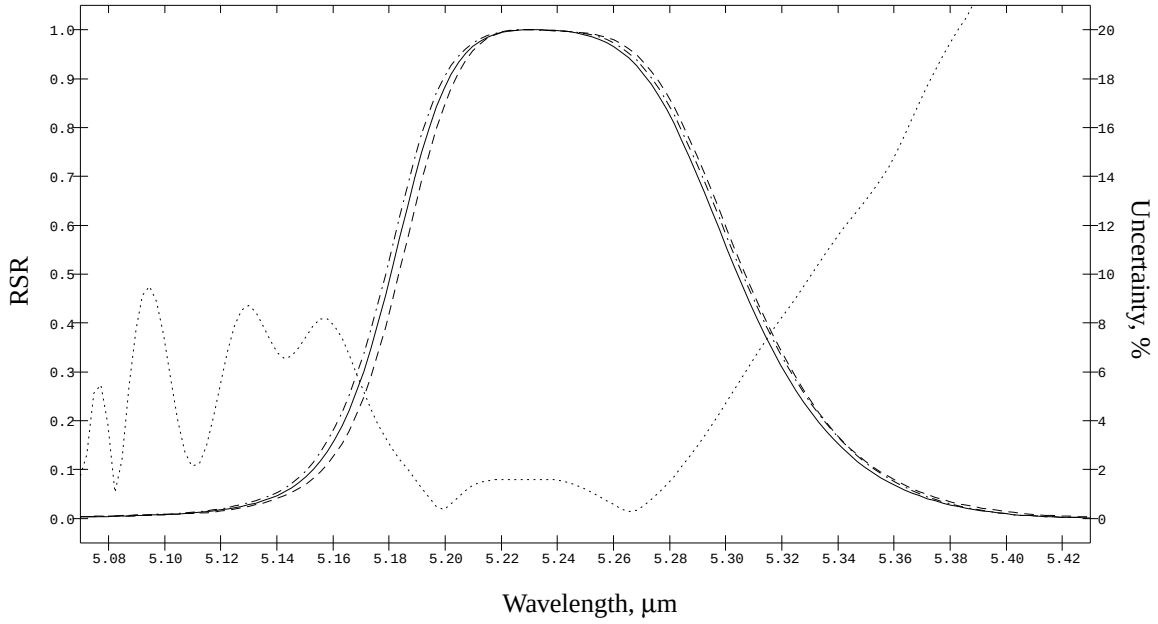

Figure 72. SABER channel 6 RSR

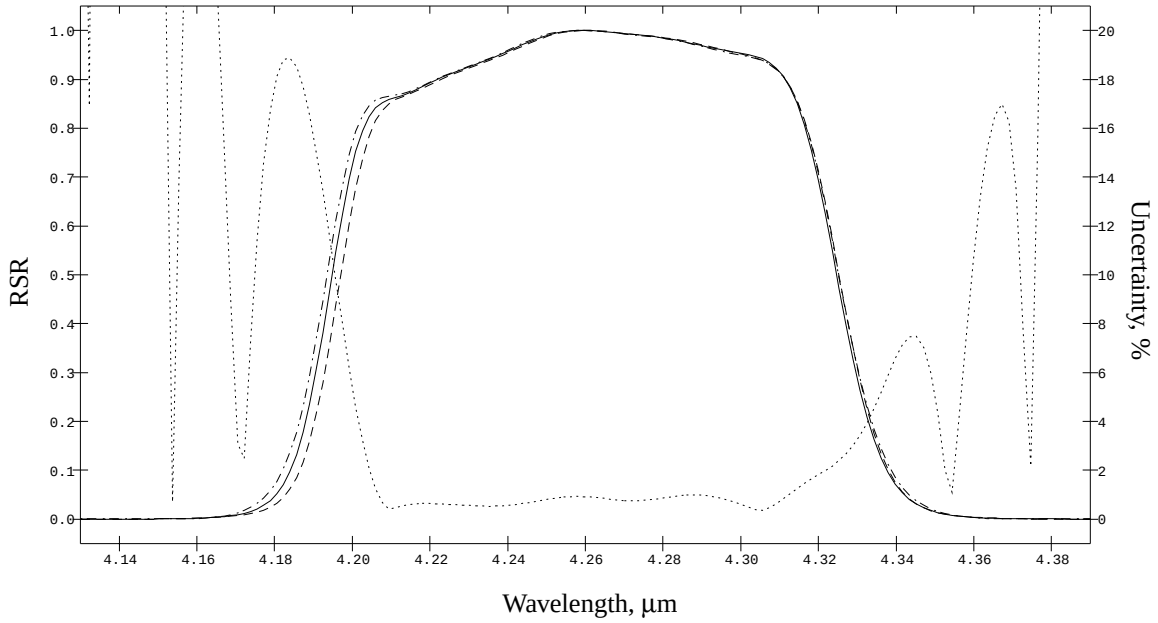

Figure 73. SABER channel 7 RSR

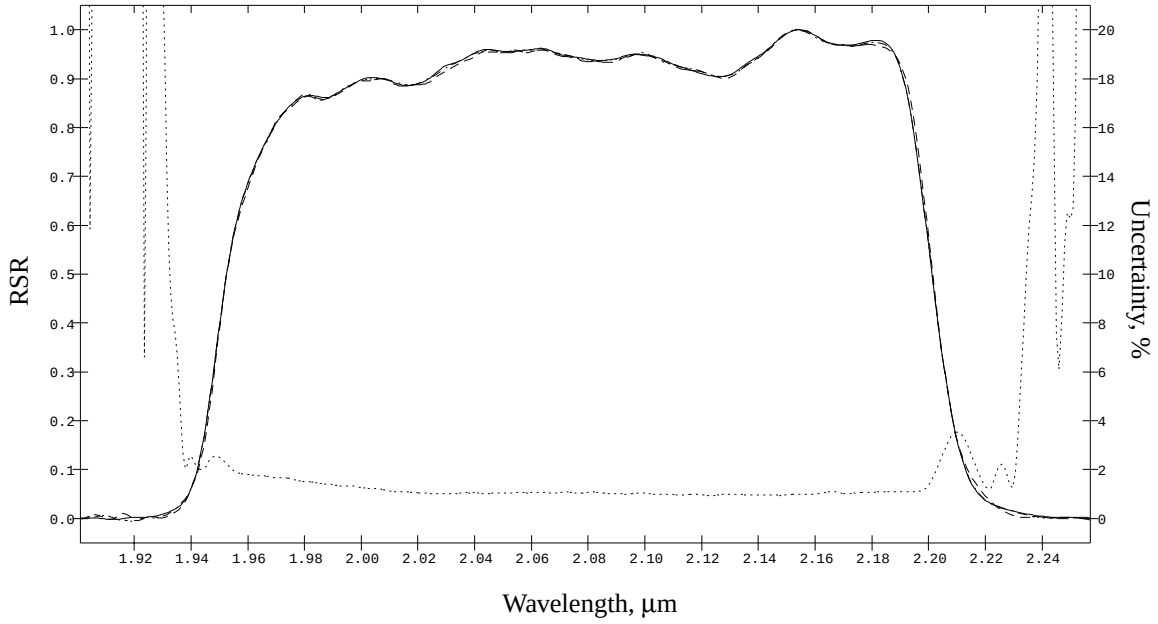

Figure 74. SABER channel 8 RSR

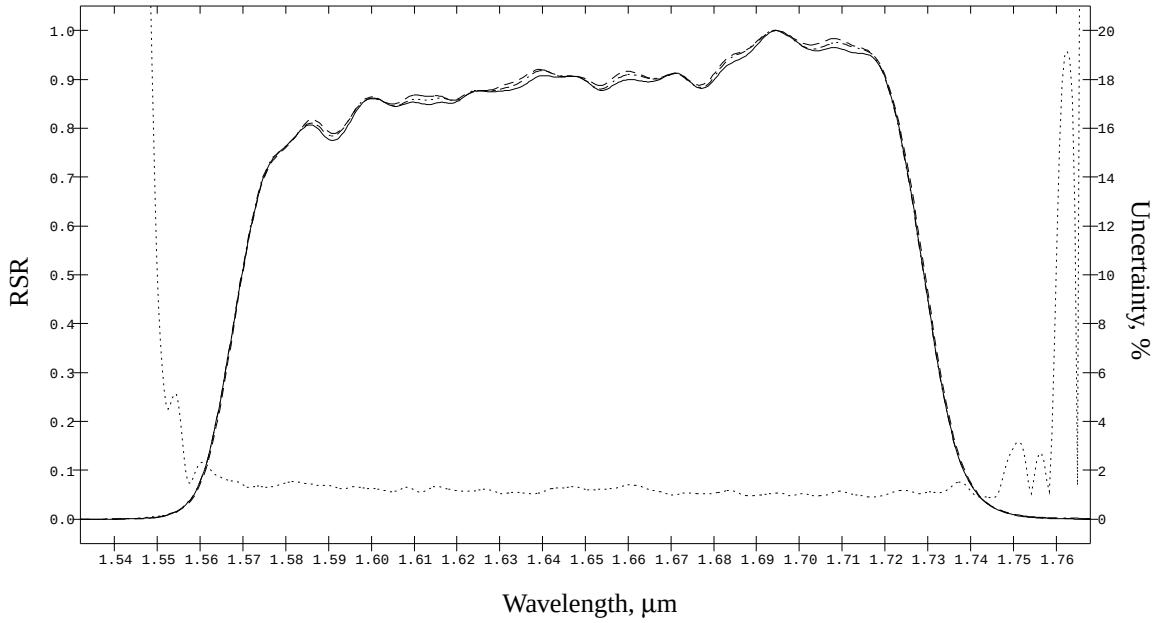

Figure 75. SABER channel 9 RSR

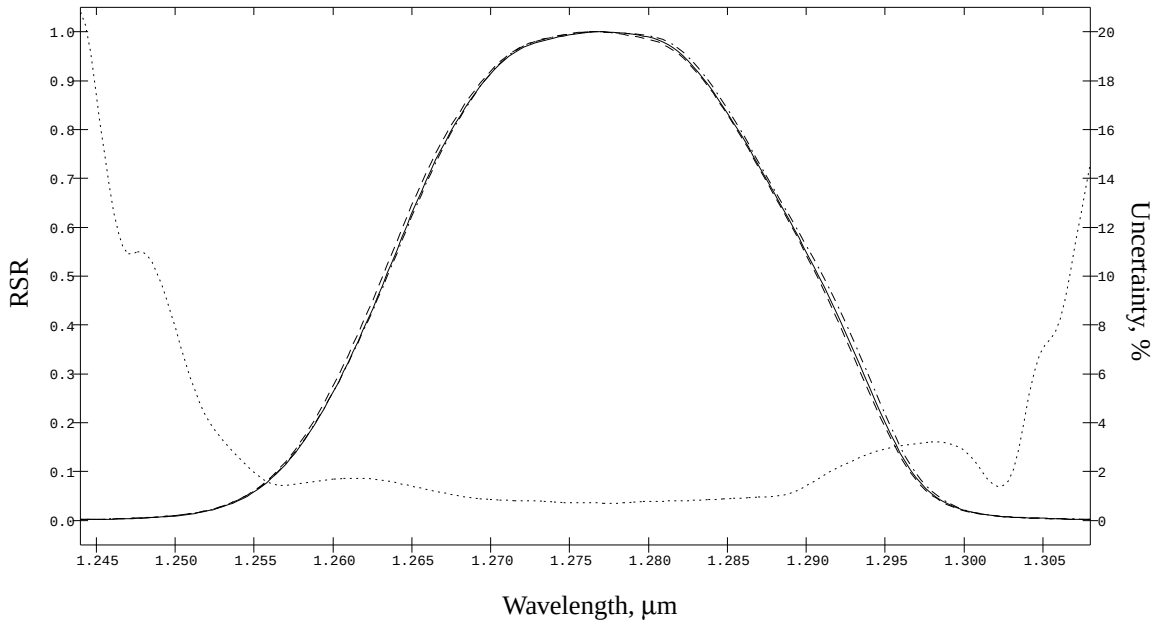

Figure 76. SABER channel 10 RSR

A more careful examination of the RSR temperature dependence is quantified by calculating various figures of merit for the curves shown in Figures 67 through 76. The first of these is the mean in-band standard deviation of the 3 curves, compared to the mean measurement uncertainty from Table 58. This comparison is shown in Table 60. All but three channels show a standard deviation of the RSR temperature data that is less than the measurement uncertainty. The data that do show greater variability than the measurement uncertainty are not believed to represent a systematic effect, but only variability in a limited data set. The standard deviation values that do exceed the corresponding measurement uncertainty are comparable to the uncertainties for other channels having larger measurement repeatabilities than the channels in question. The overall similarity between the variability of the temperature data and the measurement repeatability suggests that the differences observed in the temperature data are not significant.

Table 60. Standard deviation of RSR at 3 focal plane temperatures

SABER Channel	Standard Deviation (%)	Measurement Uncertainty (%)	Ratio of Standard Deviation to Measurement Uncertainty
1	1.63	1.07	1.52
2	1.34	1.86	0.72
3	2.59	1.57	1.65
4	1.45	1.97	0.74
5	0.77	0.87	0.89
6	2.21	1.65	1.34
7	1.10	1.21	0.91
8	0.31	1.16	0.27
9	0.54	1.18	0.46
10	0.76	0.96	0.79

A second figure of merit that is useful in examining the effect of focal plane temperature on RSR is the change in band edge position as a function of temperature. The points at which the transmittance drops to 5% of the peak transmittance were identified, and the mean position over the 3 focal plane temperatures was calculated. The differences in μm between this mean and the individual values at each temperature were plotted against focal plane temperature and are shown in Figure 77. For most of the channels, there is no readily identifiable overall systematic effect, only apparently random variations of band edge as a function of focal plane temperature. Whatever differences may not be random are extremely small. The standard deviation repeatability analysis and the band edge analysis together suggest that there is no effect of focal plane temperature on the relative spectral response that is measurable with the data available. Any focal plane temperature dependence that may exist is less than the uncertainty in the data available.

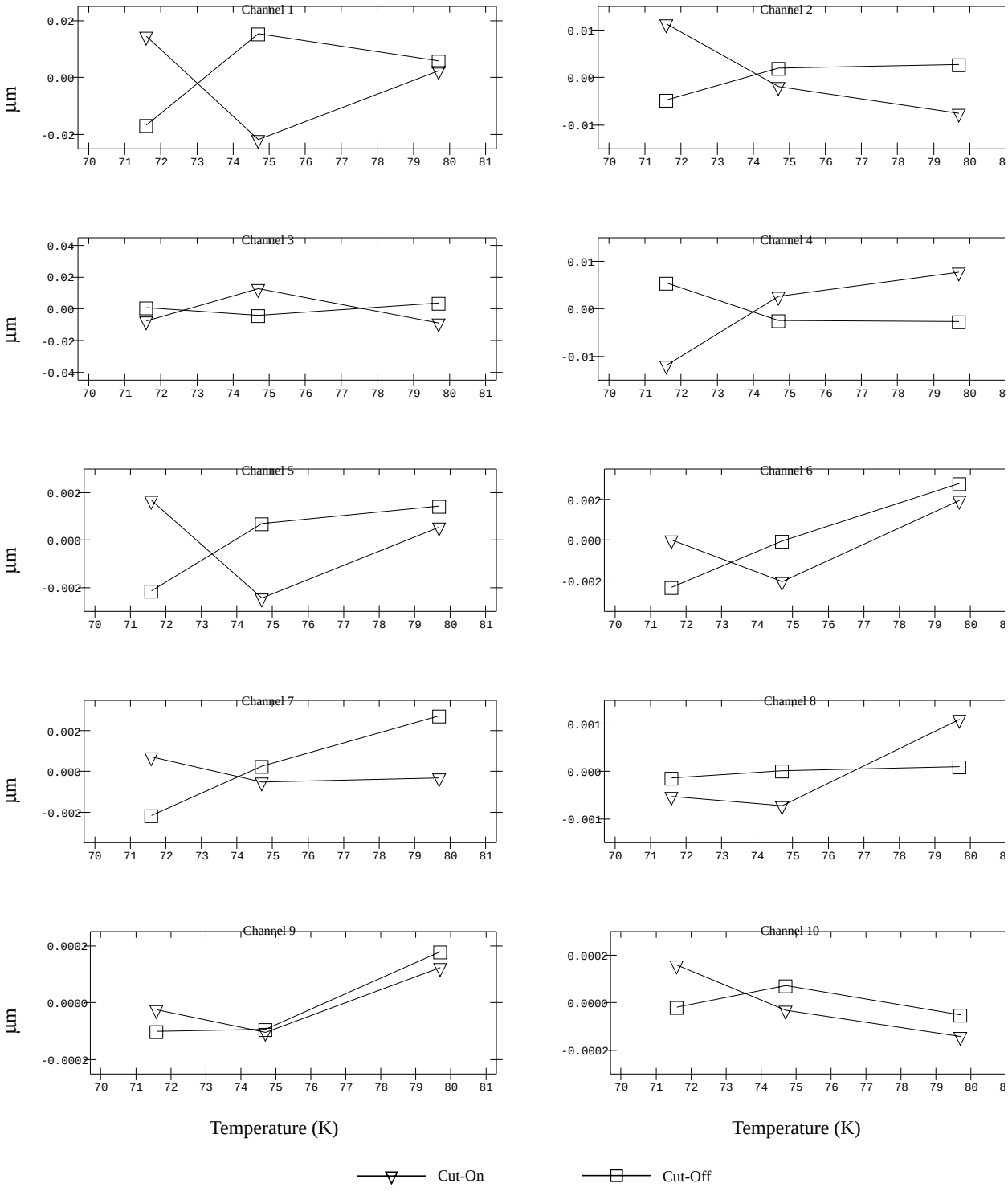

Figure 77. RSR 5% band edge temperature dependence

In conclusion, the SABER relative spectral response has been successfully measured and shown to be independent of focal plane temperature within the limits imposed by the data uncertainty. No RSR correction due to focal plane temperature dependence is needed for focal plane operating conditions between 72 and 80 K. To summarize, a comparison of the measured SABER relative spectral response to requirements is shown in Table 61. The actual relative spectral response of the SABER instrument meets contract requirements within acceptable limits.

Table 61. SABER in-band spectral measurements

Channel Number and Species		Center Wavenumber (Wavelength) (cm^{-1})		Spectral Bandpass (cm^{-1})		5% Relative Transmittance Limits (cm^{-1})	
		Req.	Meas.	Req.	Meas.	Req.	Meas.
1	CO_2 (N)	673	674	45	49	695 - 650	698 - 649
2	CO_2 (W)	670	672	180	183	760 - 580	763 - 580
3	CO_2 (W)	670	671	180	184	760 - 580	763 - 579
4	O_3	1075	1080	130	133	1140 - 1010	1146 - 1013
5	H_2O	1470	1468	180	199	1560 - 1380	1567 - 1368
6	NO	1895	1904	65	82	1930 - 1865	1945 - 1863
7	CO_2	2360	2348	80	89	2400 - 2320	2392 - 2303
8	OH (A)	4850	4833	700	648	5200 - 4500	5157 - 4509
9	OH (B)	6088	6079	695	675	6435 - 5740	6416 - 5741
10	O_2	7850	7837	240	268	7970 - 7730	7971 - 7703

3.4 Out-of-Band RSR

To characterize the out-of-band blocking below the in-band RSR measurement limit of approximately 0.1% of the in-band peak, the out-of-band relative spectral responsivity was measured using the Cascaded Filter Fourier Transform Spectrometer (CFFTS) method (Kemp et al., 1989). These measurements used the same setup as the in-band RSR measurement, except a bandpass filter was used to avoid saturation and to define the bandpass of the out-of-band blocking measurement. The blocking filters used for the out-of-band RSR measurements are described in Peterson (1998).

The out-of-band RSR measurements were performed at nominal optics cavity, baseplate, and focal plane temperatures. The measurement resolution of the out-of-band RSR measurements were 32 cm^{-1}, defined by full-width-first-zero (FWFZ). The nominal temperature, out-of-band RSR measurements were combined to the nominal temperature in-band RSR and the high and low temperature in-band RSR to create an overall RSR at each temperature. This is based on the assumption that the out-of-band RSR does not change significantly over this temperature range.

The measured out-of-band RSR data were Fourier transformed and normalized to the in-band RSR to give a composite in-band and out-of-band RSR curve. Response interferograms were generated and converted into raw response spectra using the same procedure used for the in-band RSR measurements. The raw response amplitude spectra were converted to out-of-band RSR curves by correcting for the relative spectral intensity of the incident beam and normalizing to the in-band RSR. This process was quantified using Equation (19):

$$RSR_O(\bar{\upsilon}) = \left(\frac{S_{CF}(\bar{\upsilon})}{S_i(\bar{\upsilon})}\right)\left(\frac{1}{\tau_{BF}(\bar{\upsilon})}\right)\left(\frac{1}{\tau_{ND}}\right)\left(\frac{1}{G_E}\right)\left(\frac{1}{K_{Norm}}\right) \tag{19}$$

where

$RSR_O(\bar{\upsilon})$ = measured out-of-band RSR

$S_{CF}(\bar{\upsilon})$ = cascaded filter spectrum

$S_i(\bar{\upsilon})$ = relative spectral intensity of the incident beam (FFC exit beam)

$\tau_{BF}(\bar{\upsilon})$ = blocking filter transmittance

τ_{ND} = ND filter transmittance (in-band measurement)

G_E = sensor electronic gain (ratio of gain value during the out-of-band RSR measurement to the gain value during in-band RSR measurement)

K_{Norm} = in-band RSR peak normalization factor

$\bar{\upsilon}$ = wavenumber (cm^{-1})

The average ND filter transmittance over each SABER channel was used to compute the ND filter transmittance (τ_{ND}). The ND transmittances were computed from measurements made during SABER calibration using the FTI and spectral measurement detector (SMD). The elec-

tronic gain values for each SABER channel were computed as part of the gain-mode normalization and are given in Section 2.2.

The standard uncertainty of the out-of-band RSR is based on NIST guidelines (NIST, 1994) as given in Equation (20):

$$\sigma_{OOB}(\bar{\upsilon}) = \sqrt{\sigma^2_{CF}(\bar{\upsilon}) + \sigma^2_{i}(\bar{\upsilon}) + \sigma^2_{BF}(\bar{\upsilon}) + \sigma^2_{ND}(\bar{\upsilon}) + \sigma^2_{GL} + \sigma^2_{SS}} \quad (20)$$

where

$\sigma_{OOB}(\bar{\upsilon})$ = standard uncertainty of the out-of-band RSR(%)

$\sigma_{CF}(\bar{\upsilon})$ = cascaded filter spectrum noise uncertainty (%)

$\sigma_{S_i}(\bar{\upsilon})$ = uncertainty of the relative spectral intensity of the incident beam (%)

$\sigma_{BF}(\bar{\upsilon})$ = blocking filter transmittance uncertainty (%)

$\sigma_{ND}(\bar{\upsilon})$ = uncertainty of throughput gain from FFC ND filtering (%)

σ_{GL} = gain mode normalization and linearity correction uncertainty (%)

σ_{SS} = FTI source switch uncertainty (%)

$\bar{\upsilon}$ = wavenumber (cm^{-1})

The cascaded filter noise uncertainty, $\sigma_{CF}(\bar{\upsilon})$, was computed by visually determining a noise threshold for each blocking-filter spectrum and processing it through Equation (19). The uncertainty of the incident beam relative spectral intensity, $\sigma_{S_i}(\bar{\upsilon})$, is given by Equation (16) and is determined separately from data that were mean normalized within each channel. The uncertainty of the incident beam relative spectral intensity for mean normalization in channel 7 is shown in Figure 66. The blocking filter transmittance uncertainty, $\sigma_{BF}(\bar{\upsilon})$, is insignificant in comparison to other terms and is ignored. The uncertainty of the ND filter attenuation, $\sigma_{ND}(\bar{\upsilon})$, is based on the standard deviation of multiple filter transmittance measurements. This measurement is discussed in Section 3.3.2. The FTI source switch uncertainty is needed to account for repeatability in the response magnitude when the FTI source was changed. This uncertainty was computed from the spectral overlap regions where data were collected in both source configurations. The gain mode normalization and linearity correction uncertainty, σ_{GL}, is the RSS of the individual gain mode normalization and linearity correction uncertainties discussed in Section 2.2 and Section 2.1.4, respectively, of this report.

The final step in the out-of-band RSR data processing was to convert the independent spectral variable from wavenumber (cm^{-1}) to wavelength (μm) and interpolate the results to an even wavelength spacing. The resulting out-of-band RSR measurements were merged with the in-band RSR measurements into a composite RSR for each SABER channel. This was done by piecing together the in-band RSR and uncertainty with the out-of-band RSR and uncertainty from each blocking filter measurement. Any out-of-band spectral regions not covered by an out-of-band blocking filter used the in-band measurement noise floor as an upper threshold to the out-of-band leakage.

The resulting in-band and out-of-band RSR, and the corresponding uncertainty, are shown in Figures 78 to 87 for each SABER channel. In spectral regions where the out-of-band RSR was above the measurement noise floor and the measurement is valid, the out-of-band RSR and corresponding uncertainty are given. These are shown in black and blue, respectively. In spectral regions were the RSR was below the measurement noise floor, only the measurement noise floor is shown. This is shown in red.

Table 62 gives the measured and required out-of-band rejection for each SABER channel. The out-of-band rejection requirement is met or exceeded on all channels except channel 1 in the 21 μm to 28 μm spectral region and channel 9 in the 3.8 μm to 4.3 μm spectral region. The SABER science team has evaluated the out-of-band performance of channel 1 and concluded the science impact is minimal. Channel 9 out-of-band rejection is only slightly larger than the requirement in a very small spectral region.

Table 62. SABER out-of-band spectral measurements

Channel Number and Species		Out-of-Band Rejection Ratio (relative to peak in-band response)	
		Req.	Meas.
1	CO_2 (N)	$< 10^{-4}$	$< 4x10^{-4}$
2	CO_2 (W)	$< 10^{-3}$	$< 10^{-4}$
3	CO_2 (W)	$< 10^{-3}$	$< 10^{-4}$
4	O_3	$< 5x10^{-4}$	$< 3x10^{-4}$
5	H_2O	$< 10^{-4}$	$< 10^{-4}$
6	NO	$< 10^{-4}$	$< 10^{-5}$
7	CO_2	$< 10^{-4}$	$< 10^{-4}$
8	OH (A)	$< 10^{-4}$	$< 10^{-4}$
9	OH (B)	$< 10^{-4}$	$< 1.9x10^{-4}$
10	O_2	$< 10^{-4}$	$< 10^{-4}$

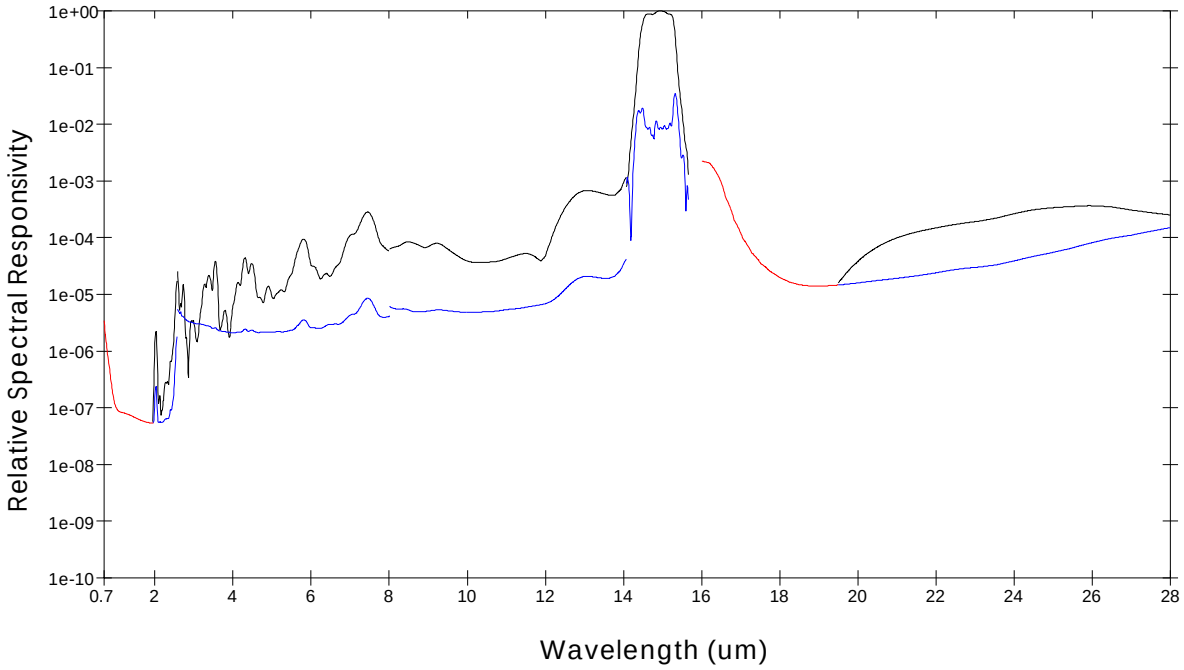

Figure 78. Out-of-band RSR - channel 1

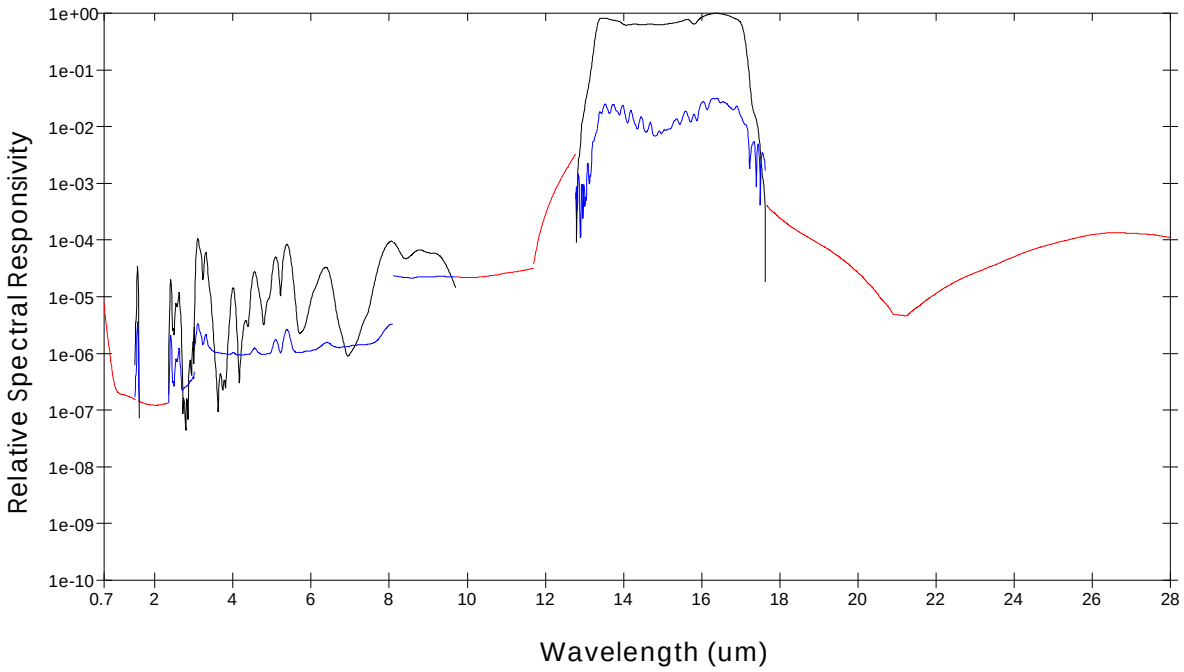

Figure 79. Out-of-band RSR - channel 2

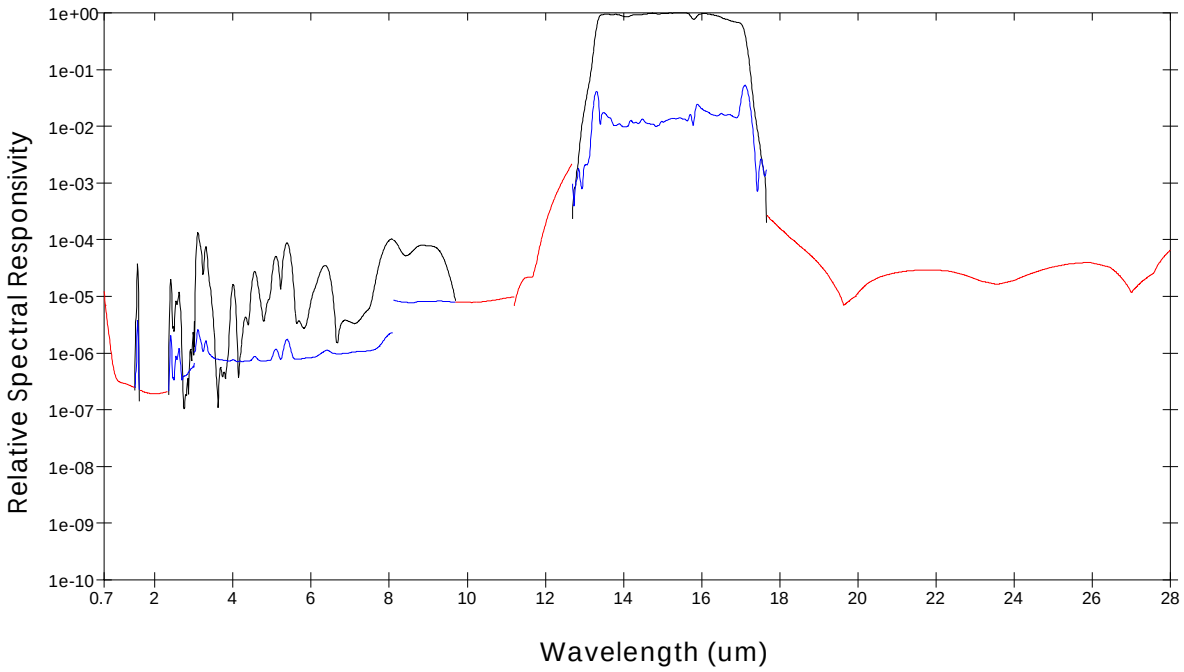

Figure 80. Out-of-band RSR - channel 3

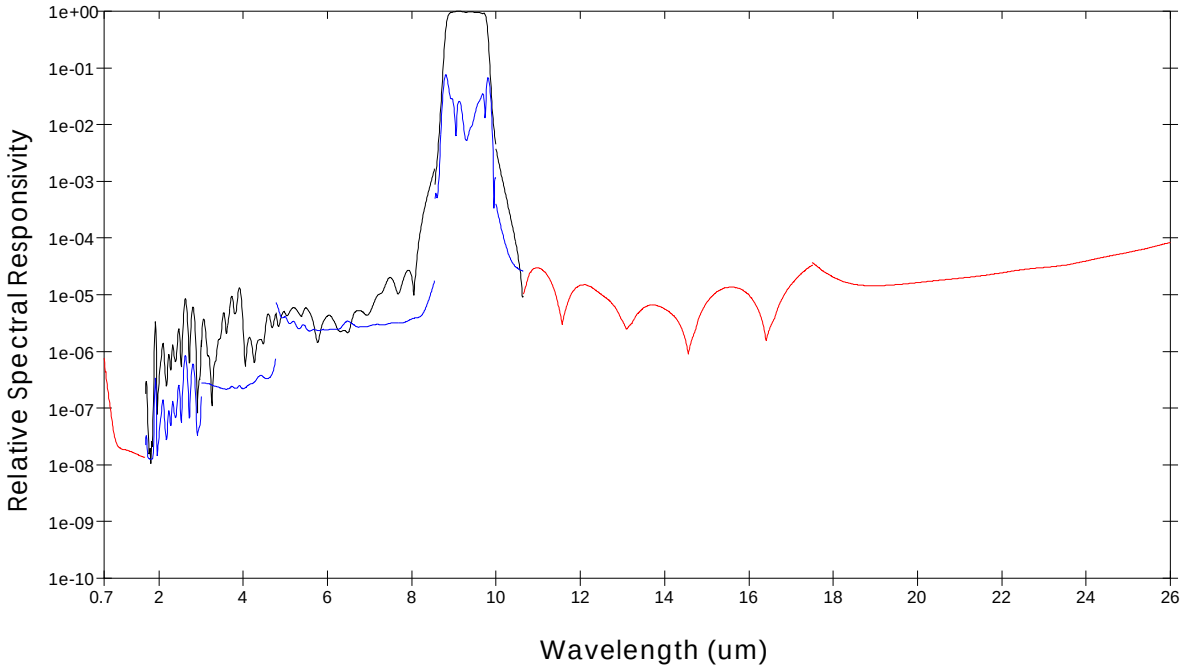

Figure 81. Out-of-band RSR - channel 4

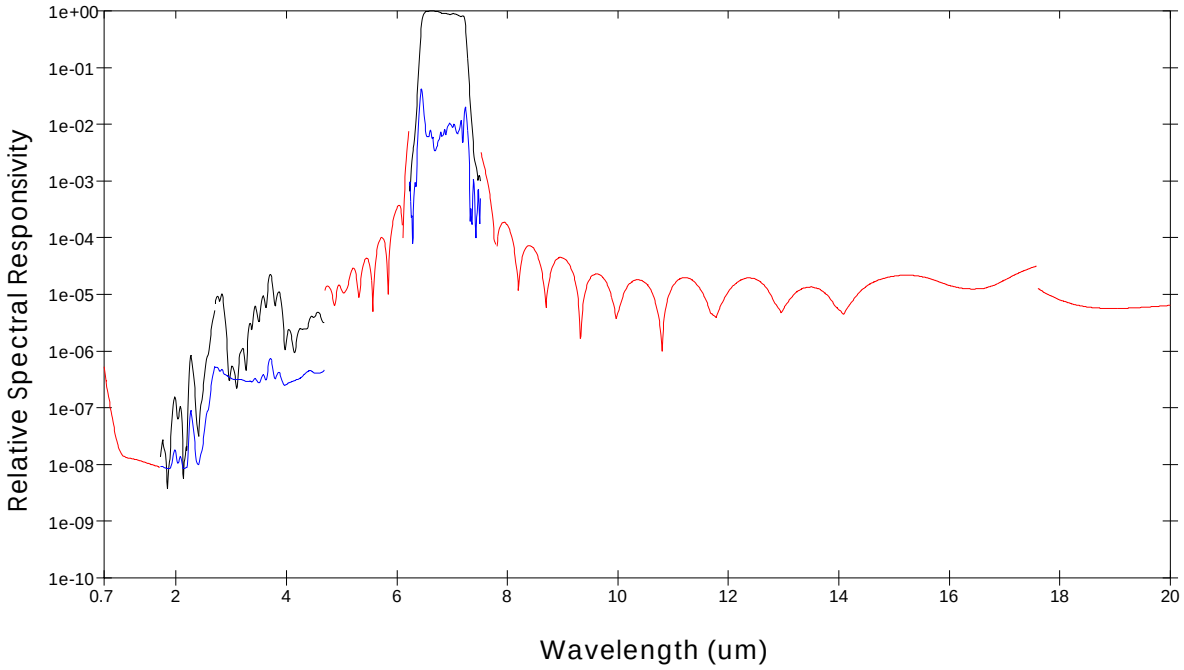

Figure 82. Out-of-band RSR - channel 5

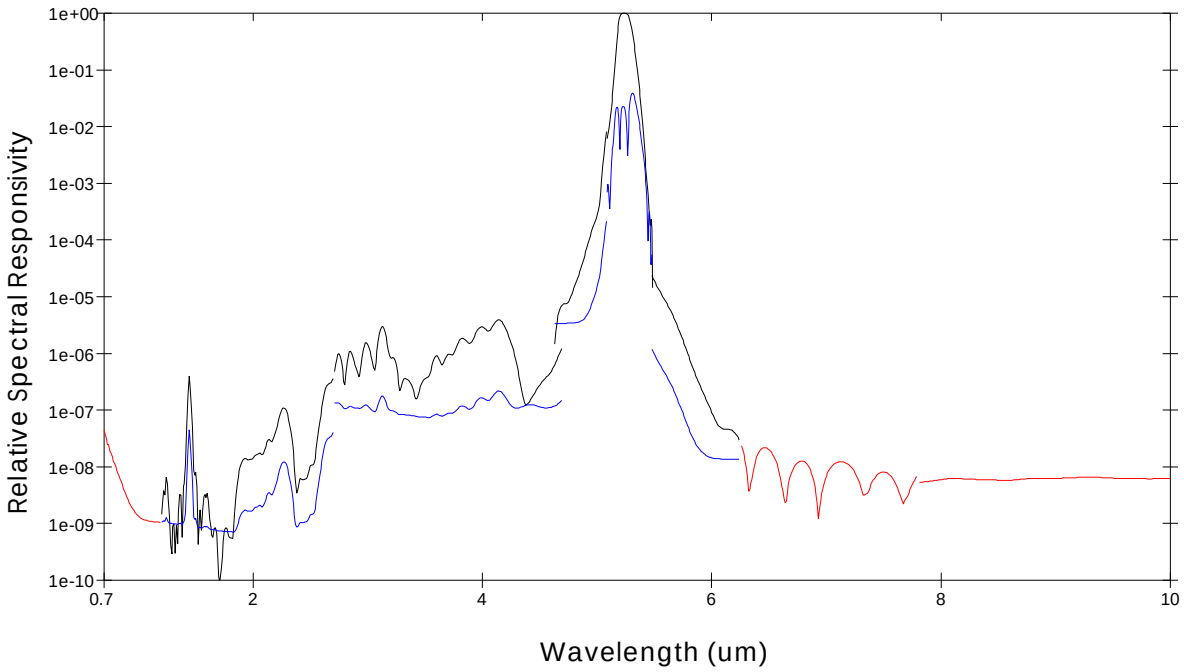

Figure 83. Out-of-band RSR - channel 6

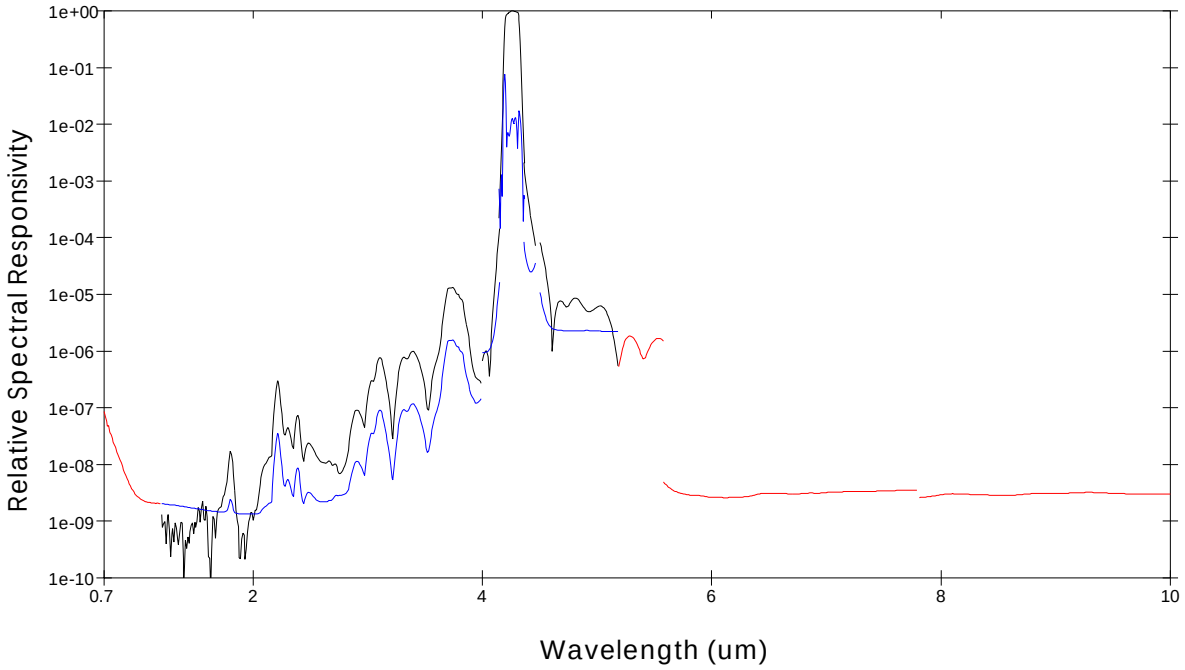

Figure 84. Out-of-band RSR - channel 7

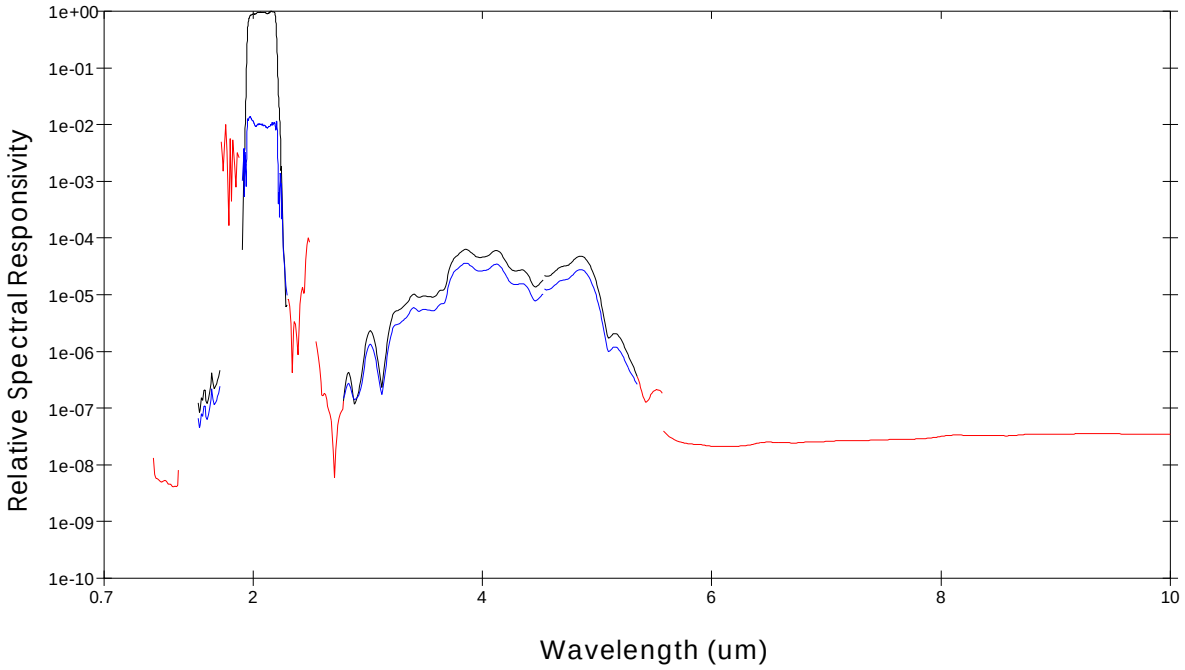

Figure 85. Out-of-band RSR - channel 8

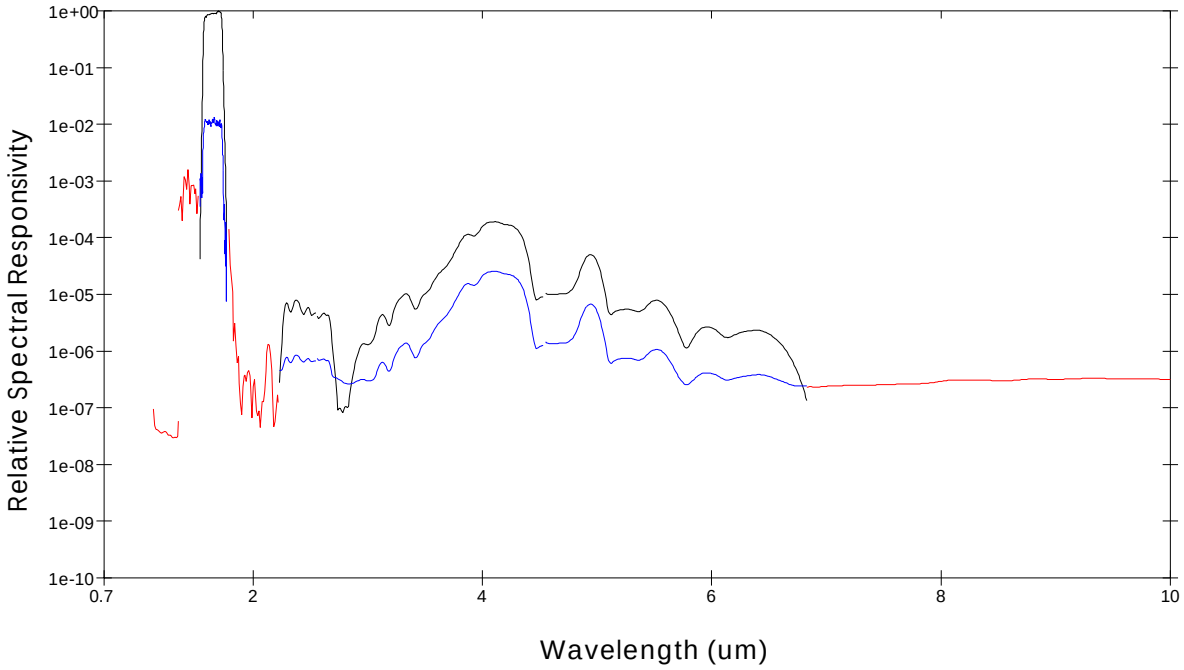

Figure 86. Out-of-band RSR - channel 9

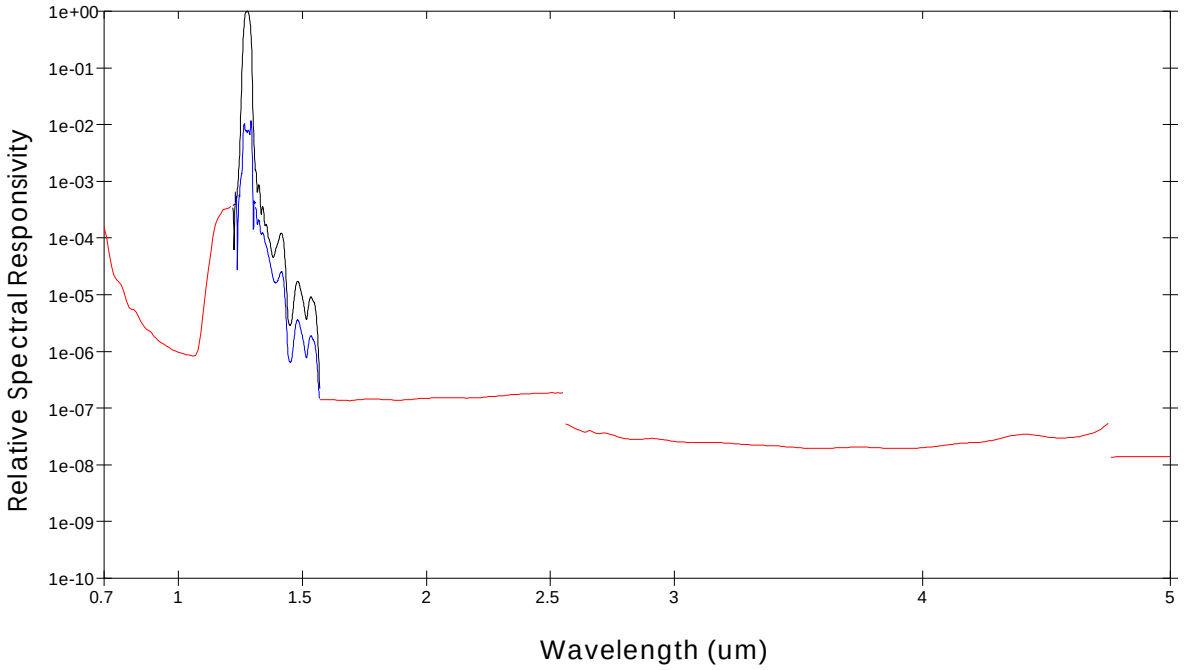

Figure 87. Out-of-band RSR - channel 10

3.5 Polarization

3.5.1 Introduction

The objective of the SABER polarization analysis was to correct the SABER relative spectral responsivity (RSR) calibration for effects of linear polarization in the Fourier transform interferometer (FTI) source and SABER response. The correction removes spectral response changes in the RSR measurements that occur due to the combined effects of source polarization and sensor polarization responsivity, and leaves only those that are true spectral intensity changes.

A generalized equation that considers both source and sensor polarization was first derived to look at polarization response correction, and is shown in Equation (21). This equation is based on Stoke's parameters and the definition of the degree and angle of linear polarization.

$$R_0 = \frac{R_M}{1 + [P_{\Re} \cdot P_S \cdot \cos(2(\alpha_{\Re} - \alpha_S))]} = \mathrm{PRC} \cdot R_M \tag{21}$$

where: PRC = polarization response correction

$$= \frac{1}{1 + [P_{\Re} \cdot P_S \cdot \cos(2(\alpha_{\Re} - \alpha_S))]}$$

R_0 = response to intensity only (sensor response units)

R_M = measured/total response signal (sensor response units)

$P_{\Re}$ = degree of linear polarization (DOLP) responsivity of the sensor

P_S = degree of linear polarization (DOLP) emitted by the source

$\alpha_{\Re}$ = angle of linear polarization (AOLP) responsivity of the sensor

α_S = angle of linear polarization (AOLP) emitted by the source

The polarization response correction (PRC) term in this equation can be explained by looking at the two extreme cases: (1) the source is completely unpolarized ($P_S = 0$) and/or the sensor is completely insensitive to polarization ($P_{\Re} = 0$). In this case there will be no polarization effects in the measured response, and the PRC is unity; (2) the source is 100% polarized ($P_S = 1$) and the sensor is 100% polarization sensitive ($P_{\Re} = 1$). When the source and sensor have the same polarization angle, the measured response (R_M) is twice the value that would result from an unpolarized source of the same intensity or an unpolarized detector with the same responsivity, resulting in a PRC of 1/2. As the difference in the polarization angle of the sensor and source approaches 45 degrees, R_M approaches the value that would result from an unpolarized source of the same intensity or an unpolarized detector with the same responsivity, and the PRC approaches 1. When the angles are 90 degrees apart, the polarization is orthogonal, R_M drops to 0, and the PRC becomes infinite.

For the SABER calibration, the sensor responsivity and source emittance parameters in Equation (21) ($P_{\Re}$, $\alpha_{\Re}$, P_S, and α_S) must be known for all wavelengths within the spectral passband of each SABER channel. The degree of linear polarization (DOLP) emitted by the source (P_S) and

the angle of linear polarization (AOLP) emitted by the source (α_S) for the Bio-Rad FTI, used in the SABER spectral calibration, were measured prior to the beginning of calibration and are discussed in Section 3.5.2.1. The DOLP responsivity of the sensor ($P_{\Re}$) and AOLP responsivity of the sensor ($\alpha_{\Re}$) were determined as part of the SABER calibration. Because the full field collimator (FFC) polarization is combined with the sensor response in this application, it is characterized as part of the sensor, and the combined results are assumed for all sensor polarization response values given in this report.

3.5.2 Polarization Measurement Equipment

The equipment used in the polarization measurements consisted of the Bio-Rad FTI, a CaF_2 and KRS-5 wire-grid polarizer (WGP), the short-wavelength-linearity integrating sphere, and an IR industries blackbody. The integrating sphere and the blackbody are both assumed to be unpolarized. The polarization characteristics of the FTI and the WGPs are given in Sections 3.5.2.1 and 3.5.2.2.

3.5.2.1 FTI Polarization Characteristics

Figures 88 and 89 show the measured DOLP and AOLP for each of the FTI beamsplitter/source combinations. These figures are overlaid with the SABER passbands. For the SABER RSR calibration, the average FTI polarization across each SABER channel varies from 1% to 6%. This is consistent with measurements made by NIST of the same model FTI. The AOLP reference for these measurements is based on an instrument looking in the FTI exit port, with zero degrees being horizontal and to the right and positive angles are in the counter clockwise direction. The average DOLP and AOLP for each SABER channel are given in Table 63.

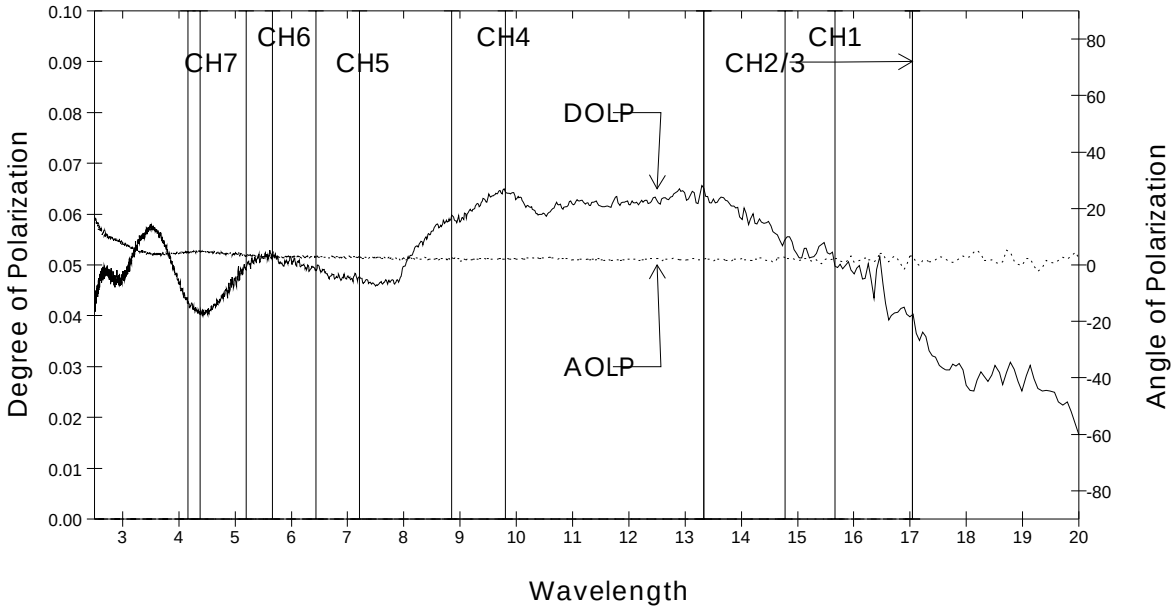

Figure 88. DOLP and AOLP emitted by FTI source 1 and KBr beamsplitter

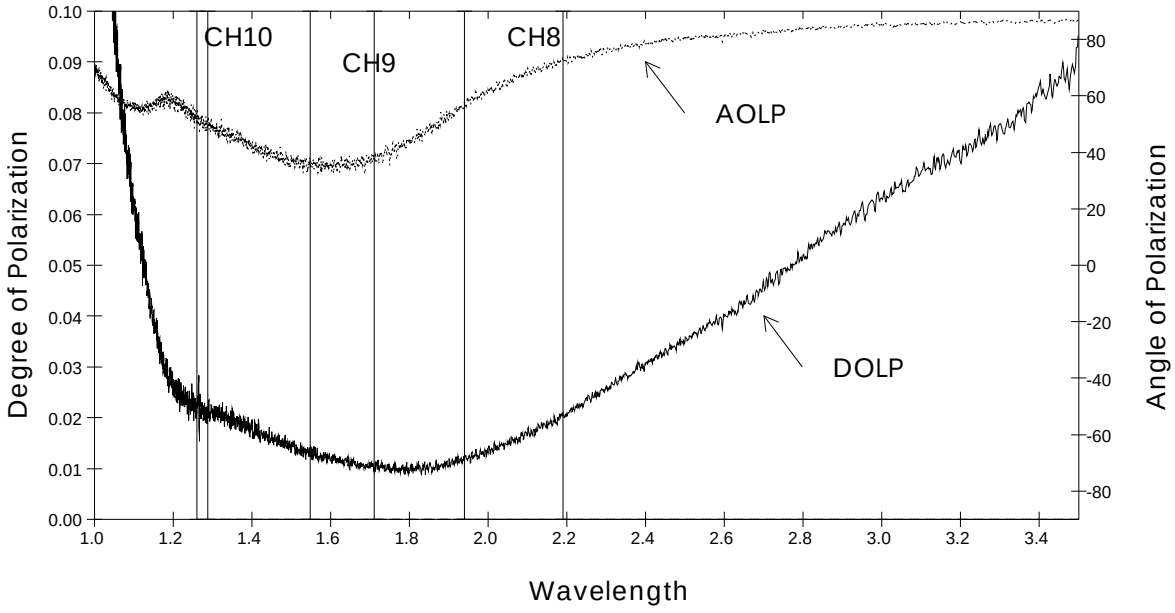

Figure 89. DOLP and AOLP emitted by FTI source 2 and quartz beamsplitter

Table 63. FTI polarization characteristics - SABER passband averages

SABER Channel	FTI Beamsplitter	FTI Source	DOLP Emitted	AOLP Emitted
1	KBr	S1-Ceramic	0.053	1.9
2	KBr	S1-Ceramic	0.054	1.9
3	KBr	S1-Ceramic	0.054	1.9
4	KBr	S1-Ceramic	0.062	2.1
5	KBr	S1-Ceramic	0.048	2.8
6	KBr	S1-Ceramic	0.051	3.2
7	KBr	S1-Ceramic	0.041	4.7
8	Quartz	S2-Tungsten	0.016	65.3
9	Quartz	S2-Tungsten	0.012	36.0
10	Quartz	S2-Tungsten	0.022	50.5

3.5.2.2 Wire-Grid Polarizer Characterization

The performance characteristics of the CaF_2 and KRS-5 wire-grid polarizers (WGPs) used in the SABER calibration were measured as a function of wavelength. The important characteristics of the polarizers are the transmittance in the axis of maximum transmittance (K1), the transmittance in the axis of minimum transmittance (K2), and the diattenuation (*D*), which is given by Equation (22).

$$D = \frac{(K_1 - K_2)}{(K_1 + K_2)} \tag{22}$$

Graphs of the WGP performance characteristics, overlaid with the SABER passbands, are given in Figures 90 and 91. The WGP average transmittance and diattenuation over the passband of each SABER channel are given in Table 64. These parameters are used in deriving the SABER/FFC polarization responsivity.

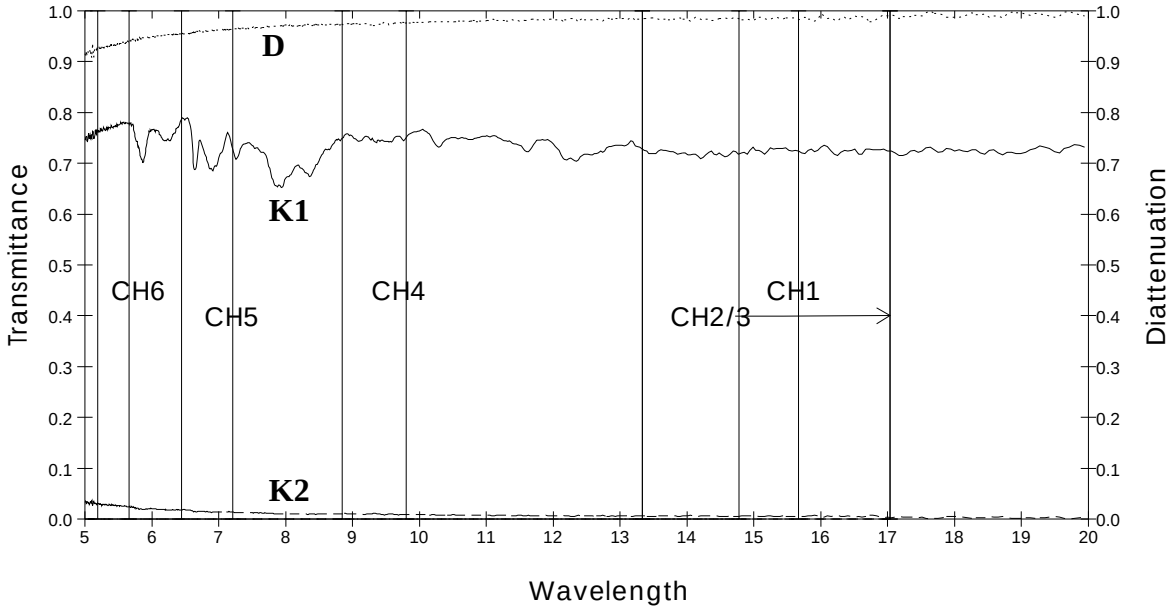

Graphed 12-JAN-99 10:51:01.836

Figure 90. KRS-5 Wire-grid polarizer (WGP) performance characteristics

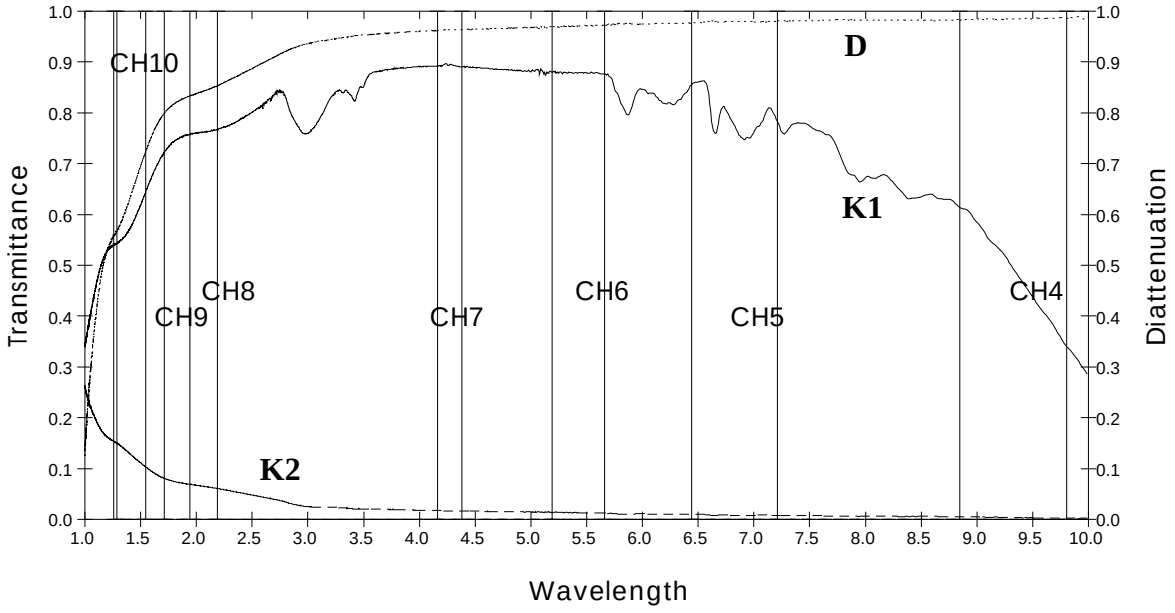

Graphed 15-JAN-99 09:21:17.109

Figure 91. CaF_2 Wire-grid polarizer (WGP) performance characteristics

Table 64. WGP performance characteristics - SABER passband averages

SABER Channel	WGP Material	K1 (Max. Trans. Axis)	K2 (Min. Trans. Axis)	D (Diattenuations)
1	KRS-5	0.7252	0.0057	0.984
2	KRS-5	0.7226	0.0056	0.985
3	KRS-5	0.7226	0.0056	0.985
4	KRS-5	0.7484	0.0096	0.975
5	CaF2	0.7978	0.0084	0.979
6	CaF2	0.8787	0.0131	0.971
7	CaF2	0.8931	0.0168	0.963
8	CaF2	0.7621	0.0651	0.843
9	CaF2	0.6862	0.0908	0.766
10	CaF2	0.5417	0.1516	0.563

3.5.3 Polarization Equations

The DOLP (P) and AOLP (α) are derived from the Stoke's parameters as given in Equation (23) (Kliger et al., 1990). When the source is unpolarized and the measurement angles of a WGP-polarization generator are separated by 60 degrees, the Stoke's parameters for the sensor linear polarization responsivity are given in Equation (24). The DOLP responsivity for the sensor ($P_{\Re}$) and the AOLP responsivity ($\alpha_{\Re}$), shown in Equation (25), can be derived directly from the sensor response by substituting Equation (24) into Equation (23). The angle reference for these measurements is zero degrees in the direction of R_1 and positive angles are in the direction from R_1 to R_2.

$$P = \frac{\sqrt{S_1 + S_2}}{S_0}$$
$$\alpha = \frac{1}{2}\text{atan}\left(\frac{S_2}{S_1}\right) \tag{23}$$

where:
P = degree of linear polarization (DOLP - unitless)
α = angle of linear polarization (AOLP - degrees)
S_0 = Stoke's parameter intensity term
S_1 = Stoke's parameter term horizontal/vertical
S_2 = Stoke's parameter term +45/-45

$$S_0 = \frac{2}{3}\left(\frac{1}{K_1 + K_2}\right)(R_1 + R_2 + R_3)$$
$$S_1 = \frac{2}{3}\left(\frac{1}{K_1 - K_2}\right)(2R_1 - R_2 - R_3)$$
$$S_2 = \frac{2}{3}\left(\frac{1}{K_1 - K_2}\right)(\sqrt{3}R_2 - \sqrt{3}R_3) \tag{24}$$

where:
K_1 = WGP transmittance in the axis of maximum transmittance
K_2 = WGP transmittance in the axis of minimum transmittance
R_1 = sensor response at WGP reference (0 degrees)
R_2 = sensor response at WGP = 60 degrees
R_3 = sensor response at WGP = 120 degrees

$$P_{\Re} = \left(\frac{2}{D}\right)\left(\frac{\sqrt{(R_1^2 + R_2^2 + R_3^2) - (R_1R_2 + R_1R_2 + R_2R_3)}}{R_1 + R_2 + R_3}\right)$$
$$\alpha_{\Re} = \frac{1}{2}\text{atan}\left(\frac{\sqrt{3}(R_2 - R_3)}{2R_1 - R_2 - R_3}\right) \times \left(\frac{180}{\pi}\right) \tag{25}$$

where:
$P_{\Re}$ = sensor degree of linear polarization responsivity (unitless)
$\alpha_{\Re}$ = sensor angle of linear polarization responsivity (degrees)
D = WGP diattenuation

The uncertainty of $P_{\Re}$ and $\alpha_{\Re}$ can be computed based on the uncertainty of the sensor response according to the NIST guidelines (NIST, 1994) using Equations 26 and 27.

$$\sigma_{P_{\Re}} = \sqrt{\left(\frac{\partial P_{\Re}}{\partial R_1}\sigma_{R_1}\right)^2 + \left(\frac{\partial P_{\Re}}{\partial R_2}\sigma_{R_2}\right)^2 + \left(\frac{\partial P_{\Re}}{\partial R_3}\sigma_{R_3}\right)^2}$$

$$= \left(\frac{2\sqrt{3}}{D}\right)\left(\frac{1}{R_1 + R_2 + R_3}\right)\sqrt{\frac{(R_1^2 + R_2^2 + R_3^2) - (R_1R_2 + R_1R_2 + R_2R_3)}{(R_1 + R_2 + R_3)^2} + \frac{1}{2}} \times \sigma_R$$

$$= \left(\frac{2}{\sqrt{3}}\right)\left(\frac{1}{K_1 + K_2}\right)\left(\frac{1}{I_S}\right)\sqrt{P_{\Re}^2 + \frac{2}{D^2}} \times \sigma_R \qquad (26)$$

$$\sigma_{\alpha_{\Re}} = \sqrt{\left(\frac{\partial \alpha_{\Re}}{\partial R_1}\sigma_{R_1}\right)^2 + \left(\frac{\partial \alpha_{\Re}}{\partial R_2}\sigma_{R_2}\right)^2 + \left(\frac{\partial \alpha_{\Re}}{\partial R_3}\sigma_{R_3}\right)^2}$$

$$= \frac{\sqrt{6}}{4}\frac{1}{\sqrt{(R_1^2 + R_2^2 + R_3^2) - (R_1R_2 + R_1R_2 + R_2R_3)}} \times \sigma_R \times \frac{180}{\pi}$$

$$= \frac{\sqrt{6}}{4}\left(\frac{1}{I_S P_{\Re}}\right)\left(\frac{1}{K_1 - K_2}\right) \times \sigma_R \times \frac{180}{\pi} \qquad (27)$$

where: $\sigma_{P_{\Re}}$ = uncertainty in sensor DOLP responsivity (unitless)

$\sigma_{\alpha_{\Re}}$ = uncertainty in sensor AOLP responsivity (degrees)

σ_R = sensor response uncertainty

It is assumed that $\sigma_R = \sigma_{R_1} = \sigma_{R_2} = \sigma_{R_3}$.

The uncertainty in the sensor DOLP responsivity in Equation (26) can be expressed as a percentage of the DOLP responsivity using Equation (28).

$$\sigma_{P_{\Re}}(\%) = \left(\frac{2}{\sqrt{3}}\right)\left(\frac{1}{K_1 + K_2}\right)\sqrt{\frac{2}{D^2 P_{\Re}^2} + 1} \times \sigma_R(\%) \qquad (28)$$

where: $\sigma_{P_{\Re}}(\%)$ = uncertainty in sensor DOLP responsivity (%)

$\sigma_R(\%) = \frac{\sigma_R}{I_S} \times 100\%$

3.5.4 SABER/FFC Polarization Response Data Sets

Several polarization data sets were collected during the SABER calibration. The data presented in this report were collected with a wire-grid polarizer (WGP) placed between a blackbody and the FFC entrance port, and is documented in "SABER Ground Calibration Test and Summary Results" (SDL/98-059). Channels 8, 9 and 10 had an integrating sphere placed between the blackbody and the WGP to further increase the spatial stability of the measurement configuration. These polarization data are referred to as blackbody polarization data.

Polarization data were also collected using the FTI as the source. These data have been analyzed, but the spatial characteristics of the source are not stable enough to accurately characterize polarization responses less than 1%. Because the SABER/FFC polarization is generally less than 1%, only the blackbody polarization data are presented.

3.5.5 SABER/FFC Polarization Data Analysis

The blackbody polarization data were collected by manually reading and recording the mean and standard deviation of 100 samples using *sabertd* (SABER real time monitor display software). Measurements were obtained at WGP rotation angles of 0, 60, 120, 180, 240 and 300 degrees. These measurement were repeated for three complete revolutions of the WGP. Dark offset and noise measurements were also collected before and after each WGP measurement set by closing the FFC aperture and manually recording the response of the SABER channel being tested. Data from these measurements were used to derive the SABER response and uncertainty required to characterize the SABER/FFC polarization response.

3.5.5.1 Raw Response

The responses R_1, R_2, and R_3 in the previous equations are the offset corrected response for WGP angles of 0, 60 and 120 degrees, respectively. They were calculated for each channel using Equation (29).

$$R_1 = \frac{1}{3}\sum_{r=1}^{3}\left\{\frac{(R_{r,0} - \mathrm{DO}) + (R_{r,180} - \mathrm{DO})}{2}\right\}$$

$$R_2 = \frac{1}{3}\sum_{r=1}^{3}\left\{\frac{(R_{r,60} - \mathrm{DO}) + (R_{r,240} - \mathrm{DO})}{2}\right\}$$

$$R_3 = \frac{1}{3}\sum_{r=1}^{3}\left\{\frac{(R_{r,120} - \mathrm{DO}) + (R_{r,300} - \mathrm{DO})}{2}\right\} \quad (29)$$

where:
R_1 = sensor response at WGP reference (0 degrees)
R_2 = sensor response at WGP = 60 degrees
R_3 = sensor response at WGP = 120 degrees
$R_{r,\theta}$ = raw response as a function of WGP repetition and angle, θ
r = WGP revolution (3 complete revolution repetitions)
DO = dark offset

Table 65 gives the response values for R_1, R_2, and R_3 calculated by substituting measured values into Equation (29).

Table 65. SABER response at each WGP rotation

SABER Channel	R_1	R_2	R_3
1	774.6	773.8	781.6
2	874.9	874.4	883.3
3	839.7	836.8	843.5
4	715.2	713.8	714.6
5	2429.2	2423.1	2429.5
6	1190.2	1219.2	1196.9
7	618.3	602.2	590.7
8	1047.7	1051.0	1052.7
9	215.1	215.5	213.9
10	533.8	537.4	536.3

3.5.6 Response Noise and Uncertainty

The response uncertainty for R_1, R_2, and R_3 measurements are assumed equal. The uncertainties were derived using the 100 sample standard deviation reported on the SABER real-time display and raw response values shown in Table 65.

The raw response uncertainty for each SABER channel was estimated using Equation (30). This uncertainty represents the short-term temporal measurement errors for each individual measurement.

$$\sigma_r = \frac{\sqrt{\bar{\sigma}_{r,\theta}^2 + \sigma_{DN}^2}}{\sqrt{100}} \tag{30}$$

where:
σ_r = raw response uncertainty
$\bar{\sigma}_{r,\theta}$ = mean of response standard deviation over all rotation angles
σ_{DN} = dark noise (dark measurement standard deviation)
$\sqrt{100}$ = square root of the number of samples in the response means

The standard deviation of repeated measurements for each polarizer angle was used to quantify medium-term temporal uncertainty. This uncertainty, which is a measurement of the configuration stability during a data collection period, was computed using Equation (31).

$$\sigma_t = \frac{1}{6}(\sigma_0 + \sigma_{60} + \sigma_{120} + \sigma_{180} + \sigma_{240} + \sigma_{300}) \tag{31}$$

where:
σ_t = medium-term temporal uncertainty
σ_θ = $std(R_{1,\theta}, R_{2,\theta}, R_{3,\theta})$
$std(\ )$ = standard deviation of bracketed numbers
$R_{r,\theta}$ = raw response as a function of WGP repetition and angle
r = WGP revolution (3 complete revolution repetitions)
θ = WGP rotation angle

In theory, the response to WGP angles separated by 180 degrees should provide identical results. Measured differences are treated as uncertainty. This uncertainty, termed spatial uncertainty, was computed using Equation (32). Spacial uncertainty measures the spatial response error that results from a 180 degree rotation of the WGP.

$$\sigma_s = \frac{1}{3}(\sigma_{0,\,180} + \sigma_{60,\,240} + \sigma_{120,\,300}) \tag{32}$$

where: σ_s = spatial response uncertainty

$$\sigma_{0,\,180} = \frac{1}{3}[std(R_{1,\,0},R_{1,\,180}) + std(R_{2,\,0},R_{2,\,180}) + std(R_{3,\,0},R_{3,\,180})]$$

$$\sigma_{60,\,240} = \frac{1}{3}[std(R_{1,\,60},R_{1,\,240}) + std(R_{2,\,60},R_{2,\,240}) + std(R_{3,\,60},R_{3,\,240})]$$

$$\sigma_{120,\,300} = \frac{1}{3}[std(R_{1,\,120},R_{1,\,300}) + std(R_{2,\,120},R_{2,\,300}) + std(R_{3,\,120},R_{3,\,300})]$$

The overall uncertainty for each SABER channel was computed as the root-sum-square (RSS) for the results from the three uncertainty terms shown in Equations 30, 31, and 32. The uncertainties from each of the individual uncertainty terms and the combined uncertainty are given in Table 66 for each SABER channel.

Table 66. Polarization response uncertainty

SABER Channel	Raw Response (σ_r)*	Medium-Term Temporal (σ_t)*	Spatial (σ_s)*	Total (σ_R)*
1	0.060	0.715	0.438	0.840
2	0.045	0.833	0.172	0.852
3	0.063	0.731	0.174	0.754
4	0.046	0.652	0.257	0.703
5	0.172	2.962	2.151	3.665
6	0.059	1.642	0.413	1.694
7	0.132	0.833	1.150	1.426
8	0.095	3.504	4.982	6.092
9	0.051	1.642	0.780	1.819
10	0.076	5.311	1.382	5.488

* All units are in sensor response counts

3.5.7 SABER/FFC Polarization Response Results

The SABER/FFC polarization response and uncertainty were computed using Equations (25) and (28) and using values in Tables 65 and 66. The SABER/FFC polarization response and uncertainty for each SABER channel are given in Table 67.

Table 67. SABER/FFC polarization response and uncertainty

SABER Channel	DOLP Responsivity ($P_{\Re}$)	DOLP Responsivity Uncert ($\sigma_{P_{\Re}}$)	AOLP Responsivity ($\alpha_{\Re}$)	AOLP Responsivity Uncert ($\sigma_{\alpha_{\Re}}$)
1	0.0064	0.0009	-57.4	4.0
2	0.0066	0.0008	-58.7	3.5
3	0.0046	0.0007	-47.2	4.6
4	0.0011	0.0008	-16.0	20.6
5	0.0018	0.0013	-31.5	20.5
6	0.0150	0.0013	66.4	2.3
7	0.0275	0.0020	12.3	2.1
8	0.0033	0.0056	-80.0	48.5
9	0.0058	0.0090	36.9	44.2
10	0.0071	0.0149	81.5	60.2

3.5.8 Results and Conclusions

The percent error that occurs in the SABER RSR measurements if the polarization response correction (PRC) is not applied can be computed from Equation (21) and is given in Equation (33).

$$\sigma_{RSR_{Polar}}(\%) = \frac{R_0 - R_M}{R_0} \times 100\% = [P_{\Re} \cdot P_S \cdot \cos(2(\alpha_{\Re} - \alpha_S))] \times 100\% \quad (33)$$

where: $\sigma_{RSR_{Polar}}(\%)$ = RSR errors due to polarized signal response

The other parameters in Equation (33) are defined in Equation (21).

Because the SABER/FFC polarization response angle has such a high uncertainty, the worst-case effects of polarization can be estimated by setting the term $\cos(2(\alpha_{\Re} - \alpha_S))$ to its maximum possible value (1), then computing the worst-case percent error due to polarization as $\sigma_{RSR_{Pola}}(\%) = P_{\Re} \cdot P_S \times 100\%$. Using the FTI polarization characteristics given in Table 63 and the SABER/FFC polarization responses given in Table 67, the worst-case percent error in the RSR results are given in Table 68.

Table 68. RSR Measurement Uncertainty due to polarization

SABER Channel	DOLP Emitted by FTI (P_S)	SABER/FFC DOLP Responsivity ($P_{\Re}$)	Worst-Case RSR Errors Due to Polarized Signal Response ($\sigma_{RSR_{Polar}}(\%)$)
1	0.053	0.0064	0.034%
2	0.054	0.0066	0.036%
3	0.054	0.0046	0.025%
4	0.062	0.0011	0.007%
5	0.048	0.0018	0.009%
6	0.051	0.0150	0.077%
7	0.041	0.0275	0.113%
8	0.016	0.0033	0.005%
9	0.012	0.0058	0.007%
10	0.022	0.0071	0.016%

The results shown in Table 68 show that the effect of polarization on the RSR measurements is small compared to the overall RSR measurement uncertainty, and can be included as an RSR measurement uncertainty without significantly affecting the overall measurement uncertainty.

3.6 Total RSR Uncertainty for Ground Calibration

The relative uncertainty of IFC channel radiance, $\sigma_{RSR,\,tot}$, due to the uncertainty of relative spectral response, was calculated using Equation (34).

$$\sigma_{RSR,\,tot} = \sqrt{(\sigma_{RSR})^2 + (\sigma_{oob,\,noiseflr})^2 + (\sigma_{RSR_{Polar}})^2} \tag{34}$$

where
$\sigma_{RSR,\,tot}$ = uncertainty of channel radiance due to total RSR uncertainty (%)
σ_{RSR} = uncertainty of channel radiance due to in-band and out-of-band RSR measurement uncertainty (%)
$\sigma_{oob,\,noiseflr}$ = uncertainty of channel radiance due to out-of-band RSR measurement noise floor (%)
$\sigma_{RSR_{Polar}}$ = uncertainty of RSR due to polarized signal response (%)

The uncertainty of channel radiance due to in-band and out-of-band RSR measurement uncertainty, σ_{RSR}, was calculated by computing GSE blackbody effective radiance. Equation (7) was used to calculate the effective blackbody radiance using wavelength integration limits given in Table 22. The GSE low temperature blackbody radiance was first calculated using the measured relative spectral responsivity (Section 3.3). Then a new GSE low temperature blackbody radiance was calculated with the RSR set equal to the addition of the measured RSR and its uncertainty (Section 3.3). The percent differences in these values for each channel are shown graphically in Figure 92 as a function of blackbody temperature. The RSR uncertainty was estimated at a blackbody temperature of 250 K for channels 1 to 7, 460 K for channel 8, 595 K for channel 9, and 620 K for channel 10. These uncertainties range from 1% to 2.7%, depending on channel. These blackbody temperatures were chosen because they give response levels that are similar in magnitude to nominal IFC source settings.

The uncertainty of channel radiance due to out-of-band RSR measurement noise floor, $\sigma_{oob,\,noiseflr}$, was also calculated by computing GSE blackbody effective radiances. The GSE blackbody radiance was first calculated using the measured relative spectral responsivity (Section 3.3). Then a new GSE low temperature blackbody radiance was calculated using the measured relative spectral responsivity with additional spectral regions that were dominated by measurement noise floor (Section 3.3). For these spectral regions, the noise floor was assumed to be the out-of-band spectral responsivity. The percent difference in these values for each channel are shown graphically in Figure 93 as a function of blackbody temperature. These graphs show the uncertainty of channel radiance due to out-of-band RSR measurement noise floor to be less than 0.1% for all channels and blackbody temperatures.

For RSR measurements, polarized channel response is due to (1) polarization of the interferometer output, (2) polarization due to full field collimator optics, and (3) polarization of SABER optics. Because blackbody sources and SABER atmospheric emissions do not contain polarization, the unpolarized SABER RSR is needed for calibration and on-orbit data reduction. The RSR uncertainty due to polarized signal response, $\sigma_{RSR_{Polar}}$, is the uncertainty of the ground cali-

bration RSR measurements due to SABER polarization responsivity. Polarization and RSR uncertainty due to polarized signal response is discussed further in Section 3.5. These results show RSR uncertainty due to out-of-band RSR measurement noise floor to be less than 0.1% for all channels. This results in a worst case integrated band radiance uncertainty of 0.1%. Because this uncertainty is sufficiently small, the RSR uncertainty due to polarized signal response, $\sigma_{RSR_{Polar}}$, is set to 0.1%.

Table 69 gives individual uncertainty terms and the combined channel radiance uncertainty due to total RSR uncertainty, $\sigma_{RSR,\,tot}$, calculated using Equation (34). The combined uncertainty values range from 1% to 2.7%, depending on channel.

Table 69. Channel radiance uncertainty due to out-of-band RSR uncertainty

Channel	σ_{RSR} (%)	$\sigma_{oob,\,noiseflr}$ (%)	$\sigma_{RSR_{Polar}}$ (%)	$\sigma_{RSR,\,tot}$ (%)
1	1.56	0.1	0.1	1.57
2	1.94			1.95
3	1.72			1.73
4	2.43			2.43
5	0.99			1.00
6	2.72			2.72
7	1.47			1.48
8	1.89			1.90
9	1.79			1.80
10	1.17			1.18

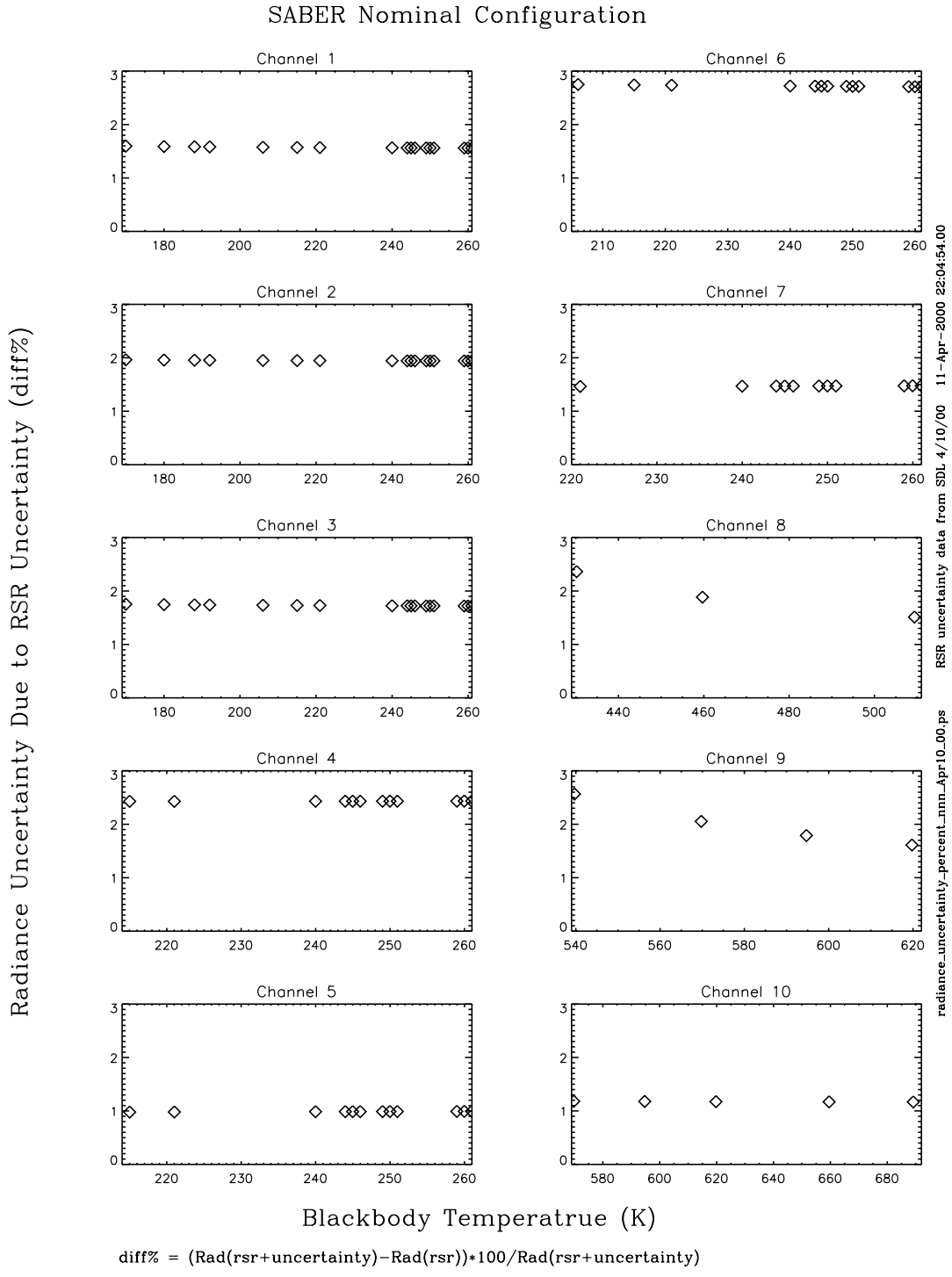

Figure 92. Uncertainty of blackbody radiance due to RSR measurement uncertainty

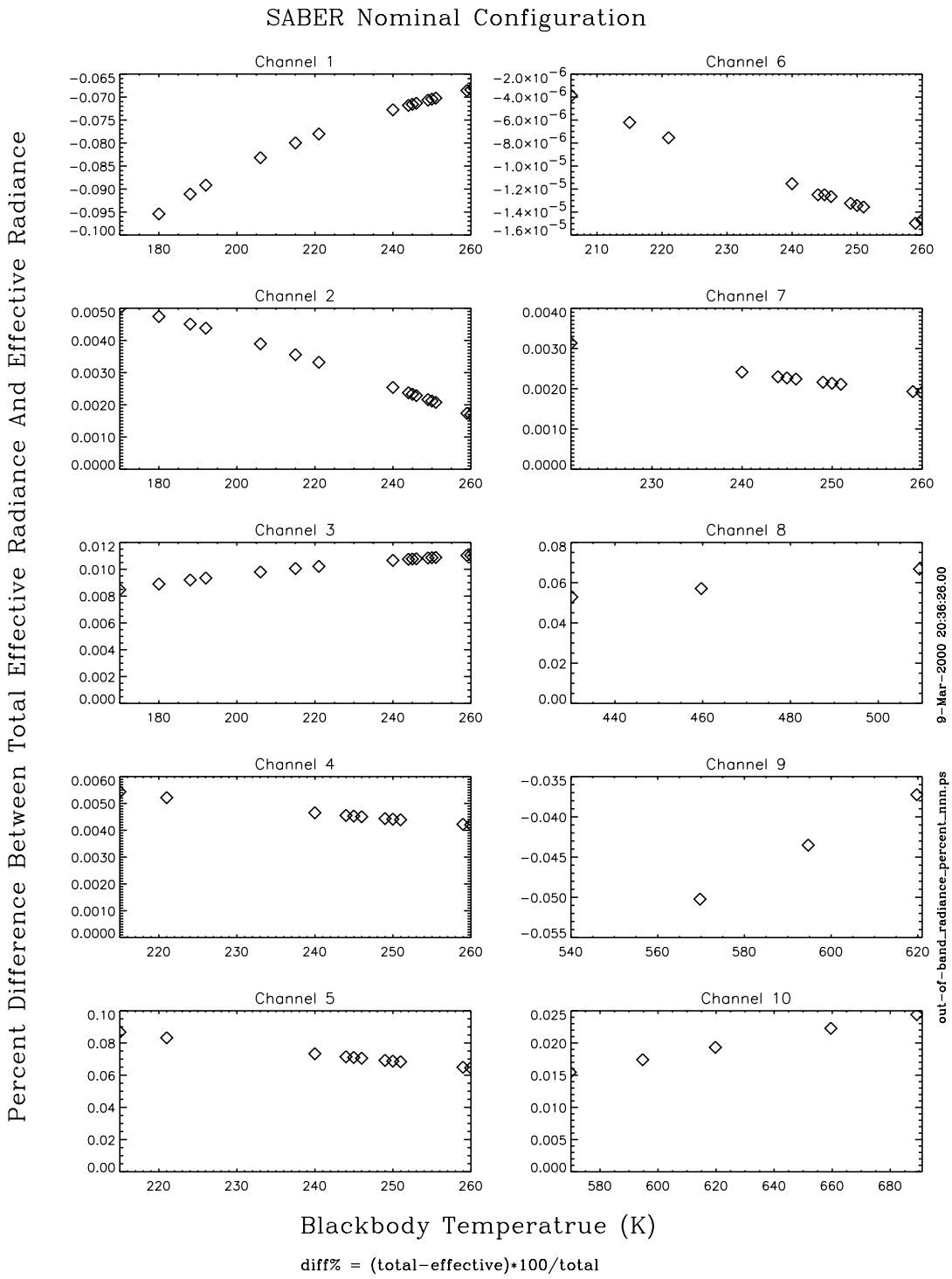

Figure 93. Uncertainty of blackbody radiance due to out-of-band RSR measurement noise floor

3.7 Instantaneous Field of View (IFOV)

The SABER instrument in-scan IFOV requirement is 2 km full-width at half-maximum (FWHM) at 60 km earthlimb tangent height. The actual value of this parameter was determined from data collected during ground IFOV calibration tests and are documented in static and dynamic IFOV data collection procedures contained in "SABER Ground Calibration and Preliminary Results" (SDL/98-059). Angular results obtained from these measurements were converted to tangent height altitude in units of km assuming a 6367-km earth radius and a 625-km orbital altitude.

A blackbody located behind a small slit aperture at the focus of the full field collimator was used to simulate SABER's point response. The slit length was orientated parallel to the length of the detectors and was approximately 1/10 the length of the detectors. Theodolite measurements were used to verify this slit orientation prior to IFOV measurements.

The full field collimator pointing mirror was used to position the source in the cross-scan direction, and the SABER instrument scan mirror was used to scan the source in the in-scan direction. A total of 31 cross-scan positions with a range of ± 15 mrad and a resolution of 1 mrad were obtained for each IFOV measurement. In addition, different neutral density filters were placed in front of the source to expand the dynamic range of the measurement and identical scans using a blank position in the filter wheel were used to make chamber background measurements.

3.7.1 Static Instantaneous Field-of-View (IFOV)

The static instantaneous field-of-view data collection procedure provides up and down scan data at scan speeds that are a factor of 4 slower than the nominal scan speed. This is to reduce any variation in the IFOV profile for different scan directions. Some variation in the uncorrected IFOV curve may occur as a function of scan direction because of the low pass filter in the instrument signal path. However, these effects can be largely removed by data processing, as explained in Section 3.11.

Data from the static field-of-view data collection procedure were background, gain mode, linearity, and low-pass filter corrected before being plotted to show the in-scan IFOV of the instrument. Up and down scans were separately integrated in the cross-scan direction and peak normalized to generate 1-dimensional plots of IFOV response for each scan direction. A linear-scale plot of the IFOV for each channel is shown in the upper part of Figure 94, while a log-scale plot of the same data is shown in the lower half.

Each plot shows separate curves for up and down scans as dotted and solid lines, respectively. The curves for the different scan directions are indistinguishable. The log-scale plots show near angle scatter composed of optical scatter or electrical cross-talk from areas of the focal plane other than the SABER channel under test. A qualitative investigation of near angle scatter is made in Section 3.7.4.1.

The FWHM of the IFOV for each channel was determined by calculating the mean IFOV response for up and down scans together, and determining the width of the central lobe at half the peak value. The resulting FWHM IFOV for each channel is listed in Table 70. The FWHM IFOV

at 60 km tangent height varies between 1.63 km for channel 3 and 2.10 km for channel 7. There are 7 channels with a 60 km tangent height FWHM IFOV less than the 2 km requirement, while 3 channels (4, 6, and 7) each have a field of view covering slightly greater than 2 km at 60 km tangent height. The uncertainties of the FWHM IFOV values listed in Table 70 were determined by computing the RSS of one-half the difference in the FWHM IFOV calculated using up and down scans separately, and the full-field collimator aperture size and image quality uncertainties.

Table 70. In-scan fields of view (static FWHM, 60 km tangent height)

Channel #	FWHM IFOV		Uncertainty
	degrees	km, at 60 km tangent height	km, at 60 km tangent height
1	0.037	1.79	0.07
2	0.035	1.69	0.07
3	0.034	1.63	0.07
4	0.041	2.03	0.06
5	0.038	1.86	0.06
6	0.041	2.01	0.06
7	0.044	2.10	0.06
8	0.042	1.98	0.06
9	0.042	1.98	0.06
10	0.040	1.87	0.06

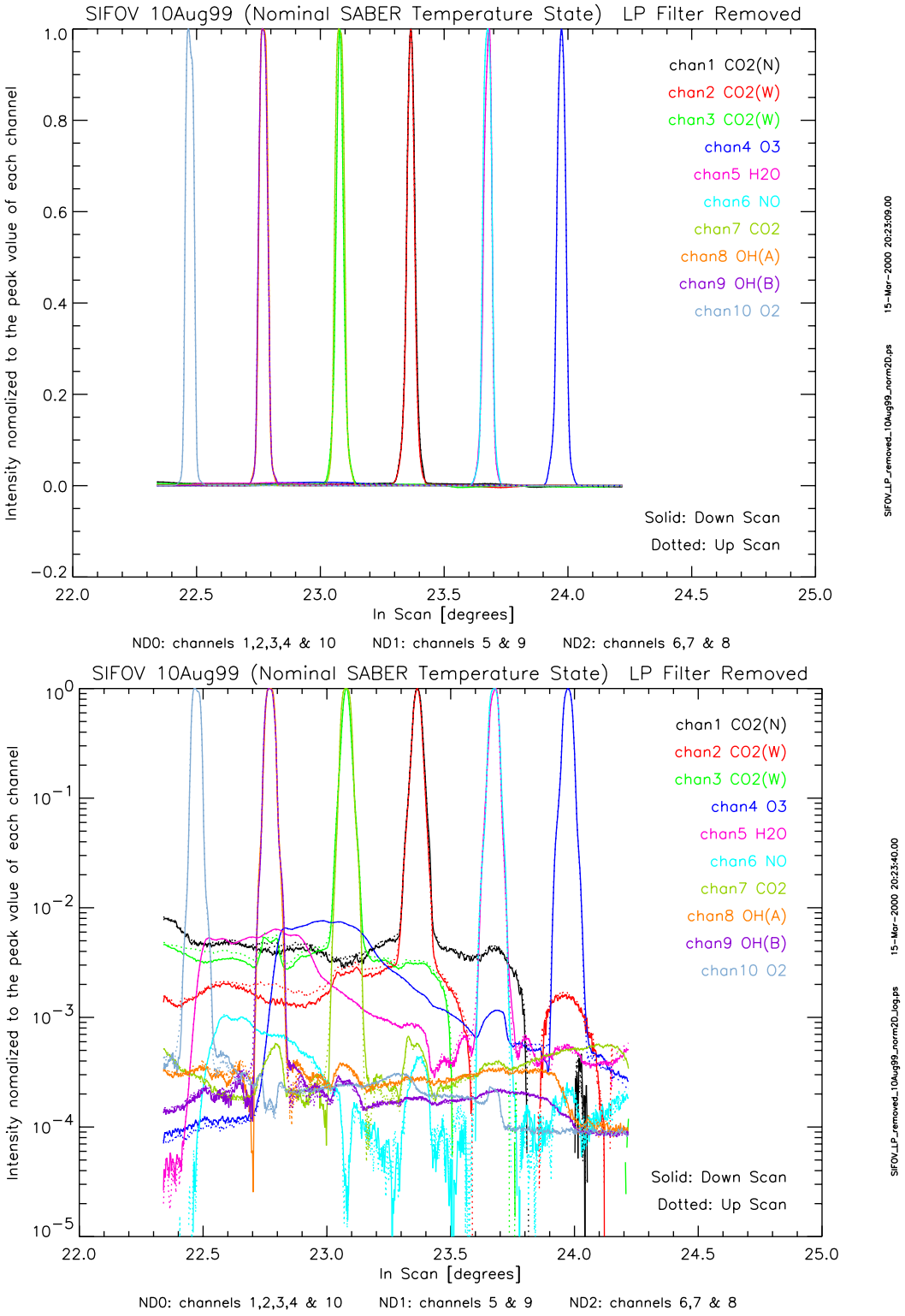

Figure 94. Static in-scan IFOV

3.7.2 Dynamic Instantaneous Field-of-View (IFOV)

The dynamic instantaneous field-of-view data collection procedure provides up and down scan data at nominal on-orbit scan speed. Any dependence of IFOV on scan direction is likely to be more significant in these data than in the static IFOV measurements. Dynamic IFOV scans were collected at instrument pointing angles corresponding to nominal on-orbit tangent heights of 30, 60, and 130 km.

Data from the dynamic field-of-view data collection procedure were background, gain mode, linearity, and low-pass filter corrected before being plotted to show the in-scan dynamic IFOV of the instrument. Up and down scans were separately integrated in the cross-scan direction and peak normalized to generate 1 dimensional plots of IFOV response for each scan direction.

Linear-scale plots of the dynamic IFOV for each channel for each tangent height are shown in the upper half of Figures 95 to 97. Log-scale plots are shown in the second graph in each figure. Each plot shows separate curves for up and down scans as dotted and solid lines, respectively. There are no significant differences in the corrected IFOV shape between up and down scans.

The log-scale plots shown in Figures 95 to 97 show near angle scatter similar to that observed in the static IFOV data. A qualitative investigation of this near angle scatter is given in Section 3.7.4.1.

The FWHM IFOV at tangent heights of 30, 60, and 130 km was determined for each channel by calculating the width at half-maximum of the mean of the up and down scan IFOV curves shown in Figures 95 to 97. No visible variation in FWHM IFOV as a function of scan angle or direction was observed. The mean FWHM IFOV at 60 km tangent height is listed for each channel in both degrees and km in Table 71. The uncertainty of the 60 km FWHM IFOV is determined from the RSS of one-half the difference in the FWHM IFOV calculated using up and down scans separately at the 60 km tangent height, and the full-field collimator aperture size and image quality uncertainties.

Overall, the FWHM of the 60 km tangent height IFOV measured using the dynamic IFOV data is comparable to the 2 km requirement. There are 5 channels having a measured FWHM IFOV less than this value, and 5 channels that exceed this value. All FWHM dynamic IFOV measurements are within +0.13 km or -0.06 km of the 2 km nominal value at 60 km tangent height.

Table 71. In-scan fields of view (dynamic FWHM, 60 km tangent height)

Channel #	FWHM IFOV		Uncertainty
	degrees	km, at 60 km tangent height	km, at 60 km tangent height
1	0.040	1.94	0.083
2	0.040	1.94	0.078
3	0.041	1.96	0.084
4	0.043	2.13	0.064
5	0.040	1.96	0.066
6	0.043	2.11	0.070
7	0.044	2.11	0.063
8	0.043	2.03	0.061
9	0.043	2.03	0.068
10	0.042	1.96	0.066

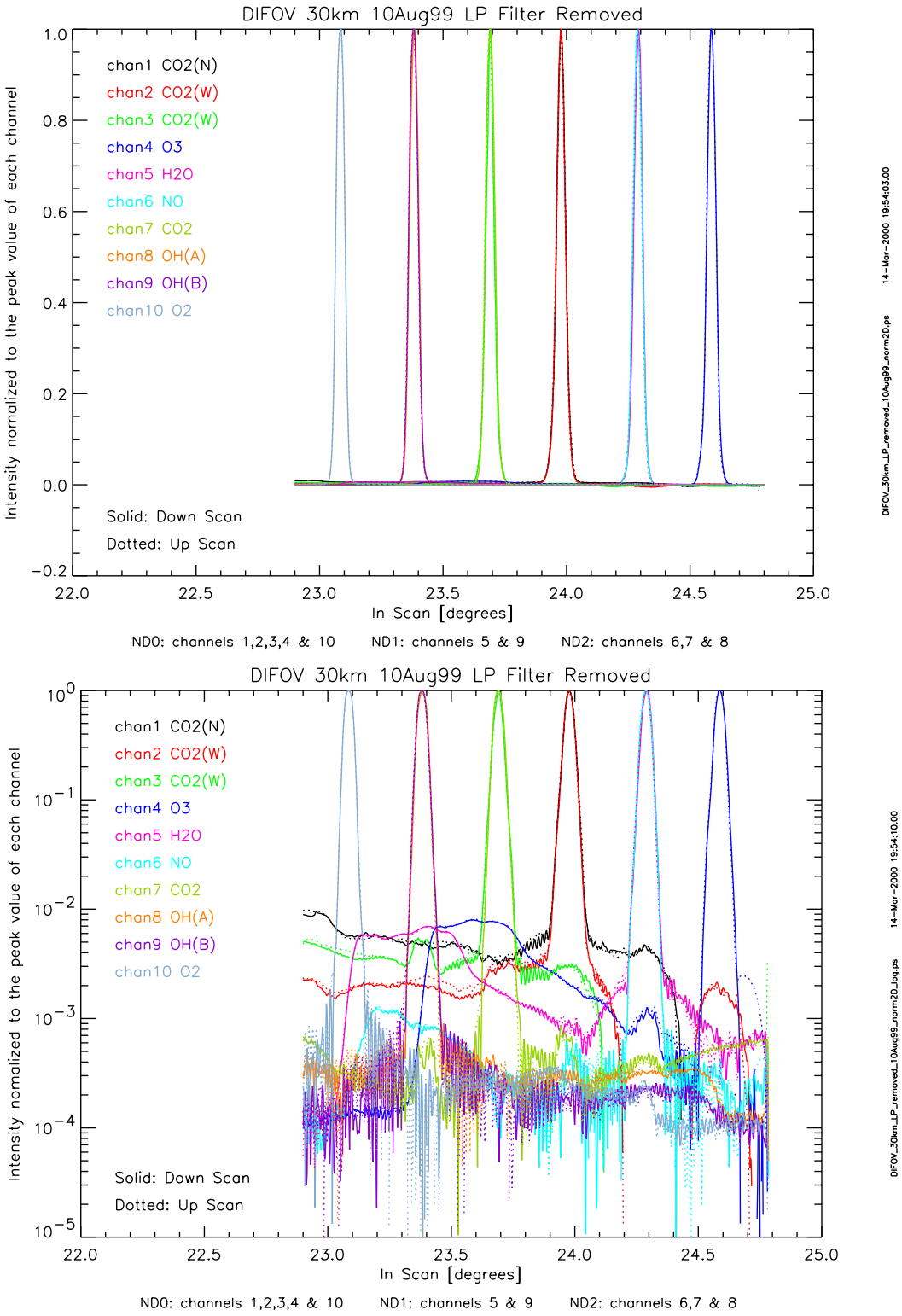

Figure 95. Dynamic in-scan IFOV (30 km tan. ht.)

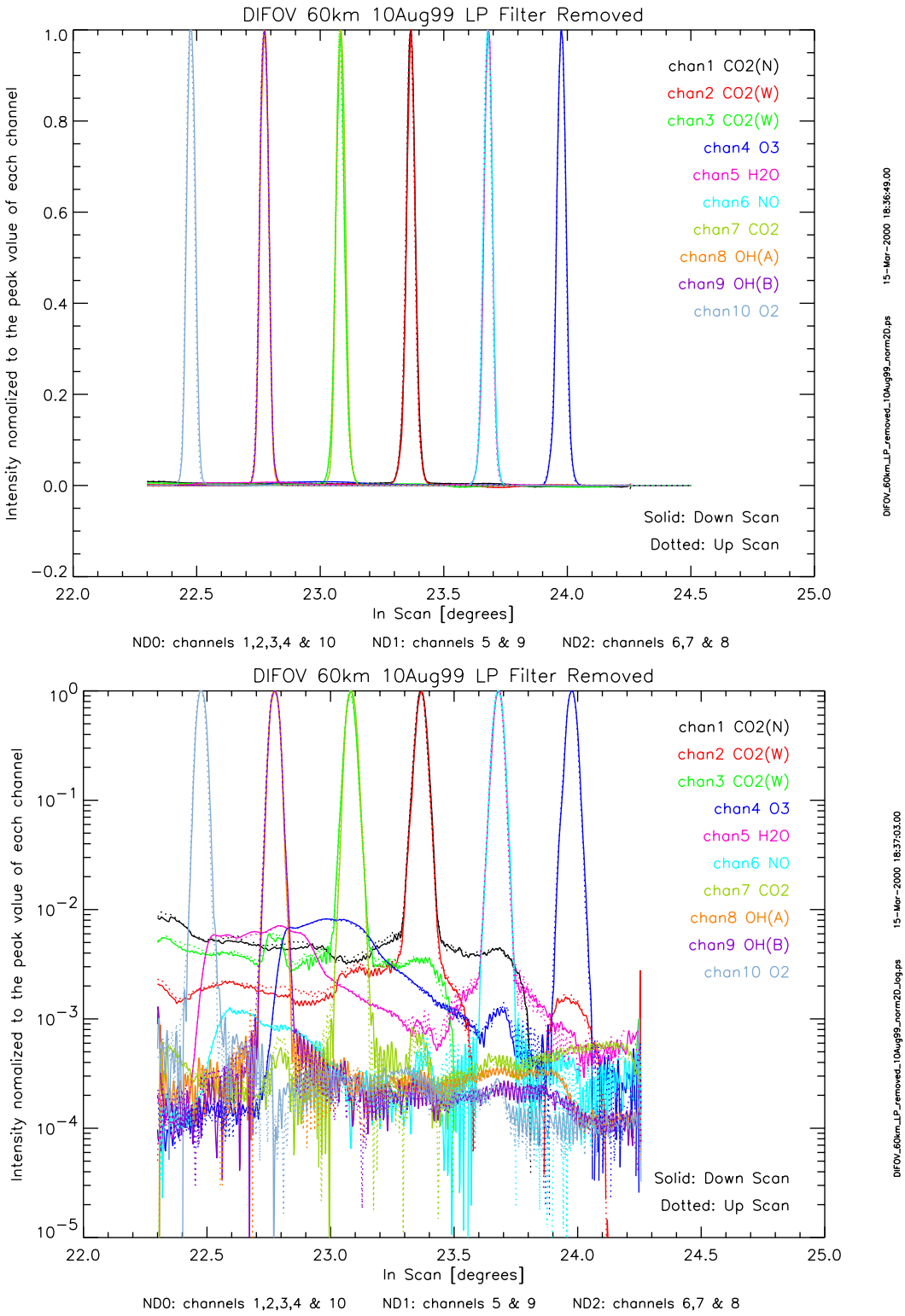

Figure 96. Dynamic in-scan IFOV (60 km tan. ht.)

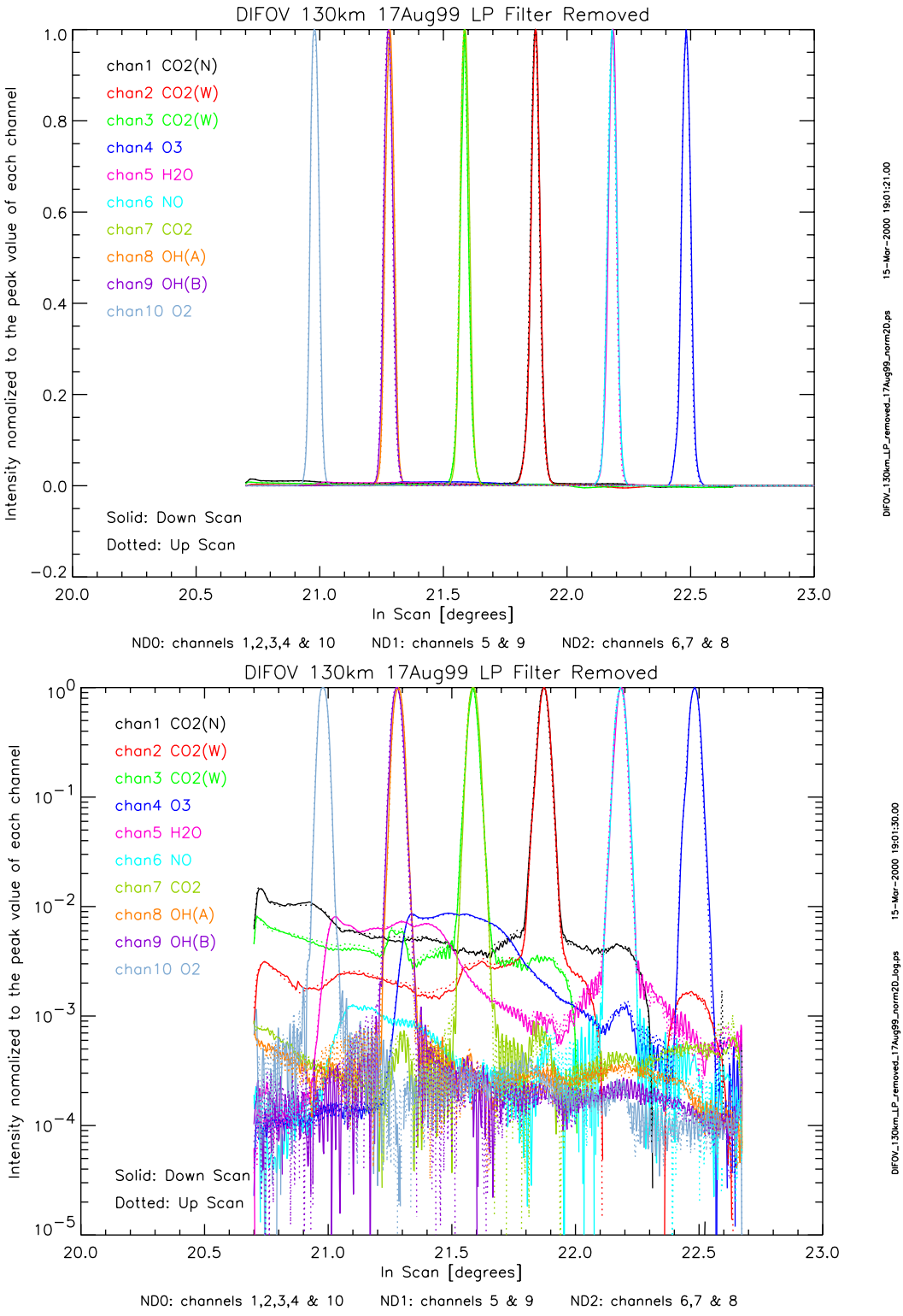

Figure 97. Dynamic in-scan IFOV (130 km tan. ht.)

3.7.3 Summary of IFOV Analysis

The FWHM of the 60 km tangent height IFOV measured using the nominal scan velocity (dynamic IFOV) measurements is on average 0.12 km larger than the value measured using the slower scan speed measurements acquired in the static IFOV measurements. This is a difference of about 6% of the nominal 2 km field of view at this tangent height. The difference may be a remaining artifact of the low-pass filter in the instrument signal path. The 60 km tangent height IFOV measurements made using the slower scan speed are in general slightly less than the 2 km requirement, verifying that the 2 km requirement is met.

3.7.4 Channel Object Space Positions

Intensity plots as a function of in-scan and cross-scan angle were generated to show the relative orientation of each detector on the focal plane. Figure 98 shows a 60 km static IFOV contour plot of the focal plane where 10, 50, and 90 percent response contour lines are displayed for each channel. The sign convention for this plot indicates the FOV for channels 5, 1, 3, and 8 are looking left and the FOV for channel 10 is looking down for an expected on-orbit orientation. This verifies the relative detector orientations.

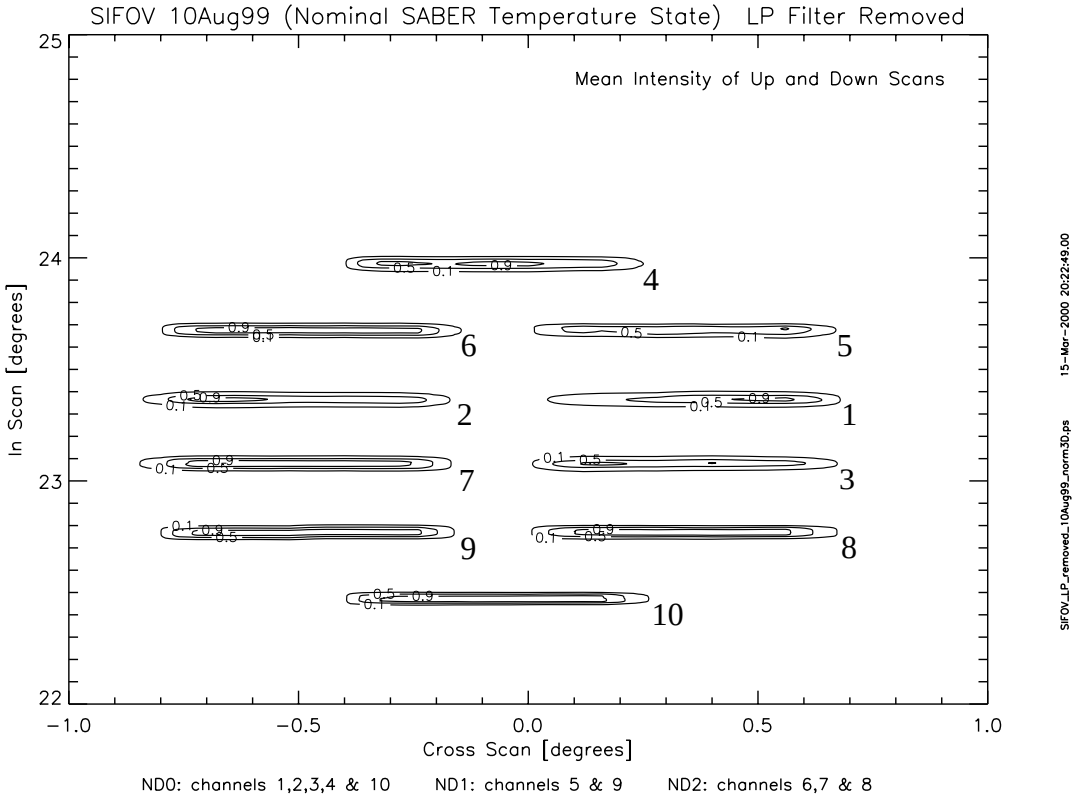

Figure 98. Relative detector orientation (static in-scan IFOV contour plot)

More quantitative relative object space channel positions were determined during radiometric calibration by calculating the centroid of the IFOV response for each channel. Data from the static field-of-view data collection procedure were used. The scan mirror was positioned to a nominal 60 km tangent height for these measurements. The mean in-scan IFOV curve using both up and down scans was calculated for each channel, processed to determine the centroid of each curve, and the position of each centroid relative to the center of the focal plane (boresight) was determined. The center of the focal plane was determined by the average in-scan position of all 10 channels. The uncertainties of the in-scan positions were determined by computing the RSS of the difference in the centroid position determined using up and down scans separately, and the scan mirror transfer function uncertainty. These results are shown in Table 72.

The cross-scan channel position was determined by separately integrating each in-scan static IFOV curve and using these numbers to generate a cross scan IFOV curve and centroid. The position of each cross-scan centroid relative to the mean cross-scan position for all 10 channels was determined. The uncertainties of the cross-scan positions were determined by computing the RSS of the difference in the cross-scan centroid position determined using up and down scans separately, and the pointing mirror calibration equation and theodolite pointing uncertainties. These results are also shown in Table 72.

Table 72. Object space channel positions (static IFOV)

	In-Scan		Cross-Scan	
Channel	Position (degrees)	Uncertainty (degrees)	Position (degrees)	Uncertainty (degrees)
1	0.144	0.0006	0.489	0.0015
2	0.143	0.0006	-0.427	0.0015
3	-0.145	0.0006	0.400	0.0015
4	0.752	0.0006	-0.018	0.0011
5	0.454	0.0011	0.411	0.0011
6	0.453	0.0011	-0.410	0.0011
7	-0.145	0.0006	-0.424	0.0011
8	-0.452	0.0006	0.404	0.0011
9	-0.454	0.0006	-0.414	0.0011
10	-0.750	0.0006	-0.007	0.0015

3.7.4.1 Near Angle Scatter

Near angle scatter (NAS) occurs when signals are registered from regions that are outside the nominal field of view for that channel, and can result from electrical crosstalk and/or optical scatter mechanisms. NAS signals can be observed in the log-scale static IFOV plots shown in Figure 94. These curves show channel signals between 3 and 4 orders of magnitude below the central peak. Different features that are characteristic of both electrical crosstalk and optical scatter are apparent in the plots.

Channel crosstalk occurs when a signal registers on a channel when another channel is being illuminated. This can occur through electronic means within the signal path, or by optical means when energy is scattered from the illuminated channel and is intercepted by another channel. No distinction is made in this discussion between the two kinds of crosstalk. In the plots shown in Figure 94, crosstalk is evident as channel response away from the IFOV central lobe, corresponding to the location of another channel. For example, the IFOV response curve for channel 2 shows crosstalk in the location of channel 4. Channel crosstalk is less than 1% for all SABER channels.

Elevated channel response away from the central IFOV lobe that shows no correlation with another channel's location is characteristic of optical scatter. Little or no change in channel response away from the central IFOV lobe is observed for channels 7, 8, 9, and 10 in the plots shown in Figure 94. These channels all show consistent backgrounds across the focal plane, apart from the limited crosstalk observations discussed above. The remaining channels on the focal plane do show a larger response beginning about halfway across the focal plane and continuing toward the channel 10 side of the focal plane. The source of this response has not been identified, but may be caused by optically scattered energy. However, this response is below 1% of the central IFOV peak.

3.8 Sensor Boresight

The SABER boresight is defined as the look angle for the center of the array when the scan mirror is positioned at an equivalent on-orbit tangent height look angle of 60 km assuming a 625-km orbit height and an earth radius of 6367 km.

The boresight measurement was used to determine four instrument parameters: the scan mirror encoder calibration constant, the 60-km tangent height boresight, the focal plane clocking, and the scan plane angle of the SABER instrument. Four types of data collection events were used to determine values and uncertainties for these instrument parameters: 1) room temperature baseline measurements, 2) operational temperature measurements at both the warm and cold operational limits, 3) pre-shake measurements, and 4) post-shake measurements.

All measurements were made using the channel 10 detector of the SABER instrument, since it is the only SABER detector that responds at both operational and room temperature. The line of sight of the channel 10 detector was measured relative to an alignment cube mounted on the SABER instrument interface plate. A theodolite was used to measure the angle between the alignment cube and the light from a collimated pinhole illuminating SABER's channel 10 detector. The image of the pinhole on the detector was a factor of five smaller than the detector width, so the locations of the point image yielding half power detector response accurately identified the locations of the edges of the channel 10 detector.

Angles between the SABER mounting surfaces and the alignment cube were measured and the final results are reported relative to the SABER mounting surfaces rather than relative to the alignment cube. Alignment angles relative to the SABER alignment cube can be computed from the final results using the angles between the SABER's alignment cube and SABER's mounting surfaces. The SABER mounting surfaces define an XYZ coordinate system that is parallel to the ideal spacecraft coordinate system; that is, the positive Z axis points towards nadir, the positive Y axis is the outward normal of the ideal SABER radiators, and the X axis follows from the right-hand rule. Several figures illustrating the orientation of this coordinate system relative to SABER are given in the boresight section of "SABER Ground Calibration and Preliminary Results" (SDL/98-059).

Uncertainties are reported at the 1 σ level.

The boresight measurements, data reduction, and results are given in the boresight section of "SABER Ground Calibration and Preliminary Results" (SDL/98-059).

3.8.1 Orientation of the SABER Alignment Cube

The orientation and uncertainty of SABER's alignment cube relative to the coordinate system defined by SABER's mounting surfaces are described in Tables 73 and 74, respectively. Faces 1 and 6 are shown because they are nominally in the XZ and YZ coordinate planes. The relatively large uncertainty in the orientation of the SABER alignment cube is due to variation in the orientation of the alignment cube each time the electronics box is installed.

Table 73. Best estimate of the outward normals of the SABER alignment cube relative to the XYZ coordinate system defined by SABER's mounting surfaces

	Direction Cosines			Direction Angles (Degrees)		
Face	X	Y	Z	X	Y	Z
1	-0.0000640	0.9999995	-0.000953	90.0037	0.0547	90.0546
6	0.0015689	-0.000953	-0.9999983	89.9101	90.0546	179.8948

Table 74. Uncertainty of SABER alignment cube normals

	Direction Angles (Degrees)		
Face	X	Y	Z
1	0.0090	0.0096	0.0113
6	0.0043	0.0113	0.0092

3.8.2 Scan Mirror Encoder Calibration Constant

The scan mirror encoder calibration constant is used to ascertain the encoder counts corresponding to line-of-sight angles. The scan mirror encoder calibration constant C is defined by Equation (35).

$$N_{sm} = (C + \theta_{los})\left(\frac{2^{20}}{720}\right) \tag{35}$$

where

N_{sm} =encoder counts

C =calibration constant

θ_{los} =line-of-sight depression angle

The depression angle is defined as the rotation of the line of sight of the center of the focal plane about the X axis with zero degrees in the direction of the positive Y axis and the sign determined by the right-hand rule.

The best estimate of the scan mirror encoder constant C and its uncertainties are shown in Table 75.

Table 75. Scan mirror encoder constant best estimate and uncertainty

C	Value (Degrees)
Best Estimate	90.0127
Uncertainty	
Cube to SABER mounting surfaces with no electronics box	0.0064
Thermal (maximum measured change)	0.0156
Launch stress (maximum measured change)	0.0154
1 g release (measured change)	0.0012
Average change in cube orientation with electronics box installed	0.0358
Total uncertainty (RSS)	0.0425

3.8.3 Boresight

The SABER boresight is defined as the SABER line of sight when the scan mirror is nominally set to observe 60-km tangent height assuming a 625-km orbit height and an earth radius of 6367 km. The best estimate of the boresight and its uncertainty is given in Table 76.

Table 76. Best estimate of 60 km boresight

	Direction Cosines			Direction Angles (Degrees)		
	X	Y	Z	X	Y	Z
Best Estimate	-0.000529	0.919192	0.3938105	90.0303	23.1918	66.8082
				Uncertainty		
Cube to SABER mounting surface with no electronics box				0.0069	0.0064	0.0041
Thermal (maximum measured change)				0.0472	0.0155	0.0156
Launch stress (maximum measure change)				0.0060	0.0154	0.0154
1g release (measured change)				0.0035	0.0013	0.0012
Average change in cube orientation with electronics box installed				0.0075	0.0358	0.0358
Total uncertainty (RRS)				0.0487	0.0425	0.0422

3.8.4 Clocking Error

Clocking error is defined as rotation of the FPA about the line of sight axis. Each detector has its own clocking error which can vary from the average clocking angle by as much as 0.25 degrees determined by the placement of the individual detector on the focal plane. The clocking error of only detector 10 was measured by the boresight alignment procedure. The clocking error of the other detectors can be ascertained using the clocking error of detector 10 and the results of the IFOV measurement procedure, which gives the orientation of each detector relative to each other. The clocking error is the angle from the X axis to the channel 10 detector centerline with its sign determined by the right hand rule. That is, if the thumb of the right hand is pointed in the direction of the outward line of sight, a positive clocking error angle is in the direction that the fingers curl. This is equivalent to rotating the SABER coordinate system about the X axis until the YZ plane contains the outward line of sight and then applying the conventional right hand rule to rotate the X axis into the detector centerline. The channel 10 clocking error is given in Table 77.

Table 77. Channel 10 clocking error best estimate and uncertainty

	Value (Degrees)
Best Estimate	0.1388
Uncertainty:	
Measurement accuracy (standard deviation of shake measurement)	0.0276
Thermal (maximum measured value)	0.0010
Launch stress (maximum measured value)	0.0623
1 g release (measured value)	0.0035
Maximum change in cube orientation with electronics box installed	0.0520
Total uncertainty (RRS)	0.0864

3.8.5 Scan Plane Error

The best-fit plane to the line of sight of the center of the focal plane as the scan mirror turns defines a scan plane. Ideally this plane should lie in the YZ plane and its normal should coincide with the X axis. Scan plane error is defined as the angle from the X axis to the best-fit scan plane normal projected onto the XZ plane. The sign of this angle is determined by the right hand rule. The scan plane error best estimate and uncertainty are given in Table 78.

Table 78. Scan plane angle best estimate and uncertainty

	Value (Degrees)
Best Estimate	0.0936
Uncertainty:	
Measurement accuracy (standard deviation of all measurements)	0.0143
Thermal (maximum measured change)	0.0402
Launch (maximum measured change)	0.0168
1 g release (measured change)	0.0035
Maximum measured change in cube orientation with electronics box installed	0.0038
Total uncertainty (RRS)	0.0461

3.9 Scan Mirror Transfer Function

The SABER scan mirror is designed to rotate about an axis coincident with the scan mirror surface. The mechanical position of the scan mirror is monitored with a digital encoder that measures rotation of the scan mirror. The scan mirror encoder was designed and built by BEI. The encoder provides two signals, each having 2^{18} cycles per mechanical revolution. The SABER electronics combine these two signals into a single 20-bit binary word with output values between 0 and 1048575 counts for a full mechanical rotation. The encoder output is reset to a hexadecimal value of 5EF0B by a pulse at 177˚ relative to instrument horizontal, between the science and IFC positions. This ensures that the encoder count is corrected during every calibration sequence. The encoder zero point corresponds to a vertical mirror pointing angle relative to instrument horizontal. The equation relating object space angle and encoder counts is

$$\theta_{los} = N_{sm}\frac{720}{2^{20}} - \mathrm{C} \tag{36}$$

where:

θ_{los}	=	line-of-sight angle in degrees, referenced to instrument horizontal
N_{sm}	=	encoder counts
C	=	calibration constant = 90.0127 degrees (Section 3.8.2)

A diagram of the scanner mechanism showing the location of important angular positions is shown in Figure 99.

The scan mirror encoder was calibrated by BEI during acceptance testing. Plots of the encoder error as a function of encoder position were generated for each encoder signal by BEI, showing limits of position accuracy over a full encoder rotation (BEI, 1977). Over the encoder position range of 55.0 to 57.2 degrees used for science scans, the encoder position falls within a limiting range of 12 μrad. The corresponding limiting range for scan mirror optical angle is 24 μrad. Assuming a uniform probability distribution for the true position within this range, the 1 σ optical angle uncertainty is 7 μrad (24 μrad / $\sqrt{12}$). The RSS total of the uncertainties from the two encoders is 9.9 μrad.

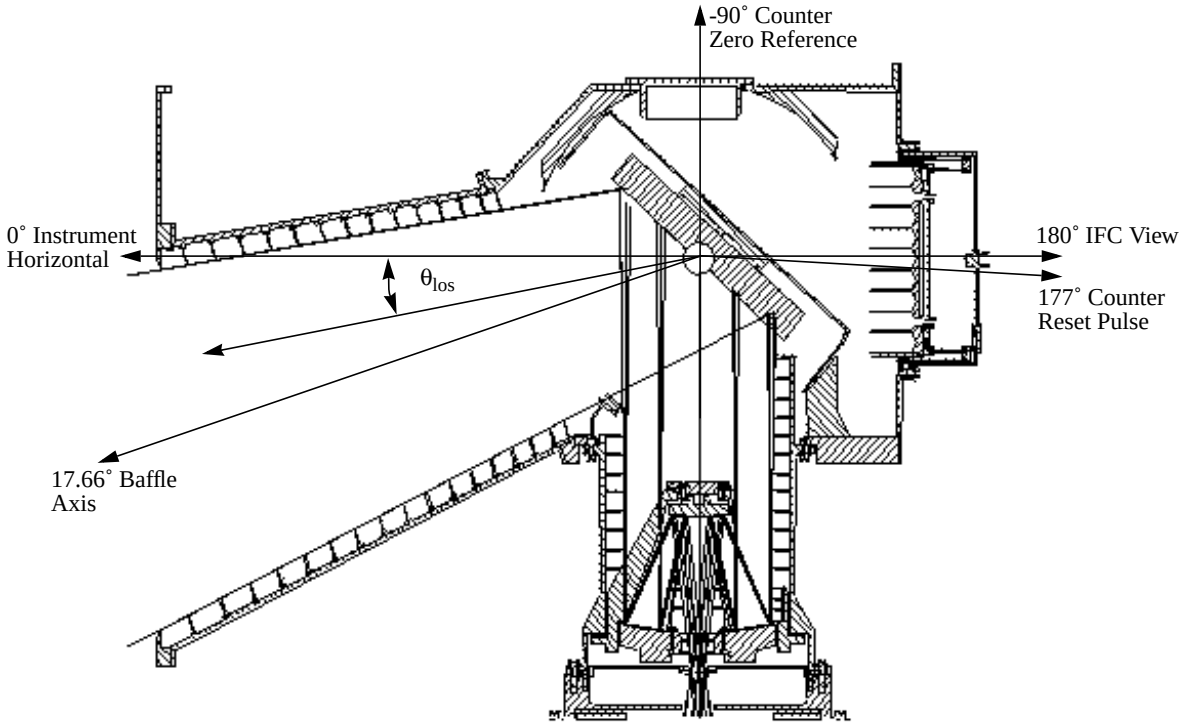

Figure 99. Scanner mechanism

3.9.1 Radiometric Verification of Scan Mirror Transfer Function

Radiometric verification of the scan mirror transfer function was achieved by comparing the angular difference of the SABER scan mirror with the angular difference recorded by the instrument rotary table for IFOV measurements between tangent height look angles of 30, 60, and 130 km.

IFOV measurements were performed during the dynamic IFOV data collection procedure (Appendix A). Data from this data collection were analyzed as described in Section 3.7.2. Plots of the dynamic IFOV for each detector at tangent height look angles of 30, 60, and 130 km are shown in Figures 95 to 97. The in-scan centroid of each detector's IFOV was calculated to give the scan mirror location in object space angle that centers the IFOV source on each detector. The difference in IFOV centroid locations between instrument rotation angles for individual detectors was calculated to give the relative angular difference between IFOV measurements, independent of detector position on the focal plane. The angular difference was calculated for each channel. The average and standard deviation of this difference for all channels was calculated to estimate the relative angle and uncertainty, respectively. These values are given in Table 79.

Table 79. Relative SABER scan mirror angles between 30, 60, and 130 km for IFOV measurements

Tangent Height Delta	Relative Angle (mrad)	Uncertainty (μrad)
30 km - 60 km	10.64	31.0
60 km - 130 km	26.09	31.3
30 km - 130 km	36.73	37.7

The angular difference of the instrument rotary table was determined from the change in angular position reported by the rotary table encoder between the 30, 60, and 130 km IFOV measurements. These values are given in Table 80. The uncertainty of the rotary table angle was determined from rotary table measurements where a theodolite was used to measure the angle of the rotary table as it was repeatedly commanded away from and back to the same position. This was repeated for two different positions, and the angular difference reported by the encoder was compared to the angle measured by theodolite. A difference of +1.8% was observed in this test in the rotary table encoder value relative to the theodolite measurement. This error is far larger than the statistical variation of the measurements, and is taken to be the total uncertainty of the rotary table encoder output. The results of these measurements are summarized in Table 80.

Table 80. Relative rotary table angle between 30 km and 130 km for IFOV measurements

Tangent Height Delta	Relative Angle (mrad)	Uncertainty (%)
30 km - 60 km	10.70	1.8
60 km - 130 km	26.28	
30 km - 130 km	36.98	

Comparison of the angular intervals determined from the SABER scan mirror (Table 79) with the angular intervals determined from the rotary table (Table 80) verifies the scan mirror transfer function within the uncertainty given by the RSS of the uncertainties given in Tables 79 and 80. This comparison is summarized in Table 81. The actual differences between the angular intervals determined using the scan mirror transfer function and the rotary table encoder are shown and compared to the overall uncertainty.

Table 81. Comparison of rotary table and scan mirror relative angle measurements

Tangent Height Delta	Difference in Relative Angle Measurements		Uncertainty	
	(μrad)	(%)	(μrad)	(%)
30 km - 60 km	62.8	0.59	209.6	2.0
60 km - 130 km	193.7	0.74	484.8	1.9
30 km - 130 km	256.6	0.70	657.3	1.8

3.9.2 Theodolite Verification of Scan Mirror Transfer Function

To improve verification of the scan mirror transfer function, data from boresight measurements were analyzed to compare the angle determined using the scan mirror encoder and transfer function with the angle measured using a theodolite. This measurement was performed for 6 scan mirror positions from 33 to 301 km equivalent tangent height, using a theodolite to observe the edges of detector 10. The data used for this analysis were collected on 23 July 1999, and are documented in the boresight data collection procedure. The analysis is summarized in Table 82, where it is shown that the scan mirror transfer function value agrees with the theodolite measurement within 0.2% for equivalent tangent heights from 33 to 301 km.

Table 82. Comparison of rotary table and scan mirror relative angle measurements

Tangent Height Delta	Scan Interval (mrad)		Difference	
	Transfer Function	Theodolite	(μrad)	(%)
33 km - 60 km	9.14	9.16	-19.0	-0.21
60 km - 100 km	15.35	15.35	5.0	0.033
33 km - 100 km	24.50	24.51	-14.0	-0.057
100 km - 138 km	15.32	15.32	-1.8	-0.012
138 km - 224 km	33.77	33.77	4.3	0.013
100 km - 224 km	49.09	49.08	2.4	0.0049
224 km - 301 km	33.76	33.78	-17.4	-0.052
33 km - 301 km	107.34	107.37	-29.0	-0.027

The measurements used to make the scan mirror transfer function verification shown in Table 82 were made with the instrument at room temperature, although no significant change in relative scan mirror angles is expected when the instrument is at operational temperatures. This verification covers most of the scan range required for science measurements. This, along with the radiometric verification previously discussed, verifies the scan mirror transfer function within the program requirement of 1% (Miller, 1997).

3.10 Knife Edge Response

The response of the SABER instrument to a knife edge source was measured to verify SABER's off-axis performance. The knife edge was located inside the test chamber at the end of the radiometric cavity next to the shutter. The instrument scan mirror was used to scan the instrument FOV over the knife edge. A 16° forward and reverse scan was obtained at each SABER rotation angle. Data were obtained at 10 different rotation angles placing the knife edge at equivalent on-orbit tangent height look angles between -10 km and 200 km for a 625 km orbit.

An initial measurement of background radiation was performed with the knife edge at about 100 K. The knife edge heater was then powered to warm the knife edge. While the knife edge was warming, the SABER temperatures began drifting and channel offset values had to be reset. The knife edge stabilized at 170 K, channel offsets were reset, and data collection was repeated. Data were again collected when the knife edge was warmed to 300 K. Channel offsets were reset before the start of the 300 K data collection event.

A detailed discussion of the knife edge data analyses is given in the Knife Edge data collection procedure of "SABER Ground Calibration and Preliminary Results" (SDL/98-059). This section provides a summary of the test.

The 300 K background-corrected knife edge response was plotted as a function of SABER scan angle for channels 1 to 7 and for SABER rotation angles of 0, 20, 70, and 200 km. The data were corrected to account for short term and long term drift. Short term drift corrections were made by performing a spatial average of both the forward and reverse scans for each SABER rotation angle. The long term drift was corrected by assuming 100 K and 300 K knife edge responses were equal when SABER was looking at the portion of the shutter farthest from the knife edge plate. Figure 100 is a graph of the knife edge response uncorrected for offset drift and background and Figure 101 shows the knife edge response corrected for drift and background. For this measurement, the knife edge was located at an equivalent on-orbit tangent height altitude of 0 km.

Data were reduced to tabulate off-axis response levels. The off-axis response with the detector FOV located 1.6° (~80 km) above on-axis flux ranges from 0.3*(required NER) to 6.5*(required NER) or 2.3e-5*(peak response) to 7.4e-5*(peak response), depending on the SABER channel.

An APART analysis was performed on channels 3 and 7 to estimate SABER's response to a 300 K knife-edge for comparison to the measured results. The geometry of the model closely matched that of the knife edge located inside the test chamber. The model used the SABER stray light model, which accounts for mirror scatter, diffraction, and triple diffraction. The model, however, does not account for thermal radiation being emitted by the knife edge scattering inside the radiometric cavity of the test chamber.

The modeled response for both channels is generally lower than the measured response by about an order of magnitude. Mostly, the character of the modeled off-axis response does follow closely to the measured data. This difference in magnitude may be due to: (1) the chopper hole

size producing the average response is smaller than used in the model and (2) a stray light path exists inside the test chamber that is not modeled in APART. Modeling the test chamber for off-axis scatter paths is a large effort that may not give results with high confidence. In general, this measurement produced better quality results than expected because of stray light paths that were likely to exist inside the radiometric cavity of the test chamber.

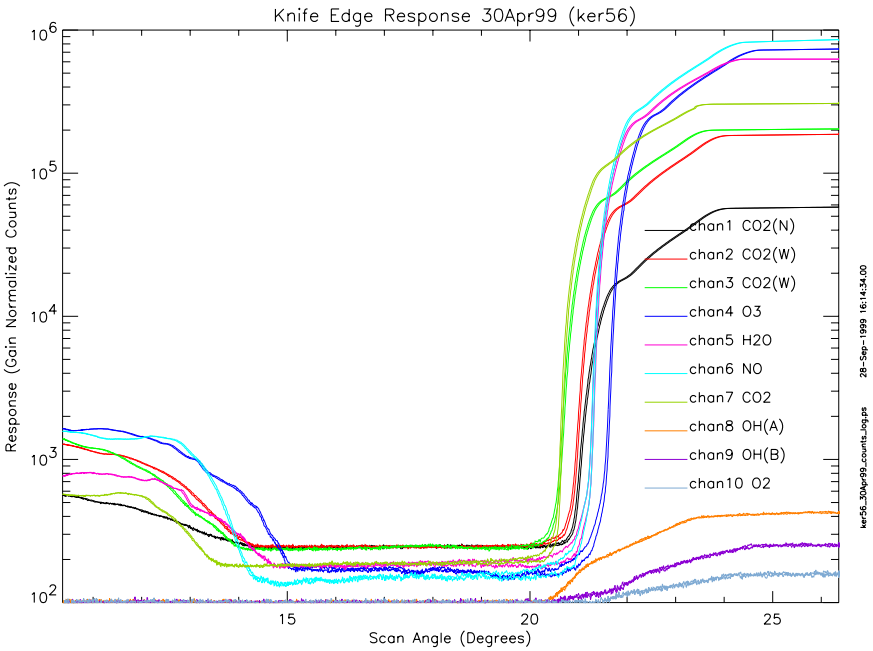

Figure 100. Scan of 300 K knife edge (not corrected for offset drift and background)

Figure 101. Scan of 300 K knife edge (corrected for offset drift and background)

From an on-orbit science measurement perspective, the 300k knife-edge induces a factor 2 to 10 (depending on channel) more energy than would ever be encountered in orbit from the underlying Earth. Therefore, this test shows that the upper limit of expected signal due to off axis scatter for channels 1 to 7 is less than 3 times the noise.

In addition, with channels 5, 6 and 7 showing off axis rejection of 1 X 10^-5 or better, it is very likely that the even shorter wavelength channels, 8, 9, and 10 will achieve the 2-3 X 10^-6 rejection required to limit solar scatter to a one bit effect in the upper mesosphere. This is because channels 8, 9, and 10 were positioned on the FPA to minimize effects of off-axis scatter from other channels. Strong evidence of the success of this strategy can be seen in IFOV data plotted on a log scale in Figure 94.

Signal in channels 8 - 10 is due to electronic cross-talks, which is 3-4 orders of magnitude less than source signals. This will have negligible effect on results.

3.11 Temporal Frequency Response

The temporal frequency response of the SABER instrument, based on theoretical equations of the low-pass filter assembly, is used to remove low pass filter effects from on-orbit science data. This section discusses the temporal frequency analysis and its verification.

3.11.1 Theoretical

The SABER signal processing system uses a 4-pole butterworth filter design to remove unwanted signals resulting from coherent rectification of the chopped detector output (SABER Critical Design Review Document). An equation for the transfer function of the SABER low-pass filter assembly was obtained by analysis of the filter design, and is given in Equation (37).

$$G(s) = \frac{1}{(1 + 2RC_2s + R^2C_1C_2s^2)(1 + 2RC_4s + R^2C_3C_4s^2)} \tag{37}$$

where

$G(s)$ = transfer function
R = 100 KΩ
C_1 = 0.39 μF
C_2 = 0.33 μF
C_3 = 0.80 μF
C_4 = 0.1 μF
s = complex factor jω

The magnitude of $G(s)$ gives the amplitude response of the filter, while the phase response is given by $\text{atan}(ImG(s)/ReG(s))$, where Re and Im refer to real and imaginary parts, respectively. Plots of the frequency response amplitude as a function of frequency are shown in Figure 102, while phase plots as a function of frequency are presented in Figure 103.

Because on-orbit data as a function of tangent height altitude are obtained dynamically through the use of a moving scan mirror, knowledge of SABER's temporal frequency response is needed to make corrections. These measurements can be corrected by deconvolving the temporal fre-

quency response from earth limb or point source scan data. This deconvolution is illustrated in Equation (38).

$$S'(f) = \frac{S(f)}{G(f)} A(f) \tag{38}$$

where

$S(f)$ = complex Fourier transform of the uncorrected SABER measurement

$G(f)$ = SABER temporal response function

$A(f)$ = apodization function

= $\exp(-0.5(f / f_c)^2)$, where $f_c = 4.430$ Hz

The apodization function is used to eliminate signal boost caused by division by small numbers at high frequencies. The corrected time response of the measurement is given by the inverse transform of $S'(f)$.

3.11.2 Subsystem Measurements

The frequency response of the low-pass filter electronics was measured during instrument assembly. This test was performed using a Phillips PM5193 programmable frequency synthesizer to present a step function input to the signal processing system, while a TEK TDS744 oscilloscope was used to simultaneously record both the step function input and the resulting output. The procedure, measurements, and results are documented in Appendix F. The digitized data were processed using Fourier transform techniques to remove noise and calculate the system transfer function. The resulting amplitude frequency response is plotted as a function of signal frequency in Figure 102, alongside the theoretically determined response. Measured phase response is plotted as a function of signal frequency with the corresponding theoretically determined curve in Figure 103.

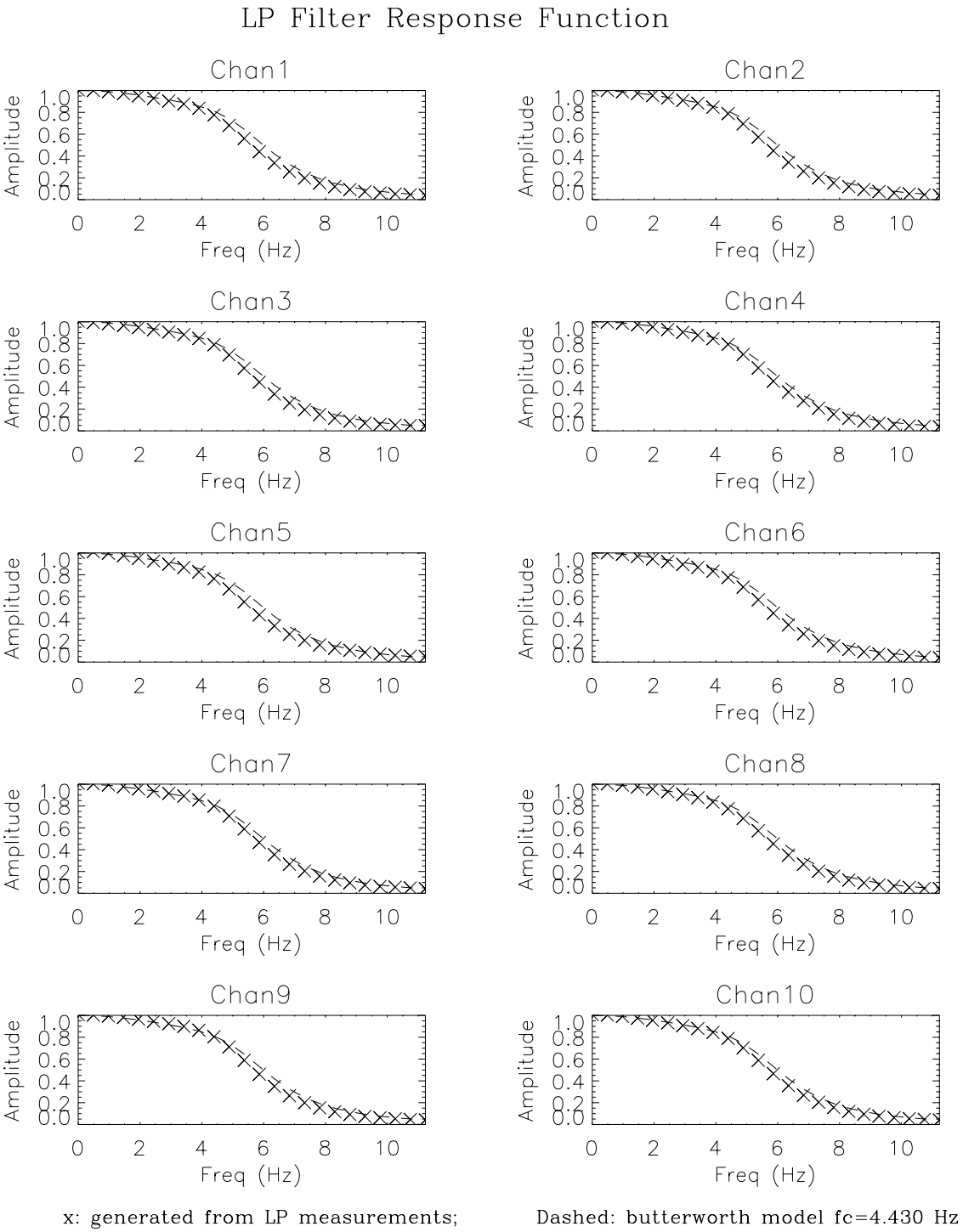

Figure 102. Low-pass filter amplitude response

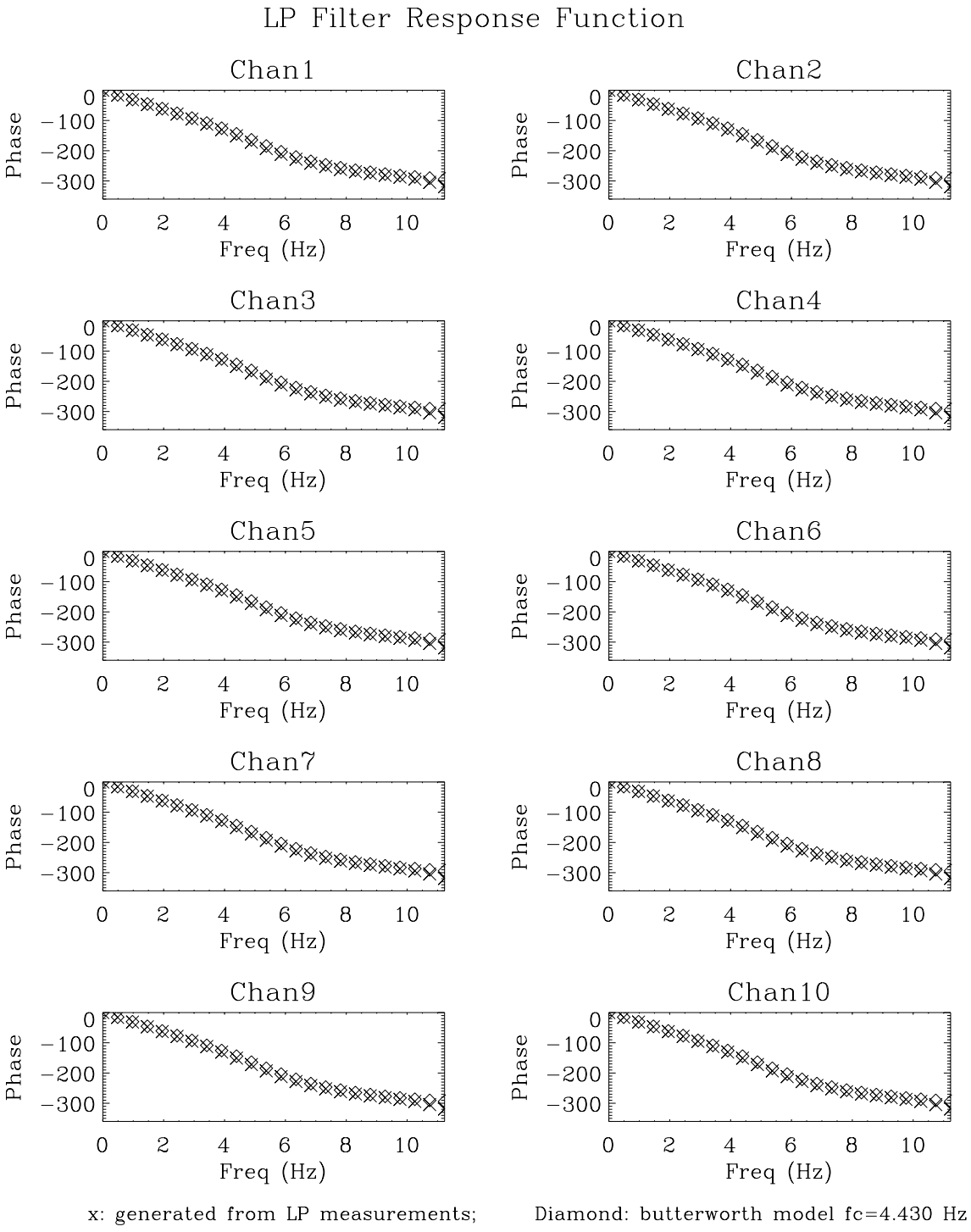

Figure 103. Low-pass filter phase response

3.11.2.1 Ground Calibration Verification

During ground calibration, verification of the temporal response removal algorithm was performed using the external shutter of the full-field collimator. A blackbody at the entrance port of the FFC was used to stimulate each focal plane detector, while the shutter was made to open and close at 5 second intervals. Data were collected separately for a 1 minute interval for each detector. Details of this data collection can be found in the temporal response data collection procedure documented in “SABER Ground Calibration and Preliminary Results” (SDL/98-059).

Data from the temporal response data collection procedure were processed to remove the effect of the low pass filter. Figure 104 shows channel 1 response to the radiometric step function. Overplotted is the low-pass-filter-corrected response using equations described in Section 3.11.1. This plot is similar to the response of other channels. The sampling rate of the SABER instrument was not adequate to allow calculation of the system transfer function from this data, to permit direct comparison to results shown in Section 3.11.2. However, the phase shift and suppression of ringing in the low-pass-filter-corrected radiometric step function data give a qualitative verification of the temporal frequency response correction.

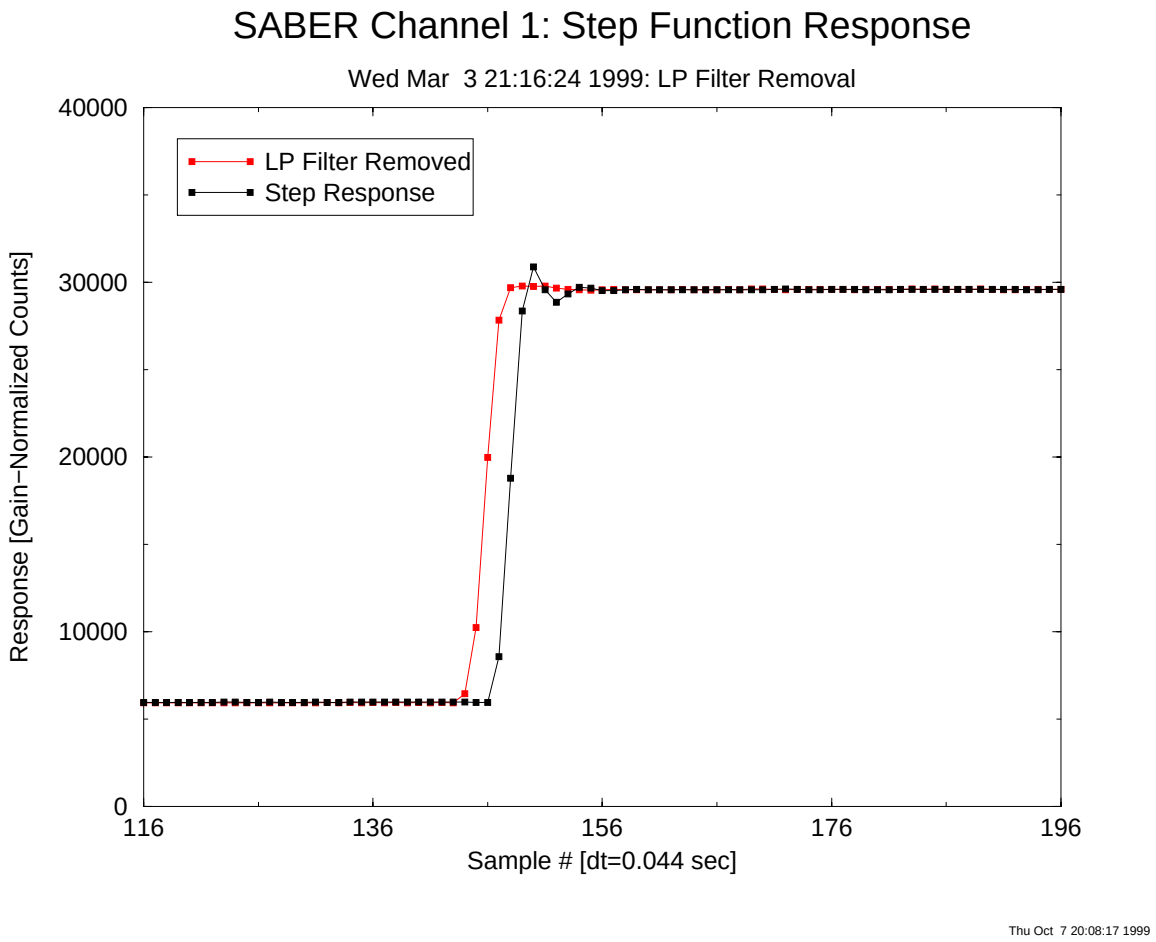

Figure 104. Radiometric step response

REFERENCES

BEI Sensor & Systems Co., Acceptance Test Procedure for the SDL/USU SABER Instrument Scan Motor/Encoder, TP995-0375-100, Precision Systems and Space Division, 1100 Murphy Drive, Maumelle, AR, 72113, 1997.

Dyer J.S., R.C. Benson, T.E. Phillips, and J.J. Guregian, "Outgassing Analyses Performed During Vacuum Bakeout of Components Painted with Chemglaze Z306-9922," *Proc. SPIE* 1754, p. 177, July 1992.

Esplin, R. and M. Jensen, *S*ABER System Model version 1.6, Space Dynamics Laboratory, Utah State University, Logan, UT, August 1996.

Folkman, M. and M. Flannery, Results of CERES Shortwave In-flight Calibration Sources (SWICS) Lamp Evaluation Testing, TRW Interoffice Correspondence, February 1993.

Gordley, L., personnel communication, GATS Inc., 28 November 1995.

Gordley, L., Presentation at SABER TIM #9, July 1997.

Hansen, S.M. and J. J. Tansock, SABER Calibration Relative Spectral Response Reference Detector Demonstration of Method, Space Dynamics Laboratory, Utah State University, Logan, UT, SDL/97-054, June 1997.

International Organization for Standardization (ISO), *Guide to the Expression of Uncertainty in Measurement*, 1st edition, ISO/TAG4/WG3, June 1992.

Kemp, J., E.R. Huppi, and M. Madigan, "Measurements of High Out-of-Band Filter Rejection Characteristics," *Proc. of SPIE* 1112:433-441, 1989.

Kliger, D.S., J.W. Lewis, C.E. Randall, *Polarized Light in Optics and Spectroscopy*, Academic Press, 1990.

Miller, J. B., SABER Instrument Pointing Requirements, Langley Researcy Center, Nov. 19, 1997.

NIST Technical Note 1297, "Guidelines for Evaluating and Expressing the Uncertainty of NIST Measurement Results," 1994.

Peterson, J.Q., "SABER Spectral Responsivity Calibration Plan," Space Dynamics Laboratory, Utah State University, Logan, UT, SDL/98-022, February 1998.

SDL/94-088, SABER Product Assurance Plan, Space Dynamics Laboratory, Utah State University, Logan, UT, 1994.

SDL/95-006, Rev. A, SABER Instrument Requirements Document (IRD), Space Dynamics Laboratory, Utah State University, Logan, UT, November 1996.

SDL/95-009, SABER Instrument Specification, Space Dynamics Laboratory, Utah State University, Logan, UT, 1995.

SDL/96-049, SABER Ground Support Equipment Specification, Space Dynamics Laboratory, Utah State University, Logan, UT, August 1996.

SDL/97-020, SABER Instrument Integration and Test Plan, Space Dynamics Laboratory, Utah State University, Logan, UT, September 1997.

SDL/97-065, SABER Jones Source Incandescent Lamp Test Plan, Space Dynamics Laboratory, Utah State University, Logan, UT, July 1997.

SDL/98-059, SABER Ground Calibration Test and Summary Results, Space Dynamics Laboratory, Utah State University, Logan, UT, June 1999.

SDL/98-112, GSE Low Temperature Blackbody Performance Report, Space Dynamics Laboratory, Utah State University, Logan, UT, August 1999.

SDL/99-040, Test and Qualification Results of SABER Jones Source Incandescent Lamps, Space Dynamics Laboratory, Utah State University, Logan, UT, April 1999.

TIMED Component Environment Specification, Applied Physics Laboratory, The Johns Hopkins University, Laurel, MD, No. 7363-9010, 1998.

Wang, Yunfei, email correspondence to Joe Tansock, Space Dynamics Laboratory, Utah State University, Logan, UT, 18 January 2000.

Wyatt, C.L., *Radiometric Calibration: Theory and Methods*, Academic Press, New York, 1978.

Wyatt, C.L., "Sources of Error in Radiometric and Spectrometric Measurements," Space Dynamics Laboratory, Utah State University, Logan, UT, SDL/90-060-II, September 1991.

APPENDIX A- ELECTRONIC SUBSYSTEM GAIN-MODE NORMALIZATION CALIBRATION

APPENDIX B - DEPENDENCE OF ELECTRONIC OPERATING TEMPERATURE AND TOTAL DOSE RADIATION ON GAIN-MODE NORMALIZATION

APPENDIX C - HTBB PARABOLA REFLECTANCE

SABER GSE HTBB Parabola Reflectance 8/9/1999, Updated 1/14/00
File: /sabercal/LTBB_HTBB/HTBB/parab_r.mcd

Measured SABER RSR results, James Peterson 11/99 $i := 1,2..10$ i channels

Center Wavelength	FWHM Band Limits		Channel name	Detector type
$\nu_{1,0} := 672.46 \cdot cm^{-1}$	$\nu_{1,1} := 691.38 \cdot cm^{-1}$	$\nu_{1,2} := 653.53 \cdot cm^{-1}$	CO_2-N	MCT-PC
$\nu_{2,0} := 668.80 \cdot cm^{-1}$	$\nu_{2,1} := 751.62 \cdot cm^{-1}$	$\nu_{2,2} := 585.97 \cdot cm^{-1}$	CO_2-W	MCT-PC
$\nu_{3,0} := 668.68 \cdot cm^{-1}$	$\nu_{3,1} := 751.98 \cdot cm^{-1}$	$\nu_{3,2} := 585.38 \cdot cm^{-1}$	CO_2-W	MCT-PC
$\nu_{4,0} := 1078.0 \cdot cm^{-1}$	$\nu_{4,1} := 1134.9 \cdot cm^{-1}$	$\nu_{4,2} := 1021.06 \cdot cm^{-1}$	O_3	MCT-PC
$\nu_{5,0} := 1466.4 \cdot cm^{-1}$	$\nu_{5,1} := 1552.3 \cdot cm^{-1}$	$\nu_{5,2} := 1380.43 \cdot cm^{-1}$	H_2O	MCT-PC
$\nu_{6,0} := 1907.8 \cdot cm^{-1}$	$\nu_{6,1} := 1930.27 \cdot cm^{-1}$	$\nu_{6,2} := 1885.28 \cdot cm^{-1}$	NO	InSb-PV
$\nu_{7,0} := 2348.1 \cdot cm^{-1}$	$\nu_{7,1} := 2383.9 \cdot cm^{-1}$	$\nu_{7,2} := 2312.30 \cdot cm^{-1}$	CO_{2B}	InSb-PV
$\nu_{8,0} := 4832.3 \cdot cm^{-1}$	$\nu_{8,1} := 5121.5 \cdot cm^{-1}$	$\nu_{8,2} := 4543.06 \cdot cm^{-1}$	OH_A	InSb-PV
$\nu_{9,0} := 6076.8 \cdot cm^{-1}$	$\nu_{9,1} := 6370.43 \cdot cm^{-1}$	$\nu_{9,2} := 5783.23 \cdot cm^{-1}$	OH_B	InSb-PV
$\nu_{10,0} := 7831.2 \cdot cm^{-1}$	$\nu_{10,1} := 7915.28 \cdot cm^{-1}$	$\nu_{10,2} := 7747.14 \cdot cm^{-1}$	O_2	STD InGaAs-PV

$$\lambda_{i,0} := \frac{1}{\nu_{i,0}} \qquad \lambda_{i,1} := \frac{1}{\nu_{i,1}} \qquad \lambda_{i,2} := \frac{1}{\nu_{i,2}}$$

Center Wavelength $\frac{\lambda_{i,0}}{\mu m} =$	FWHM Band Limits $\frac{\lambda_{i,1}}{\mu m} =$	$\frac{\lambda_{i,2}}{\mu m} =$	$\frac{\lambda_{i,2} - \lambda_{i,1}}{\mu m} =$
14.871	14.464	15.302	0.838
14.952	13.305	17.066	3.761
14.955	13.298	17.083	3.785
9.276	8.811	9.794	0.982
6.819	6.442	7.244	0.802
5.242	5.181	5.304	0.124
4.259	4.195	4.325	0.13
2.069	1.953	2.201	0.249
1.646	1.57	1.729	0.159
1.277	1.263	1.291	0.027

Define Planck Function

$$N(\lambda_1,\lambda_2,T) := \int_{\lambda_1}^{\lambda_2} \frac{c1}{\lambda^5 \cdot \left(\exp\left(\frac{c2}{\lambda \cdot T \cdot K}\right) - 1\right)} d\lambda \qquad \Delta N(\lambda 1,\lambda 2,T) := \frac{d}{dT} N(\lambda 1,\lambda 2,T)$$

Temperature Uncertainty Corresponding to Radiance Uncertainty for Each Channel

$$\sigma_T(\lambda_1,\lambda_2,T,\sigma_R) := \frac{\sigma_R}{\left(\frac{\Delta N(\lambda_1,\lambda_2,T)}{N(\lambda_1,\lambda_2,T)}\right)}$$

<- Response or Radiance Uncertainty

<- (d Radiance / dT) / Radiance
or (d Radiance/Radiance) / dT

$$\sigma_R(\lambda_1,\lambda_2,T,\sigma_T) := \frac{\Delta N(\lambda_1,\lambda_2,T)}{N(\lambda_1,\lambda_2,T)} \cdot \sigma_T$$

((d Radiance / dT) / Radiance) * dT
or ((d Radiance/Radiance) / dT) * dT
or d Radiance/Radiance

Reflectance values of 3 witness samples measured by NIST (Leonard Hanssen, June 16, 1999)

Reference: SDL Labbook, Andrew Shumway, 5/99, Pg 32

$i := 0..15$

$wl_i := (1 + .1 \cdot i) \cdot \mu m$

$\rho_{avg_i} := \frac{\rho 1_i + \rho 2_i + \rho 3_i}{3}$

$\sigma_i := \sqrt{\frac{1}{3} \cdot \left[\left(\rho 1_i - \rho_{avg_i}\right)^2 + \left(\rho 2_i - \rho_{avg_i}\right)^2 + \left(\rho 3_i - \rho_{avg_i}\right)^2\right]}$

$\frac{wl_i}{\mu m} =$	$\rho 1_i :=$	$\rho 2_i :=$	$\rho 3_i :=$
1	.956	.926	.934
1.1	.960	.93	.939
1.2	.965	.938	.944
1.3	.966	.942	.948
1.4	.968	.946	.951
1.5	.97	.948	.953
1.6	.971	.951	.955
1.7	.9718	.952	.956
1.8	.972	.954	.958
1.9	.9725	.955	.959
2	.973	.956	.9595
2.1	.974	.957	.960
2.2	.974	.958	.960
2.3	.9741	.959	.961
2.4	.9742	.9595	.9615
2.5	.9743	.960	.962

1 Standard Deviation Uncertainty

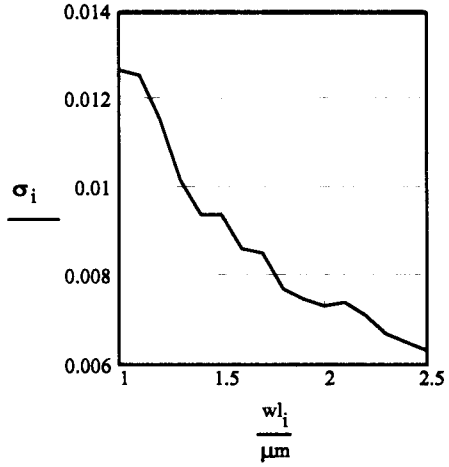

Tabular Results of mirror reflectance

Wavelength $\frac{wl_i}{\mu m}$	Mirror Reflectance ρ_{avg_i}	Mirror Reflectance plus one sigma uncertainty $\rho_{avg_i}+\sigma_i$	Mirror Reflectance minus one sigma uncertainty $\rho_{avg_i}-\sigma_i$
1	0.9387	0.9514	0.926
1.1	0.943	0.9556	0.9304
1.2	0.949	0.9606	0.9374
1.3	0.952	0.9622	0.9418
1.4	0.955	0.9644	0.9456
1.5	0.957	0.9664	0.9476
1.6	0.959	0.9676	0.9504
1.7	0.9599	0.9685	0.9514
1.8	0.9613	0.9691	0.9536
1.9	0.9622	0.9697	0.9547
2	0.9628	0.9702	0.9555
2.1	0.9637	0.9711	0.9563
2.2	0.964	0.9711	0.9569
2.3	0.9647	0.9714	0.958
2.4	0.9651	0.9716	0.9586
2.5	0.9654	0.9718	0.9591

Graphical results of mirror reflectance

Reflectance of 3 HTBB Parabola Witness Mirrors with mean and 1 stdev error bars

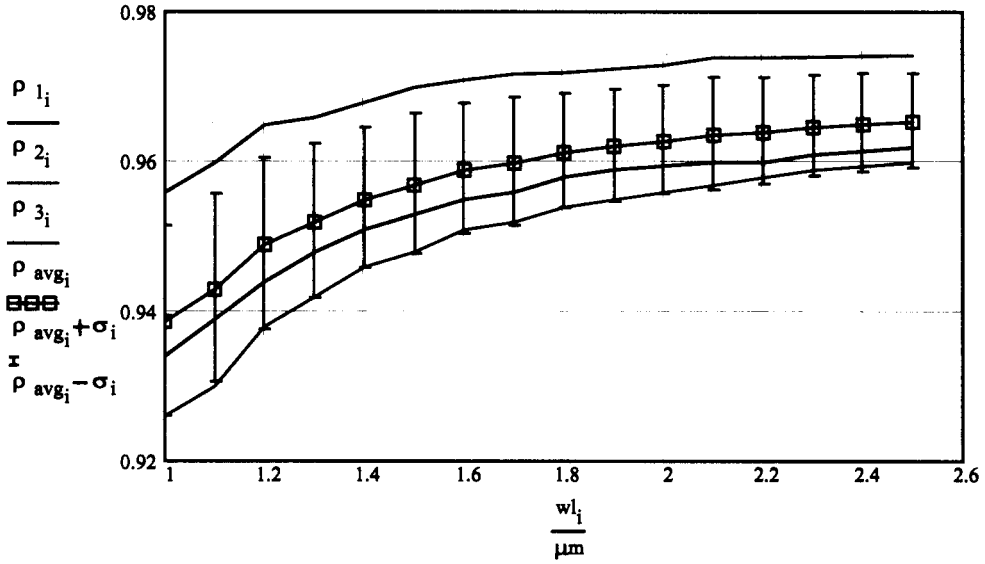

Write reflectance data to file

$write\_vec_{i,0} := \frac{wl_i}{\mu m}$ $write\_vec_{i,1} := \rho\,avg_i - \sigma_i$ $write\_vec_{i,2} := \rho\,avg_i$ $write\_vec_{i,3} := \rho\,avg_i + \sigma_i$

WRITEPRN("parab_r.dat") := write_vec

Integrate reflectance and uncertainty over bandpasses to get average values

$$\rho avg(\lambda_1, \lambda_2) := \frac{\int_{\lambda_1}^{\lambda_2} linterp(wl, \rho\,avg, \lambda)\, d\lambda}{\lambda_2 - \lambda_1}$$ Reflectance in bandpass

$$\sigma cont(\lambda_1, \lambda_2) := \frac{\int_{\lambda_1}^{\lambda_2} linterp(wl, \sigma, \lambda)\, d\lambda}{\lambda_2 - \lambda_1}$$ Uncertainty in bandpass

Channel	Reflectance	Uncertainty
ch := 8	$\rho avg(\lambda_{ch,1}, \lambda_{ch,2}) = 0.963$	$\sigma cont(\lambda_{ch,1}, \lambda_{ch,2}) = 7.325 \cdot 10^{-3}$
ch := 9	$\rho avg(\lambda_{ch,1}, \lambda_{ch,2}) = 0.959$	$\sigma cont(\lambda_{ch,1}, \lambda_{ch,2}) = 8.595 \cdot 10^{-3}$
ch := 10	$\rho avg(\lambda_{ch,1}, \lambda_{ch,2}) = 0.951$	$\sigma cont(\lambda_{ch,1}, \lambda_{ch,2}) = 0.011$

Global constants

J≡joule W≡watt $\mu m \equiv cm \cdot 10^{-4}$ $Hz \equiv sec^{-1}$ $rtHz \equiv \sqrt{Hz}$ $mW \equiv watt \cdot 10^{-3}$

$h \equiv 6.62618 \cdot 10^{-34} \cdot J \cdot sec$	Planck's Constant
$c \equiv 2.99792458 \cdot 10^{10} \cdot cm \cdot sec^{-1}$	Speed of Light
$k \equiv 1.38066 \cdot 10^{-23} \cdot J \cdot K^{-1}$	Boltzmann's Constant
$\sigma \equiv 5.67032 \cdot 10^{-12} \cdot W \cdot cm^{-2} \cdot K^{-4}$	Stefan-Boltzmann Constant
$c1 \equiv 1.191066 \cdot 10^{4} \cdot W \cdot \mu m^4 \cdot cm^{-2}$	First Radiation Constant -> 2 hc^2
$c2 \equiv 1.43883 \cdot 10^{4} \cdot \mu m \cdot K$	Second Radiation Constant -> hc/k
$q \equiv 1.60219 \cdot 10^{-19} \cdot coul$	Electron charge
$eV \equiv 1.603 \cdot 10^{-19} \cdot J$	Electron volt
sr≡1	Steradian
count≡1	Counts

APPENDIX D - HTBB CAVITY EMISSIVITY

High Temperature Blackbody (HTBB) Emissivity, 1/14/00
File: /sabercal/LTBB_HTBB/HTBB/htbb_emissivity.mcd

Cavity surface emissivity, obtained from Mikron (builder of HTBB)

Pyromark Paint Emissivity Data

Pyromark 1200 paint vacuum baked
Incident angle 20 degrees from normal
Directional emittance versus wavelength from 1.5 to 25 microns
Measurement made at 202.4 C
Mikron Instruments sample FS9516: #4, P-1200 VBAKE (sdl)
Measurements obtained before August 25, 1999

$\lambda_0 := 1.5 \quad i := 1..24 \quad \lambda_i := 1 + i \quad i := 0..24$

$\varepsilon_{n_i} :=$ $\lambda_i =$

ε_{n_i}	λ_i
.94	1.5
.94	2
.945	3
.94	4
.94	5
.94	6
.94	7
.95	8
.94	9
.92	10
.93	11
.93	12
.93	13
.93	14
.91	15
.87	16
.85	17
.85	18
.86	19
.82	20
.80	21
.80	22
.82	23
.84	24
	25

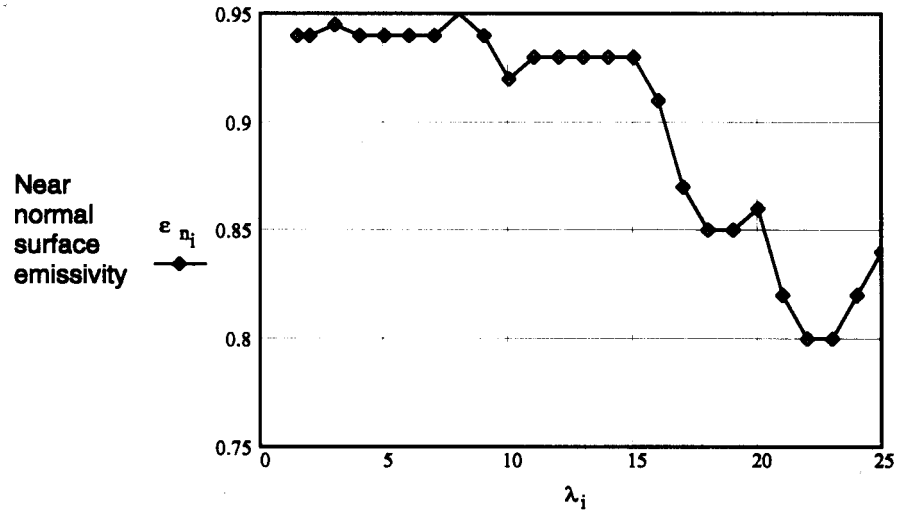

Estimated hemispherical emissivity based on Z306 type reflectance variation where hemispherical reflectance is double the normal reflectance.

$\varepsilon_h := \varepsilon_n - (1 - \varepsilon_n)$ surface hemispherical emissivity

$\sigma_h := 1 - \varepsilon_n$ surface hemispherical emissivity uncertainty

Write to file: $outvecter_{i,0} := \lambda_i$ $outvecter_{i,2} := \varepsilon_{h_i}$ $outvecter_{i,1} := \varepsilon_{n_i}$

$outvecter_{i,3} := \sigma_{h_i}$ WRITEPRN("e_pyromark1200.prn") := outvecter

pyromark := READPRN("e_pyromark1200.prn") read surface emissivity from file

pyromark =

1.5	0.94	0.88	0.06
2	0.94	0.88	0.06
3	0.945	0.89	0.055
4	0.94	0.88	0.06
5	0.94	0.88	0.06
6	0.94	0.88	0.06
7	0.94	0.88	0.06
8	0.95	0.9	0.05
9	0.94	0.88	0.06
10	0.92	0.84	0.08
11	0.93	0.86	0.07
12	0.93	0.86	0.07
13	0.93	0.86	0.07
14	0.93	0.86	0.07
15	0.93	0.86	0.07
16	0.91	0.82	0.09
17	0.87	0.74	0.13
18	0.85	0.7	0.15
19	0.85	0.7	0.15
20	0.86	0.72	0.14
21	0.82	0.64	0.18
22	0.8	0.6	0.2
23	0.8	0.6	0.2
24	0.82	0.64	0.18
25	0.84	0.68	0.16

$n := 0 .. rows(pyromark) - 1$

$\lambda_n := pyromark_{n,0}$ wavelength (um)

$\varepsilon_{n_n} := pyromark_{n,1}$ surface near normal emissivity

$\varepsilon_{h_n} := pyromark_{n,2}$ surface hemispherical emissivity

$\sigma_{h_n} := pyromark_{n,3}$ surface hemispherical emissivity uncertainty

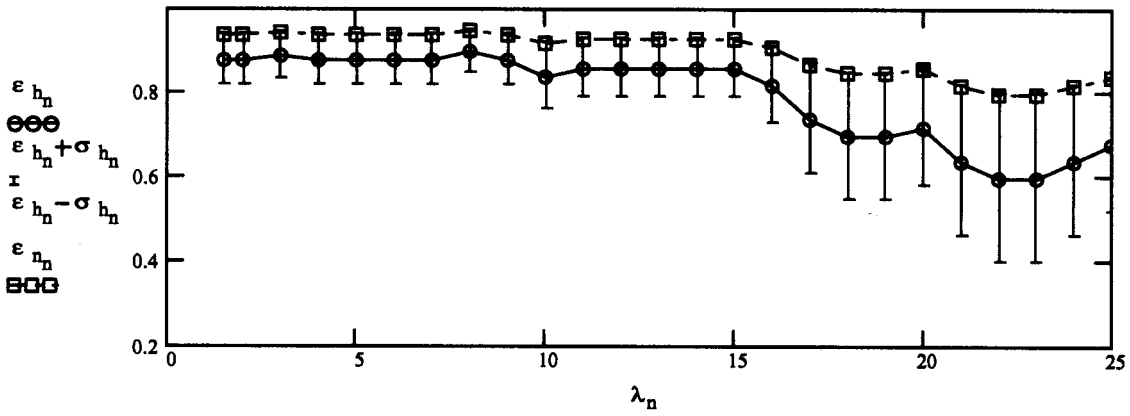

HTBB cavity enhanced emissivity

$\varepsilon_{h\_to\_bb} := READPRN("cavemittance\_curve.prn")$

Surface hemispherical emissivity to cavity enhanced BB emissivity curve. Calculated based on BB geometry and techniques described in "Determination of Diffused-Wall Blackbody Cavity Emittance", Andrew Shumway, May 1995 SDL/USU Calibration Symposium

$\varepsilon_{h\_to\_bb} =$

0.5	0.987
0.55	0.99
0.6	0.992
0.65	0.994
0.7	0.995
0.75	0.996
0.8	0.997
0.85	0.998
0.9	0.999
0.95	0.999
1	1

$k := 0 .. rows(\varepsilon_{h\_to\_bb}) - 1$

$\varepsilon_{surf_k} := \varepsilon_{h\_to\_bb_{k,0}} \qquad \varepsilon_{BB_k} := \varepsilon_{h\_to\_bb_{k,1}}$

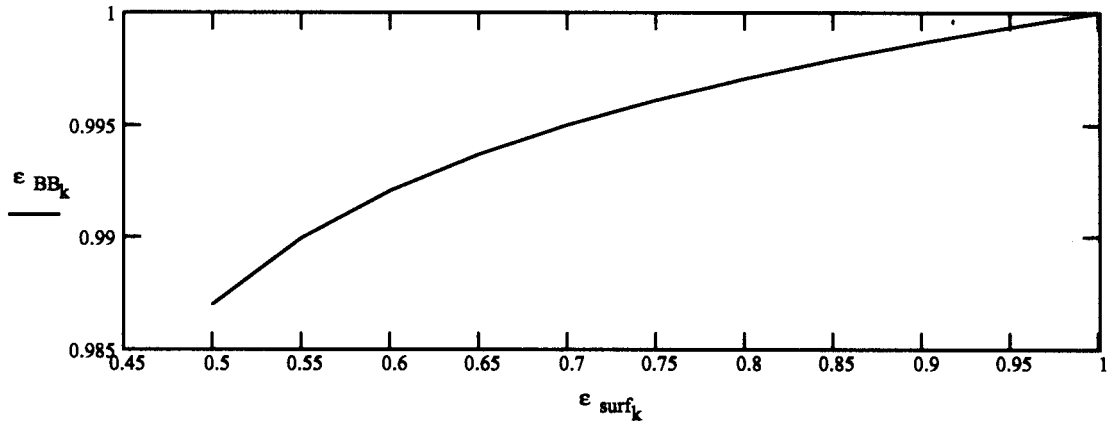

$\varepsilon_{bb\_high_n} := linterp(\varepsilon_{surf}, \varepsilon_{BB}, \varepsilon_{h_n} + \sigma_{h_n})$ Upper limit of HTBB cavity enhanced BB emissivity uncertainty

$\varepsilon_{bb\_nom_n} := linterp(\varepsilon_{surf}, \varepsilon_{BB}, \varepsilon_{h_n})$ Nominal cavity enhanced BB emissivity uncertainty

$\varepsilon_{bb\_low_n} := linterp(\varepsilon_{surf}, \varepsilon_{BB}, \varepsilon_{h_n} - \sigma_{h_n})$ Lower limit of HTBB cavity enhanced BB emissivity uncertainty

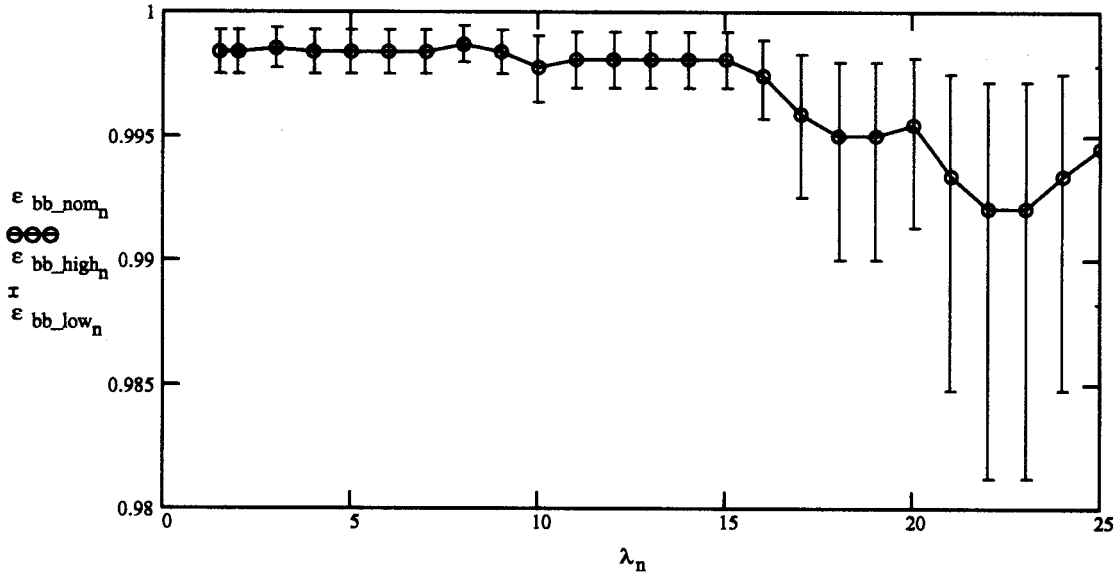

λ_n =	$\varepsilon_{bb\_low_n}$ =	$\varepsilon_{bb\_nom_n}$ =	$\varepsilon_{bb\_high_n}$ =
1.5	0.997422	0.998381	0.999232
2	0.997422	0.998381	0.999232
3	0.997675	0.998532	0.9993
4	0.997422	0.998381	0.999232
5	0.997422	0.998381	0.999232
6	0.997422	0.998381	0.999232
7	0.997422	0.998381	0.999232
8	0.997928	0.998683	0.999369
9	0.997422	0.998381	0.999232
10	0.996316	0.997759	0.998957
11	0.996892	0.998079	0.999095
12	0.996892	0.998079	0.999095
13	0.996892	0.998079	0.999095
14	0.996892	0.998079	0.999095
15	0.996892	0.998079	0.999095
16	0.995678	0.997422	0.99882
17	0.992379	0.995901	0.99823
18	0.989938	0.99501	0.997928
19	0.989938	0.99501	0.997928
20	0.991207	0.995456	0.998079
21	0.984675	0.993359	0.997422
22	0.981166	0.992053	0.997084
23	0.981166	0.992053	0.997084
24	0.984675	0.993359	0.997422
25	0.988184	0.99448	0.997759

APPENDIX E - PREDICTED RELATIVE SENSOR OFFSET DUE TO RADIOMETRIC PERFORMANCE OF GSE

Calculate relative offset variation as function of scan angle while viewing 110 K blackbody,
File: /sabercal/DCPs/mcd/sab_cal_pred.mcd, Section 5, 1/20/00

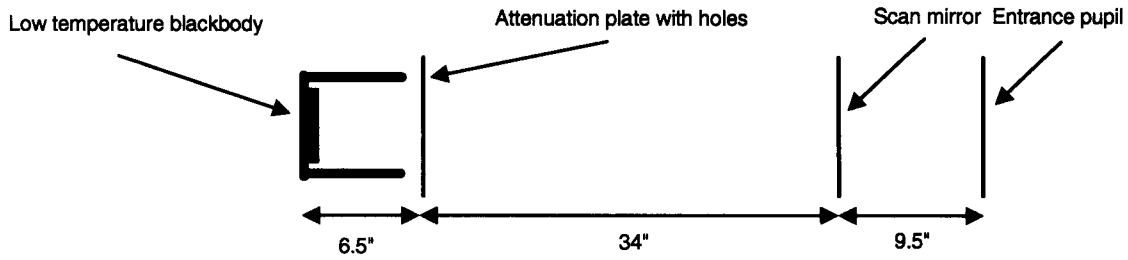

$d_{bb\_to\_ap} := 6.5\cdot in + 34\cdot in - d_{sm\_to\_ap}$ $d_{bb\_to\_ap} = 2.5008\cdot 10^{1}\ \cdot in$

Approximate SABER thermal FOV area

$A_{ex\_sab} := A_{sab}\cdot 1.1^2 + 2\cdot in\cdot 3\cdot in$ $A_{ex\_sab} = 4.7254\cdot 10^{1}\ \cdot in^2$ $A_{sab} = 3.4094\cdot 10^{1}\ \cdot in^2$

$Clear\_ap_{BB} := 5.75\cdot in$ $A_{bb} := \pi\cdot\left(\frac{Clear\_ap_{BB}}{2}\right)^2$

$\gamma_{sab\_ap\_to\_bb}(\theta) := \frac{A_{ex\_sab}\cdot A_{bb}}{d_{bb\_to\_ap}^{2}}\cdot\cos(\theta)$ throughput between SABER and LTBB

$T_{sab} := 237$ Average SABER telescope temperature $T_{back} := 300$ Background temp

$rfl_{bb} := 0.06$ Approximate LTBB normal reflectance

$yvec_0 := 0.08$ $yvec_1 := 0.005$ $\theta vec_0 := 14\cdot deg$ $\theta vec_1 := 25\cdot deg$
Attenuation factor for 300K radiation between test chamber baffles and SABER, reasonable guess

$seal(\theta) := linterp(\theta vec, yvec, \theta)$ $seal(14\cdot deg) = 8\cdot 10^{-2}$

SABER thermal emission radiance reflected off surface of BB

$$Flux_{tel}(\theta, ch, T_{sab}) := \frac{\gamma_{sab\_ap\_to\_bb}(\theta)\cdot N(\lambda_{ch,1}, \lambda_{ch,2}, T_{sab})\cdot rfl_{bb}}{A_{bb}\cdot\pi}$$

$$Flux_{back}(\theta, ch, T_{back}) := \frac{\gamma_{sab\_ap\_to\_bb}(0\cdot deg)\cdot 0.3\cdot N(\lambda_{ch,1}, \lambda_{ch,2}, T_{back})\cdot seal(\theta)\cdot rfl_{bb}}{A_{bb}\cdot\pi}$$

$$L_{BB\_rfl}(\theta, ch, T_{sab}, T_{back}) := Flux_{tel}(\theta, ch, T_{sab}) + Flux_{back}(\theta, ch, T_{back})$$

R_meas_k

$\left(\frac{count}{\frac{W}{cm^2 \cdot sr}}\right)$
$1.04 \cdot 10^8$
$8.08 \cdot 10^7$
$8.82 \cdot 10^7$
$8.31 \cdot 10^8$
$1.28 \cdot 10^9$
$1.98 \cdot 10^{10}$
$2.28 \cdot 10^{10}$

Measured responsivity. SABER calibration summary report Jan. 2000

$\theta := 14 \cdot deg, 14.5 \cdot deg .. 25 \cdot deg$

$Resp(\theta, ch, T_{sab}, T_{back}) := \left(L_{BB\_rfl}(\theta, ch, T_{sab}, T_{back}) - L_{BB\_rfl}(14 \cdot deg, ch, T_{sab}, T_{back})\right) \cdot R\_meas_{ch}$

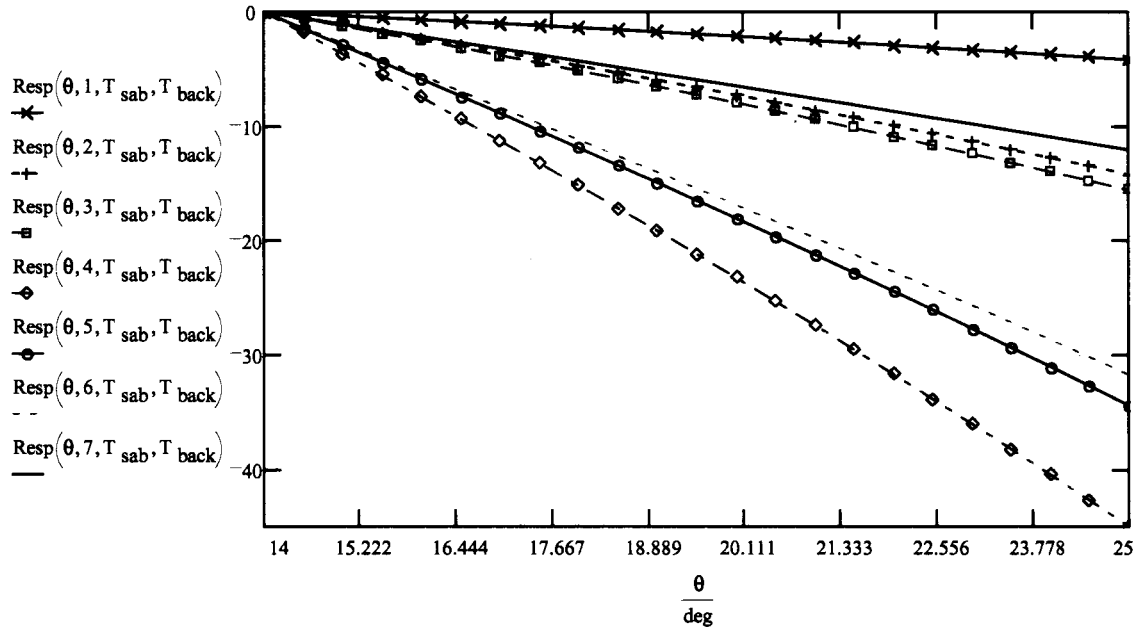

$Resp(14 \cdot deg, k, T_{sab}, T_{back}) - Resp(25 \cdot deg, k, T_{sab}, T_{back})$ Maximum change as function of angle

4.1736
$1.4186 \cdot 10$
$1.5575 \cdot 10$
$4.5077 \cdot 10$
$3.4445 \cdot 10$
$3.1793 \cdot 10$
$1.2039 \cdot 10$

APPENDIX F - ELECTRONIC SUB-SYSTEM LOW PASS FILTER MEASUREMENTS

APPENDIX G - JONES SOURCE REPEATABILITY DUE TO ELECTRONICS TEMPERAURE AND TOTAL DOSE RADIATION